

Quasi-free cross section measurements for the  $\pi^+\pi^-$   
electroproduction off the proton in deuterium with  
CLAS and a 2.039 GeV beam

Iuliia A. Skorodumina<sup>1,a</sup>, Gleb V. Fedotov<sup>2</sup>, Ralf W. Gothe<sup>1</sup>

<sup>1</sup>*Department of Physics and Astronomy, University of South Carolina, Columbia, SC*

<sup>2</sup>*National Research Centre “Kurchatov Institute” B. P. Konstantinov Petersburg Nuclear Physics Institute,  
Gatchina, St. Petersburg, Russia*

*E-mail:* <sup>a</sup>*skorodumina@gmail.com*

# <sup>1</sup> Contents

<sup>2</sup> 1	<b>Introduction</b>	<b>4</b>
<sup>3</sup> 2	<b>Event selection</b>	<b>7</b>
<sup>4</sup> 2.1	Particle identification . . . . .	8
<sup>5</sup> 2.1.1	Electron identification . . . . .	9
<sup>6</sup> 2.1.2	Hadron identification . . . . .	21
<sup>7</sup> 2.2	Momentum corrections . . . . .	26
<sup>8</sup> 2.2.1	Proton momentum correction (energy loss) . . . . .	26
<sup>9</sup> 2.2.2	Electron momentum correction . . . . .	27
<sup>10</sup> 2.3	Other cuts . . . . .	30
<sup>11</sup> 2.3.1	Fiducial cuts . . . . .	30
<sup>12</sup> 2.3.2	Data quality check . . . . .	39
<sup>13</sup> 2.3.3	Vertex cut . . . . .	40
<sup>14</sup> 2.4	Exclusivity cut in the presence of Fermi smearing and FSI . . . . .	45
<sup>15</sup> 2.4.1	Fully exclusive topology . . . . .	50
<sup>16</sup> 2.4.2	$\pi^-$ missing topology . . . . .	54
<sup>17</sup> 3	<b>Cross section calculation</b>	<b>57</b>
<sup>18</sup> 3.1	$W$ -smearing and boundary blurring of the $Q^2$ versus $W$ distribution . . . . .	57
<sup>19</sup> 3.2	Lab to CMS transformation . . . . .	60
<sup>20</sup> 3.3	Kinematic variables . . . . .	62
<sup>21</sup> 3.4	Binning and kinematic coverage . . . . .	67
<sup>22</sup> 3.5	Cross section formulae . . . . .	70

23	3.5.1 Electron scattering cross section . . . . .	70
24	3.5.2 Virtual photoproduction cross section . . . . .	71
25	3.6 Efficiency evaluation . . . . .	73
26	<b>4 Corrections to the cross sections</b>	<b>76</b>
27	4.1 Filling kinematic cells with zero acceptance . . . . .	76
28	4.2 Radiative correction . . . . .	81
29	4.3 Unfolding the effects of the target motion . . . . .	83
30	4.4 Correction for binning effects . . . . .	87
31	<b>5 Other issues</b>	<b>92</b>
32	5.1 The cross section dependence on the beam energy . . . . .	92
33	5.2 Off-shell effects . . . . .	93
34	<b>6 Normalization verification</b>	<b>94</b>
35	<b>7 Cross section uncertainties</b>	<b>101</b>
36	7.1 Statistical uncertainties . . . . .	101
37	7.2 Model dependent uncertainties . . . . .	103
38	7.3 Systematic uncertainties . . . . .	104
39	7.4 Summary for the cross section uncertainties . . . . .	107
40	<b>8 Results and conclusion</b>	<b>109</b>
41	<b>Appendices</b>	<b>114</b>
42	A: Features of missing mass distributions . . . . .	114
43	B: Lab to CMS transformation for the case of proton at rest . . . . .	120
44	C: The reaction phase-space . . . . .	122
45	D: Uncertainties for indirect measurements . . . . .	123
46	E: Analysis procedure and code availability . . . . .	124
47	F: Measured single-differential cross sections . . . . .	126
48	<b>Bibliography</b>	<b>177</b>

<sup>49</sup> **Chapter 1**

<sup>50</sup> **Introduction**

<sup>51</sup> Exclusive meson photo- and electroproduction reactions off protons are intensively studied  
<sup>52</sup> in laboratories all over the world as a very powerful tool for the investigation of nucleon  
<sup>53</sup> structure and the principles of the strong interaction. These studies include the extraction  
<sup>54</sup> of various observables through the analysis of the experimental data and the consequent  
<sup>55</sup> theoretical and phenomenological interpretations of these observables [1–3].

<sup>56</sup> By now exclusive reactions off the free proton have been studied in considerable de-  
<sup>57</sup> tail, and a lot of information on differential cross sections and different single and double-  
<sup>58</sup> polarization asymmetries with almost complete coverage of the final hadron phase-space is  
<sup>59</sup> available. A large part of this information came from the analysis of data collected in Hall  
<sup>60</sup> B at Jefferson Lab with the CLAS detector [4] and stored in the CLAS physics database [5].

<sup>61</sup> Meanwhile, reactions occurring in photon and electron scattering off nuclei are less ex-  
<sup>62</sup> tensively investigated, i.e. the experimental information on these processes is scarce and  
<sup>63</sup> mostly limited to the inclusive measurements of total nuclear photoproduction cross sec-  
<sup>64</sup> tions [6–8] and nucleon structure function  $F_2$  [9–11]. The available inclusive data, however,  
<sup>65</sup> exhibit some surprising peculiar features not fully elucidated over the years, which are now  
<sup>66</sup> attracting significant scientific attention. Specifically, the nuclear photoproduction cross sec-  
<sup>67</sup> tion (per nucleon) turns out to be less pronounced and damped in strength compared with  
<sup>68</sup> the cross section off the free proton. This effect manifests itself differently depending on the  
<sup>69</sup> invariant mass range, i.e. the  $\Delta(1232)$ -resonance peak is damped, but still evident for all nu-  
<sup>70</sup> clei, however, the second resonance region becomes somewhat less pronounced and damped  
<sup>71</sup> for the deuteron and strongly suppressed and structureless for all heavier nuclei. A similar  
<sup>72</sup> effect is observed in the behavior of the nucleon structure function  $F_2$ , which in the case of  
<sup>73</sup> the deuteron shows moderate damping and flattening [10] and completely loses its structure,  
<sup>74</sup> when measured off carbon [11] (compared with the free proton structure function [12]). A  
<sup>75</sup> fact of particular interest is that the intensity of this effect increases as  $Q^2$  grows, i.e. as  $Q^2 =$   
<sup>76</sup>  $3 \text{ GeV}^2$  is reached, the structure function  $F_2$  becomes almost flat even for the deuteron [11].  
<sup>77</sup> These peculiar features can not be explained by the Fermi motion of nucleons in the nucleus

78 and are thought to be an indication that nucleons and their excited states, bound inside the  
79 nuclear medium, may be subject to some modifications of their properties [6–8, 13, 14].

80 This phenomenon, which is still not fully understood, generates lots of debates among  
81 scientists, triggering efforts to describe the processes that happen in reactions off bound  
82 nucleons. These studies rely heavily on the experimental data, which at the moment are  
83 mostly limited to inclusive measurements [6–11] and lack information on exclusive reactions.  
84 This information, however, is crucial, since various exclusive channels have different energy  
85 dependencies and different sensitivity to reaction mechanisms. This situation creates a strong  
86 demand for exclusive measurements off bound nucleons, and the deuteron, being the lightest  
87 and weakly-bound nucleus, is the best target for initiating these efforts.

88 This study provides the first results of cross section measurements for the exclusive  
89 process of charged double-pion electroproduction off the proton bound in the deuteron. The  
90 results are obtained through the analysis of experimental data on electron scattering off the  
91 deuteron target, collected with the CLAS detector. The measurements are performed in  
92 the second resonance region, where the double-pion production plays an important role, i.e.  
93 the channel opens at the double-pion production threshold at  $W \approx 1.22$  GeV, contributes  
94 significantly to the total inclusive cross section for  $W \lesssim 1.6$  GeV, and starts to dominate all  
95 other exclusive channels for  $W \gtrsim 1.6$  GeV .

96 The experimental identification of exclusive multi-particle final states is a rather sophisti-  
97 cated task, which requires certain analysis techniques to be elaborated and established. This  
98 was carried out over the last twenty years as the different studies of double-pion production  
99 off the free proton were being performed [15–23], and currently a solid framework for such  
100 studies is in place. For this particular study, focused on the  $N\pi\pi$  final state, this framework  
101 laid the foundation. However, the deuteron as a target introduces some specific issues, which  
102 are external to the free proton data analysis and originate from (a) the motion of the target  
103 proton in the deuteron and (b) complex effects of the final state interactions due to the  
104 presence of the additional nucleon. This caused some difficulties that were encountered and  
105 needed to be overcome during the analysis and, therefore, in this report special attention is  
106 paid to a detailed description of these issues.

107 Specifically, the report presents the integrated and single-differential cross sections of the  
108 reaction  $\gamma_vp(n) \rightarrow p'(n')\pi^+\pi^-$  in the kinematic region of invariant mass  $W$  from 1.3 GeV  
109 to 1.825 GeV and photon virtuality  $Q^2$  from 0.4 GeV $^2$  to 1 GeV $^2$ . Sufficient experimental  
110 statistics allows narrow binning, e.g. 25 MeV in  $W$  and 0.05 GeV $^2$  in  $Q^2$ , while maintaining  
111 an adequate statistical uncertainty. Cross sections are extracted in the quasi-free regime,  
112 which implies that only events not affected by final state interactions were selected.

113 This study benefits from the fact that the corresponding cross sections of the same exclu-  
114 sive reaction off the free proton have been recently extracted from CLAS data [22, 23]. These  
115 free proton measurements were performed under the same experimental conditions as the  
116 cross sections of this study, including the beam energy value and the target setup. For the  
117 majority of  $(W, Q^2)$  points, the statistical uncertainty combined with the model dependent

<sup>118</sup> uncertainty ( $\delta_{\text{stat, mod}}^{\text{tot}}$ ) is on a level of  $\sim 1\%-3\%$  for the free proton integral cross sections and  
<sup>119</sup> on a level of  $\sim 4\%-6\%$  for the quasi-free integral cross sections obtained in this study. Being  
<sup>120</sup> performed in the same experimental configuration, both measurements have identical bin-  
<sup>121</sup> ning in all kinematic variables and similar inherent systematic inaccuracies. Therefore, the  
<sup>122</sup> direct comparison of these two sets of cross sections provides experimentally the best possi-  
<sup>123</sup> ble opportunity to investigate the differences and alterations (including possible in-medium  
<sup>124</sup> modifications) that occur in the exclusive reaction off the bound proton in comparison with  
<sup>125</sup> that off the free proton. This comparison also allows us to better understand the influence  
<sup>126</sup> of Fermi motion and final state interactions on the cross sections.

<sup>127</sup> A few example plots, which demonstrate the difference between integral cross sections  
<sup>128</sup> obtained in this analysis and their free proton analogue from Ref. [22, 23] are given in Sect. 8  
<sup>129</sup> of this report. Meanwhile, the complete compilation of this comparison as well as the full  
<sup>130</sup> physical discussion of the results and their physical interpretation will be presented in the  
<sup>131</sup> PhD thesis (which is in preparation) and a future publication on the subject.

<sup>132</sup> **Chapter 2**

<sup>133</sup> **Event selection**

<sup>134</sup> This report presents the analysis of experimental data that were collected at JLab Hall B  
<sup>135</sup> with the CLAS detector [4]. The measurements were part of the “e1e” run period that  
<sup>136</sup> lasted from November 2002 until January 2003 and included several parts with different  
<sup>137</sup> beam energies (1 GeV and 2.039 GeV) and different target cell content (liquid hydrogen and  
<sup>138</sup> liquid deuterium). The torus current was 2250 A and the mini torus current 5995 A. This  
<sup>139</sup> particular analysis concentrates on the dataset obtained with the 2-cm-long liquid deuterium  
<sup>140</sup> target and a 2.039 GeV polarized electron beam. The range of run numbers is 36516 - 36615.

<sup>141</sup> All data collected with the CLAS detector is stored in a specific format, which is BOS  
<sup>142</sup> format [24, 25]. The information on the detector response to particles passing through is  
<sup>143</sup> recorded for each event and sorted into the set of BOS banks. The original BOS files store the  
<sup>144</sup> data in terms of “raw” signals (like TDC, ADC). These “raw” files are then “cooked” with  
<sup>145</sup> the reconstruction software (reccsis), which converts the detector response to the variables  
<sup>146</sup> that characterize the events directly, i.e. the particle momentum, the track coordinates,  
<sup>147</sup> timing, etc. This information is also stored in BOS banks. However, since the cooking  
<sup>148</sup> process introduces new variables, the structure of the “cooked” BOS files is different from  
<sup>149</sup> that for the “raw” files. The “cooked” data is stored in various formats including BOS files  
<sup>150</sup> and ROOT ntuples. In this analysis the latter were used<sup>1</sup>.

<sup>151</sup> Events corresponding to the investigated reaction  $ep(n) \rightarrow e'p'(n')\pi^+\pi^-$  are distinguished  
<sup>152</sup> among all other registered events through the event selection procedure, described in detail  
<sup>153</sup> in this Section. The selected exclusive events, however, represent only a part of the total  
<sup>154</sup> number of events produced in the reaction, while the remainder were not registered due to  
<sup>155</sup> (i) geometrical holes in the detector acceptance and (ii) less than 100% efficiency of particle  
<sup>156</sup> detection within the detector acceptance. Therefore, to extract the reaction cross section,  
<sup>157</sup> the experimental event yield should be adjusted for the geometric and detection efficiency,  
<sup>158</sup> thus accounting for the lost events.

---

<sup>1</sup> The location of the data files is provided in App. E. The link to the scripts, which were used in the simulation/reconstruction sequence for this analysis is also given there.

159 In order to determine the detector efficiency, a Monte Carlo simulation is typically per-  
160 formed. In this analysis, double-pion events are generated with TWOPEG-D, which is an  
161 event generator for the double-pion electroproduction off a moving proton [26]. These events  
162 are hereinafter called “generated” events.

163 The generated events are passed through a standard multi-stage procedure of simulating  
164 the detector response [4]. At the first stage the interaction of the generated events with the  
165 CLAS detector is simulated. For this purpose, the GSIM package (GEANT SIMulation) is  
166 used. GSIM incorporates information about the detector geometry and materials with their  
167 electromagnetic properties, magnetic fields, target material and geometry, etc. It propagates  
168 all the particles through the CLAS detector from the vertex produced by the event generator  
169 and provides the detector response in terms of the same “raw” signals as the actual CLAS  
170 detector does.

171 Although the GSIM package includes all the detector geometry and properties, it still  
172 does not properly reproduce the resolution of the drift chambers and the TOF system. So  
173 the GSIM Post Processor (GPP) is used to better match the resolution as well as to include  
174 the effects of less-than-perfect detector response (due to broken drift wires, problematic  
175 phototubes, etc.). The latter effects are unique for a particular run period, and therefore the  
176 information on the detector imperfections is usually provided along with the data files to be  
177 then used in the GPP. Meanwhile, the GPP parameters intended to adjust the resolution  
178 (DC and TOF smearing factors) are typically determined individually during a particular  
179 analysis as the resolution depends on kinematics and hence on experimental conditions.  
180 This analysis uses the same resolution related GPP parameters as those determined in the  
181 study [22, 23], which reports the cross section measurements off the free proton performed  
182 under the same experimental conditions (as they were also a part of the “e1e” run period).

183 At the final stage the GPP output files are “cooked” using the same reconstruction  
184 software that was used for the real data (recois). Events that survive after the “cooking”  
185 process are hereinafter called “reconstructed” Monte Carlo events. They are analyzed in the  
186 same way as real experimental events.

## 187 2.1 Particle identification

188 The CLAS detector consists of six sectors that are operated as independent detectors [4].  
189 Each sector includes four sub-detectors: Drift Chambers (DC), Čerenkov Counters (CC),  
190 Time-of-Flight System (TOF), and Electromagnetic Calorimeters (EC).

191 In the initial analysis step, all collected events are subject to a standard event preselec-  
192 tion<sup>2</sup>, which is performed using specific variables from the BOS banks [24, 25]. Firstly, to

---

<sup>2</sup>In this analysis this preselection is performed when converting the “h10” ROOT ntuples to the “t21” ROOT ntuples. See more details in App. E.

193 ensure that particles within an event were properly reconstructed, the number of geometri-  
194 cally reconstructed particles (*gpart*) is required to be greater than zero for each event. The  
195 *gpart* variable is extracted from the variable *NPGP* in the HEVT bank according to the  
196 following relation,

$$NPGP = (\text{Number of final reconstructed particles}) \times 100 + gpart. \quad (2.1.1)$$

197 Then, to exclude from consideration out-of-time particles, the status word *stat* (which  
198 corresponds to the variable *Status* in the EVNT bank) is required to be greater than zero  
199 for each particle candidate.

200 For each event the electron candidate is defined as the first in time particle that gives  
201 signals in all four parts of the CLAS detector (DC, CC, TOF, and EC), which means that the  
202 variables *DCStat*, *CCStat*, *SCStat*, and *ECStat* from the EVNT bank should be greater  
203 than zero. To select hadron candidates, signals only in two sub-detectors (DC and TOF)  
204 are required, i.e. the variables *DCStat* and *SCStat* from the EVNT bank should be greater  
205 than zero.

206 Finally, all particle candidates should have an appropriate charge, i.e. the variable  
207 *Charge* from the EVNT bank is required to be  $\pm 1$  depending on the candidate type.

208 The particle candidates that survive this event preselection are then subject to further  
209 detailed selection, which is described below.

### 210 2.1.1 Electron identification

211 Firstly, the electromagnetic calorimeter (EC) and Čerenkov counter (CC) responses need to  
212 be examined, to reveal good electrons among all electron candidates and to separate them  
213 from electronic noise, accidentals and the contamination from negative pions.

#### 214 EC cuts

215 According to [27], the overall EC resolution as well as uncertainties from the EC output  
216 summing electronics lead to fluctuations of the EC response near the hardware threshold.  
217 Therefore, to select only reliable EC signals, a minimal cut on the scattered electron mo-  
218 mentum  $P_{e'}$  should be applied in the software. The value of this cut is chosen according to  
219 the relation (2.1.2) suggested in [27],

$$P_{e'}^{min} \text{ (in MeV)} = 214 + 2.47 \cdot V_{th} \text{ (in mV)}, \quad (2.1.2)$$

220 where  $V_{th}$  is the calorimeter threshold voltage.

221 For “e1e” run  $V_{th} = 100$  mV, which results in  $P_{e'}^{min} = 461$  MeV.

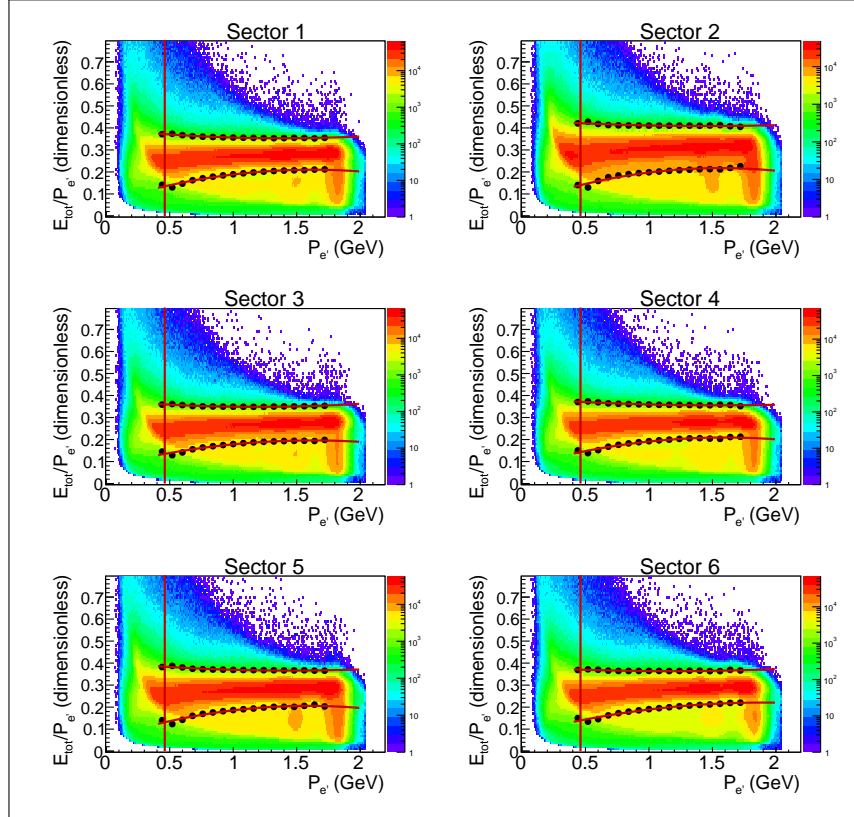


Figure 2.1: Sampling fraction distributions for the data. The six plots correspond to the six CLAS sectors. The vertical red line at  $P_{e'} = 0.461$  GeV shows the EC threshold cut. Black points correspond to the positions of Gaussian fit maxima  $\pm 3\sigma$  for different  $X$ -slices of the 2D histograms. These points are fit by a second order polynomial, the resulting functions are shown by the red curves. Events between the red curves are selected for further analysis.

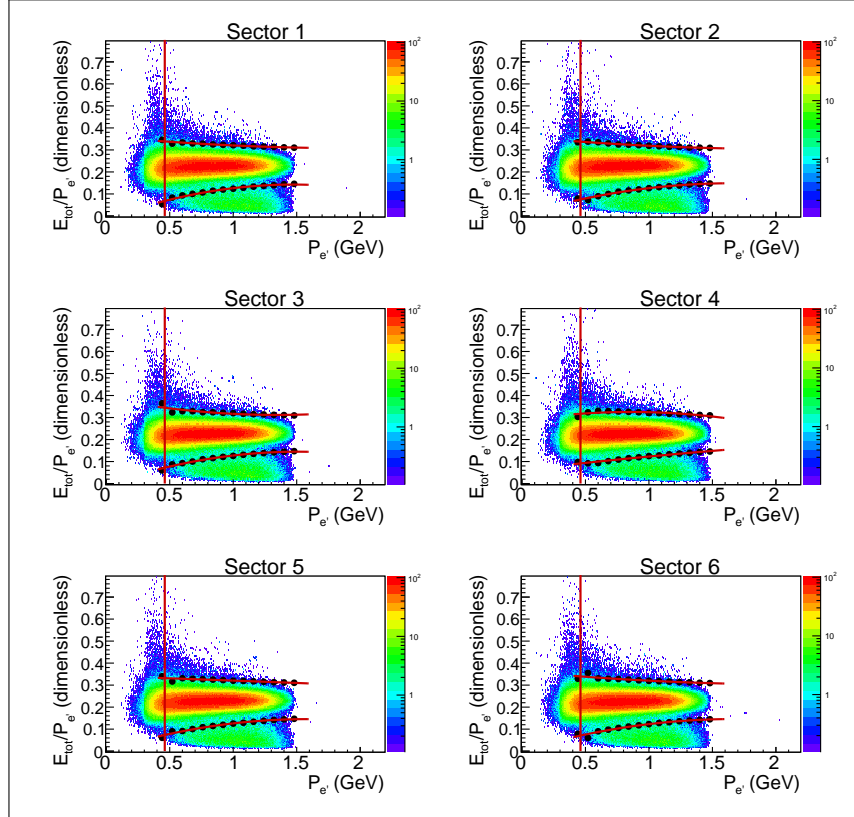


Figure 2.2: Sampling fraction distributions for the reconstructed Monte Carlo events. The six plots correspond to the six CLAS sectors. The vertical red line at  $P_{e'} = 0.461$  GeV shows the EC threshold cut. Black points correspond to the positions of Gaussian fit maxima  $\pm 3\sigma$  for different  $X$ -slices of the 2D histograms. These points are fit by a second order polynomial, the resulting functions are shown by the red curves. Events between red curves are selected for further analysis.

Then, the so-called sampling fraction cut is applied to eliminate part of the pion contamination. To develop this cut, the fact that electrons and pions have different energy deposition patterns in the EC is used. An electron produces an electromagnetic shower, where the deposited energy  $E_{tot}$  is proportional to the scattered electron momentum  $P_{e'}$ , while a  $\pi^-$  loses a constant amount of energy per scintillator ( $\sim 2$  MeV/cm) independently of its momentum. Therefore, for electrons the quantity  $E_{tot}/P_{e'}$  plotted as a function of  $P_{e'}$  should follow the straight line that is parallel to the  $x$ -axis and located around the value  $1/3$  on the  $y$ -axis, since electrons lose about  $2/3$  of their energy in lead sheets (in reality this line has a slight slope).

In Fig. 2.1 the total energy deposited in the EC divided by the particle momentum is shown as a function of particle momentum. The six plots correspond to the six CLAS sectors. Events between the red curves are selected as good electron candidates for further analysis. The vertical red line at  $P_{e'} = 0.461$  GeV shows the EC threshold cut. The upper and lower red curves are obtained in the following way:  $X$ -slices of the 2D histograms are fit by Gaussians. In this way points that correspond to the positions of the fit maxima  $\pm 3\sigma$  are obtained. These points are shown by black circles in Fig. 2.1. They determine the upper and lower boundaries for the cut. Finally, to obtain smooth curves, all points are fit by a second order polynomial.

Cuts on the minimal electron momentum and on sampling fraction are applied both to the experimental and reconstructed Monte Carlo events. Since the Monte Carlo simulation does not reproduce electromagnetic showers well enough, the sampling fraction distributions for the simulation are slightly lower than for the data. EC cuts for the simulation, obtained using the same procedure as for the data, are shown in Fig. 2.2. These plots contain no events with  $P_{e'} > 1.5$  GeV since only double-pion events were generated, while for the data events with  $P_{e'} > 1.5$  GeV exist since Figure 2.1 was plotted for inclusive electrons.

## CC cuts

To improve the quality of the electron candidate selection and  $\pi^-/e^-$  separation, a Čerenkov counter is used [28]. As shown in [29], there is a contamination in the measured CC spectra that manifests itself as a so-called single-photoelectron peak, which is actually located at a few photoelectrons (see the distributions shown in black in Fig. 2.5). The main source of this contamination are accidental coincidences of PMT noise signals with measured pion tracks [29]. The goal of CC cuts is to separate the spectrum of good electron candidates (it corresponds to the main maximum of the photoelectron distribution) from the single-photoelectron peak, but at the same time to minimize the loss of good events. As seen in Fig. 2.5 (black curves), where photoelectron distributions are plotted, the single-photoelectron peak is rather pronounced and it significantly overlaps with the spectrum of good electron candidates. Thus the elimination of this contamination is not a straightforward task and a special procedure has been developed for this purpose.

260 The following set of CC cuts was applied:

- 261 • fiducial cut,  
262 •  $\varphi_{cc}$  matching cut,  
263 •  $\theta_{cc}$  matching cut,  
264 • geometrical cut that removes inefficient zones, and  
265 • standard procedure of dealing with the single-photoelectron peak contamination based  
266 on the fit of the photoelectron distributions by the modified Poisson function.

267 All these cuts, except the last one, are defined in the so-called “CC projective plane” [29].  
268 This is an imaginary plane behind the CC where the Čerenkov radiation would arrive if its  
269 polygonal (due to reflections in the mirror system) path from the emission point to the PMT  
270 was substituted by a straight line preserving the initial propagation direction and the total  
271 distance traveled [28, 29]. The polar and azimuthal angles ( $\theta_{cc}, \varphi_{cc}$ ), which are defined in  
272 this projective plane, are not directly available in the BOS banks [24]. Therefore, some  
273 calculations are made to derive these angles from the variables available in the DCPB bank.  
274 Figure 2.3 illustrates these calculations.

275 The CC projective plane is defined in the sector reference coordinate system, i.e. the  
276 sector is bisected in the middle by the  $xz$ -plane with the  $z$ -axis directed along the beam line.  
277 In this reference system the equation of the projective plane is the following (according to  
278 Ref. [29]),

$$\begin{aligned} Ax + By + Cz + D &= 0, \\ A &= -0.000785, \quad B = 0, \\ C &= -0.00168, \quad D = 1, \\ \vec{S} &= (A, B, C), \end{aligned} \tag{2.1.3}$$

279 where  $\vec{S}$  is a vector perpendicular to the projective plane.

280 In Fig. 2.3 the particle track in the DC is shown by the thin dashed curve. Since the  
281 particle moves through a magnetic field in the DC, the track is curved. Having left the  
282 magnetic field region of the DC, the particle moves further along a straight line, tangential  
283 to a curved DC track in the point of its intersection with the CC. The unit vector that  
284 defines the direction of this tangent is known from the DCPB bank  $\vec{n} = (n_x, n_y, n_z) =$   
285  $(\text{CX\_SC}, \text{CY\_SC}, \text{CZ\_SC})$ . In Fig. 2.3 the vector  $\vec{t}$  is pointing this direction and goes from  
286 the SC hit point to the CC projective plane.

287 The  $(\theta_{cc}, \varphi_{cc})$  angles in the projective plane are determined by the vector  $\vec{P} = \vec{P}_0 + \vec{t}$ ,  
288 where  $\vec{P}_0$  is a vector that goes from the vertex to the point of the track intersection with the  
289 SC. Its components are known from the DCPB bank<sup>3</sup>  $\vec{P}_0 = (p_x^0, p_y^0, p_z^0) = (\text{x\_SC}, \text{y\_SC}, \text{z\_SC})$ .

---

<sup>3</sup> In the DCPB bank both  $\vec{n}$  and  $\vec{P}_0$  are defined in the sector reference frame.

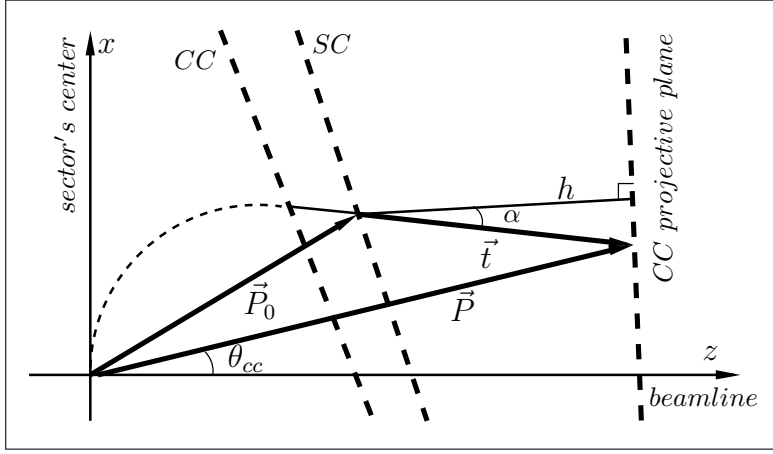


Figure 2.3: Illustration for the calculation of the polar  $\theta_{cc}$  and azimuthal  $\varphi_{cc}$  angles in the CC projective plane (see text for details).

<sup>290</sup> The vector  $\vec{t}$  can be defined as

$$\vec{t} = |\vec{t}| \cdot \vec{n} = \frac{h}{\cos \alpha} \cdot \vec{n}, \quad (2.1.4)$$

<sup>291</sup> where  $\vec{n}$  is the unit vector in the  $\vec{t}$ -direction defined above, while  $h$  is the distance from  
<sup>292</sup> the SC hit point to the CC projective plane, which is given by<sup>4</sup>

$$h = \frac{|(\vec{S} \cdot \vec{P}_0) + D|}{|\vec{S}|}, \quad (2.1.5)$$

<sup>293</sup> where  $\vec{S}$  is the vector normal to the CC projective plane defined by Eq. (2.1.3).

<sup>294</sup> In turn  $\cos \alpha$  can be calculated as

$$\cos \alpha = \frac{|(\vec{S} \cdot \vec{n})|}{|\vec{S}|}, \quad (2.1.6)$$

<sup>295</sup> since  $\vec{S}$  is directed along  $h$  and  $\vec{n}$  is directed along  $\vec{t}$ .

<sup>296</sup> This leads to the following expression for the vector  $\vec{t}$ ,

$$\vec{t} = |\vec{t}| \cdot \vec{n} = \left| \frac{(\vec{S} \cdot \vec{P}_0) + D}{(\vec{S} \cdot \vec{n})} \right| \cdot \vec{n} = \left| \frac{A \cdot p_x^0 + B \cdot p_y^0 + C \cdot p_z^0 + D}{A \cdot n_x + B \cdot n_y + C \cdot n_z} \right| \cdot \vec{n}. \quad (2.1.7)$$

---

<sup>4</sup>This is a standard relation for the distance from the point (given here by the vector  $\vec{P}_0$ ) to the plane  $Ax + By + Cz + D = 0$ .

297 Then, obtaining the required vector  $\vec{P}$  as the sum of  $\vec{P}_0$  and  $\vec{t}$ , one can finally calculate  
 298 the angles  $\theta_{cc}$  and  $\varphi_{cc}$  as

$$\begin{aligned}\theta_{cc} &= \arccos\left(\frac{P_z}{|\vec{P}|}\right), \\ \varphi_{cc} &= \arctan\left(\frac{P_y}{P_x}\right).\end{aligned}\tag{2.1.8}$$

299 The angle  $\varphi_{cc}$  defined by Eq. (2.1.8) is determined with respect to the center of each  
 300 sector. This means that  $\varphi_{cc} = 0$  is the middle of the sector,  $\varphi_{cc} < 0$  is on the left side of the  
 301 sector, and  $\varphi_{cc} > 0$  is on its right side.

302 One should also define the variables *CC segment number* (that indicates which segment  
 303 has been hit) and *index* (that indicates which PMT has fired). They are taken from the  
 304 CCPB bank *Status* variable according to the following relation,

$$Status = 10 \times (\text{CC segment number}) + 1000 \times (1 + \text{index}),\tag{2.1.9}$$

305 where *index* is 1 for right PMTs,  $-1$  for left PMTs, and 0 when both PMTs have fired.

306 After all needed variables have been defined, all the cuts from the list specified above  
 307 can be implemented.

308 First of all the fiducial cut in the CC plane is applied. The shape of this cut is taken  
 309 from [30] and is given by

$$\begin{aligned}\theta_{cc} &> 7.0 + 0.0032 \cdot \varphi_{cc} + 0.0499 \cdot \varphi_{cc}^2, \\ \left(\frac{\theta_{cc} - 45.5^\circ}{34.5^\circ}\right)^2 + \left(\frac{\varphi_{cc}}{21^\circ}\right)^2 &\leq 1, \\ \left(\frac{\theta_{cc} - 45.5^\circ}{1.75^\circ}\right)^2 + \left(\frac{\varphi_{cc}}{21^\circ}\right)^2 &> 1, \text{ and} \\ \theta_{cc} &< 45^\circ.\end{aligned}\tag{2.1.10}$$

310 Then the so-called  $\varphi_{cc}$  and  $\theta_{cc}$  matching procedures (based on the studies [29] and [31]) are  
 311 performed. The idea of this matching is quite simple: there must be one-to-one correspon-  
 312 dence between the angles in the CC plane (which are calculated based on the information  
 313 from the DC) and PMT signals in the CC for real events, while background noise and  
 314 accidentals should not show such correlation.

315 The principle of the  $\varphi_{cc}$  matching cut is the following: when the track is on the right side  
 316 of the CC segment, the right PMT should be fired, and vice versa. Therefore, if  $\varphi_{cc} < 0$ ,  
 317 the *index* defined in Eq. (2.1.9) is required to be  $-1$  and if  $\varphi_{cc} > 0$ , the *index* is required  
 318 to be 1. Events that do not satisfy these conditions are removed. All events with *index* = 0  
 319 are kept.

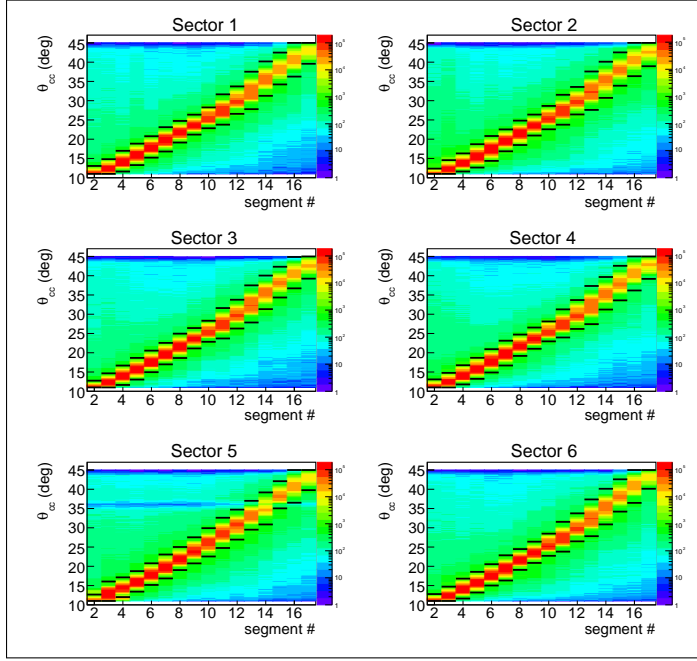


Figure 2.4:  $\theta_{cc}$  versus segment distributions for six CLAS sectors. Events between the horizontal black lines are treated as good electron candidates.

321 In order to perform  $\theta_{cc}$  matching, the  $\theta_{cc}$  versus segment number cut should be done.  
 322 Figure 2.4 shows  $\theta_{cc}$  versus segment distributions for the six CLAS sectors. Event distri-  
 323 butions in each segment have been plotted as a function of  $\theta_{cc}$  and fit by Gaussians. The  
 324 horizontal black lines correspond to the positions of the fit maxima  $\pm 4\sigma$ . Events between  
 325 these black lines are treated as good electron candidates.

326 The influence of  $\varphi_{cc}$  and  $\theta_{cc}$  matching cuts on the photoelectron distributions is demon-  
 327 strated in Fig. 2.5, where the distributions before matching cuts are plotted in black, distri-  
 328 butions after the  $\varphi_{cc}$  matching are plotted in red, and after the subsequent  $\theta_{cc}$  versus segment  
 329 cut are plotted in blue. As seen in Fig. 2.5 both these cuts reduce the single-photoelectron  
 330 peak, but leave the main part of the spectrum unchanged. The same  $\varphi_{cc}$  and  $\theta_{cc}$  matching  
 331 cuts are also applied to the reconstructed Monte Carlo events.

322 The accidental noise and pion background are not the only source of the single-  
 323 photoelectron peak contamination. The peak also partially corresponds to electrons that  
 324 hit some specific geometrical zones with low CC efficiency. When an electron hits such a  
 325 zone the number of detected photoelectrons turns out to be significantly less than expected.  
 326 This leads to the fact that the region of the photoelectron spectrum, which corresponds to the  
 327 low number of photoelectrons, appears to be overpopulated by events. Since low efficiency  
 328 zones are distributed inhomogeneously in the CC plane and the Monte Carlo simulation do  
 329 not reproduce them properly, it is better to remove them from the consideration completely.

340 For this purpose a special geometrical cut is established.

341 This geometrical cut is done in the following way. Distributions  $\varphi_{cc}$  versus  $\theta_{cc}$  are plotted  
342 for each CLAS sector (see Fig. 2.6, upper frame) with the quantity (2.1.11) as a color code.

$$\frac{\text{number of events inside } (\theta_{cc}, \varphi_{cc}) \text{ bin with more than five photoelectrons}}{\text{total number of events inside } (\theta_{cc}, \varphi_{cc}) \text{ bin}} \quad (2.1.11)$$

343 This quantity varies from zero to one and shows the proportion of electron candidates with  
344 number of photoelectrons greater than five inside a  $(\theta_{cc}, \varphi_{cc})$  bin. The value for this criterion  
345 (five photoelectrons) was chosen rather arbitrarily, since its only purpose is to facilitate the  
346 separation of inefficient zones (which correspond mostly to low numbers of photoelectrons)  
347 from the regular zones (which correspond to the full photoelectron spectrum).

348 The curved vertical stripe in sector five in Fig. 2.6 corresponds to an inefficient zone that  
349 will be discussed further in Sec. 2.3.1.

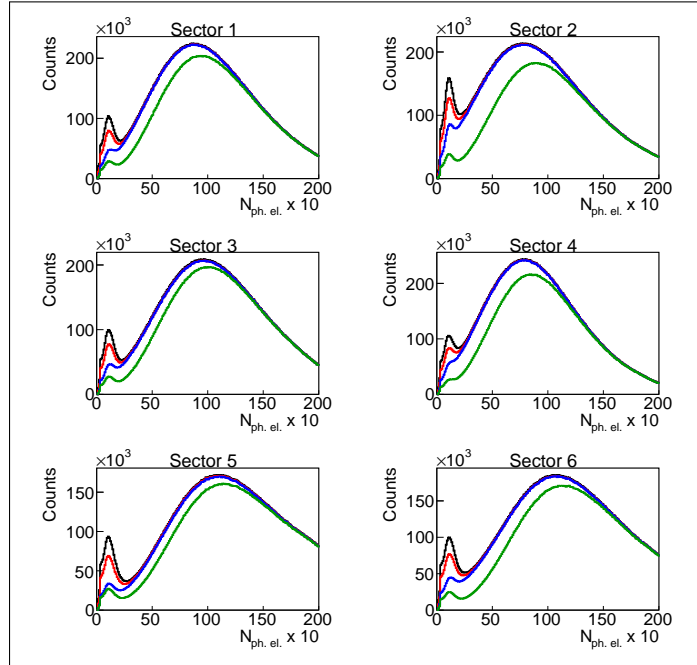


Figure 2.5: Influence of different CC cuts on the distributions of the number of photoelectrons multiplied by ten for the six CLAS sectors. Black curve – only fiducial cut in the CC plane is applied, red curve – the  $\varphi_{cc}$  matching cut is added, blue curve – the  $\theta_{cc}$  matching cut is added, and green curve – the geometrical cut in the CC plane that removes inefficient zones is finally added.

350 For further analysis only fiducial areas with a ratio (2.1.11) greater than the certain  
351 threshold value are selected. This threshold value was chosen to be 0.7, 0.65, 0.7, 0.65,  
352 0.8, and 0.8 for sectors 1, 2, 3, 4, 5, and 6, respectively. Since inefficient zones are not

353 identical for various CLAS sectors (see Fig. 2.6), different threshold values are needed for  
 354 them. Geometrical zones, which are selected for further analysis, are shown in black in the  
 355 lower plots of Fig. 2.6. All zones shown in white are treated as inefficient and are removed  
 356 from the analysis. As seen in Fig. 2.6, there is an inefficient zone in the middle of each sector.  
 357 This is expected since two CC mirrors are joined here.

358 The threshold values for the ratio (2.1.11) were chosen in order to keep the balance be-  
 359 tween the intention to reduce the amount of low efficient zones as much as possible and the  
 360 desire to preserve most of the statistics. The influence of this geometrical cut on the photo-  
 361 electron distributions in different sectors is demonstrated in Fig. 2.5, where the distributions  
 362 after the cut are plotted in green. As was expected, this cut leads to some reduction in the  
 363 low lying part of the photoelectron spectrum, including the region of the single-photoelectron  
 364 peak, and leaves the high lying part of the spectrum unchanged.

365 This geometrical cut is fully based on the experimental data. It acts as a fiducial cut,  
 366 because it simply removes certain geometrical regions in the CC plane. This means that  
 367 it can be safely applied to the Monte Carlo simulation, too. Thus, the same geometrical  
 368 regions (shown in white in the lower plots in Fig. 2.6) are removed both for the experimental  
 369 and reconstructed Monte Carlo events.

370 After the geometrical cut discussed above is applied, the single-photoelectron peak ap-  
 371 pears to be significantly smaller and better separated from the main spectrum, but still  
 372 remains (see Fig. 2.5). Therefore, in order to completely get rid of this contamination, the  
 373 standard procedure should then be applied [17].

374 To apply the standard procedure of dealing with the single-photoelectron peak contami-  
 375 nation, the photoelectron distributions are plotted for each PMT on the left and right sides  
 376 of each CC segment and for each CLAS sector (see Fig. 2.7).

377 In Fig. 2.7 the red lines show the cuts that are made in order to eliminate events under  
 378 the single-photoelectron peak. The cut position is individually optimized for each PMT in  
 379 each sector. The distributions of events, for which both right and left PMTs have fired  
 380 (*index* = 0) are not subject to this cut, since their contamination caused by the single-  
 381 photoelectron peak is assumed negligible.

382 Since the Monte Carlo does not reproduce photoelectron distributions well enough, the  
 383 cut shown by the red lines in Fig. 2.7 is applied only to the data. To recover the good electrons  
 384 that were cut off in this way, a special procedure is applied. The part of the distributions  
 385 on the right side of the red line is fit by the function (2.1.12), which is a slightly modified  
 386 Poisson distribution.

$$y = P_1 \left( \frac{P_3^{\frac{x}{P_2}}}{\Gamma \left( \frac{x}{P_2} + 1 \right)} \right) e^{-P_3}, \quad (2.1.12)$$

387 where  $P_1$ ,  $P_2$ , and  $P_3$  are free fit parameters.

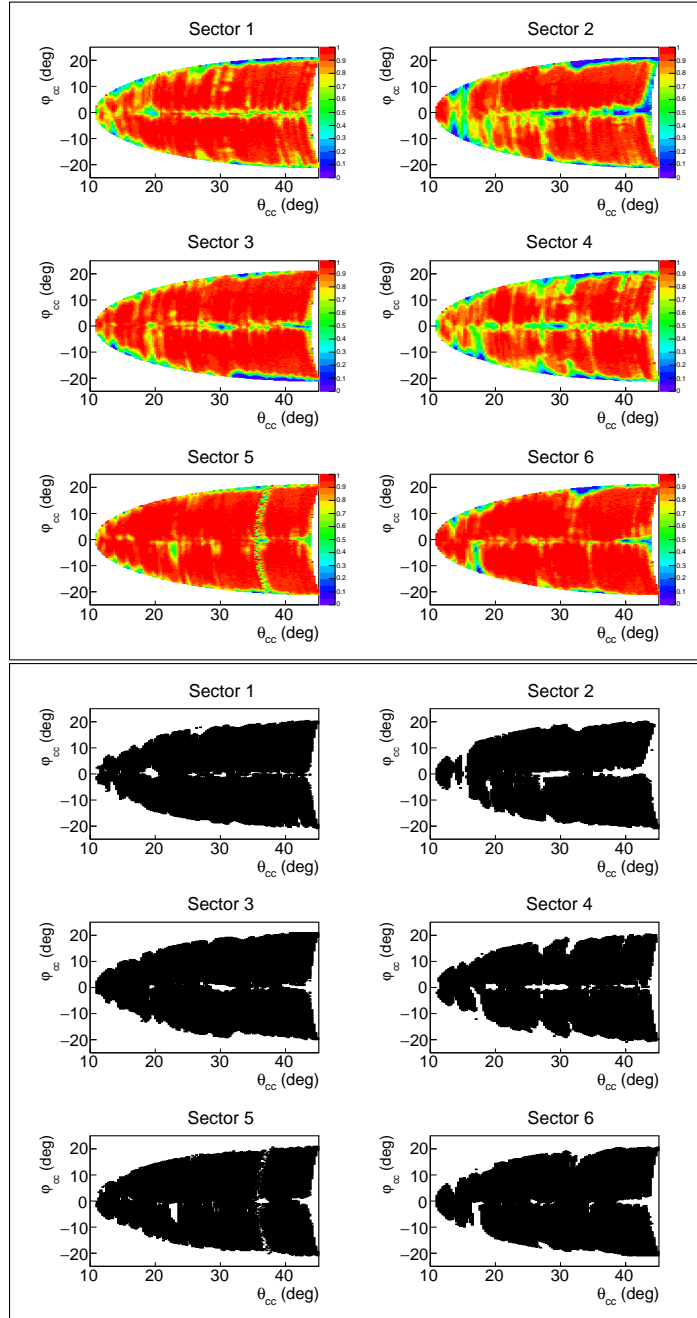


Figure 2.6: Upper frame: Distributions of the quantity (2.1.11) as a function of the polar  $\theta_{cc}$  and azimuthal  $\varphi_{cc}$  angles in the CC plane for the six CLAS sectors. This quantity varies from zero to one and shows the proportion of electron candidates with number of photoelectrons greater than five inside a  $(\theta_{cc}, \varphi_{cc})$  bin. Lower frame: Black zones correspond to the fiducial areas with the ratio (2.1.11) greater than 0.7, 0.65, 0.7, 0.65, 0.8, and 0.8 for sectors 1, 2, 3, 4, 5, and 6, respectively. These zones are selected for further analysis. All zones shown in white are treated as inefficient and removed from the analysis.

388     The fitting function is then continued into the region on the left side of the red line.  
 389     In this way the two regions, shown in blue and green in Fig. 2.7, are determined. Finally  
 390     the correction factors are defined by (2.1.13) and applied as a weight for each event, which  
 391     goes to the particular PMT. These correction factors depend on the PMT number and are  
 392     typically on a level of a few percent.

$$F_{ph. el.} = \frac{\text{green area} + \text{blue area}}{\text{green area}} \quad (2.1.13)$$

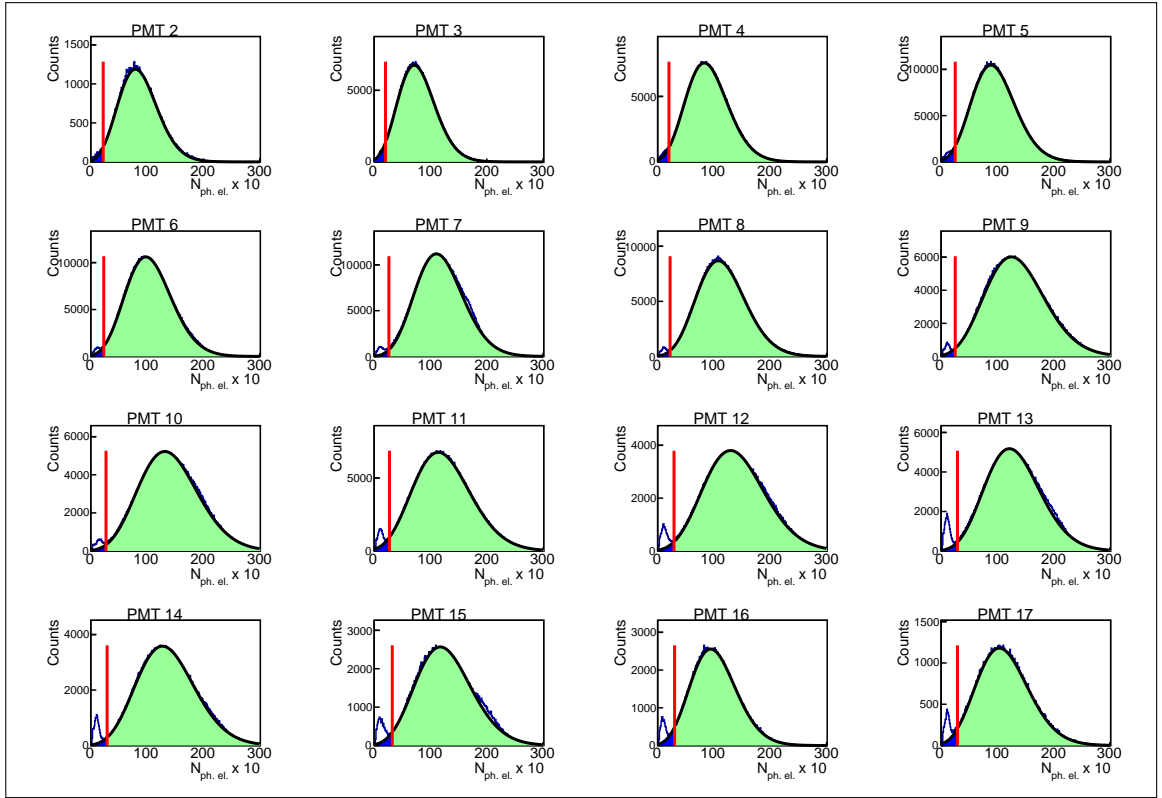


Figure 2.7: Distributions of number of photoelectrons multiplied by ten for the left side of sector one of the CC. Various plots correspond to various CC segments. Black curves show the fit by the function (2.1.12). Red vertical lines show the applied cut. Regions that are needed to calculate the correction ratio (2.1.13) are shown in blue and green.

393     Note that segments #1 and #18 are removed from the analysis completely (both in data  
 394     and Monte Carlo), since they are dominated by events from the single-photoelectron peak.

<sup>395</sup> **2.1.2 Hadron identification**

<sup>396</sup> The CLAS TOF system provides information, based on which the particle velocity can be  
<sup>397</sup> determined. In this analysis for this purpose the following calculations were done.

$$\beta_h = \frac{v_h}{c} = \frac{l_h}{t_h \cdot c}, \quad (2.1.14)$$

<sup>398</sup> where  $v_h$  is the hadron velocity,  $c$  the speed of light,  $l_h$  the hadron path length from the  
<sup>399</sup> vertex to the SC-plane (variable *Path* in the SCPB bank), and  $t_h$  the time that it took  
<sup>400</sup> the hadron to travel from the vertex to the SC-plane. This time can be calculated in the  
<sup>401</sup> following way.

$$t_h = t_e + (t_h^{tof} - t_e^{tof}) = \frac{l_e}{c} + (t_h^{tof} - t_e^{tof}), \quad (2.1.15)$$

<sup>402</sup> where  $t_e = \frac{l_e}{c}$  is the time that the electron spent on traveling from the vertex to the SC-plane  
<sup>403</sup> and  $l_e$  the electron path length.  $t_e^{tof}$  and  $t_h^{tof}$  are the times, when the electron and hadron  
<sup>404</sup> hit the SC-plane, respectively (the variable *Time* in the SCPB bank).

<sup>405</sup> Equation (2.1.15) assumes that the hadron and electron departed from the vertex at the  
<sup>406</sup> same time, but the electron traveling with the speed of light reached the SC-plane earlier  
<sup>407</sup> than the hadron. The difference  $t_h^{tof} - t_e^{tof}$  indicates the hadron delay time, which is the  
<sup>408</sup> consequence of traveling with the velocity  $v_h < c$ . Thus Eq. (2.1.15) makes the hadron time  
<sup>409</sup> related to that of electron for each event<sup>5</sup>.

<sup>410</sup> The charged hadron can be identified by the comparison of  $\beta_h$  determined from TOF  
<sup>411</sup> according to Eqs. (2.1.14) and (2.1.15) with  $\beta_n$  given by

$$\beta_n = \frac{p_h}{\sqrt{p_h^2 + m_h^2}}. \quad (2.1.16)$$

<sup>412</sup> In Eq. (2.1.16)  $\beta_n$  is a so-called nominal value that is calculated using the particle mo-  
<sup>413</sup> mentum ( $p_h$ ) known from the DC and the exact particle mass assumption ( $m_h$ ).

<sup>414</sup> The usual way to develop hadron id cuts is to investigate  $\beta$  versus momentum distribu-  
<sup>415</sup> tions for different TOF paddles for each hadron type separately. This investigation reveals  
<sup>416</sup> three types of problematic paddles, i.e.

<sup>417</sup> A Paddles which signals are completely unreliable (bad paddles). These are paddles #16  
<sup>418</sup> in sector 2, #44 in sector 3, #17 in sector 5, and #48 in each sector. They are excluded  
<sup>419</sup> from this analysis both for experimental data and reconstructed Monte Carlo events.

---

<sup>5</sup> It worth noting that usually one uses the value of  $\beta$  directly defined in the EVNT bank (variable *Betta*), but it turned out that this quantity shows noticeable inaccuracies in electron bunch determination, which were made during the cooking. The value of  $\beta$  calculated by Eqs. (2.1.14) and (2.1.15) do not show these inaccuracies because in this method the timing of the hadron is related to that of electron for each event.

420 B Paddles in which the distributions are shifted from their expected positions. The reason  
 421 for this is most likely mistakes during data cooking/calibration. Typical examples of  
 422 such paddles are shown in Fig. 2.8.

423 C Paddles for which the distributions for a given hadron have double band structure. This  
 424 problem appears for most of the paddles with number  $\geq 40$  and originates from the  
 425 fact that (along with the mistakes during cooking/calibration) for these paddles two  
 426 scintillation bars were connected to one TDC [32]. Typical examples of such paddles  
 427 are shown in Fig. 2.9.

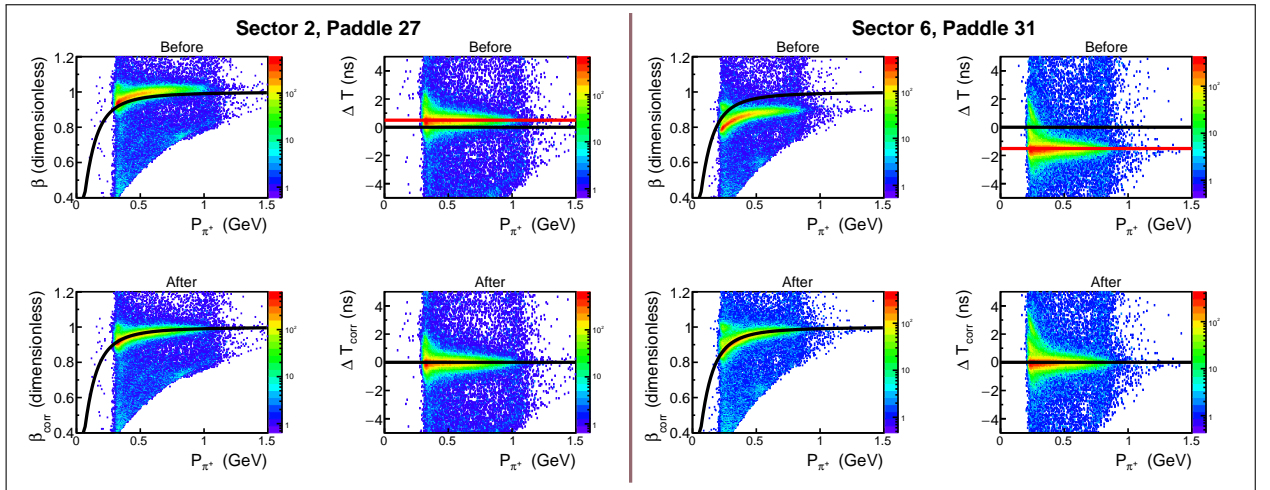


Figure 2.8: Timing correction for type B problematic paddles #27 in sector 2 (left side) and #31 in sector 6 (right side) for  $\pi^+$  candidates. The first column in each side shows the  $\beta_h$  versus momentum distributions with the black curve corresponding to the nominal  $\beta_n$  defined by Eq. (2.1.16). The second column in each side corresponds to the  $\Delta T$  versus momentum distributions, where the black horizontal line shows the position of zero and the red line shows the position of shifted  $\Delta T$ -band. The uncorrected distributions are given in the first row, while the influence of the correction is shown in the second row.

428 To cure the latter two types of problems, a so-called timing correction is developed.  
 429 To perform this correction, the quantity  $\Delta T$  is calculated, which corresponds to the time  
 430 difference between the real TOF signal and the expected one.

$$\Delta T = \frac{l_h}{c} \left( \frac{1}{\beta_n} - \frac{1}{\beta_h} \right). \quad (2.1.17)$$

431 Figure 2.8 illustrates the timing correction for type B problematic paddles #27 in sector  
 432 2 (left side) and #31 in sector 6 (right side) for  $\pi^+$  candidates. The plots in the first row  
 433 correspond to the  $\beta_h$  versus momentum and  $\Delta T$  versus momentum distributions before the

434 correction. It is seen that  $\beta_h$  versus momentum bands are shifted from their expected position  
 435 shown by the black curve, which corresponds to the nominal  $\beta_n$  defined by Eq. (2.1.16). These  
 436 shifts of  $\beta_h$  versus momentum bands are caused by the corresponding shifts of the  $\Delta T$  versus  
 437 momentum bands from zero position shown by the black horizontal lines. The idea of the  
 438 timing correction is to move  $\Delta T$  bands back to the position around zero, as shown in the  
 439 corrected  $\Delta T$  versus momentum plots in the second row. The corrected value of  $\beta$  is then  
 440 calculated as

$$\beta_{corr} = \frac{1}{\frac{1}{\beta_n} - \frac{(\Delta T - t_{shift}) \cdot c}{l_h}}, \quad (2.1.18)$$

441 where  $t_{shift}$  is the position of shifted  $\Delta T$ -band shown by the corresponding red horizontal  
 442 line in Fig. 2.8.

443 The  $\beta_{corr}$  versus momentum distributions are shown in second row in Fig. 2.8. As seen in  
 444 these plots,  $\beta_{corr}$  versus momentum bands demonstrate no shift from the black curves after  
 445 the timing correction is applied.

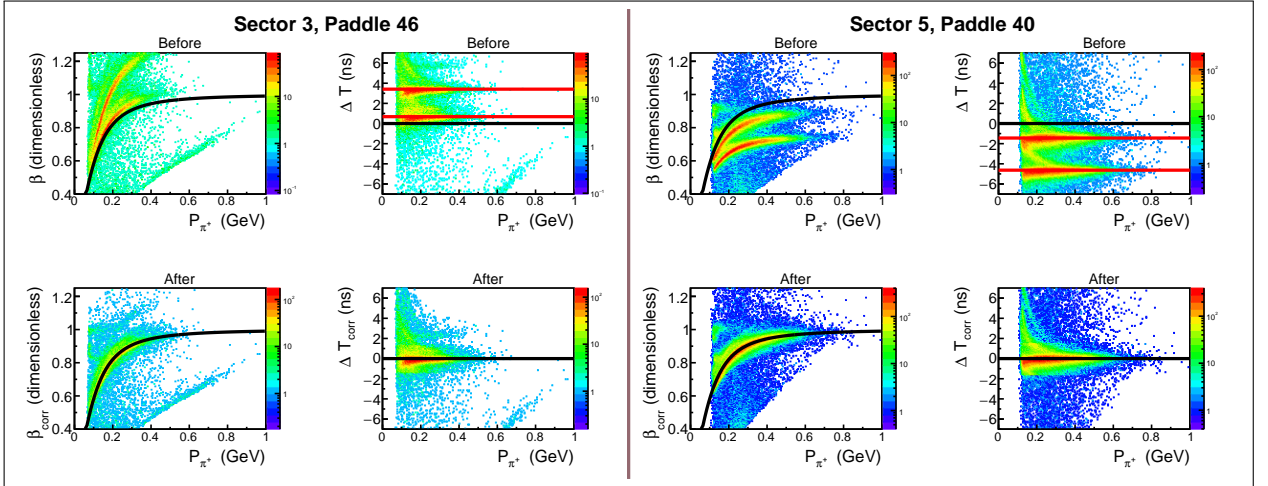


Figure 2.9: Timing correction for type C problematic paddles #46 in sector 3 (left side) and #40 in sector 5 (right side) for  $\pi^+$  candidates. The first column in each side shows the  $\beta_h$  versus momentum distributions with the black curve corresponding to the nominal  $\beta_n$  defined by Eq. (2.1.16). The second column in each side corresponds to the  $\Delta T$  versus momentum distributions, where the black horizontal line shows the position of zero and the red lines show the position of shifted  $\Delta T$ -bands. The uncorrected distributions are given in the first row, while the influence of the correction is shown in the second row.

446 Figure 2.9 illustrates the timing correction for type C problematic paddles #46 in sector  
 447 3 (left side) and #40 in sector 5 (right side) for  $\pi^+$  candidates. The plots in the first row  
 448 clearly show the double band structures in  $\beta_h$  versus momentum and  $\Delta T$  versus momentum  
 449 distributions. To perform timing correction for this type of paddles, one needs to determine  
 450 the position  $t_{shift}$  of each incorrect  $\Delta T$ -band (see horizontal red lines in Fig. 2.9) and then

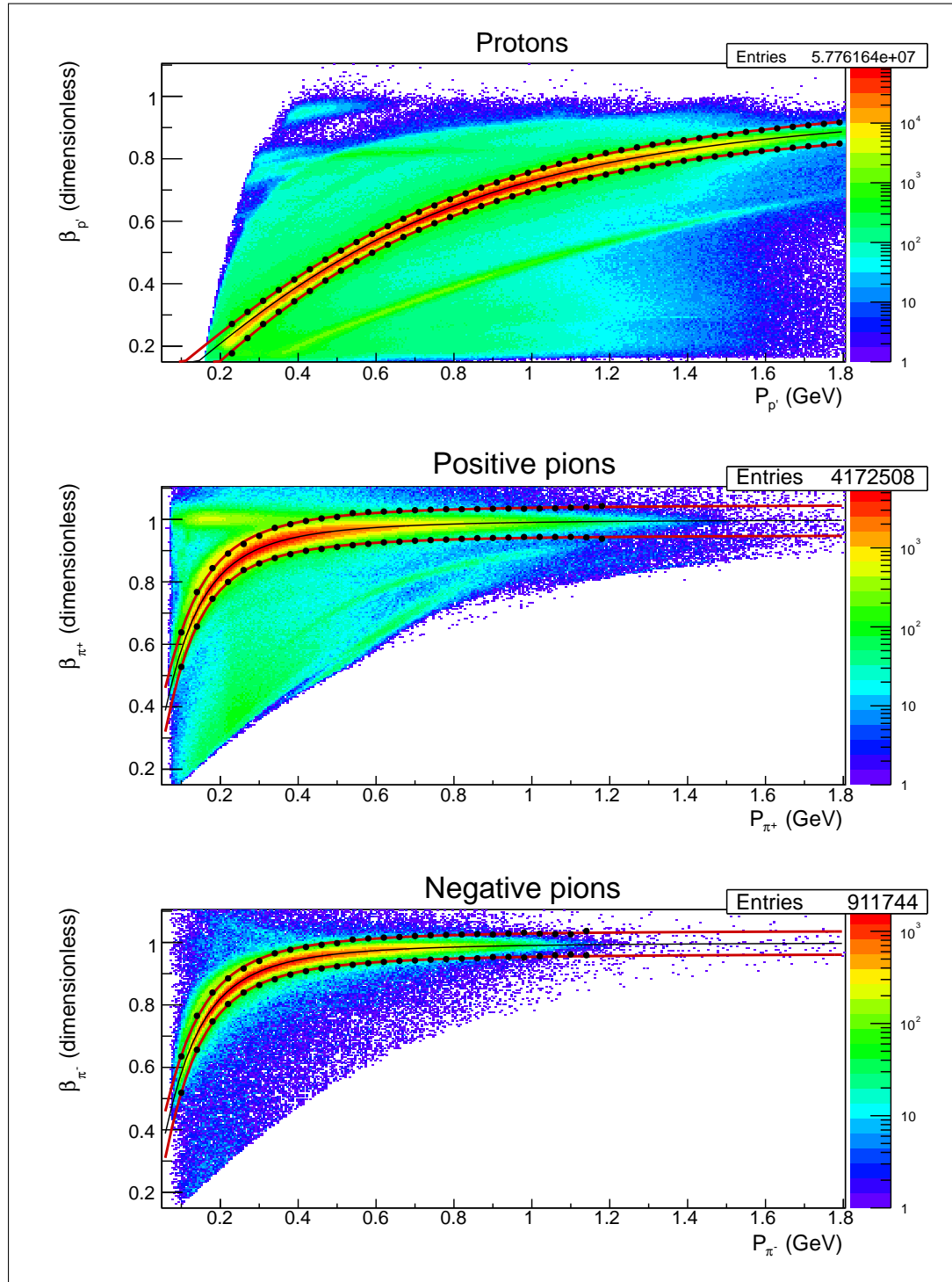


Figure 2.10:  $\beta_{corr}$  versus momentum distributions for proton (upper plot), positive pion (middle plot), and negative pion (bottom plot) candidates. Thin black solid curves in the middle of each band correspond to the nominal  $\beta_n$  given by Eq. (2.1.16). Black points correspond to the positions of Gaussian fit maxima  $\pm 3\sigma$  for individual x-slices of the 2D histograms. These points are fit by the function Eq. (2.1.19), the resulting functions are shown by the red curves. Events between the red curves are selected for further analysis.

451 to move both of them to the correct position around zero, as demonstrated in the second  
 452 row. The corrected value of  $\beta$  is again calculated according to Eq. (2.1.18) with the only  
 453 distinction, that events from different  $\Delta T$ -bands are treated separately and different  $t_{shift}$   
 454 values are used for them.

455 The  $\beta_{corr}$  versus momentum distributions are shown in the second row in Fig. 2.9. As  
 456 seen in these plots, after the timing correction is applied  $\beta_{corr}$  versus momentum bands  
 457 demonstrate neither double band structures nor shifts from the black curves.

458 Figures 2.8 and 2.9 give examples of the timing correction for  $\pi^+$  candidates. Similar  
 459 corrections have also been performed for proton and  $\pi^-$  candidates.

460 After the timing problems are eliminated in each TOF paddle, the hadron identification  
 461 can be made. For the hadron identification, only events with good electron candidates that  
 462 have been selected in the previous step are used. Figure 2.10 shows  $\beta_{corr}$  versus momentum  
 463 distributions for each type of hadron candidate: protons (upper plot), positive pions (middle  
 464 plot), and negative pions (bottom plot). These distributions include all sectors and all TOF  
 465 paddles (with the exclusion of bad ones). The red curves show the corresponding hadron id  
 466 cuts. These curves were obtained in the following way. Firstly, x-slices of the 2D histograms  
 467 are fit by Gaussians. In this way points that correspond to the positions of the fit maxima  
 468  $\pm 3\sigma$  are obtained<sup>6</sup>. These points are shown by black bullets in Fig. 2.10. They determine  
 469 the upper and lower boundaries for the cut. Finally, to obtain smooth curves, all points are  
 470 fit by the following function,

$$f(p_h) = \frac{a_0 \cdot p_h}{\sqrt{a_1 \cdot p_h^2 + m_h^2 + a_2}} + a_3, \quad (2.1.19)$$

471 where  $p_h$  is the hadron momentum,  $m_h$  hadron mass, and  $a_0, a_1, a_2, a_3$  are fit parameters.

472 Events which are located between the red curves in Fig. 2.10 are selected for further  
 473 analysis and treated as good corresponding hadron candidates. It also needs to be mentioned  
 474 that the distribution for positive pions was plotted only for events that already have a good  
 475 proton candidate, and the distribution for negative pions was plotted only for events with  
 476 good proton and positive pion candidates. Furthermore, in order to simplify the analysis  
 477 process, all hadrons were preselected on an initial analysis step. The consequence of this  
 478 preselection is the fact that distributions shown in Fig. 2.10 contain areas that are not  
 479 populated with events.

480 These established hadron id cuts are also applied to the reconstructed Monte Carlo events.

---

<sup>6</sup>Note that to establish the upper cut boundary for pions, the  $3\sigma$  value was used only for  $p_\pi > 0.54$  GeV. For  $p_\pi < 0.54$  GeV different smaller values were used. This was done in order to better separate good pion candidates from the small upper band that is located very close to the pion band and most likely corresponds to muons.

## 481 2.2 Momentum corrections

### 482 2.2.1 Proton momentum correction (energy loss)

483 While traveling through the detector and the target, the final state particles lose a part  
 484 of their energy due to the interactions with the medium. Therefore, the measured particle  
 485 momentum appears to be lower than the actual value. GSIM simulation of the CLAS detector  
 486 correctly propagates particles through the media and, therefore, the effect of the energy loss  
 487 is included into the efficiency and does not impact the extracted cross sections. However, in  
 488 order to avoid shifts in the distributions of some kinematic quantities (e.g. missing masses)  
 489 from their expected values, an energy loss correction is applied to the proton momentum  
 490 magnitude, since the low-energy protons are affected the most by energy loss in the materials.  
 491 This correction is based on the GSIM simulation of the CLAS detector and is performed for  
 492 both experimental and reconstructed Monte Carlo events.

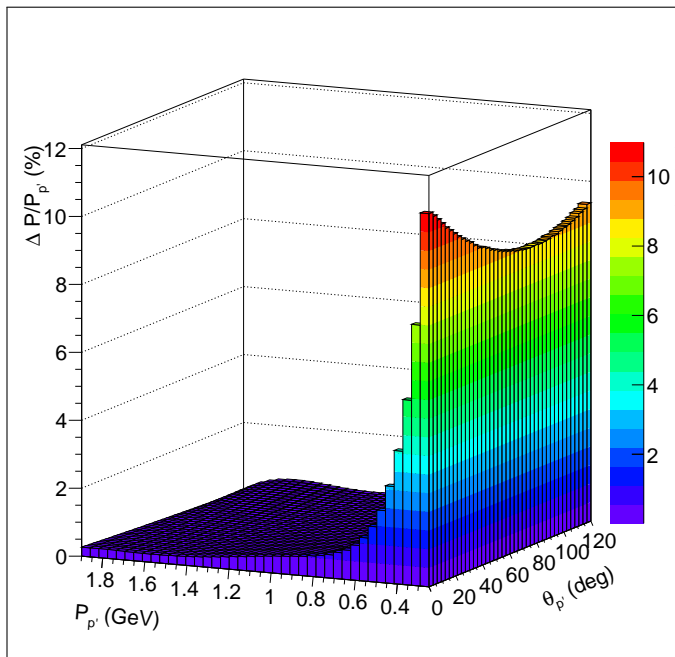


Figure 2.11: Percentage of momentum that protons lose when they move through the detector and target media as a function of the momentum  $P_{p'}$  and scattered angle  $\theta_{p'}$  of the final proton.

493 To obtain the correction function, the quantity  $\Delta P$  that is the difference between the  
 494 generated and reconstructed proton momenta was considered. This quantity was binned in  
 495 the reconstructed proton momentum  $P_{p'}$  and polar angle  $\theta_{p'}$  and fit by a Gaussian in each  
 496 ( $P_{p'}$ ,  $\theta_{p'}$ ) bin. The obtained mean values were further fit by a fifth order polynomial as a  
 497 function of  $P_{p'}$  in each  $\theta_{p'}$  bin. Then the parameters of the resulting fit functions were fit as  
 498 a function of  $\theta_{p'}$  by a second order polynomial.

499        The resulting energy loss correction function is shown in Fig. 2.11. It gives the percentage  
500 of the momentum that protons lose when they move through the detector and target media.

501        Note that if one wants to isolate the pure effect of the energy loss, the difference between  
502 proton momenta for events reconstructed with and without detector and target materials  
503 must be considered. Since in the applied procedure the difference between generated and  
504 reconstructed proton momenta is analyzed, the correction function shown in Fig. 2.11 can  
505 also include other effects that lead to improper proton momentum reconstruction.

### 506        2.2.2 Electron momentum correction

507        Due to slight misalignments in the DC position, small inaccuracies in the description of  
508 the torus magnetic field, and other possible reasons the momentum and angle of particles  
509 may have some small systematic deviations from their real values. These effects being of  
510 undefined origin cannot be simulated in GSIM, therefore a special momentum correction  
511 procedure is needed for the experimental data. According to [33], the evidence of the need  
512 for such corrections is most directly seen in the dependence of the elastic peak position on the  
513 azimuthal angle of the scattered electrons. It is shown in [33] that the elastic peak position  
514 is shifted from the true value (0.938 GeV) and this shift is sector dependent.

515        The significance of this effect depends on the beam energy. In the analysis [22] it is  
516 shown that a beam energy of 2.039 GeV leads to the small shift ( $\sim 3$  MeV) in elastic peak  
517 position, while the study [33] demonstrates that in case of 5.754 GeV beam energy this shift  
518 reaches 20 MeV. Moreover, the study [33] also shows that this effect becomes discernible  
519 only if the particle momentum is sufficiently high (e.g. for pions the correction is needed  
520 only if their momentum is higher than 2 GeV). Thus, the small beam energy of this analyzed  
521 dataset and the fact that in double-pion kinematics hadrons carry only a small portion of  
522 the total momentum allows us to come to the conclusion that the correction is needed only  
523 for electrons, while deviation in hadron momenta can be neglected.

524        Since this analysis suffers from additional complications as binding and motion of the  
525 target proton inside the deuteron, it was considered sensible to use the electron momentum  
526 corrections that have previously been developed and tested in the analysis of the free proton  
527 part of “e1e” dataset at the same beam energy [22]. To establish them, the approach [33],  
528 which is based on elastic kinematics, was used. These corrections include electron momentum  
529 magnitude correction as well as electron polar angle correction, which were developed for  
530 each CLAS sector individually.

531        Figure 2.12, which was taken from the analysis [22], demonstrates that after the electron  
532 momentum corrections the elastic peak position for all CLAS sectors gets closer to the proton  
533 mass, shown by the red horizontal line.

534        The correction discussed above is applied only for experimental data. As for the Monte  
535 Carlo simulation, it turns out that due to unknown reasons (most likely because electrons

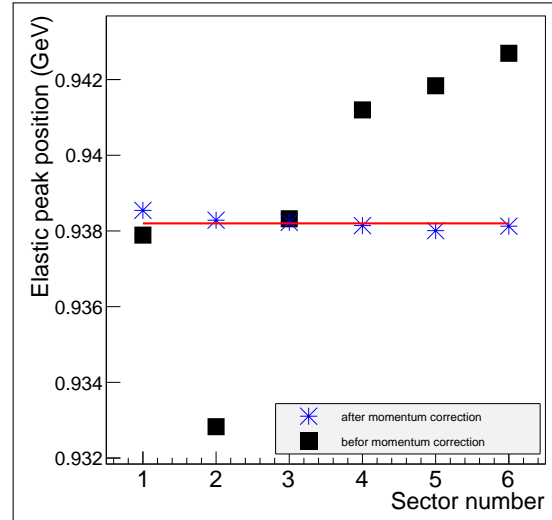


Figure 2.12: Elastic peak position for the six CLAS sectors before (black squares) and after (blue stars) electron momentum correction for the proton part of “e1e” dataset. The horizontal red line shows the proton mass. This figure is taken from the analysis [22].

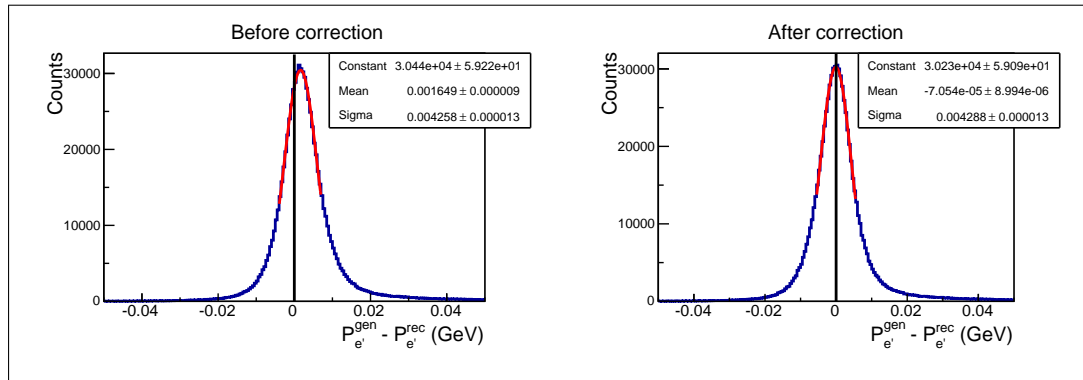


Figure 2.13: Difference between generated and reconstructed electron momenta before (left plot) and after (right plot) the correction of the momentum magnitude, which has been applied to the reconstructed electrons. The vertical black line shows the position of zero.

536 lose some energy when they travel through the detector and target media) the reconstructed  
537 electron momentum appears to be slightly lower than the generated one. This effect is  
538 demonstrated in the left plot of Fig. 2.13, where the event distribution of the quantity  $\Delta P$   
539 (which is the difference between generated and reconstructed electron momenta) is presented.  
540 Therefore, an adapted procedure of correcting the electron momentum magnitude is also  
541 applied to the reconstructed Monte Carlo events. This procedure is similar to that used  
542 for the proton energy loss (see Sect. 2.2.1). The correction depends only on the scattered  
543 electron momentum and polar angle, but not on the CLAS sector. The typical value of this  
544 correction is 0.2%. The right plot in Fig. 2.13 shows the result of the correction. As seen  
545 in this plot, the mean value of the quantity  $\Delta P$  demonstrates no shift from zero when the  
546 momentum magnitude for reconstructed electron is corrected.

## **2.3 Other cuts**

### **2.3.1 Fiducial cuts**

The active detection solid angle of the CLAS detector is smaller than  $4\pi$  [4]. This is in part due to the space filled with the torus field coils: the angles covered by the coils are not equipped with any detection system and therefore form a “dead” area for detection. Additionally, the detection area is also limited in polar angle from  $8^\circ$  up to  $45^\circ$  for electrons and up to  $140^\circ$  for other charged particles [4]. Moreover, different studies and analyses have shown that also the edges of the active area do not provide a safe region for the particle reconstruction, being affected by rescattering from the coil, field distortions, and similar effects. Therefore, it is now common practice to accept for the analysis only events inside specific fiducial cuts, i.e. cuts on the kinematic variables (momentum and angles) of each particle. This method guarantees that events accepted in the analysis include only particles detected in “safe” areas of the detector, where the acceptance is thought to be well understood. These cuts are applied to both real events and reconstructed Monte Carlo events.

#### **Fiducial cuts for negatively charged particles**

In CLAS experiments with normal direction of the torus magnetic field, like in the “e1e” experiment, negatively charged particles are inbending, which means that their trajectories are bent in the forward direction. For these particles sector independent, symmetrical, and momentum dependent cuts are applied.

For electron and negative pion candidates the analytical shapes of fiducial cuts are given by Eq. (2.3.1) and Eq. (2.3.2), respectively. The shapes of these cuts were taken from the similar analysis [22] of the “e1e” dataset (but off proton target) and carefully adjusted to the data.

In Eq. (2.3.1) and Eq. (2.3.2) polar and azimuthal angles of electrons ( $\theta_{e'}$ ,  $\varphi_{e'}$ ) and negative pions ( $\theta_\pi$ ,  $\varphi_\pi$ ) are assumed to be in degrees, while their momenta ( $p_{e'}$ ,  $p_\pi$ ) are in GeV, respectively. The angles are taken at the interaction vertex. Events that satisfy the criteria  $\theta^{min} < \theta < \theta^{max}$  and  $\varphi^{min} < \varphi < \varphi^{max}$  are selected for the analysis.

$$\begin{aligned}
\theta_{e'}^{min}(p_{e'}) &= 11.7398 + \frac{8.21504}{0.433327 \cdot p_{e'} + 0.158076} \\
\theta_{e'}^{max}(p_{e'}) &= 76.8617 - 76.537 \cdot p_{e'} + 77.9387 \cdot p_{e'}^2 - 28.389 \cdot p_{e'}^3 \\
\varphi_{e'}^{min}(\theta_{e'}) &= -41.3 \cdot \sin [a_3 \cdot (\theta_{e'} - \theta_{e'}^{min})]^{[a_1 + a_2 / \theta_{e'} + 1485 / \theta_{e'}^2]} - 1 \\
\varphi_{e'}^{max}(\theta_{e'}) &= +41.3 \cdot \sin [a_3 \cdot (\theta_{e'} - \theta_{e'}^{min})]^{[a_1 + a_2 / \theta_{e'} + 1485 / \theta_{e'}^2]} + 1. \\
a_1(p_{e'}) &= 0.85 + 1.1 \cdot p_{e'} \\
a_2(p_{e'}) &= -62.8 - 30 \cdot p_{e'} \\
a_3(p_{e'}) &= 0.0047 \cdot p_{e'} + 0.0079.
\end{aligned} \tag{2.3.1}$$

$$\begin{aligned}
\theta_\pi^{min}(p_\pi) &= 10.09 + \frac{8}{0.472 \cdot (p_\pi - 0.03) + 0.117}, \text{ if } p_\pi > 0.3. \\
\theta_\pi^{min2}(p_\pi) &= 33 + \frac{5.24894 \cdot 10^{-5}}{5.71075 \cdot 10^{-5} \cdot (p_\pi + 0.004)^2}, \text{ if } p_\pi < 0.3. \\
\theta_\pi^{max} &= 140. \\
\varphi_\pi^{min}(\theta_\pi) &= \begin{cases} -23.5 \cdot \sin [0.015 \cdot (\theta_\pi - \theta_\pi^{min})]^{[a_1 + a_2 / \theta_\pi + 1400 / \theta_\pi^2]} - a_3, & \text{if } \theta_\pi < \theta_\pi^* \\ \varphi_\pi^{min}(\theta_\pi^*), & \text{if } \theta_\pi > \theta_\pi^* \end{cases} \\
\varphi_\pi^{max}(\theta_\pi) &= \begin{cases} +23.5 \cdot \sin [0.015 \cdot (\theta_\pi - \theta_\pi^{min})]^{[a_1 + a_2 / \theta_\pi + 1400 / \theta_\pi^2]} + a_3, & \text{if } \theta_\pi < \theta_\pi^* \\ \varphi_\pi^{max}(\theta_\pi^*), & \text{if } \theta_\pi > \theta_\pi^* \end{cases} \\
a_1(p_\pi) &= 0.61 + 1.18 \cdot p_\pi. \\
a_2(p_\pi) &= -59.2 - 35.3 \cdot p_\pi. \\
a_3(p_\pi) &= 17.2 \cdot p_\pi - 11.9 \cdot p_\pi^2 - 2.5. \\
\theta_\pi^* &= \theta_\pi^{max} - \frac{13}{15} \cdot (\theta_\pi^{max} - \theta_\pi^{min}).
\end{aligned} \tag{2.3.2}$$

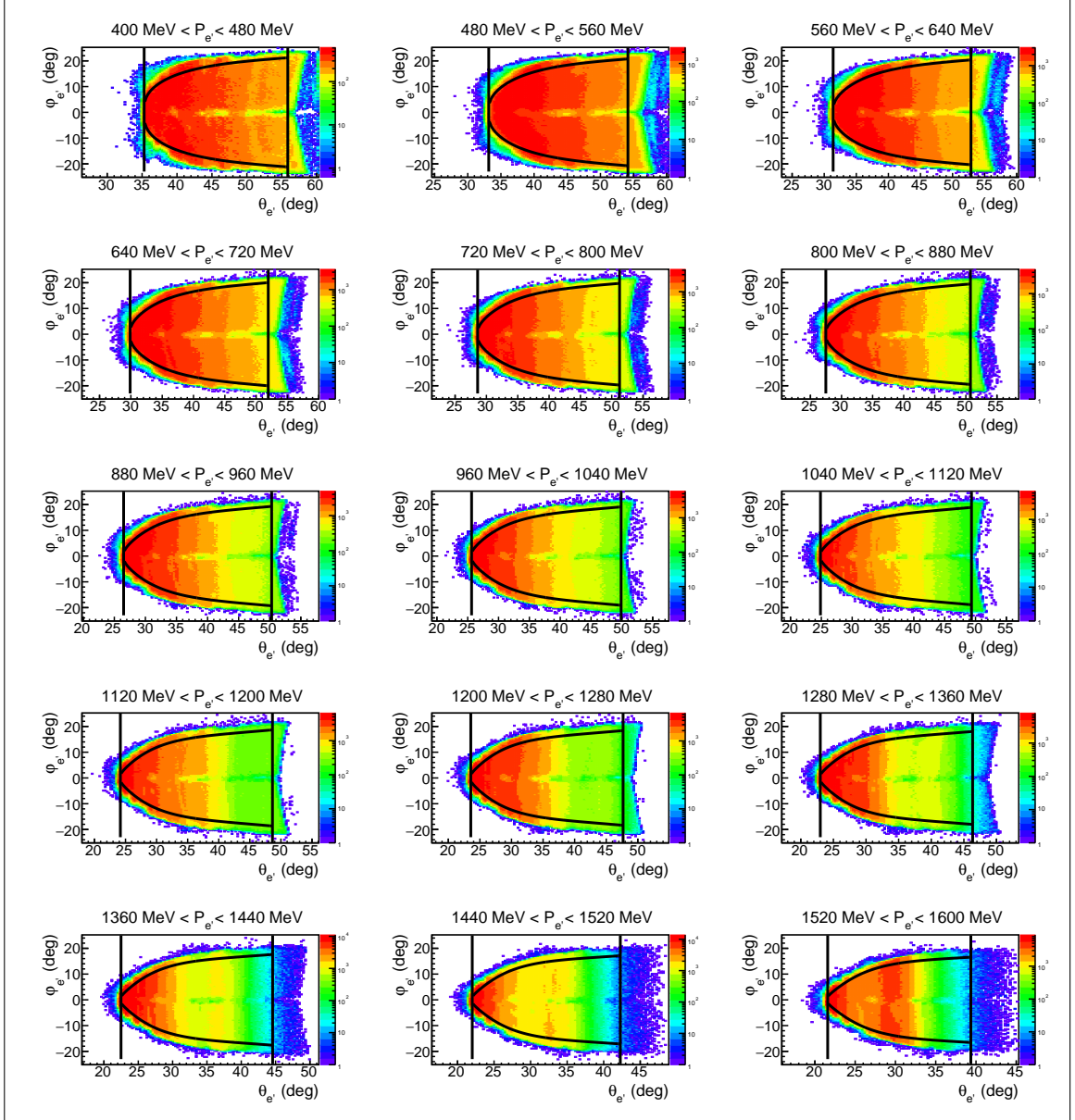


Figure 2.14:  $\varphi$  versus  $\theta$  distributions for electron candidates for different 80-MeV-wide momentum slices plotted for events from all CLAS sectors. Curves show the applied fiducial cuts given by Eq. (2.3.1), vertical lines stand for  $\theta_{e'}^{\min}$  and  $\theta_{e'}^{\max}$ . The angles are taken at the interaction vertex. For each momentum slice the shape of the fiducial cut was calculated for the value of the electron momentum taken in the center of the momentum bin.

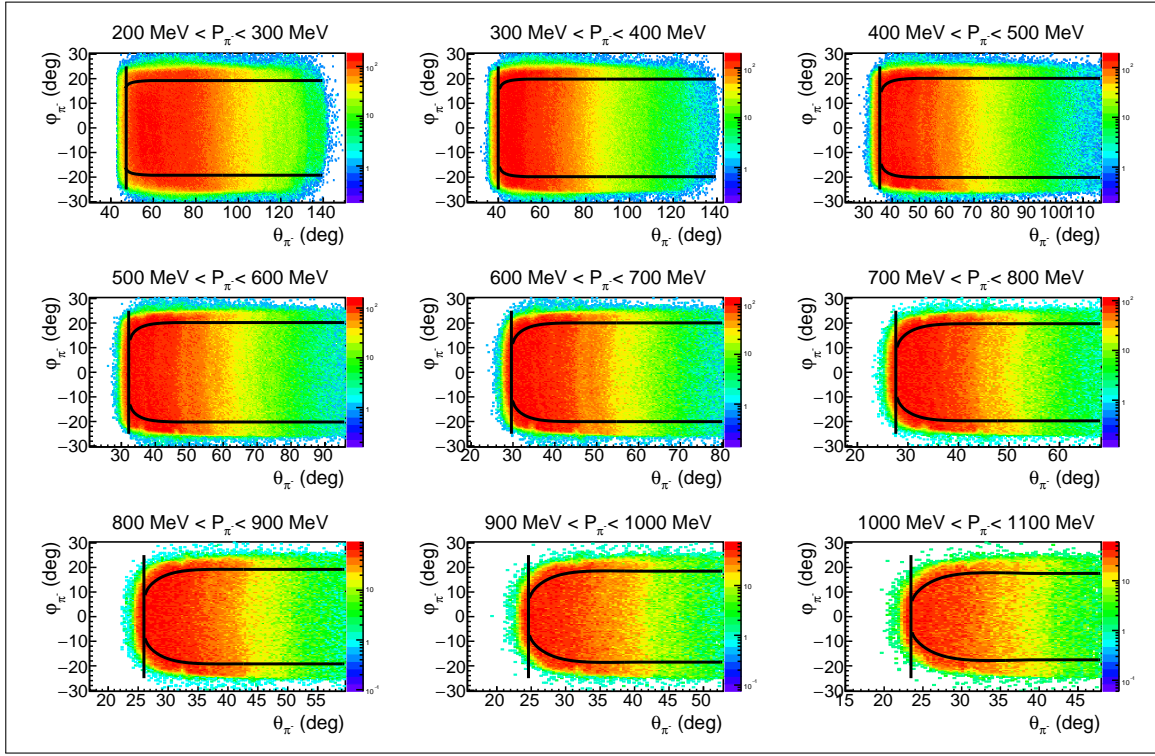


Figure 2.15:  $\varphi$  versus  $\theta$  distributions for negative pion candidates for different 100-MeV-wide momentum slices plotted for events from all CLAS sectors. Curves show the applied fiducial cuts given by Eq. (2.3.2), vertical lines stand for  $\theta_{\pi}^{min}$  and  $\theta_{\pi}^{max}$ . The angles are taken at the interaction vertex. For each momentum slice the shape of the fiducial cut was calculated for the value of the pion momentum taken in the center of the momentum bin.

The fiducial cut for electron candidates is illustrated in Fig. 2.14, where the curves given by Eq. (2.3.1) are superimposed on the  $\varphi$  versus  $\theta$  distributions for different 80-MeV-wide momentum slices. Vertical lines correspond to  $\theta_{e'}^{min}$  and  $\theta_{e'}^{max}$ . For each momentum slice the shape of the fiducial cut was calculated for the value of the electron momentum taken in the center of the momentum bin. The depleted area around  $\varphi_{e'} = 0$  corresponds to the inefficient region in CC and was discussed above in Sect. 2.1.1.

The fiducial cut for negative pion candidates is illustrated in Fig. 2.15, where the curves given by Eq. (2.3.2) are superimposed on the  $\varphi$  versus  $\theta$  distributions for different 100-MeV-wide momentum slices. Vertical lines correspond to  $\theta_{\pi}^{min}$  and  $\theta_{\pi}^{max}$ . For each momentum slice the shape of the fiducial cut was calculated for the value of the pion momentum taken in the center of the momentum bin.

The same fiducial cuts for negatively charged particles are also applied to the reconstructed Monte Carlo events.

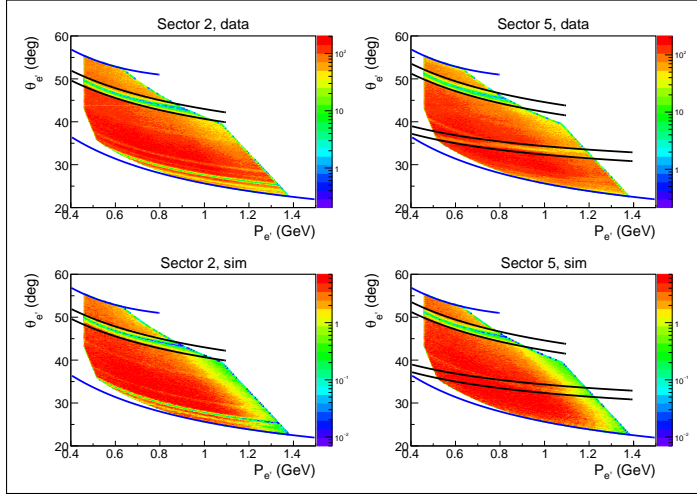


Figure 2.16:  $\theta$  versus momentum distributions for electron candidates for CLAS sectors two (left side) and five (right side). The angle  $\theta$  is taken at the interaction vertex. Top row corresponds to the data, bottom row corresponds to the reconstructed Monte Carlo events. Blue curves correspond to  $\theta_{e'}^{min}$  and  $\theta_{e'}^{max}$  in Eq. (2.3.1). Black curves correspond to additional fiducial  $\theta$  versus momentum cuts. These distributions are plotted under the conditions  $1.3 \text{ GeV} < W < 1.825 \text{ GeV}$  and  $0.4 \text{ GeV}^2 < Q^2 < 1.0 \text{ GeV}^2$  which account for the extra cuts of the distribution edges. Other small inefficiencies that are seen in these plots are due to the geometrical cut in the CC plane (see Sect. 2.1.1).

588 There are some additional dead areas in CLAS acceptance that are not related to the  
 589 gaps between the sectors and limitations on the detection polar angle. They are typically  
 590 caused by some inefficiencies in the Drift Chambers and Time-of-Flight system (dead wires  
 591 or PMTs). Some of them are well reproduced in the Monte Carlo simulation, while others  
 592 are not. To exclude the latter from the analysis and to eliminate events near the acceptance  
 593 edges, additional fiducial cuts on  $\theta$  versus momentum distributions are applied. These cuts  
 594 are individual for each CLAS sector. They are shown by the black curves for real and Monte  
 595 Carlo events in Fig. 2.16 for electron candidates and in Fig. 2.17 for negative pion candidates.

596 For the electron distributions shown in Fig. 2.16 inefficient areas in sectors two and five  
 597 correspond to bad TOF paddles #16 and #17, respectively. Other small inefficiencies that  
 598 are seen in these plots are due to the geometrical cut in the CC plane (see Sect. 2.1.1), they  
 599 are almost identical for data and Monte Carlo events and, therefore, no additional fiducial  
 600 cuts are needed for them.  $\theta$  versus momentum distributions for electron candidates in other  
 601 sectors do not show significant inefficiencies.

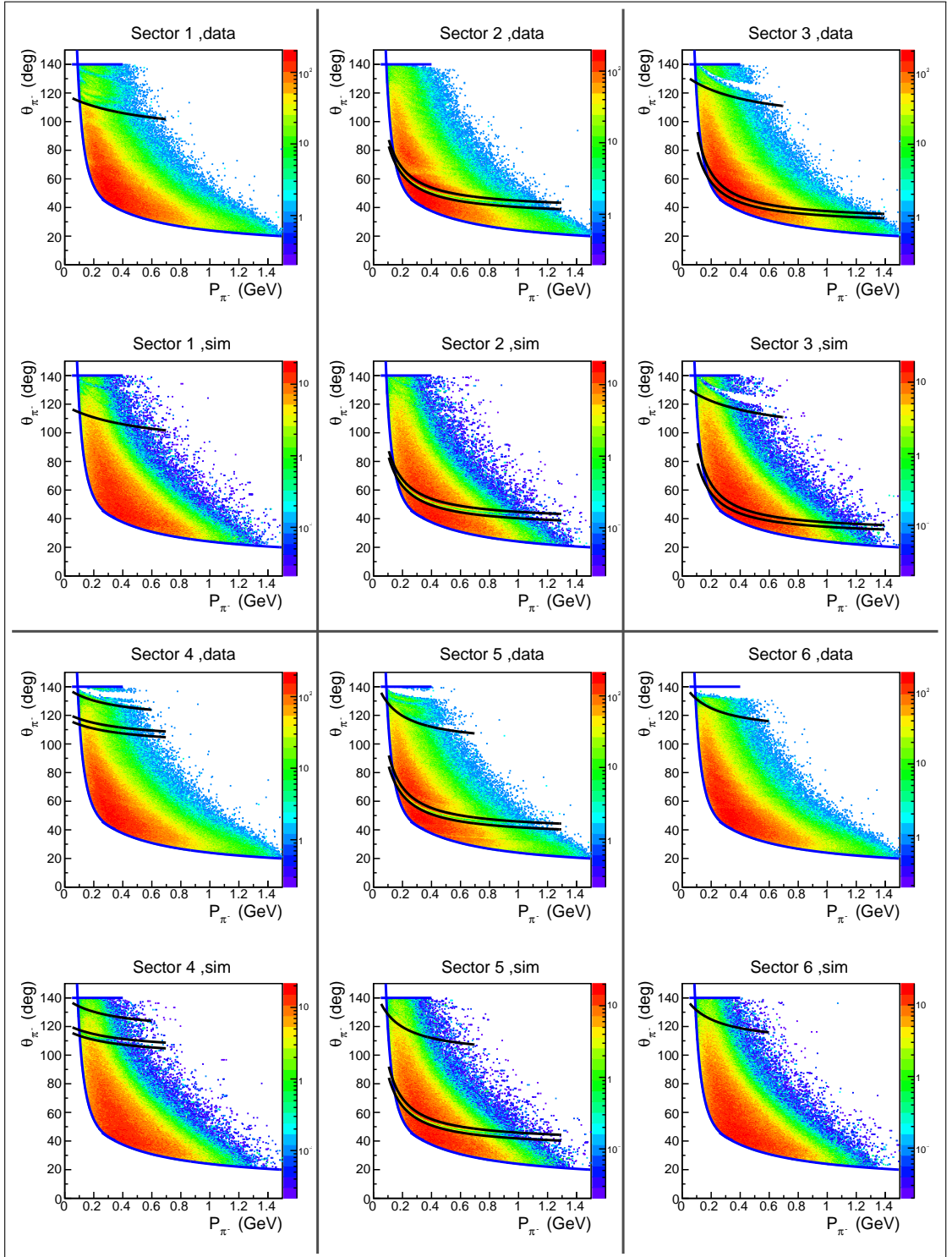


Figure 2.17:  $\theta$  versus momentum distributions for negative pion candidates for different CLAS sectors. The angle  $\theta$  is taken at the interaction vertex. Plots are given both for real data and reconstructed Monte Carlo events. Blue curves correspond to  $\theta_{\pi}^{\min}$  and  $\theta_{\pi}^{\max}$  in Eq. (2.3.2). Black curves correspond to additional fiducial  $\theta$  versus momentum cuts.

602 **Fiducial cuts for positively charged particles**

603 For positively charged particles, which are outbending in the “e1e” experiment, momentum  
 604 independent and symmetrical fiducial cuts suit our purpose best. The analytical shape of  
 605 these cuts is given by Eq. (2.3.3), which was also taken from the analysis [22] and carefully  
 606 adjusted to the data. All angles in Eq. (2.3.3) are taken at the interaction vertex and assumed  
 607 to be in degrees. Events that satisfy the criteria  $\theta^{min} < \theta < \theta^{max}$  and  $\varphi^{min} < \varphi < \varphi^{max}$  are  
 608 selected for the analysis.

$$\theta^{min} = 12.$$

$$\begin{aligned} \theta^{max} &= \begin{cases} 60 & \text{for protons} \\ 120 & \text{for pions} \end{cases} \\ \varphi^{min}(\theta) &= -25 \cdot [1 - e^{-[0.12 \cdot (\theta - 10)]}] + 3. \\ \varphi^{max}(\theta) &= +25 \cdot [1 - e^{-[0.12 \cdot (\theta - 10)]}] - 3. \end{aligned} \quad (2.3.3)$$

609 Fiducial cuts for positive hadron candidates are illustrated in Fig. 2.18, where the curves  
 610 given by Eq. (2.3.3) are superimposed on the  $\varphi$  versus  $\theta$  distributions for protons (left plot)  
 611 and pions (right plot). Vertical lines correspond to  $\theta^{min}$  and  $\theta^{max}$ . The same fiducial cuts  
 612 for positively charged particles are also applied to the reconstructed Monte Carlo events.

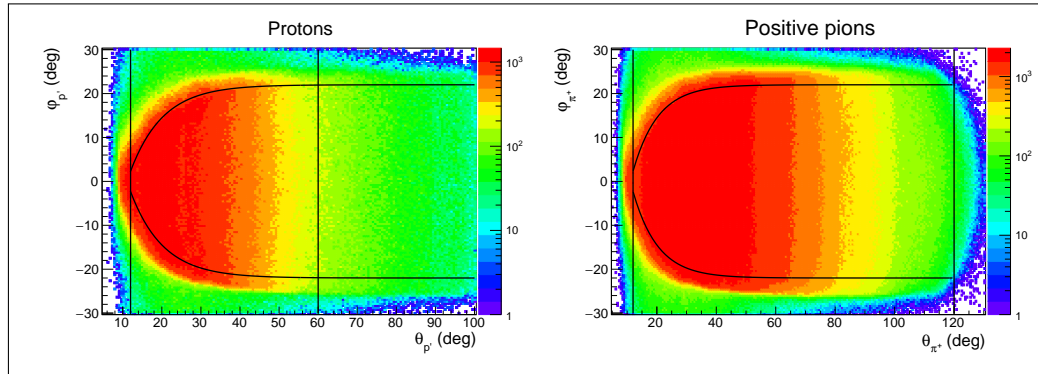


Figure 2.18:  $\varphi$  versus  $\theta$  distributions for positive hadron candidates: left plot – for protons, right plot – for positive pions. The distributions are plotted for events from all CLAS sectors. Curves show the applied fiducial cuts given by Eq. (2.3.3), vertical lines stand for  $\theta^{min}$  and  $\theta^{max}$ . The angles are taken at the interaction vertex.

613 Additional fiducial cuts in  $\theta$  versus momentum coordinates are shown by the black curves  
 614 for the data and reconstructed Monte Carlo events in Fig. 2.19 for protons and in Fig. 2.20  
 615 for  $\pi^+$ .

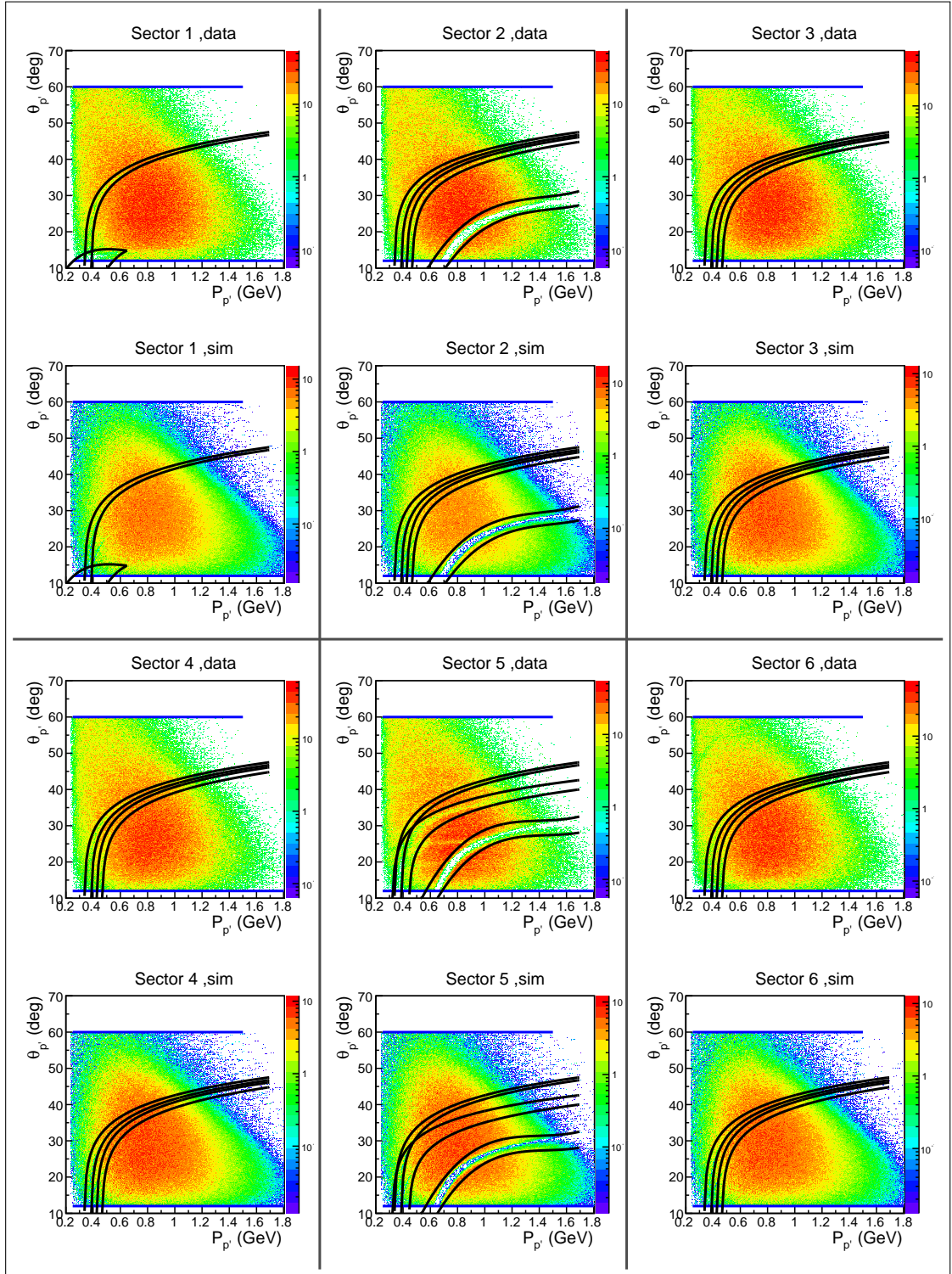


Figure 2.19:  $\theta$  versus momentum distributions for proton candidates for different CLAS sectors. The angle  $\theta$  is taken at the interaction vertex. Plots are given both for the real data and reconstructed Monte Carlo events. Blue lines correspond to  $\theta_{\min}^{\text{real}}$  and  $\theta_{\max}^{\text{real}}$  in Eq. (2.3.3). Black curves correspond to additional fiducial  $\theta$  versus momentum cuts.

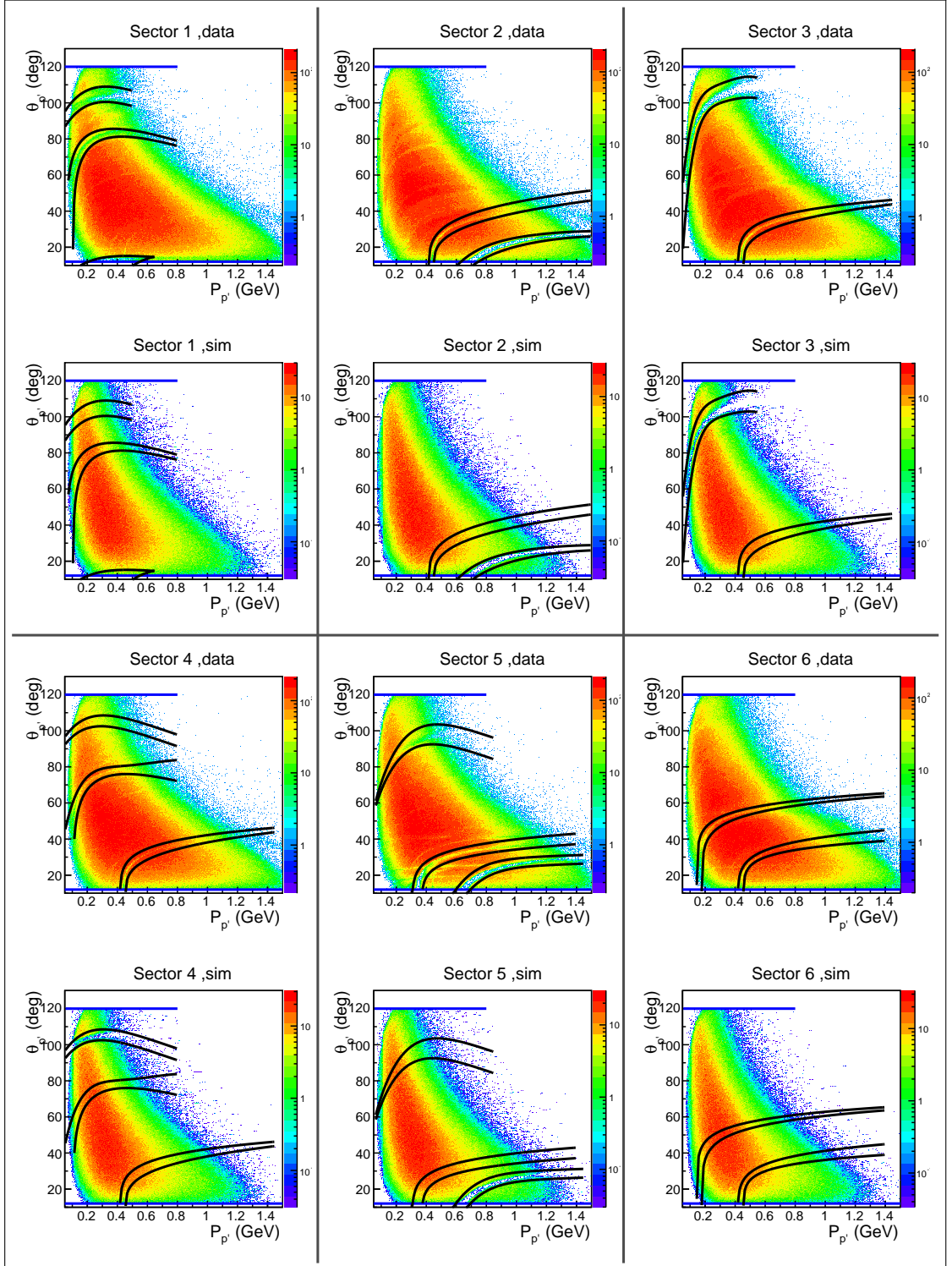


Figure 2.20:  $\theta$  versus momentum distributions for positive pion candidates for different CLAS sectors. The angle  $\theta$  is taken at the interaction vertex. Plots are given both for the real data and reconstructed Monte Carlo events. Blue lines correspond to  $\theta^{min}$  and  $\theta^{max}$  in Eq. (2.3.3). Black curves correspond to additional fiducial  $\theta$  versus momentum cuts.

### 616 2.3.2 Data quality check

617 During a long experimental run, variations of the experimental conditions, e.g. fluctuations  
 618 in the target density, deviations of the beam current and position as well as changes in the  
 619 response of parts of the detector, can lead to fluctuations in event yields. Only the parts of  
 620 the run with relatively stable event rates are selected for the analysis. Therefore, cuts on  
 621 Data Acquisition (DAQ) live time and number of events per Faraday cup (FC) charge need  
 622 to be established.

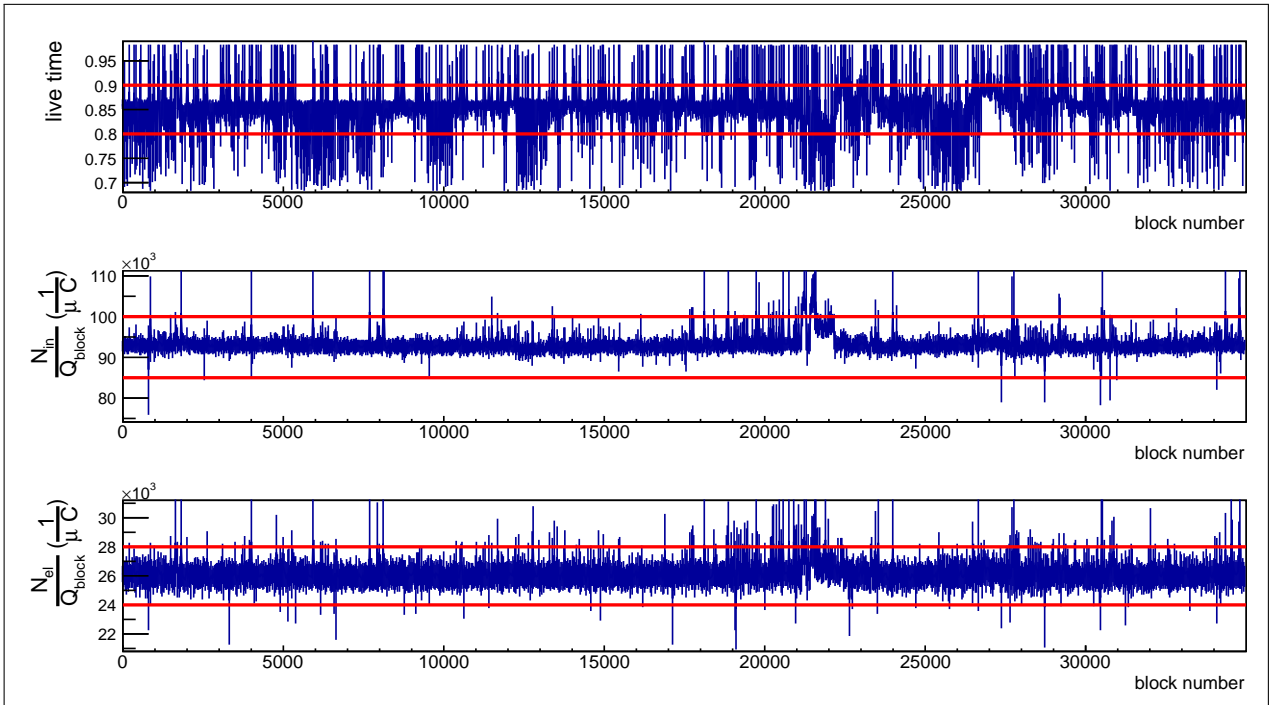


Figure 2.21: In the top plot DAQ live time is shown as a function of *block* number. Each *block* corresponds to the portion of events that is accumulated during a single Faraday cup charge reading cycle. *Block* numbers range from one to the maximum number and represent the run duration in the units of Faraday cup readouts. In the middle plot the number of inclusive events accumulated within each *block* divided by FC charge accumulated during the *block* is plotted versus *block* number. The bottom plot shows the number of elastic events accumulated within each *block* divided by FC charge accumulated during the *block* as a function of *block* number. Horizontal red lines show the applied cuts.

623 The FC charge updates with a given frequency, so the whole run time can be divided  
 624 into so-called *blocks*. Each *block* corresponds to the portion of time between two FC charge  
 625 readouts. FC charge readouts happen approximately once every ten seconds. The *block*  
 626 number ranges over the run time from one to a certain maximum number. The first and last  
 627 *blocks* in each run file are excluded from the analysis, since FC readout is not synchronized  
 628 in time with the start/stop of writing to the file.

629        The DAQ live time is the portion of time within the *block* during which the DAQ system  
 630        is able to accumulate events. A significant deviation of the live time from the average value  
 631        indicates event rate alteration. For instance, if the live time is close to one, then the event  
 632        rate is too low and vice versa. In Fig. 2.21 the DAQ live time (top plot) as well as the  
 633        yields of inclusive (middle plot) and elastic (bottom plot) events normalized to FC charge  
 634        are shown as a function of *block* number. *Blocks* between the horizontal red lines in Fig. 2.21  
 635        are selected for the analysis. Due to the enormous amount of *blocks* all of them cannot  
 636        be made visible in two-dimensional histograms, therefore, to have a general feeling of what  
 637        amount of blocks are removed, the *y*-axis projections of the histograms in Fig. 2.21 are given  
 638        in Fig. 2.22. The horizontal red cut lines in Fig. 2.21 correspond to the vertical red cut lines  
 639        in Fig. 2.22.

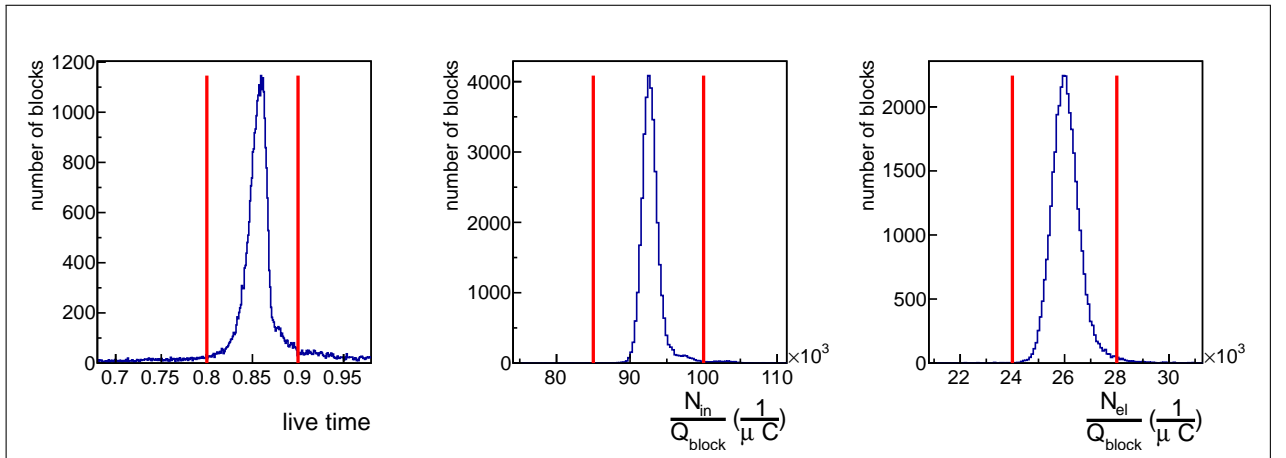


Figure 2.22: Number of *block* occurrences (see explanation in the text) as a function of DAQ live time (left plot), inclusive event yield normalized to FC charge (middle plot), and elastic event yield normalized to FC charge (right plot). The vertical red cut lines correspond to the horizontal red cut lines in Fig. 2.21.

### 640        2.3.3 Vertex cut

641        The “e1e” experiment employed a specific target [34] with the same assembly for the hydro-  
 642        gen and the deuterium parts of the run period. The target setup is presented in Fig. 2.23.  
 643        The conical shape of the target (with the diameter varying from 0.35 to 0.6 cm) serves the  
 644        purpose of effective extraction of gas bubbles, which are formed in the liquid target content  
 645        due to the heat that either originates from the beam and/or comes from outside through  
 646        the target walls. Due to the conical shape, the bubbles are drained upwards and into a  
 647        wider area of the target thus clearing the beam interaction region and allowing the boiled  
 648        deuterium to be effectively delivered back to the cooling system to be condensed.

649     The target cell had 15- $\mu\text{m}$ -thick aluminum entrance and exit windows. In addition, an  
 650   aluminum foil was located 2.0 cm downstream of the target. This foil was made exactly the  
 651   same as the entry/exit windows of the target cell and served for both the estimation of the  
 652   number of events that originated in the target windows and the precise determination of the  
 653   target  $z$ -position along the beamline.

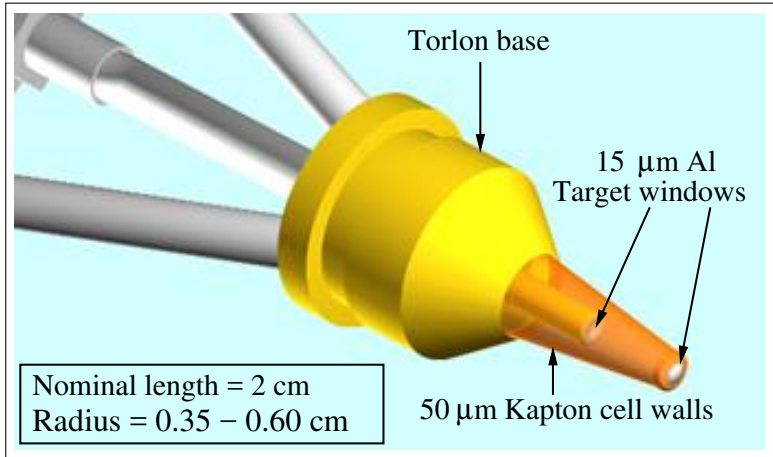


Figure 2.23: LH<sub>2</sub>/LD<sub>2</sub> target cell and its support structure used during “e1e” run period [34].

654     In Fig. 2.24 distributions of electron  $z$ -coordinate at the interaction vertex are shown for  
 655   events from both empty and full target runs for all six CLAS sectors. The vertical red lines  
 656   show the cut that is applied in addition to the empty target event subtraction. The vertical  
 657   dashed line marks the position  $z = -0.4$  cm, where the center of the target is expected to  
 658   be. However, as seen in Fig. 2.24, the  $z_{e'}$  distributions demonstrate small sector dependent  
 659   deviations from their expected position. The source of these deviations is an offset of the  
 660   beam position from the CLAS central line  $(x, y) = (0, 0)$ .

661     To estimate the beam offset, the  $y_{e'}^{dc}$  versus  $x_{e'}^{dc}$  distribution was investigated, where  $x_{e'}^{dc}$   
 662   and  $y_{e'}^{dc}$  are the corresponding coordinates of an electron at the point of interaction, which  
 663   are taken from the DCPB bank (variables X\_v and Y\_v, respectively). This distribution is  
 664   shown in Fig. 2.25, where the intersections of black dashed and solid red lines indicate the  
 665   nominal and actual beam positions, respectively. The actual beam position was found to  
 666   be  $(x, y) = (0.057 \text{ cm}, -0.182 \text{ cm})$ . The generated Monte Carlo events were reconstructed  
 667   taking into account the determined beam offset to improve resemblance to the real data<sup>7</sup>.

668     In Fig. 2.26 event distributions after the subtraction of the empty target contribution are  
 669   shown in comparison with Monte Carlo events reconstructed taking into account the beam  
 670   offset. As can be seen in this figure the simulation matches the data well enough and almost  
 671   completely reproduces the sector dependent deviation of the distributions from the nominal  
 672   position marked by the black dashed lines.

<sup>7</sup> The following option was used in the *ffread card*: POSBEAM 0.057 -0.182.

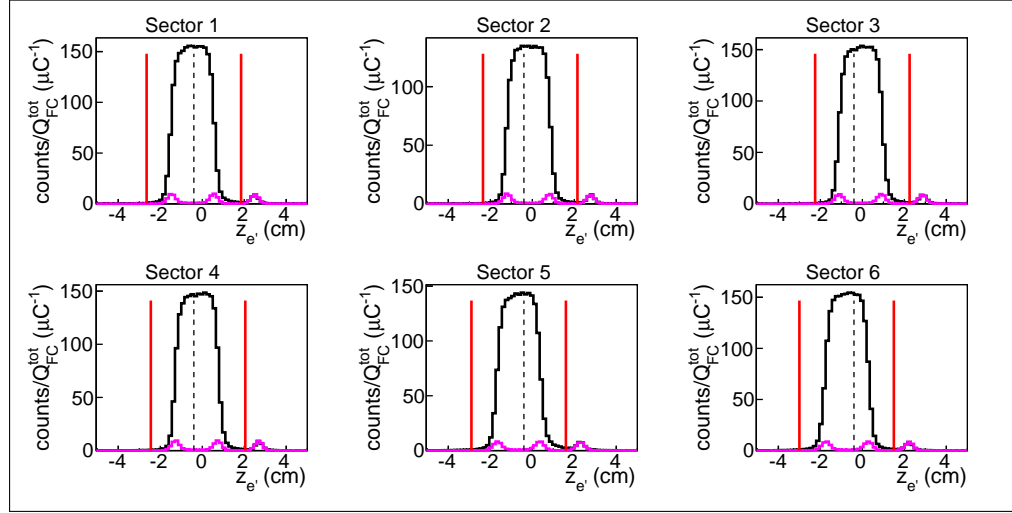


Figure 2.24: Distributions of the electron  $z$ -coordinate at the vertex for full (black curves) and empty (magenta curves) target runs for the six CLAS sectors. Vertical dashed lines mark the position  $z = -0.4$  cm, where the center of the target is expected to be. Vertical red lines show the applied cuts. Both full and empty target distributions are normalized to the corresponding FC charge.

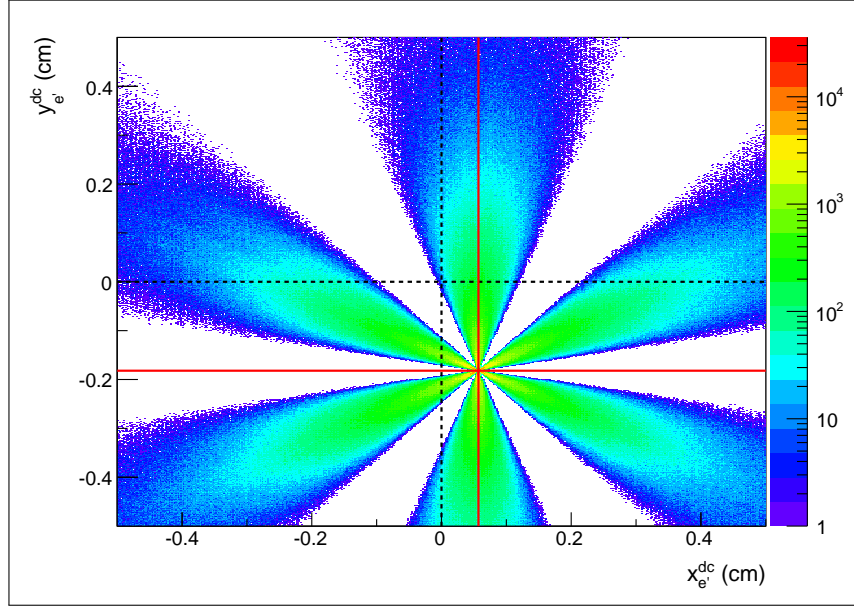


Figure 2.25:  $y_{e'}^{dc}$  versus  $x_{e'}^{dc}$  distribution that demonstrates the beam offset. Black dashed lines mark the position  $(x, y) = (0, 0)$ , where the beam is expected to be. Red lines demonstrate the actual beam position at  $(x, y) = (0.057 \text{ cm}, -0.182 \text{ cm})$ .

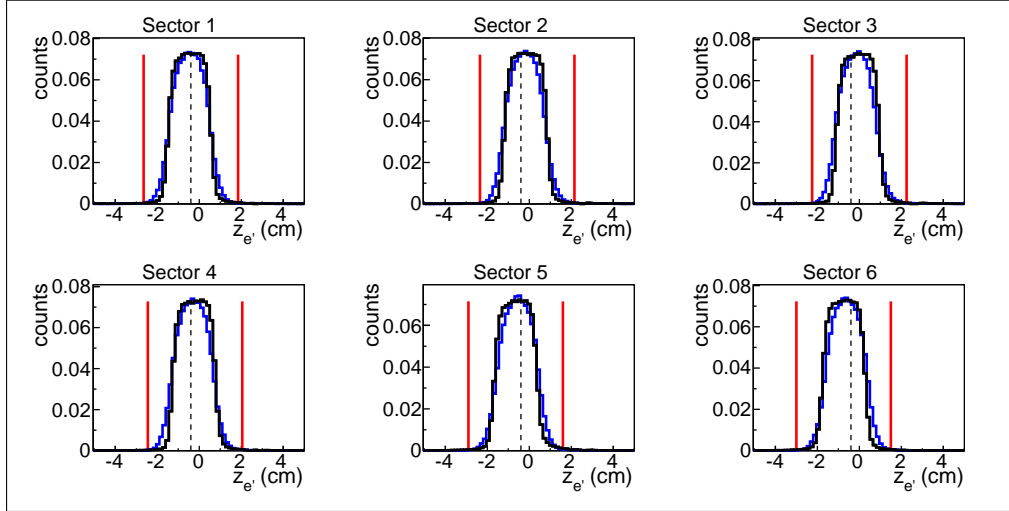


Figure 2.26: Distributions of the electron  $z$ -coordinate at the vertex for the experimental data (black curves) and the Monte Carlo events reconstructed taking into account the beam offset (blue curves) for the six CLAS sectors. For the data empty target contributions are subtracted. Vertical dashed lines mark the position  $z = -0.4$  cm, where the center of the target is expected to be. Vertical red lines show the applied cuts. All distributions are normalized to the integral.

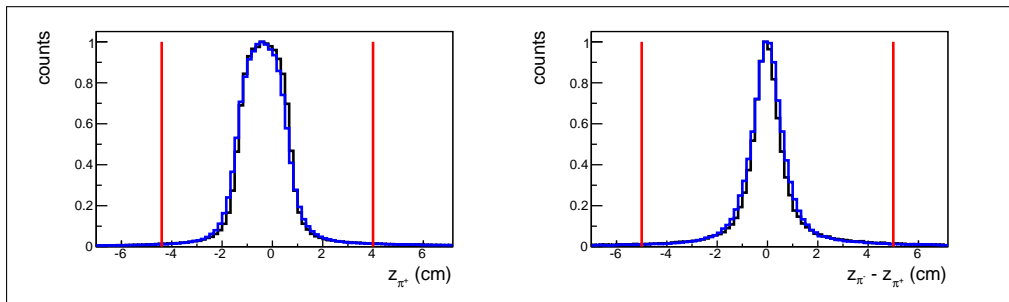


Figure 2.27: Left plot: an example of the cut on the hadron  $z$ -coordinate,  $|z_{\pi^+} + 0.4| < 4.4$  cm. Right plot: an example of the cut on the difference of the vertex  $z$ -coordinates of the final particles,  $|z_{\pi^-} - z_{\pi^+}| < 5$  cm. The black curves correspond to the data, while the blue ones correspond to the reconstructed Monte Carlo events. All histograms are normalized to their maxima.

673 To reduce the number of events in which the final state particles came from different  
674 events and/or took part in final state interactions, the following two additional cuts on the  
675 particle  $z$ -coordinates at the vertex are applied. The first cut is  $|z_h + 0.4| < 4.4$  cm, where the  
676 index  $h$  corresponds to the final hadron type (proton,  $\pi^+$ , and  $\pi^-$ ). The left side of Fig. 2.27  
677 shows an example of this cut for the case  $h = \pi^+$ . The second cut is  $|z_i - z_j| < 5$  cm, where  
678 the indices  $i$  and  $j$  ( $i \neq j$ ) correspond to the final particle type (electron, proton,  $\pi^+$ , and  
679  $\pi^-$ ). The right side of Fig. 2.27 shows an example of this cut for the case  $i = \pi^-$ ,  $j = \pi^+$ .  
680 These additional cuts are made rather loose in order to avoid unjustified loss of good events.

## 681    2.4 Exclusivity cut in the presence of Fermi smearing 682    and FSI

683    For picking out certain exclusive reactions one needs to register the scattered electron and  
684    either all final hadrons or all except one. In the latter case the four-momentum of the unreg-  
685    istered hadron can be restored using energy-momentum conservation (a so-called “missing  
686    mass technique”). Thus for the reaction  $ep \rightarrow e'p'\pi^+\pi^-$  one can in general distinguish be-  
687    tween four so-called “topologies” depending on the specific combination of registered final  
688    hadrons. In this particular analysis the following two topologies are analyzed,

- 689    • the fully exclusive topology (all final particles are registered)  $ep \rightarrow e'p'\pi^+\pi^-X$ , and  
690    • the  $\pi^-$  missing topology  $ep \rightarrow e'p'\pi^+X$ .

691    Due to the experimental conditions the statistics of the fully exclusive topology is very  
692    limited. This happens mainly because CLAS does not cover the polar angle range  $0^\circ < \theta_{lab} <$   
693     $8^\circ$  [4]. The presence of this forward acceptance hole does not affect much the registration of  
694    the positive particles ( $p$  and  $\pi^+$ ), since their trajectories are bent by the magnetic field away  
695    from the hole. Meanwhile, the negative particles ( $e$  and  $\pi^-$ ) are inbending, which means that  
696    their trajectories are bent into the forward direction. Electrons being very light and rapid  
697    undergo small track curvature, and the presence of the forward hole leads for them only to  
698    a constraint on the minimum achievable  $Q^2$ . However, for negative pions the situation is  
699    dramatic: being heavier and slower they are bent dominantly into the forward detector hole  
700    and, therefore, most of them cannot be registered. This leads to the fact that the  $\pi^-$  missing  
701    topology contains the dominant part of the statistics. The contribution of the fully exclusive  
702    topology to the total analyzed statistics<sup>8</sup> varies from  $\sim 5\%$  near the reaction threshold to  
703     $\sim 25\%$  at  $W \sim 1.7 - 1.8$  GeV.

704    For reactions with multi-particle final states the problem of limited acceptance is an  
705    essential issue. Specifically, in the case of the  $p\pi^+\pi^-$  final state the cross section depends  
706    on five final hadron variables and hence is multi-dimensional, but the limited statistics only  
707    allows the extraction of a set of one-fold differential cross sections (see Sects. 3.3 and 3.5).  
708    This leads to the necessity to fill kinematic cells with zero acceptance (so-called “empty  
709    cells”) based on some model assumptions, which leads to model dependent results (see  
710    Sect. 4.1). The fully exclusive topology suffers from the problem of limited acceptance (and  
711    therefore large amount of empty cells) that along with the problem of limited statistics does  
712    not allow any sensible cross section information to be obtained from this topology alone. The  
713     $\pi^-$  missing topology, having significantly fewer empty cells, serves the purpose of the cross  
714    section extraction best. The use of both topologies combined allows the model dependence  
715    of the cross section (that originates from empty cells filling) to be reduced as well as slightly  
716    increasing the statistics.

---

<sup>8</sup>The combined statistics of both the  $\pi^-$  missing and the fully exclusive topologies.

717 The aforementioned features of the two topologies are caused by the experimental con-  
718 ditions and valid either for an experiment off the free proton or for one off the proton bound  
719 in the deuteron. Meanwhile, there are also some features that appear only in bound proton  
720 experiments. Those that are crucial for exclusive event selection are addressed later in this  
721 Section, while others are discussed later in the report.

722 Actually, two more topologies can be distinguished, i.e. the proton missing topology  
723 and the  $\pi^+$  missing topology. Both require registration of the  $\pi^-$  in the final state and as a  
724 consequence suffer from the similar problems of suppressed statistics<sup>9</sup> and limited acceptance  
725 as in the case of the fully exclusive topology. Therefore, these two topologies are usually  
726 ignored in analyses of the reaction  $ep \rightarrow e'p'\pi^+\pi^-$  [15–19]. Nevertheless, as demonstrated  
727 in the sophisticated analysis of this reaction off the free proton target [22, 23], they can  
728 be used as complimentary topologies to the main  $\pi^-$  missing topology, that allows a slight  
729 increase in the statistics and a reduction in the amount of empty cells as much as possible,  
730 therefore minimizing the model dependence of the extracted cross sections. However, if  
731 the pion pair is produced off the proton bound in the deuteron, additional complications  
732 appear: these topologies turn out to be polluted with events from other reaction channels.  
733 In the proton missing topology the missing mass technique fails to distinguish whether the  
734 pion pair was produced off the proton or off the neutron, because their masses are almost  
735 identical. A similar situation occurs for the  $\pi^+$  missing topology, where the same reason  
736 prevents distinguishing between the production of  $\pi^+\pi^-$  pair off the proton and  $\pi^0\pi^-$  pair  
737 off the neutron, if only the proton and the  $\pi^-$  in the final state are registered. Moreover,  
738 the event sample in the  $\pi^+$  missing topology demonstrates strong admixture of events from  
739 the reaction  $en(p) \rightarrow e'p'(p')\pi^-$ , which was found to be not very easy to remove.

740 Taking into account all the above arguments, the following topology ranking takes place  
741 in this particular analysis: the  $\pi^-$  topology is the main one and the fully exclusive topology  
742 is treated as the complimentary one, which gives a slight increase in statistics as well as  
743 some reduction in the amount of empty cells, while the proton missing and the  $\pi^+$  missing  
744 topologies are not used at all.

745 Meanwhile, an experiment on bound nucleons has some specific features, which are ex-  
746 trinsic to the free proton experiments. Those of them that are related to the problem of the  
747 channel identification are listed below.

- 748 • The Fermi motion of the target proton.
  - 749 • Complex effects of Final State Interactions (FSI) due to the presence of the neutron  
750 and the multi-particle final state.
- 751 The manifestations of these effects in the  $\pi^-$  missing and fully exclusive topologies differ.

---

<sup>9</sup> Each of them contains about 10% of the full statistics of all four topologies combined.

752        The movement that the target proton undergoes in the deuterium nucleus is concealed  
753 from the observer and is not measured<sup>10</sup>. However, if all particles in the final state are  
754 registered, one can restore the information about the momentum distribution of the target  
755 proton via energy-momentum conservation (see Sect. 2.4.1 for details). This is not the  
756 case for the  $\pi^-$  missing topology, where incomplete knowledge about the final state leads  
757 to the fact that information about the motion of the initial proton turns out to be totally  
758 lost. Therefore, one is forced to work under a so-called “target-at-rest-assumption” that  
759 considers the target proton to have no motion and as a consequence inevitably leads to  
760 the smearing of various kinematic quantities, such as missing mass, reaction invariant mass  
761 ( $W$ ), etc [35]. Although the fully exclusive topology has the advantage of the possibility  
762 of avoiding the smearing<sup>11</sup>, all kinematic quantities are nevertheless calculated under the  
763 target-at-rest-assumption in order to treat this complimentary topology in the same way as  
764 the main one.

765        In order to reliably identify the exclusive channel and correctly calculate the detector ef-  
766 ficiency, the distributions of the reconstructed Monte Carlo events must match experimental  
767 ones as well as possible. As mentioned above, the necessity to work under the target-at-  
768 rest-assumption smears the experimental distributions, which in turn demands the simulated  
769 distributions reproduce this smearing. Therefore, the effects of the target motion must be  
770 properly included in the Monte Carlo simulation.

771        That is why the event generator TWOPEG-D [26] was used to perform the Monte Carlo  
772 simulation. It is a version of the TWOPEG (event generator for double-pion electroproduction  
773 off the free proton [36]) that was developed for this analysis in order to simulate the  
774 effects of the target motion. In this version of the event generator the Fermi motion of the  
775 initial proton is generated according to Bonn potential [37] and then naturally merged into  
776 the specific kinematics of double-pion electroproduction.

777        The second intrinsic feature of a bound nucleon experiment is the complex effects of FSI.  
778 This phenomenon is driven by the strong interaction and consists in the fact that after the  
779 production of the final state hadrons and before their registration they manage to interact  
780 with each other and/or the recoil nucleon. These interactions include (but are not limited  
781 to) the simple momentum exchange between the hadrons as well as the process of exciting  
782 nucleon resonances with their subsequent decay that may lead to the production of new  
783 particles.

784        Final hadrons produced off the free proton are also subject to the FSI, but in the absence  
785 of the recoil neutron these interactions are not substantial. The arguments for that are the  
786 following. The probability to interact in the final state depends on the distance between

---

<sup>10</sup>In general it can be measured by detecting the recoil nucleon (neutron in this case), but it was not an option in this experiment.

<sup>11</sup>For example, in the fully exclusive topology the value of  $W$ , being calculated using the four-momenta of the registered final hadrons, turns out to be determined within the detector resolution and not affected by the effects of the target motion.

hadrons and their relative velocity, i.e. for slower and closer travelling hadrons the chance to interact is higher than for distant and rapid hadrons. Final state hadrons are produced in one vertex, which means that in the beginning they are very close to each other and therefore have a high chance to interact. However, immediately after the production they start to fly apart from the vertex in radial directions increasing the distance between each other, which causes the interaction probability drop.

The presence of an additional recoil nucleon changes the situation drastically. The neutron, which initially was not involved into the reaction of hadron production, is located slightly aside of the interaction vertex but at the same time very close to it, so that the flying-off final hadrons can impact the neutron. In addition to that, the neutron also moves with Fermi momentum, thus the FSI are brought to the usual hadron-hadron collisions, which may result in the resonance excitation and/or particle production. Direct hadron-hadron collisions, which are unlikely to occur in the reaction off the free proton, since the final hadrons fly apart from one point, start to play a role in the reaction off the bound proton in the presence of the neutron. Therefore, FSI effects in the bound nucleon experiment are rather strong in contrast to those in the free proton one.

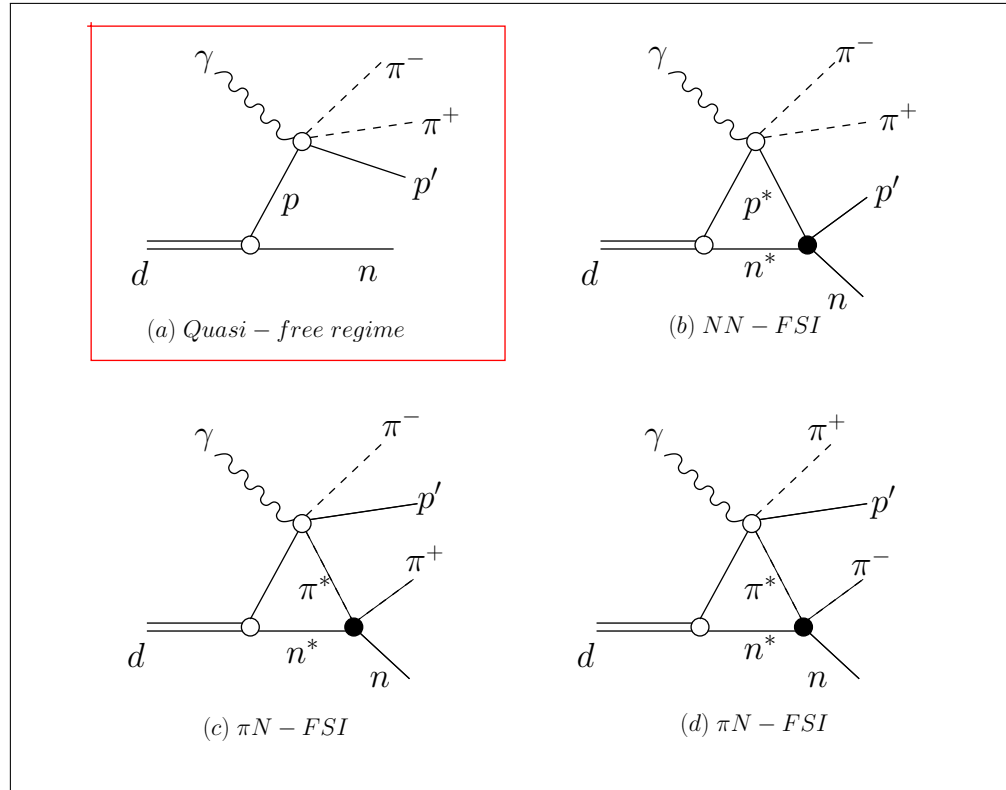


Figure 2.28: Illustration of the leading contributors to the process of the double-pion production off the proton bound in deuteron. (a) Quasi-free regime, (b) NN-FSI, and (c-d)  $\pi N$ -FSI.

803 FSI affect the final hadron momenta, making them either distorted by rescattering ef-  
804 fects or leak away via the production of extra particles in hadron-hadron collisions. This  
805 leads to the distortion of various kinematic quantities, such as missing masses. If the final  
806 hadrons manage to avoid any interaction with the neutron, then the neutron is treated as  
807 a spectator and the reaction is considered to occur in a so-called “quasi-free regime”. Fig-  
808 ure 2.28 schematically illustrates the production of the pion pair off the bound proton in  
809 the quasi-free regime (a) as well as the leading components for FSI of the final hadrons with  
810 the neutron (b-d), which result in so-called “FSI-disturbed kinematics”. The goal of this  
811 study is to extract the cross sections of the process (a), which implies the need to select  
812 for the analysis only events in quasi-free kinematics. This in turn means removing from  
813 consideration those events in which final hadrons have undergone FSI.

814 In contrast to the effects of the target motion, which can be simulated fairly easy, the  
815 effects of FSI can hardly be taken into account in the simulation because they are of very  
816 complex nature and hence not yet fully understood. Therefore, the Monte Carlo simulation  
817 is not able to reproduce the distortions due to FSI that occur in some experimental distribu-  
818 tions, but this is not a problem if events in quasi-free kinematics are properly separated from  
819 those in FSI-disturbed kinematics. This leads to the necessity to develop special procedures  
820 of selecting quasi-free events as well as correcting for the remaining admixture of undesired  
821 events, if they cannot be fully eliminated.

822 The yield of events in FSI-disturbed kinematics turned out to strongly depend on (i) the  
823 reaction invariant mass ( $W$ ) and (ii) on the hadron scattering angles. The latter issue causes  
824 FSI effects to manifest themselves differently depending on the reaction topology, since the  
825 topologies have non-identical geometrical acceptance.

826 As follows from the above, the two analyzed topologies differ from each other both in  
827 treating of the Fermi motion of the initial proton and in FSI manifestations. Therefore, the  
828 channel identification in the quasi-free regime was performed in each topology individually  
829 (see subsequent subsections).

830 The problem of background channels is also an issue that deserves special attention for  
831 the bound proton experiment. For the reaction of double-pion production off the free proton  
832 the main background channel is  $ep \rightarrow e'p'\pi^+\pi^-\pi^0$ . In the analysis [22] that was carried out  
833 for the same beam energy  $E_{beam} = 2.039$  GeV, it is shown that although the admixture of  
834 the events from this background channel becomes discernible at  $W \gtrsim 1.6$  GeV, it remains  
835 negligible and well separated from the double-pion events via the exclusivity cuts. For the  
836 experiments with the deuteron target the reaction  $en(p) \rightarrow e'p'(p')\pi^+\pi^-\pi^-$  can also act as  
837 a background channel for the investigated  $ep(n) \rightarrow e'p'(n')\pi^+\pi^-$  reaction, however it is also  
838 expected to give an insignificant and well separated admixture. Here and hereinafter the term  
839 “background channel” is used to denote the reaction that happened in electron scattering  
840 off the target nucleon along with the investigated double-pion reaction. Any reaction that  
841 might occur during the FSI is not treated as the contribution from “background channels”,  
842 but is attributed to the FSI-background.

### 843 2.4.1 Fully exclusive topology

844 In the fully exclusive topology for the selection of double-pion events in quasi-free kinematics  
 845 the distributions of the following quantities were investigated: the missing momentum  $P_X$   
 846 and the missing mass squared  $M_{X[0]}^2$  for the reaction  $ep(n) \rightarrow e'p'(n')\pi^+\pi^-X$  as well as the  
 847 missing mass squared  $M_{X[\pi^-]}^2$  for the reaction  $ep(n) \rightarrow e'p'(n')\pi^+X$ . These quantities are  
 848 defined by

$$\begin{aligned} P_X &= |\vec{P}_e - \vec{P}_{e'} - \vec{P}_{p'} - \vec{P}_{\pi^+} - \vec{P}_{\pi^-}|, \\ M_{X[0]}^2 &= [P_e^\mu + P_p^\mu - P_{e'}^\mu - P_{p'}^\mu - P_{\pi^+}^\mu - P_{\pi^-}^\mu]^2, \\ M_{X[\pi^-]}^2 &= [P_{\pi^- \text{ miss}}^\mu]^2 = [P_e^\mu + P_p^\mu - P_{e'}^\mu - P_{p'}^\mu - P_{\pi^+}^\mu]^2, \end{aligned} \quad (2.4.1)$$

849 where  $P_i^\mu$  are the four-momenta and  $\vec{P}_i$  the three-momenta of the particle  $i$ . All three quanti-  
 850 ties are calculated under the target-at-rest-assumption, i.e. considering  $P_p^\mu = (0, 0, 0, m_p)$ ,  
 851 where  $m_p$  is the proton mass.

852 The quantities  $P_X$  and  $M_{X[0]}^2$  are unique for the fully exclusive topology, they can be  
 853 calculated only if all final hadrons are registered. Although adding the missing mass squared  
 854  $M_{X[\pi^-]}^2$  to this set seems not to provide any additional information, it is investigated in order  
 855 to observe consistency with the  $\pi^-$  missing topology, where the distribution of this quantity  
 856 is the only source for developing a criterion for channel identification. See App. A for details  
 857 on features of missing mass distributions.

858 Distributions of the quantities  $P_X$  (first column),  $M_{X[0]}^2$  (second column), and  $M_{X[\pi^-]}^2$   
 859 (third column) for five 100-MeV-wide bins<sup>12</sup> in  $W$  are shown in Fig. 2.29 both for the  
 860 experimental data (black curves) and reconstructed Monte Carlo events (blue curves).

861 The quantity  $P_X$  (first column in Fig. 2.29) is the missing momentum of the initial  
 862 proton calculated under the target-at-rest-assumption, therefore the blue curves stand for  
 863 the Fermi momentum (simulated according to Bonn potential [37]) convoluted with the  
 864 detector resolution, whereas the black ones correspond to the experimental momentum of  
 865 initial proton, mixed with the FSI effects, contributions from background channels, and the  
 866 detector resolution. As seen in the left column of Fig. 2.29, the simulated distributions  
 867 perfectly match the experimental ones for  $P_x < 0.2$  GeV, while for  $P_x > 0.2$  GeV the  
 868 simulation underestimates data. Such behavior is mostly related to the fact that relative  
 869 contributions from FSI, which were not included into the Monte Carlo simulation, turn out  
 870 to be the most significant outside of the peak region. The background channels, being not  
 871 included into the Monte Carlo as well, also contribute to this mismatch, but as mentioned  
 872 above their contribution is minor. The value  $P_x = 0.2$  GeV (marked by the red dashed lines  
 873 in each plot in the left column) was chosen as a criterion for the selection of events in quasi-

---

<sup>12</sup>The value of  $W$  is calculated for the initial state under the target-at-rest-assumption by  $W = \sqrt{(P_e^\mu + P_p^\mu - P_{e'}^\mu)^2}$ .

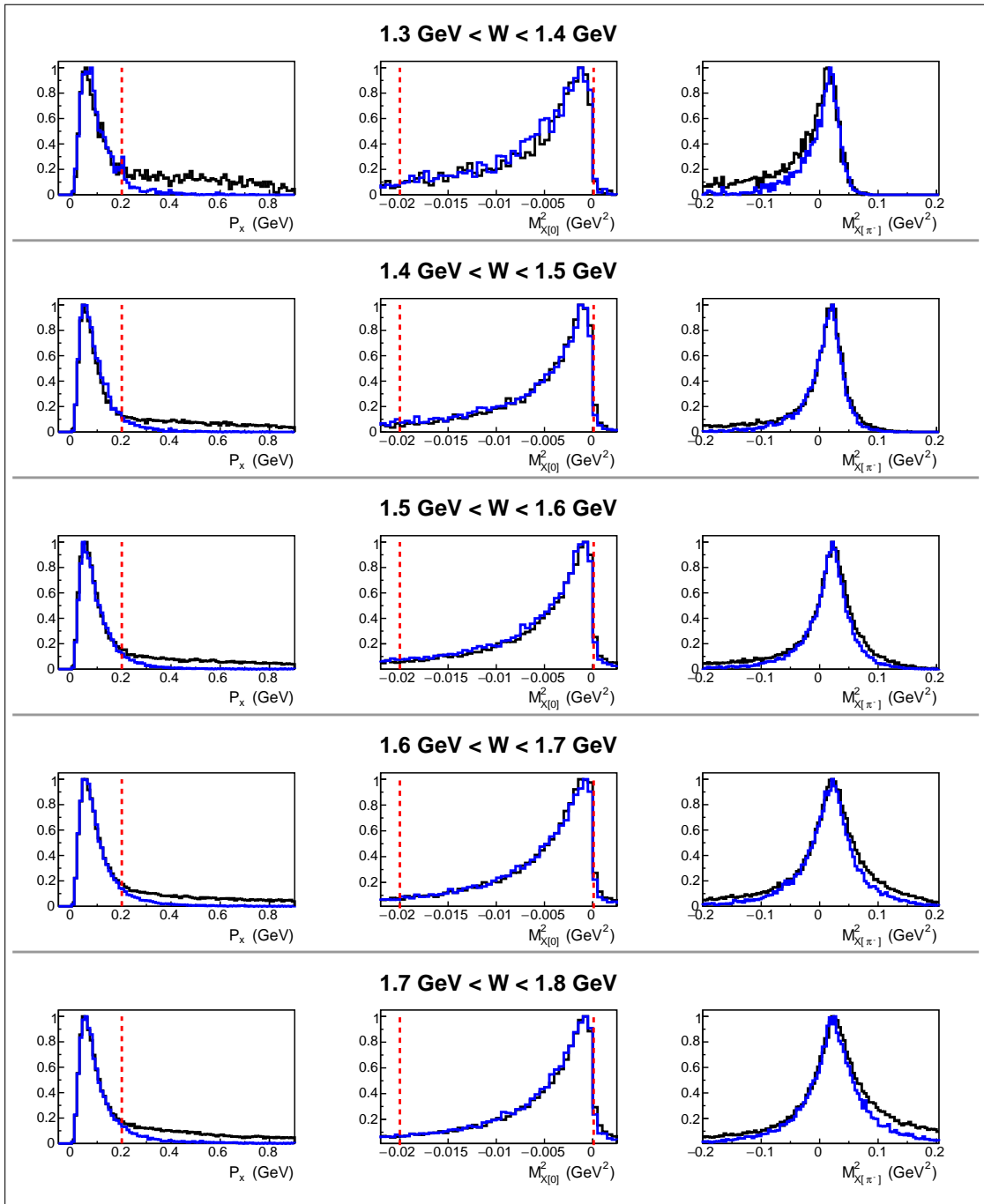


Figure 2.29: Distributions of the quantities  $P_X$  (left column),  $M_{X[0]}^2$  (middle column), and  $M_{X[\pi^-]}^2$  (right column) defined in Eq. (2.4.1) for experimental data (black curves) and Monte Carlo simulation (blue curves) for different 100-MeV-wide  $W$  bins. Vertical red lines indicate the cuts applied for the selection of exclusive quasi-free events. All plotted quantities as well as the values of  $W$  are calculated under the target-at-rest-assumption. All distributions are normalized to their maxima.

874 free kinematics. Thus, experimental events located at the left side of this line correspond  
 875 to the reaction in the quasi-free regime, while events at the right side correspond mostly to  
 876 “disturbed” kinematics with great impact of FSI.

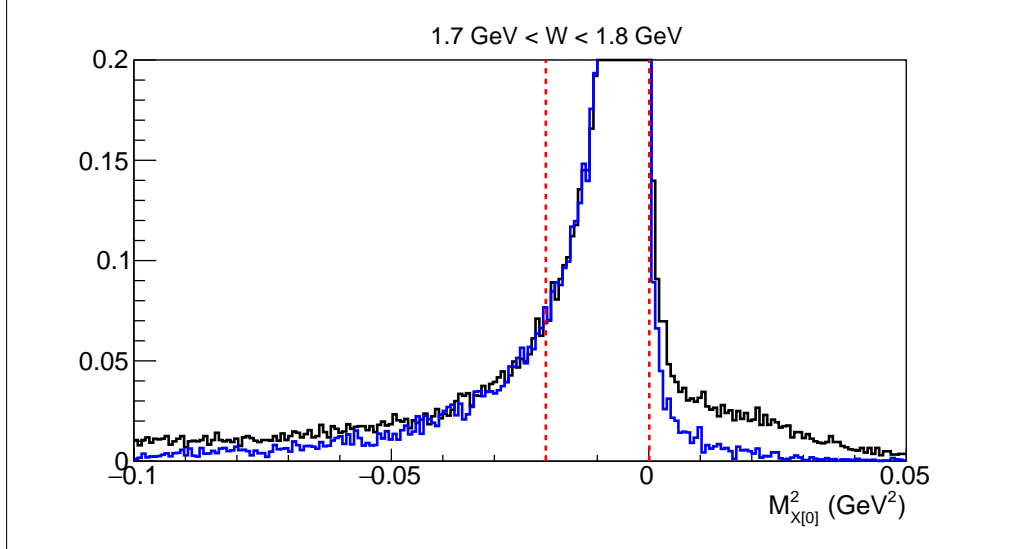


Figure 2.30: Distributions of the missing mass squared  $M_{X[0]}^2$  for experimental data (black curves) and Monte Carlo simulation (blue curves) zoomed at the foot. Vertical red lines indicate the applied cut. The mismatch between data and simulation originates from FSI effects at the left and three-pion background at the right. The example is given for  $1.7 \text{ GeV} < W < 1.8 \text{ GeV}$ , where the latter is greatest over the whole  $W$  range. The agreement between data and simulation within the cut boundaries is better shown in Fig. 2.29 (middle column).

877 The distributions of the quantity  $M_{X[0]}^2$  shown in the middle column in Fig. 2.29 deserve  
 878 more attention. As demonstrated in Refs. [22, 23] and here in App. A, in free proton  
 879 experiments this quantity forms a very narrow peak at zero position barely affected either  
 880 by radiative effects or by detector resolution. An admixture from the three-pion background,  
 881 if present in the analyzed event sample, forms then an additional peaked structure at  $m_\pi^2$   
 882 well-separated from the main distribution peak. Meanwhile, in this analysis  $M_{X[0]}^2$ , being  
 883 calculated under the target-at-rest-assumption, loses its thinness and acquires the smearing  
 884 (mostly left-sided), which is well-reproduced by the Monte Carlo simulation.

885 In order to clean up the sample of exclusive events, the cut on the missing mass squared  
 886  $M_{X[0]}^2$  was also applied as complimentary to the cut on the missing momentum. This cut is  
 887 shown in Fig. 2.29 (middle column) by the vertical red dashed lines. The plots in the middle  
 888 column are zoomed near the peak to demonstrate good agreement between the data and the  
 889 simulation within the cut limits. The behavior of  $M_{X[0]}^2$  in a wider range is shown in Fig. 2.30,  
 890 where the distributions are zoomed at the foot. As seen, outside the cut boundaries there is  
 891 a mismatch between the data and simulation, which originates from FSI effects at the left

892 and the contribution from the three-pion background at the right. The latter forms a peaked  
 893 structure around  $m_\pi^2$  ( $\sim 0.02 \text{ GeV}^2$ ), which is more smeared compared to the free proton case  
 894 due to the target-at-rest-assumption and FSI disturbances. The example is given for high  
 895  $W$  to observe the greatest background admixture over the investigated  $W$  range.

896 The three-pion background in this topology is considered to be fully eliminated by the  
 897 described above cuts on the missing momentum  $P_X$  and the missing mass squared  $M_{X[0]}^2$ .

898 The right column in Fig. 2.29 stands for the missing mass squared  $M_{X[\pi^-]}^2$  defined by  
 899 Eq. (2.4.1) under the target-at-rest-assumption, thus being Fermi smeared. The observed  
 900 mismatch between the measured and simulated distributions is  $W$ -dependent and caused  
 mostly by the FSI effects.

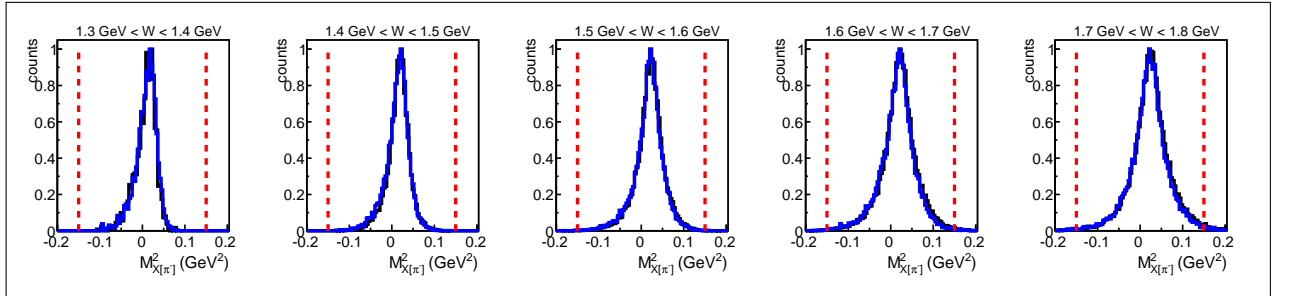


Figure 2.31: Distributions of the missing mass squared  $M_{X[\pi^-]}^2$  defined in Eq. (2.4.1) for the fully exclusive topology plotted for selected quasi-free exclusive events for experimental data (black curves) and Monte Carlo simulation (blue curves). The comparison is shown for different 100-MeV-wide  $W$  bins. The quantity  $M_{X[\pi^-]}^2$  as well as the values of  $W$  are calculated under the target-at-rest-assumption. The vertical red lines show the applied cuts. All distributions are normalized to their maxima. See text for details.

901  
 902 Figure 2.31 shows the distributions of the missing mass squared  $M_{X[\pi^-]}^2$  plotted for quasi-  
 903 free exclusive events selected by the cuts on missing momentum  $P_x$  and missing mass squared  
 904  $M_{X[0]}^2$ . The distributions for the experimental (black curves) and reconstructed Monte Carlo  
 905 (blue curves) events perfectly match each other in all  $W$  subranges, which demonstrates the  
 906 reliability of quasi-free exclusive event selection as well as the fact that effects of the target  
 907 motion are correctly implemented into the simulation. The vertical red lines in Fig. 2.31  
 908 correspond to the additional cut that was applied on the missing mass squared  $M_{X[\pi^-]}^2$ .

909 Although in the fully exclusive topology the four-momentum of the  $\pi^-$  is measured pre-  
 910 cisely within the detector resolution, it is not used in the subsequent calculation of kinematic  
 911 variables for the cross section extraction. The measured four-momentum is instead replaced  
 912 by the one that is calculated as missing ( $P_{\pi^- \text{ miss}}^\mu$  in Eq. (2.4.1)) and thus is Fermi smeared.  
 913 This is done to imitate the event selection in the main  $\pi^-$  missing topology in order to treat  
 914 events in both topologies identically.

### 915 2.4.2 $\pi^-$ missing topology

916 In the  $\pi^-$  missing topology the quantities  $P_X$  and  $M_{X[0]}^2$  defined in Eq. (2.4.1) are not avail-  
 917 able due to the incomplete knowledge about the final state, and  $M_{X[\pi^-]}^2$  is the only remaining  
 918 quantity suitable for the selection of exclusive events in quasi-free kinematics. The distri-  
 919 butions of this quantity are shown in Fig. 2.32 for five 100-MeV-wide bins in  $W$  for the  
 920 experimental data (black curves) and the Monte Carlo simulation (blue curves). The com-  
 921 parison shown in this figure demonstrates again the  $W$ -dependent mismatch between data  
 922 and simulation, which is different from that seen in the fully exclusive topology. The mis-  
 923 match is mostly observed at the right side of the distribution peak and becomes discernible  
 only for  $W \gtrsim 1.5$  GeV.

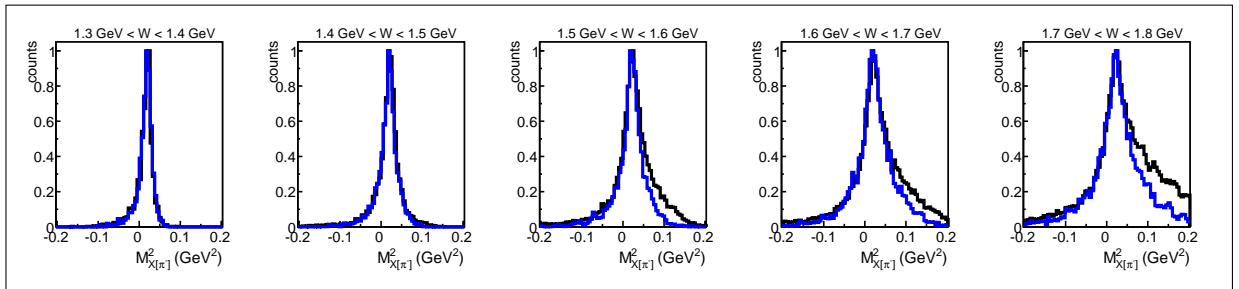


Figure 2.32: Distributions of the missing mass squared  $M_{X[\pi^-]}^2$  defined in Eq. (2.4.1) for the  $\pi^-$  missing topology plotted before the selection of quasi-free exclusive events for experimental data (black curves) and Monte Carlo simulation (blue curves). The comparison is shown for different 100-MeV-wide  $W$  bins. The quantity  $M_{X[\pi^-]}^2$  as well as the values of  $W$  are calculated under the target-at-rest-assumption. All distributions are normalized to their maxima. See text for details.

924

925 The similar analysis [22] carried out for the same beam energy but off a free proton  
 926 target did not reveal any substantial discrepancies between the experimental and simulated  
 927 distributions of the quantity  $M_{X[\pi^-]}^2$ ; they are shown to be in a very good agreement for all  
 928  $W$  values. Figure 2.31 plotted for selected exclusive quasi-free events in the fully exclusive  
 929 topology in turn proves that the Monte Carlo simulation incorporates effects of the tar-  
 930 get motion correctly. Therefore, the discrepancy between data and simulation observed in  
 931 Fig. 2.32 is attributed mainly to the FSI effects, which are not included into the simulation.

932 This mismatch between data and simulation together with the fact that in the  $\pi^-$  missing  
 933 topology the quantity  $M_{X[\pi^-]}^2$  is the only one available for the channel identification makes  
 934 the task of selecting events in quasi-free kinematic rather challenging. To accomplish this  
 935 goal, a special procedure was developed. This procedure is described below.

936 To select events in quasi-free kinematics properly, the following quantity is analyzed.

$$M_{X[\pi^-]} = \sqrt{|M_{X[\pi^-]}^2|} = \sqrt{|[P_{\pi^- miss}^\mu]^2|} = \sqrt{|[P_e^\mu + P_p^\mu - P_{e'}^\mu - P_{p'}^\mu - P_{\pi^+}^\mu]^2|}. \quad (2.4.2)$$

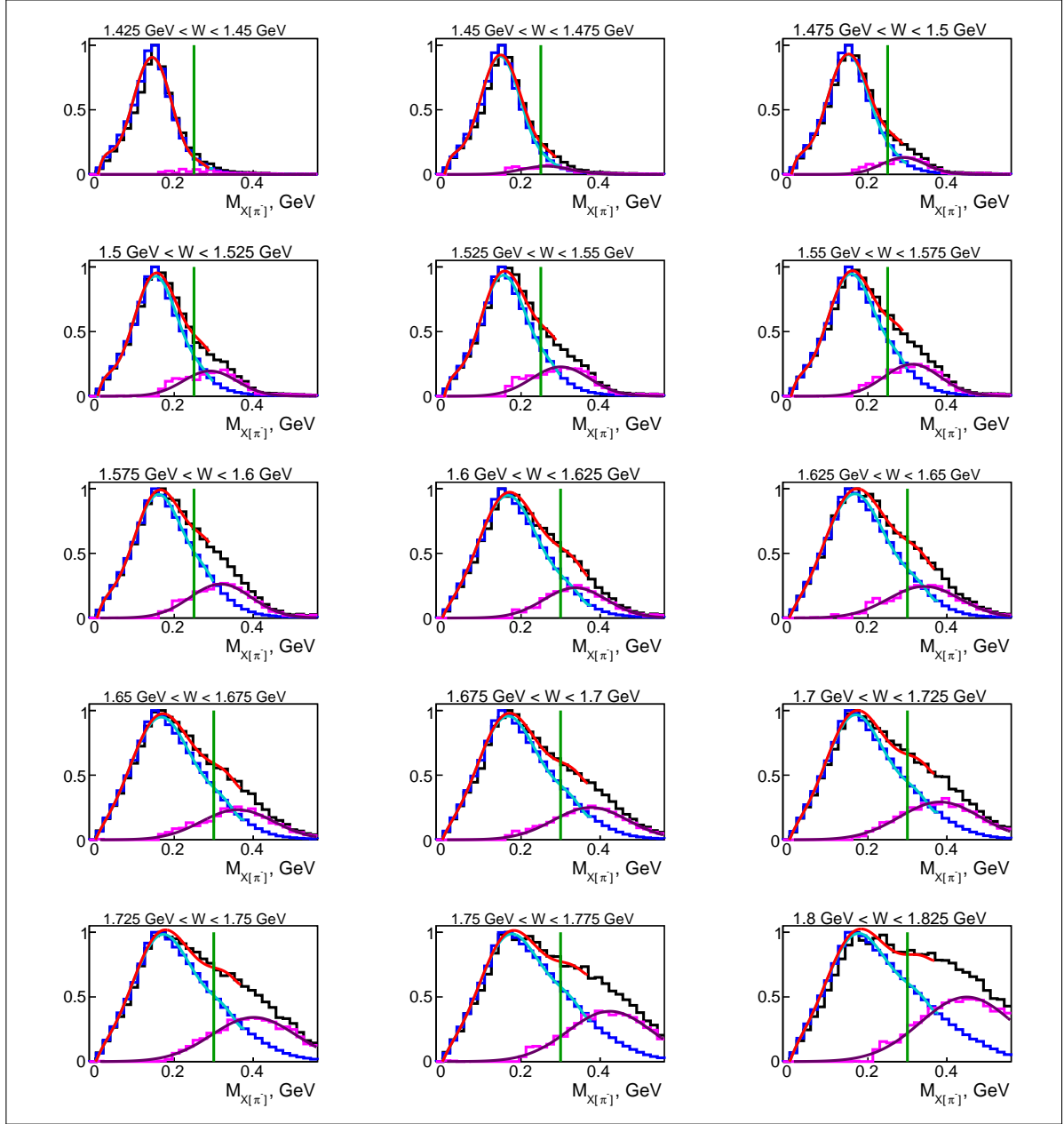


Figure 2.33: Distributions of the quantity  $M_{X[\pi^-]}$  (defined by Eq. (2.4.2)) in different 25-MeV-wide  $W$  bins for experimental data (black histograms), Monte Carlo simulation (blue histograms), and their difference (magenta histograms). The explanation of the fit curves is given in the text. Green vertical lines correspond to the position of the cut that is intended to select quasi-free events. This cut is applied to the reconstructed Monte Carlo events as well.

938        The distributions of the quantity  $M_{X[\pi^-]}$  in different 25-MeV-wide  $W$  bins are shown in  
 939        Fig. 2.33 for experimental data (black histograms) and for Monte Carlo simulation (blue  
 940        histograms). Both are normalized to their maxima. The mismatch between data and sim-  
 941        ulation becomes discernible at  $W \approx 1.5$  GeV, increases as  $W$  grows and becomes large at  
 942         $W \approx 1.8$  GeV. The magenta histogram stands for the difference between the black and blue  
 943        histograms and thus represents the distribution of background events originated mainly from  
 944        FSI effects. The green vertical lines correspond to the position of the cut that is intended  
 945        to select quasi-free events. This cut is applied to the reconstructed Monte Carlo events as  
 946        well. However, as seen in Fig. 2.33, one can hardly completely separate the quasi-free event  
 947        sample from the FSI-background by tightening the cut: in this way the statistics of quasi-  
 948        free events will be subject to significant reduction, while the background admixture will still  
 949        not be completely eliminated. Therefore, it was decided to perform a so-called “effective  
 950        correction” of the FSI-background admixture, which includes the following steps.

- 951        • The distributions of  $M_{X[\pi^-]}$  for the reconstructed Monte Carlo events (blue histograms)  
 952        were fit by a ninth order polynomial in a slightly wider range than marked by the green  
 953        cut lines. The results of the fit are shown in Fig. 2.33 by the cyan curves.
- 954        • The magenta background distributions were fit by Gaussians. The results of the fit are  
 955        shown by the dark-magenta curves.
- 956        • The cyan and dark-magenta curves were summed up to produce the red curve, which  
 957        perfectly matches the black experimental histogram in each  $W$  bin.
- 958        • The following correction factor was determined in the left side of the green cut line,

$$F_{fsi}(W) = \frac{\text{area under the cyan curve}}{\text{area under the red curve}} \leq 1. \quad (2.4.3)$$

- 959
- 960        • In each  $W$  bin the experimental event yield in the  $\pi^-$ -missing topology is multiplied by  
 961        the factor  $F_{fsi}$ , which serves as an effective correction due to the remaining admixture  
 962        of the FSI-background events.

963        The factor  $F_{fsi}$  is assumed to be only  $W$  dependent as it was found that it does not  
 964        demonstrate any  $Q^2$  dependence, and the dependence on the final hadron variables is ne-  
 965        glected due to the statistics limitation. The value of  $F_{fsi}$  varies from  $\sim 0.97$  to  $\sim 0.93$  in  
 966        the  $W$  range from 1.4625 GeV to 1.8125 GeV, while for  $W < 1.4625$  GeV  $F_{fsi} = 1$  as the  
 967        correction there is not needed.

968        Note that the exclusivity cut shown in Fig. 2.33 accompanied by the corresponding  
 969        correction cares for all other possible effects that along with the FSI effects may contribute  
 970        to the mismatch between the data and the simulation in this topology (including the three-  
 971        pion background).

<sub>972</sub> **Chapter 3**

<sub>973</sub> **Cross section calculation**

<sub>974</sub> **3.1  $W$ -smearing and boundary blurring of the  $Q^2$  ver-**  
<sub>975</sub> **sus  $W$  distribution**

<sub>976</sub> The smearing of the invariant mass  $W$  has the same origin as the smearing of the missing  
<sub>977</sub> mass, which is already discussed in Sect. 2.4, but since  $W$  is the variable needed to describe  
<sub>978</sub> the reaction (and the extracted cross section is binned in  $W$ ), the issue of  $W$ -smearing  
<sub>979</sub> requires special attention and, therefore, is separately addressed here.

<sub>980</sub> For the process of double-pion electroproduction off the proton (as for any other exclusive  
<sub>981</sub> process) the reaction's invariant mass can in general be determined in two ways, i.e. either  
<sub>982</sub> from the initial particle four-momenta<sup>1</sup> ( $W_i$ ) or from the final particle four-momenta ( $W_f$ )  
<sub>983</sub> as Eqs. (3.1.1) and (3.1.2) demonstrate.

$$W_i = \sqrt{(P_p^\mu + P_{\gamma_v}^\mu)^2} \quad (3.1.1)$$

$$W_f = \sqrt{(P_{\pi^+}^\mu + P_{\pi^-}^\mu + P_{p'}^\mu)^2} \quad (3.1.2)$$

<sub>984</sub> Here  $P_{\pi^+}^\mu$ ,  $P_{\pi^-}^\mu$ , and  $P_{p'}^\mu$  are the four-momenta of the final state hadrons,  $P_p^\mu$  is the four-  
<sub>985</sub> momentum of the initial proton and  $P_{\gamma_v}^\mu = P_e^\mu - P_{e'}^\mu$  the four-momentum of the virtual photon  
<sub>986</sub> with  $P_e^\mu$  and  $P_{e'}^\mu$  the four-momenta of the incoming and scattered electrons, respectively.

<sub>987</sub> To determine  $W_f$ , all final hadrons should be registered, while for the calculation of  $W_i$   
<sub>988</sub> it is sufficient to register the scattered electron. The latter opportunity allows event samples  
<sub>989</sub> with one unregistered final hadron, whose four-momentum is recovered via the missing mass

---

<sup>1</sup> Although the scattered electron is treated as a final particle, here it is classified as “initial”, since it defines the virtual photon, which in turn is attributed to the initial state.

990 technique, to be used. This approach allows for a significant increase of the analyzed statistics  
991 (see Sect. 2.4).

992 In experiments off protons at rest  $W_f$  and  $W_i$  may differ due to the detector resolution  
993 and the radiative effects, which electrons undergo. In moving proton experiments one more  
994 aspect takes effect, i.e. in order to calculate  $W_i$ , one needs information about the target  
995 proton momentum ( $P_p^\mu$ ), which is accessible only in the fully exclusive topology<sup>2</sup>. Therefore,  
996 the value of  $W_i$  given by Eq. (3.1.1) turns out to be ill-defined, if one of the final hadrons  
997 is not registered. This brings us to the choice to either demand the registration of all final  
998 hadrons to determine  $W_f$  (that reduces the flexibility of the analysis) or to work under a so-  
999 called “target-at-rest-assumption”, which assumes the initial proton to be at rest. In the last  
1000 approach the value of  $W_i$  appears to be smeared. This smeared value of the invariant mass  
1001 is hereinafter denoted as  $W_{sm}$ . Meanwhile, the value  $W_f$  corresponds to the true reaction  
1002 invariant mass and, therefore, is denoted as  $W_{true}$ . It can be calculated only in the fully  
1003 exclusive topology.

1004 If a smeared value  $W_{sm}$  is used to describe the reaction, the extracted cross sections  
1005 turned out to be convoluted with a function that is determined by the Fermi motion of the  
1006 initial proton [26, 35]. To retrieve the non-smeared observable, a correction that unfolds this  
1007 effect should be applied to the cross sections.

1008 Beside the  $W$ -smearing, the Fermi motion of the target proton is also responsible for the  
1009 boundary blurring of the  $Q^2$  versus  $W$  distribution<sup>3</sup>. This happens because the experiment  
1010 off the moving proton with fixed laboratory beam energy is equivalent to that off the proton  
1011 at rest performed with altered effective beam energy [26]. The boundaries of the  $Q^2$  versus  
1012  $W$  distribution, however, are beam energy dependent. Therefore, the distribution edges,  
1013 being sharp and distinct in the proton at rest experiment, become blurred in the experiment  
1014 off a moving proton.

1015 The blurring, however, affects only the edges of  $Q^2$  versus  $W_{true}$  distribution, where  $W_{true}$   
1016 is the true reaction invariant mass given by Eq. (3.1.2), since  $W_{true}$  accounts for the target  
1017 motion and, therefore, for the alteration of the effective beam energy. If the smeared value  
1018  $W_{sm}$ , calculated by Eq. (3.1.1) under the target-at-rest-assumption, is used instead, the  
1019 distribution edges are not subject to the blurring because the fixed value of the laboratory  
1020 beam energy is used in calculations.

1021 This situation is illustrated in Fig. 3.1, where the  $Q^2$  versus  $W$  distributions are shown  
1022 for  $W_{sm}$  (left) and  $W_{true}$  (right). These distributions are plotted for the fully exclusive  
1023 topology only, since it allows for the determination of both  $W_{sm}$  and  $W_{true}$ . The distributions,  
1024 therefore, contain only a small portion of the total analyzed statistics. The boundaries of  
1025 the left distribution are sharp, since the  $W_{sm}$  is calculated assuming the fixed laboratory  
1026 beam energy and the target at rest. The boundaries of the right distribution are blurred,

---

<sup>2</sup>If the spectator nucleon momentum is not directly measured in the experiment. This was not an option in the analyzed “e1e” experiment.

<sup>3</sup>This issue is addressed in more details in Ref. [26].

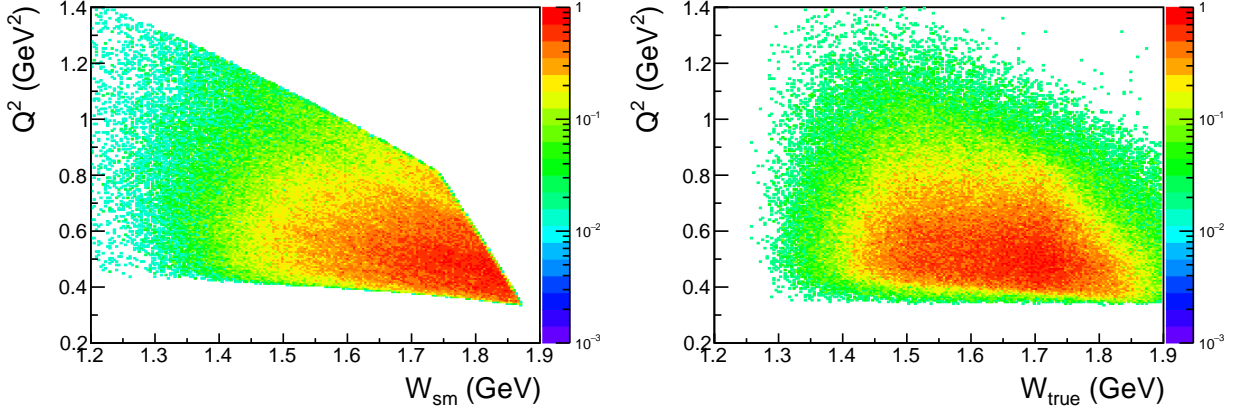


Figure 3.1: Experimental  $Q^2$  versus  $W$  distributions for  $W_{sm}$  (left) and  $W_{true}$  (right) plotted for the fully exclusive topology. The boundaries of the left distribution are sharp, since the  $W_{sm}$  is calculated under the target-at-rest-assumption and the fixed value of the laboratory beam energy is used in calculations. The boundaries of the right distribution are blurred, since the calculation of  $W_{true}$  accounts for the target proton motion and therefore for the alteration of the effective beam energy of the experiment.

since the calculation of  $W_{true}$  accounts for the target proton motion and, therefore, for the alteration of the effective beam energy of the experiment.

The event yield in the blurred region suffers from depletion of events (compared to that for the case of fixed beam energy and sharp distribution edges). To estimate this effect, one should know the function that describes the alteration of the effective beam energy. This function is in turn determined by the target proton momentum distribution. The cross sections extracted in the blurred region need a special correction, otherwise they will suffer from the underestimation.

The situation described above offers two options, i.e. to use either  $W_{sm}$  or  $W_{true}$  to describe the reaction. The former opportunity leads to the need to apply a correction that unfolds the cross section smearing, while the latter requires the correction due to the blurring effect. The first option was chosen in this analysis because it has the advantage of using the  $\pi^-$  missing topology that accumulates the majority of the experimentally available statistics.

Thus, to calculate the cross section in this analysis, events are binned in  $W_{sm}$ . Note, however, that the corresponding  $W$  points on the chosen  $W_{sm}$  grid (see Sect. 3.4) are then treated as actual  $W$ -values where the cross section is eventually reported. However, the cross section values assigned to these  $W$  points is treated as distorted. The necessary correction to the cross section is based on the TWOPEG-D event generator [26], which offers a proper Monte Carlo simulation of the double-pion electroproduction off moving protons. This correction is described in Sect. 4.3.

## 3.2 Lab to CMS transformation

Once the quasi-free double-pion events are selected as described in Chapter 2, the laboratory four-momenta of all final particles are known: they are either registered or calculated as missing. These four-momenta are then used for the calculation of the kinematic variables, which are introduced in Sect. 3.3. The cross sections meanwhile are extracted in the center-of-mass frame of the *virtual photon – initial proton* system (CMS). Therefore, to calculate the kinematic variables, the four-momenta of all particles need to be transformed from the laboratory system (Lab) to the CMS.

The CMS is uniquely defined as the system, where the initial proton and the photon move towards each other with the  $z_{CMS}$ -axis along the photon and the net momentum equal to zero. However, the procedure of the Lab to CMS transformation differs depending on the specificity of the reaction initial state (real or virtual photons, at rest or moving target). Figure 3.2 illustrates three options<sup>4</sup> for the experimental specification of the reaction initial state.

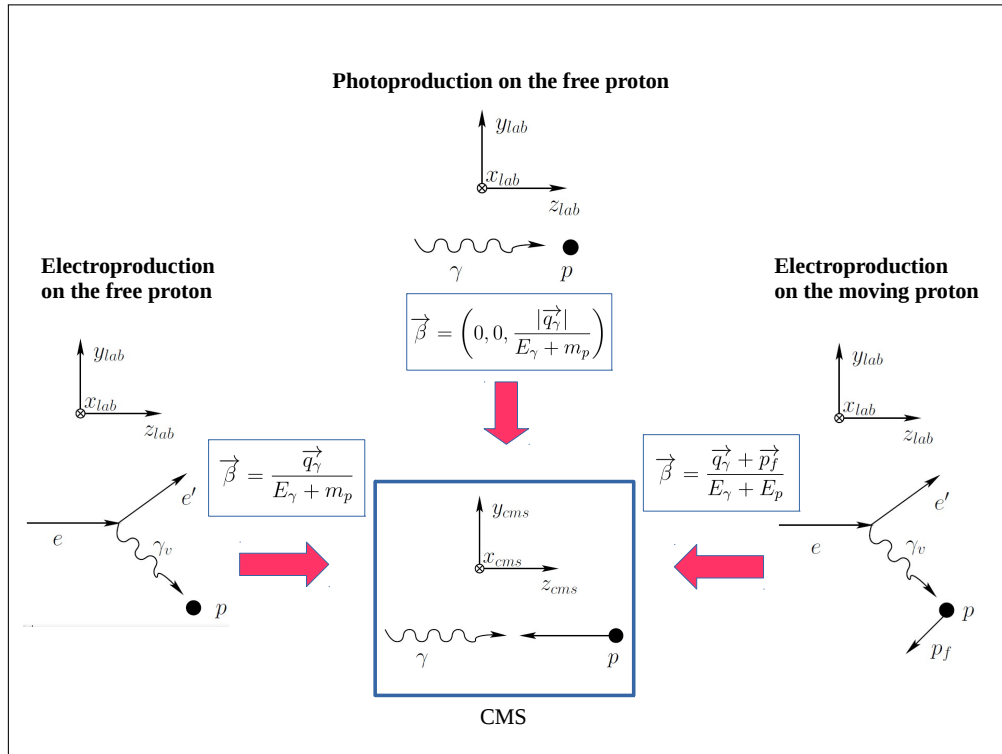


Figure 3.2: Illustration of three options for the experimental specification of the reaction initial state. Here  $m_p$  is the proton mass,  $\vec{q}_\gamma$  and  $E_\gamma$  are the three-momentum and the energy of the interacting photon, respectively, while  $p_f$  is the Fermi momentum of the target proton.

<sup>4</sup>The fourth option of the reaction off the moving proton induced by the real photons is not shown.

1061        The correct procedure of the Lab to CMS transformation for an electroproduction ex-  
1062        periment off a moving target (bottom right illustration in Fig. 3.2) can be subdivided into  
1063        two major steps.

- 1064        A. First, one needs to perform the transition to the auxiliary system, where the target  
1065        proton is at rest, while the incoming electron moves along the  $z$ -axis. This system is  
1066        called “quasi-Lab”, since the initial conditions of the reaction in this frame imitate  
1067        those existing in the Lab system in the case of the free proton experiment. The recipe  
1068        of the Lab to quasi-Lab transformations is given in detail in Ref. [26].
- 1069        B. Then, the quasi-Lab to CMS transformation should be performed by the standard  
1070        method used for an electroproduction experiment off a proton at rest [22] (bottom left  
1071        illustration in Fig. 3.2). Further details are given in App. B.

1072        To perform the first step of this procedure (Lab to quasi-Lab transformation), one should  
1073        be aware of the initial proton momentum for each reaction event [26]. In this analysis,  
1074        however, this information is available only in the fully exclusive topology, while the main  
1075         $\pi^-$  missing topology lacks this information. This situation brings us to the impossibility to  
1076        perform the correct Lab to CMS transformation for the majority of events. Therefore, in this  
1077        analysis the procedure of Lab to CMS transformation for an electroproduction experiment  
1078        off a proton at rest [22] is used (bottom left illustration in Fig. 3.2). The procedure is  
1079        described in App. B. This is done for both fully-exclusive and main  $\pi^-$  missing topologies  
1080        for consistency.

1081        This approximation in the Lab to CMS transformation introduces a systematic inaccuracy  
1082        to the extracted cross sections. A correction for this effect is included into the procedure of  
1083        unfolding the effects of the target motion (see Sect. 4.3).

### 1084 3.3 Kinematic variables

1085 When the four-momenta of all particles are defined and transformed to the CMS, one can  
 1086 calculate the kinematic variables that describe the reaction  $ep(n) \rightarrow e'p'(n')\pi^+\pi^-$ . For the  
 1087 description of the reaction initial state two variables are needed. In this study they are chosen  
 1088 in the following way: the invariant mass  $W$ , which is calculated according to Eq. (3.1.1),  
 1089 and the photon virtuality  $Q^2$ , which is defined as

$$Q^2 = -(P_{\gamma_v}^\mu)^2 = -(P_e^\mu - P_{e'}^\mu)^2, \quad (3.3.1)$$

1090 where  $P_{\gamma_v}^\mu$  is the four-momentum of the virtual photon, while  $P_e^\mu$  and  $P_{e'}^\mu$  the four-momenta  
 1091 of the incoming and scattered electrons, respectively.

1092 The three-body final hadron state is unambiguously determined by five kinematic vari-  
 1093 ables [22], and there are several options for their choice. The following generalized set of  
 1094 variables is used in this analysis<sup>5</sup>:

- 1095 • invariant mass of the first pair of the hadrons  $M_{h_1 h_2}$ ,
- 1096 • invariant mass of the second pair of the hadrons  $M_{h_2 h_3}$ ,
- 1097 • the first particle solid angle  $\Omega_{h_1} = (\theta_{h_1}, \varphi_{h_1})$ , and
- 1098 • the angle  $\alpha_{h_1}$  between the two planes (i) defined by the three-momenta of the virtual  
 1099 photon (or initial proton) and the first final hadron and (ii) defined by the three-  
 1100 momenta of all final hadrons<sup>6</sup>.

1101 The cross sections in this analysis are obtained in three sets of variables depending on  
 1102 various assignments for the first, second, and third final hadrons:

- 1103 1.  $[p', \pi^+, \pi^-] M_{p'\pi^+}, M_{\pi^+\pi^-}, \theta_{p'}, \varphi_{p'}, \alpha_{p'} \text{ (or } \alpha_{[pp'][\pi^+\pi^-]} \text{)},$
- 1104 2.  $[\pi^-, \pi^+, p'] M_{\pi^-\pi^+}, M_{\pi^+p'}, \theta_{\pi^-}, \varphi_{\pi^-}, \alpha_{\pi^-} \text{ (or } \alpha_{[p\pi^-][p'\pi^+]} \text{)},$
- 1105 3.  $[\pi^+, \pi^-, p'] M_{\pi^+\pi^-}, M_{\pi^-p'}, \theta_{\pi^+}, \varphi_{\pi^+}, \alpha_{\pi^+} \text{ (or } \alpha_{[p\pi^+][p'\pi^-]} \text{)}.$

1106 Lets explain in more detail the calculation of the kinematic variables for the case of the set  
 1107 number two. The invariant masses  $M_{\pi^+\pi^-}$  and  $M_{\pi^+p'}$  are calculated from the four-momenta  
 1108 of the final particles  $P_{\pi^-}^\mu, P_{\pi^+}^\mu, P_{p'}^\mu$  in the following way:

$$\begin{aligned} M_{\pi^+\pi^-} &= \sqrt{(P_{\pi^+}^\mu + P_{\pi^-}^\mu)^2} \quad \text{and} \\ M_{\pi^+p'} &= \sqrt{(P_{\pi^+}^\mu + P_{p'}^\mu)^2}. \end{aligned} \quad (3.3.2)$$

---

<sup>5</sup> More details on the organization of the reaction phase-space can be found in App. C.

<sup>6</sup> Note that the three-momenta of the  $\pi^+, \pi^-, p'$  are in the same plane, since in the CMS their total three-momentum has to be equal to zero.

1109 The polar ( $\theta_{\pi^-}$ ) and azimuthal ( $\varphi_{\pi^-}$ ) angles of the  $\pi^-$  in the CMS are shown in Fig. 3.3.  
 1110 In this figure the  $z$ -axis is directed along the virtual photon (with the unit vector  $\vec{n}_z$ ), while  
 1111 the  $x$ -axis is located in the electron scattering plane and follows the direction of the scattered  
 1112 electron (see App. B for details). The plane  $A$  in Fig. 3.3 is defined by the three-momenta  
 1113 of the  $\pi^-$  and initial proton.

1114 The angle  $\theta_{\pi^-}$  varies in the range  $[0, \pi]$  and is calculated as:

$$\theta_{\pi^-} = \arccos \left( \frac{(\vec{P}_{\pi^-} \cdot \vec{P}_\gamma)}{|\vec{P}_{\pi^-}| |\vec{P}_\gamma|} \right), \quad (3.3.3)$$

1115 where  $\vec{P}_\gamma$  is the three-momentum of the virtual photon and  $\vec{P}_{\pi^-}$  is the three-momentum of  
 1116 the  $\pi^-$  (both are situated in the plane  $A$ ).

1117 The angle  $\varphi_{\pi^-}$  varies in the range  $[0, 2\pi]$  and is determined as:

$$\begin{aligned} \varphi_{\pi^-} &= \arctan \left( \frac{P_y}{P_x} \right), & \text{if } P_x > 0 \text{ and } P_y > 0, \\ \varphi_{\pi^-} &= \arctan \left( \frac{P_y}{P_x} \right) + 2\pi, & \text{if } P_x > 0 \text{ and } P_y < 0, \\ \varphi_{\pi^-} &= \arctan \left( \frac{P_y}{P_x} \right) + \pi, & \text{if } P_x < 0 \text{ and } P_y < 0, \\ \varphi_{\pi^-} &= \arctan \left( \frac{P_y}{P_x} \right) + \pi, & \text{if } P_x < 0 \text{ and } P_y > 0, \\ \varphi_{\pi^-} &= \frac{\pi}{2}, & \text{if } P_x = 0 \text{ and } P_y > 0, \\ \varphi_{\pi^-} &= \frac{3\pi}{2}, & \text{if } P_x = 0 \text{ and } P_y < 0, \end{aligned} \quad (3.3.4)$$

1118 where  $P_i$  is the  $i$ -component of the  $\pi^-$  three-momentum in the CMS ( $i = x, y, z$ ).

1119 The calculation of the angle  $\alpha_{\pi^-}$ , which is shown in Fig. 3.4, is more complicated. This  
 1120 is the angle between the two planes A and B, which varies in a range  $[0, 2\pi]$ . The plane  
 1121 A is defined by the three-momentum of the initial proton and the three-momentum of the  
 1122  $\pi^-$ . The plane B is defined by the three-momenta of all final hadrons. For the calculation  
 1123 of the  $\alpha_{\pi^-}$ , one determines first three auxiliary vectors  $\vec{\gamma}$ ,  $\vec{\beta}$ , and  $\vec{\delta}$ , which are also shown in  
 1124 Fig. 3.4.

1125 The auxiliary unit vector  $\vec{\gamma}$  is situated in the plane A. This vector is perpendicular to  
 1126 the three-momentum of the  $\pi^-$  and directed toward the vector  $[-\vec{n}_z]$ , where  $\vec{n}_z$  is the unit  
 1127 vector directed along the  $z$ -axis. The vector  $\vec{\gamma}$  can be expressed as

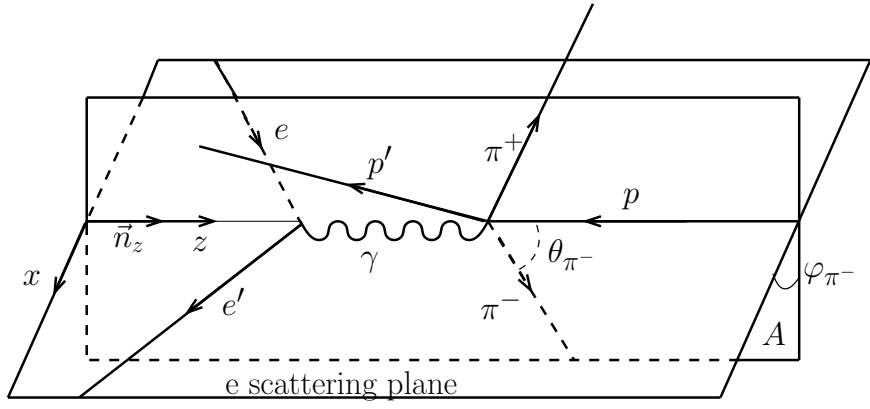


Figure 3.3: Polar ( $\theta_{\pi^-}$ ) and azimuthal ( $\varphi_{\pi^-}$ ) angles of the  $\pi^-$  in the CMS. The  $z$ -axis is directed along the virtual photon (with the unit vector  $\vec{n}_z$ ), while the  $x$ -axis is located in the electron scattering plane and follows the direction of the scattered electron. The plane  $A$  is defined by the three-momenta of the  $\pi^-$  and initial proton.

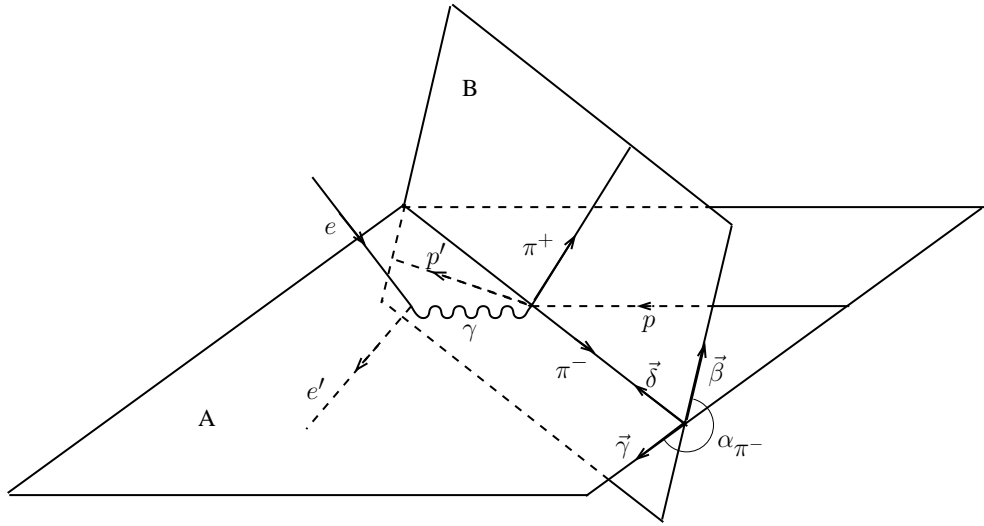


Figure 3.4: Definition of the angle  $\alpha_{\pi^-}$  between the two planes: the plane  $A$  is defined by the three-momenta of the  $\pi^-$  and initial proton, while the plane  $B$  is defined by the three-momenta of all final hadrons. The definitions of auxiliary vectors  $\vec{\beta}$ ,  $\vec{\gamma}$ , and  $\vec{\delta}$  are given in the text.

$$\vec{\gamma} = a_\alpha \cdot [-\vec{n}_z] + b_\alpha \cdot \vec{n}_{\pi^-}$$

$$\text{with } a_\alpha = \sqrt{\frac{1}{1 - (\vec{n}_{\pi^-} \cdot [-\vec{n}_z])^2}} \quad \text{and} \quad b_\alpha = -a_\alpha \cdot (\vec{n}_{\pi^-} \cdot [-\vec{n}_z]) ,$$

1128 where  $\vec{n}_{\pi^-}$  is the unit vector directed along the three-momentum of the  $\pi^-$ .

The auxiliary unit vector  $\vec{\beta}$  is situated in the plane B. This vector is perpendicular to the three-momentum of the  $\pi^-$  and directed toward the three-momentum of the  $\pi^+$ . The vector  $\vec{\beta}$  can be expressed as

$$\vec{\beta} = a_\beta \cdot \vec{n}_{\pi^+} + b_\beta \cdot \vec{n}_{\pi^-}$$

$$\text{with } a_\beta = \sqrt{\frac{1}{1 - (\vec{n}_{\pi^+} \cdot \vec{n}_{\pi^-})^2}} \quad \text{and} \quad b_\beta = -a_\beta \cdot (\vec{n}_{\pi^+} \cdot \vec{n}_{\pi^-}) ,$$

1129 where  $\vec{n}_{\pi^+}$  is the unit vector directed along the three-momentum of the  $\pi^+$ .

1130 Taking the scalar products  $(\vec{\gamma} \cdot \vec{\gamma})$ ,  $(\vec{\beta} \cdot \vec{\beta})$ ,  $(\vec{\gamma} \cdot \vec{n}_{\pi^-})$ , and  $(\vec{\beta} \cdot \vec{n}_{\pi^-})$ , it is straightforward  
1131 to verify that  $\vec{\gamma}$  and  $\vec{\beta}$  are the unit vectors perpendicular to the three-momentum of the  $\pi^-$ .

1132 The auxiliary unit vector  $\vec{\delta}$  is the vector product of the auxiliary vectors  $\vec{\gamma}$  and  $\vec{\beta}$ , i.e.

$$\vec{\delta} = [\vec{\gamma} \times \vec{\beta}] . \quad (3.3.5)$$

1133 Then the angle  $\alpha_{\pi^-}$  is determined as:

$$\begin{aligned} \alpha_{\pi^-} &= \arccos(\vec{\gamma} \cdot \vec{\beta}), & \text{if } \vec{\delta} \uparrow\uparrow \vec{n}_{\pi^-}, \\ \alpha_{\pi^-} &= 2\pi - \arccos(\vec{\gamma} \cdot \vec{\beta}), & \text{if } \vec{\delta} \uparrow\downarrow \vec{n}_{\pi^-}. \end{aligned} \quad (3.3.6)$$

1134 The kinematic variables for the first and third sets are calculated in a similar way. The  
1135 angles  $\alpha_{p'}$  and  $\alpha_{\pi^+}$  are shown for the convenience in Figs. 3.5 and 3.6. Further information  
1136 on the kinematic of reactions with multi-particle final states can be found in Ref. [38].

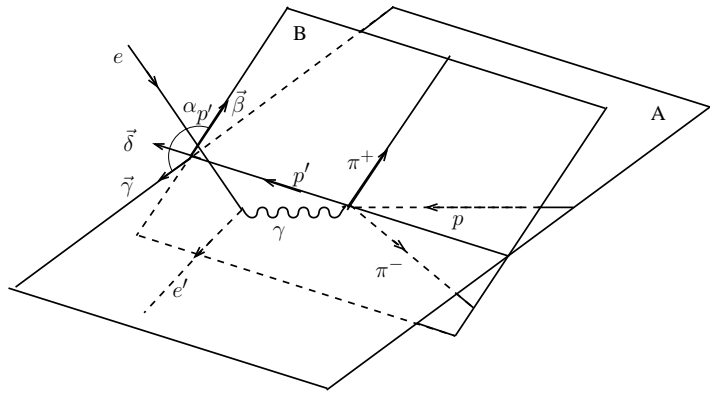


Figure 3.5: Definition of the angle  $\alpha_{p'}$  between the two planes: the plane A is defined by the three-momenta of initial and scattered protons, while the plane B is defined by the three-momenta of all final hadrons.

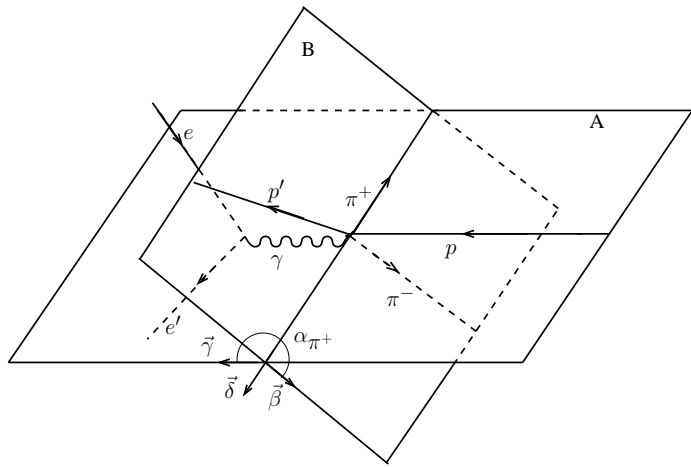


Figure 3.6: Definition of the angle  $\alpha_{\pi^+}$  between the two planes: the plane A is defined by the three-momenta of the  $\pi^+$  and initial proton, while the plane B is defined by the three-momenta of all final hadrons.

## 1137 3.4 Binning and kinematic coverage

1138 The available kinematic coverage in the initial state variables is shown by the  $Q^2$  versus  $W$   
1139 distribution<sup>7</sup> in Fig. 3.7. This distribution is filled with the double-pion events survived after  
1140 the event selection described above. The blue boundary limits the analyzed kinematic area,  
1141 where the double-pion cross sections are extracted. The black grid demonstrates the chosen  
1142 binning in the initial state variables (25 MeV in  $W$  and 0.05 GeV<sup>2</sup> in  $Q^2$ ).

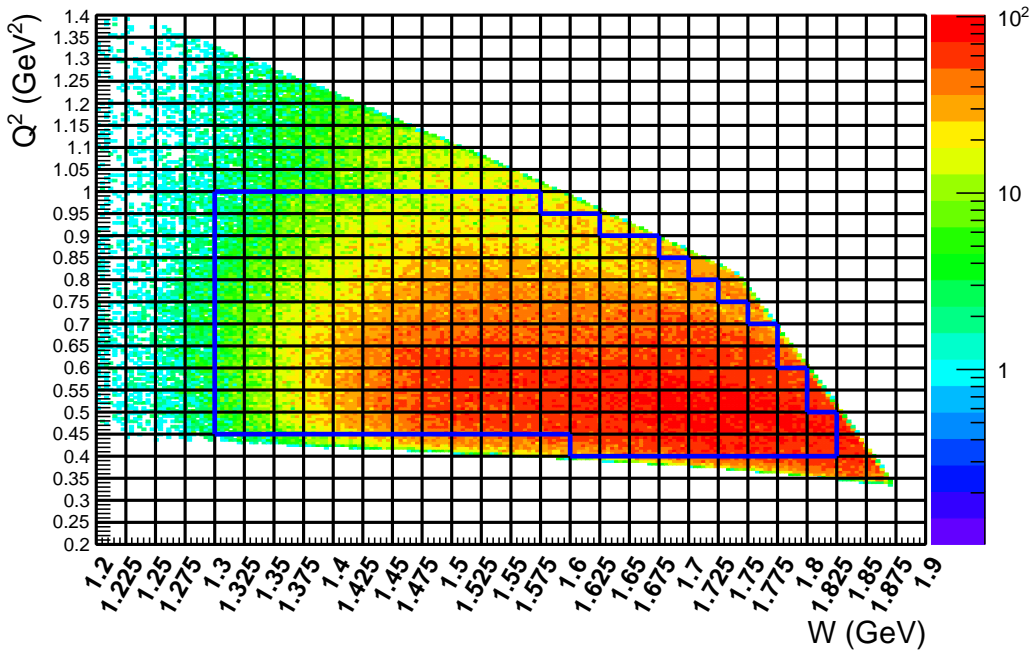


Figure 3.7:  $Q^2$  versus  $W$  distribution populated with the selected double-pion events. The cross section is calculated in 2D cells within the blue boundaries.

1143 The kinematic coverage in the final state variables has the following reaction related  
1144 features. The angular variables  $\theta_{h_1}$ ,  $\varphi_{h_1}$ , and  $\alpha_{h_1}$  vary in the fixed ranges of  $[0, \pi]$ ,  $[0, 2\pi]$ ,  
1145 and  $[0, 2\pi]$ , respectively. Meanwhile, the ranges of the invariant masses  $M_{h_1 h_2}$  and  $M_{h_2 h_3}$  are  
1146  $W$  dependent and broaden as  $W$  grows. More details on the specificity of the double-pion  
1147 production phase-space are given in App. C.

1148 The binning in the final hadron variables used in this study is listed in Tab. 3.1. In  
1149 each  $W$  and  $Q^2$  bin the range of each final hadron variable is divided into bins of equal  
1150 size. However, the number of bins differs in various  $W$  subranges, in order to take into  
1151 account (i) the statistics drop near the reaction threshold, which is at  $\approx 1.22$  GeV and (ii)  
1152 the aforementioned broadening of the reaction phase-space with increasing  $W$ . The chosen

---

<sup>7</sup> Note that  $W$  here is  $W_{sm}$ , and therefore, the distribution boundaries are not subject to the blurring. See Sect. 3.1 for details.

amount of bins in each considered  $W$  subrange reflects the intention to maintain reasonable statistical uncertainties of the single-differential cross sections for all  $W$  and  $Q^2$  bins.

For the binning in the polar angle note the following. The cross section, although being differential in  $[-\cos \theta]$ , is binned in  $\theta$ . These  $\Delta\theta$  bins are of equal size in the corresponding  $W$  subrange. See also Sect. 3.5 on this matter.

Table 3.1: Number of bins for hadronic variables.

		W subrange (GeV)			
Hadronic variable		[1.3, 1.35]	[1.35, 1.4]	[1.4, 1.475]	[1.475, 1.825]
$M_{h_1 h_2}$	Invariant mass	8	10	12	12
$M_{h_2 h_3}$	Invariant mass	8	10	12	12
$\theta_{h_1}$	Polar angle	6	8	10	10
$\varphi_{h_1}$	Azimuthal angle	5	5	5	6
$\alpha_{h_1}$	Angle between planes	5	6	8	8
Total number of bins in hadronic variables		9600	24000	57600	69120

The total numbers of multi-dimensional bins for the corresponding  $W$  ranges are listed in the last row of Tab. 3.1 and require some clarification. In fact the invariant masses border of the double-pion production phase-space is  $W$ -dependent and determined by the Byckling function (see App. C). Therefore, the bins located outside this border contain no double-pion events and hence do not contribute to the cross section. For a given  $W$  value, the border is distinct, however for a  $W$  bin, which corresponds to a range of  $W$  values, it is somewhat diffused. If events are binned in  $W_{true}$  (like in a free proton experiment) and the bin is small, e.g. 25 MeV, this diffusion is marginal. Then the quantity of bins involved in the cross section calculation (including both non-empty and empty cells) varies from 90% to 70% of the total numbers given in the last row of Tab. 3.1 as  $W$  increases from the threshold. However, if events are binned in  $W_{sm}$  (like in this analysis), each  $W_{sm}$  value in a bin corresponds to a sequence of  $W_{true}$  spread over 50-100 MeV. In this case a very pronounced boundary diffusion takes place, increasing the quantity of bins filled with events, i.e. the fraction of bins involved in the cross section calculation turn out to vary from 100% to 80% as  $W$  increases<sup>8</sup>.

<sup>8</sup>This estimation is based on the Monte Carlo simulation performed with TWOPEG [36] and TWOPEG-D [26] for the reactions off the proton at rest and off the moving proton, respectively.

1173     The specific organization of the double-pion production phase-space in the invariant  
 1174     masses ( $M_{h_1 h_2}, M_{h_2 h_3}$ ) causes the need to pay special attention to the binning in these vari-  
 1175     ables. Equation (3.4.1) gives the expressions for the lower and upper boundaries of the  $M_{h_1 h_2}$   
 1176     distribution and demonstrates that the upper boundary depends on the value of  $W$ , while  
 1177     the lower does not (see also App. C on this matter).

$$\begin{aligned} M_{lower} &= m_{h_1} + m_{h_2} \\ M_{upper}(W) &= W - m_{h_3}. \end{aligned} \quad (3.4.1)$$

1178     Here  $m_{h_1}$ ,  $m_{h_2}$ , and  $m_{h_3}$  are the masses of the final hadrons.

1179     Since the cross section is calculated in a bin  $W_{left} < W < W_{right}$ , the boundary of  $M_{upper}$   
 1180     is not distinct. For the purpose of binning in mass, the value of  $M_{upper}$  is calculated using  
 1181      $W_{center}$ , at the center of the  $W$  bin. As a result, some events with  $W > W_{center}$  turned out  
 1182     to be located beyond  $M_{upper}$ . Hence it was decided to use a specific arrangement of mass  
 1183     bins with the bin width  $\Delta M$  determined by

$$\Delta M = \frac{M_{upper} - M_{lower}}{N_{bins} - 1}, \quad (3.4.2)$$

1184     where  $N_{bins}$  is the number of bins specified in the first row of Tab. 3.1. The left boundary  
 1185     of the first bin is set to  $M_{lower}$ .

1186     The chosen arrangement of bins forces the last bin to be situated completely out of the  
 1187     boundaries<sup>9</sup> given by Eq. (3.4.1) using  $W_{center}$ . Therefore, the cross section in this extra bin  
 1188     finally is not reported. However, this bin is kept in the analysis since its content (though  
 1189     being very small) contributes to all cross sections that are obtained by integrating over the  
 1190     corresponding invariant mass distribution.

1191     Note that the cross section in the next to last bin in invariant mass needs a special  
 1192     correction. This correction is described in Sect. 4.4.

---

<sup>9</sup> Note that for each  $W$  bin and for each invariant mass,  $\Delta M$  given by Eq. (3.4.2) is greater than 12.5 MeV, which is the half of the  $W$  bin width.

## 1193 3.5 Cross section formulae

### 1194 3.5.1 Electron scattering cross section

1195 The experimental electron scattering cross section  $\sigma_e$  for the reaction  $ep(n) \rightarrow e'p'(n')\pi^+\pi^-$   
 1196 is seven-fold differential and calculated as<sup>10</sup>

$$\frac{d^7\sigma_e}{dWdQ^2d^5\tau} = \frac{1}{R \cdot \mathcal{F}} \cdot \frac{\left(\frac{N_{full}}{Q_{full}} - \frac{N_{empty}}{Q_{empty}}\right)}{\Delta W \cdot \Delta Q^2 \cdot \Delta^5\tau \cdot \left[\frac{l \cdot \rho \cdot N_A}{q_e \cdot \mu_d}\right] \cdot \mathcal{E}}, \text{ where} \quad (3.5.1)$$

- 1197 •  $d^5\tau = dM_{h_1h_2}dM_{h_2h_3}d\Omega_{h_1}d\alpha_{h_1}$  is the differential of the five independent variables of  
 1198 the  $\pi^+\pi^-p$  final state, which are described in Sect. 3.3;
- 1199 •  $N_{full}$  and  $N_{empty}$  are the numbers of selected double-pion events inside the seven-  
 1200 dimensional bin for runs with deuterium and empty target, respectively;
- 1201 • the quantity in the square brackets in the denominator corresponds to the luminosity  
 1202 of the experiment  $\mathcal{L}$  in the units  $\text{cm}^{-2} \cdot \text{C}^{-1}$  and its components are

1203      $l = 2 \text{ cm}$  the length of the target,  
 1204      $\rho = 0.169 \text{ g} \cdot \text{cm}^{-3}$  the density of liquid deuterium,  
 1205      $N_A = 6.022 \cdot 10^{-19} \text{ mol}^{-1}$  Avogadro's number,  
 1206      $q_e = 1.602 \cdot 10^{-19} \text{ C}$  the elementary charge, and  
 1207      $\mu_d = 2.014 \text{ g} \cdot \text{mol}^{-1}$  the molar mass of deuterium,

1208 which results in the luminosity value of  $\mathcal{L} = 0.63 \cdot 10^{42} \text{ cm}^{-2} \cdot \text{C}^{-1} = 0.63 \cdot 10^{12} \mu\text{b}^{-1} \cdot \text{C}^{-1}$ ;

- 1209 •  $Q_{full} = 3734.69 \mu\text{C}$  and  $Q_{empty} = 464.797 \mu\text{C}$  are the values of the charge accumulated  
 1210 in the Faraday Cup for deuterium and empty target runs, respectively<sup>11</sup>, which results  
 1211 in the corresponding values of the integrated luminosity  $L = \mathcal{L} \cdot Q$  of  $2.35 \cdot 10^9 \mu\text{b}^{-1}$   
 1212 and  $0.29 \cdot 10^9 \mu\text{b}^{-1}$ ;
- 1213 •  $\mathcal{E} = \mathcal{E}(\Delta W, \Delta Q^2, \Delta^5\tau)$  is the detector efficiency (which includes the detector accep-  
 1214 tance) for each seven-dimensional bin as determined by the Monte Carlo simulation  
 1215 (see Sect. 3.6);
- 1216 •  $R = R(\Delta W, \Delta Q^2)$  is the radiative correction factor described in Sec. 4.2;
- 1217 •  $\mathcal{F} = \mathcal{F}(\Delta W, \Delta Q^2, \Delta^5\tau)$  is the correction factor that aims at unfolding the effects of  
 1218 the target motion (see Sect. 4.3).

1219 The electron scattering cross section  $\sigma_e$  in the left hand side of Eq. (3.5.1) is assumed to  
 1220 be obtained in the center of the finite seven-dimensional kinematic bin  $\Delta W \Delta Q^2 \Delta^5\tau$ .

---

<sup>10</sup> To deal with the multi-differential cross section, THnSparse multi-dimensional root histograms are used.

<sup>11</sup> They are calculated by summing up the charges of all analyzed *blocks* (see Sect. 2.3.2 for details).

<sub>1221</sub> **3.5.2 Virtual photoproduction cross section**

<sub>1222</sub> The goal of the analysis is to extract the virtual photoproduction cross section  $\sigma_v$  of the  
<sub>1223</sub> reaction  $\gamma_vp(n) \rightarrow p'(n')\pi^+\pi^-$ . This virtual photoproduction cross section  $\sigma_v$  is five-fold  
<sub>1224</sub> differential and in the single-photon exchange approximation connected with the seven-fold  
<sub>1225</sub> differential electron scattering cross section<sup>12</sup>  $\sigma_e$  via

$$\frac{d^5\sigma_v}{d^5\tau} = \frac{1}{\Gamma_v} \frac{d^7\sigma_e}{dW dQ^2 d^5\tau}, \quad (3.5.2)$$

<sub>1226</sub> where  $\Gamma_v$  is the virtual photon flux given by

$$\Gamma_v(W, Q^2) = \frac{\alpha}{4\pi} \frac{1}{E_{beam}^2 m_p^2} \frac{W(W^2 - m_p^2)}{(1 - \varepsilon_T)Q^2}. \quad (3.5.3)$$

<sub>1227</sub> Here  $\alpha$  is the fine structure constant ( $1/137$ ),  $m_p$  the proton mass,  $E_{beam} = 2.039$  GeV  
<sub>1228</sub> the laboratory energy of the incoming electron beam, and  $\varepsilon_T$  the virtual photon transverse  
<sub>1229</sub> polarization given by

$$\varepsilon_T = \left( 1 + 2 \left( 1 + \frac{\nu^2}{Q^2} \right) \tan^2 \left( \frac{\theta_{e'}}{2} \right) \right)^{-1}, \quad (3.5.4)$$

<sub>1230</sub> where  $\nu = E_{beam} - E_{e'}$  is the virtual photon energy, while  $E_{e'}$  and  $\theta_{e'}$  are the energy and the  
<sub>1231</sub> polar angle of the scattered electron in the lab frame, respectively.

<sub>1232</sub> The value of the virtual photon flux given by Eq. (3.5.3) is calculated for the central  
<sub>1233</sub> point of the  $\Delta W \Delta Q^2$  bin.

<sub>1234</sub> The limited statistics of the experiment does not allow for estimates of the five-fold  
<sub>1235</sub> differential cross section  $\sigma_v$  with a reasonable accuracy. Therefore, the cross section  $\sigma_v$  is  
<sub>1236</sub> first obtained on the multi-dimensional grid and then is integrated over at least four hadron  
<sub>1237</sub> variables. Hence, only the sets of the single-differential and fully-integrated cross sections  
<sub>1238</sub> are obtained.

---

<sup>12</sup> Note that after the corrections introduced in Eq. (3.5.1) by the factors  $R$  and  $\mathcal{F}$ , the cross section  $\sigma_e$  is the true electron scattering cross section attributed to the central values of the corresponding  $\Delta W \Delta Q^2 \Delta^5\tau$  bin and the distinct value of the beam energy  $E_{beam} = 2.039$  GeV.

<sup>1239</sup> For each  $W$  and  $Q^2$  bin, the following cross sections are extracted for each variable set.

$$\begin{aligned}
 \frac{d\sigma_v}{dM_{h_1 h_2}} &= \int \frac{d^5\sigma_v}{d^5\tau} dM_{h_2 h_3} d\Omega_{h_1} d\alpha_{h_1}, \\
 \frac{d\sigma_v}{dM_{h_2 h_3}} &= \int \frac{d^5\sigma_v}{d^5\tau} dM_{h_1 h_2} d\Omega_{h_1} d\alpha_{h_1}, \\
 \frac{d\sigma_v}{d[-\cos\theta_{h_1}]} &= \int \frac{d^5\sigma_v}{d^5\tau} dM_{h_1 h_2} dM_{h_2 h_3} d\varphi_{h_1} d\alpha_{h_1}, \\
 \frac{d\sigma_v}{d\alpha_{h_1}} &= \int \frac{d^5\sigma_v}{d^5\tau} dM_{h_1 h_2} dM_{h_2 h_3} d\Omega_{h_1}, \quad \text{and} \\
 \sigma_v^{int}(W, Q^2) &= \int \frac{d^5\sigma_v}{d^5\tau} dM_{h_1 h_2} dM_{h_2 h_3} d\Omega_{h_1} d\alpha_{h_1}.
 \end{aligned} \tag{3.5.5}$$

<sup>1240</sup> As a final result for each  $W$  and  $Q^2$  bin, the integral cross section  $\sigma_v^{int}$ , averaged over the  
<sup>1241</sup> three variable sets, is reported together with the nine single-differential cross sections given  
<sup>1242</sup> in (3.5.6), where each column is taken from the corresponding variable set.

$$\begin{array}{ccc}
 \frac{d\sigma_v}{dM_{p'\pi^+}} & \frac{d\sigma_v}{dM_{\pi^-\pi^+}} & \frac{d\sigma_v}{dM_{\pi^-p'}} \\
 \frac{d\sigma_v}{d[-\cos\theta_{p'}]} & \frac{d\sigma_v}{d[-\cos\theta_{\pi^-}]} & \frac{d\sigma_v}{d[-\cos\theta_{\pi^+}]} \\
 \frac{d\sigma_v}{d\alpha_{p'}} & \frac{d\sigma_v}{d\alpha_{\pi^-}} & \frac{d\sigma_v}{d\alpha_{\pi^+}}
 \end{array} \tag{3.5.6}$$

<sup>1243</sup> Regarding the middle row in (3.5.6) note the following. Although being differential  
<sup>1244</sup> in  $[-\cos\theta]$ , the cross sections are calculated in  $\Delta\theta$  bins, which are of equal size in the  
<sup>1245</sup> corresponding  $W$  subrange (see Sect. 3.4 for details). This is a conventional way of presenting  
<sup>1246</sup> the  $\theta$ -distributions in the studies of double-pion cross sections [15–19, 21–23].

### 1247 3.6 Efficiency evaluation

1248 For the Monte Carlo simulation the TWOPEG-D event generator was used [26]. This is  
 1249 the version of TWOPEG (an event generator for double-pion electroproduction off the free  
 1250 proton [36]), which is able to simulate the effects of the initial proton motion. In this version  
 1251 of the event generator the Fermi motion of the initial proton is generated according to the  
 1252 Bonn potential [37] and then naturally merged into the specific kinematics of double-pion  
 1253 electroproduction. TWOPEG-D accounts for radiative effects according to the approach  
 1254 described in Refs. [36, 39].

1255 The generated events are passed through the standard detector simulation (GSIM, GPP)  
 1256 and reconstruction procedures (reccsis) with the majority of parameters kept the same as in  
 1257 the studies [22, 40], which were also devoted to the “e1e” run period<sup>13</sup>.

1258 In the studies of double-pion production cross section it is especially important to gen-  
 1259 erate enough Monte Carlo statistics in order to saturate each multi-dimensional bin of the  
 1260 reaction phase-space with events (see Tab. 3.1). Insufficient Monte Carlo statistics leads to  
 1261 an improper efficiency evaluation and an unnecessary rise in the empty cells contribution  
 1262 (see Sect. 4.1), thus systematically affecting the accuracy of the extracted cross sections. For  
 1263 this study the total of about  $4 \cdot 10^{10}$  double-pion events were generated in the investigated  
 1264 kinematic region, which is considered adequate.

1265 The TWOPEG-D event generator performs a weighted event generation [36], i.e. all  
 1266 kinematic variables are generated randomly according to the double-pion production phase-  
 1267 space, while each event generated at a particular kinematic point acquires an individual  
 1268 weight, which corresponds to the cross section at this point. Therefore, the efficiency factor  
 1269  $\mathcal{E}$  from Eq. (3.5.1) is calculated in each  $\Delta W \Delta Q^2 \Delta^5 \tau$  bin as

$$\mathcal{E}(\Delta W, \Delta Q^2, \Delta^5 \tau) = \frac{\mathbb{N}_{rec}}{\mathbb{N}_{gen}} = \frac{\sum_{i=1}^{N_{rec}} w_i}{\sum_{j=1}^{N_{gen}} w_j}, \quad (3.6.1)$$

1270 where  $N_{gen}$  is the number of generated double-pion events (without any cuts) inside the  
 1271 multi-dimensional bin,  $N_{rec}$  is the number of reconstructed double-pion events that survived  
 1272 in the bin after the event selection, while  $\mathbb{N}_{gen}$  and  $\mathbb{N}_{rec}$  are the weighted numbers of the  
 1273 corresponding events and  $w$  is a weight of an individual event.

1274 The efficiency in some kinematic bins could not be reliably determined due to boundary  
 1275 effects, bin to bin event migration, and limited Monte Carlo statistics. Such cells were  
 1276 excluded from consideration. They can be differentiated from the cells with reliable efficiency  
 1277 by a larger relative efficiency uncertainty  $\delta\mathcal{E}/\mathcal{E}$ .

---

<sup>13</sup> See the beginning of Sect. 2 and also App. E for more details on the simulation/reconstruction procedure and for the information on the corresponding parameters used in this analysis.

Meanwhile, the calculation of the efficiency uncertainty  $\delta\mathcal{E}$  is not straightforward and needs special attention, since (i)  $N_{gen}$  and  $N_{rec}$  in Eq. (3.6.1) are not independent and (ii) Monte Carlo events in this equation are subject to weighting. Therefore, the special approach described in Ref. [41] was used to calculate  $\delta\mathcal{E}$ . Neglecting the event migration between the bins, this approach gives the following expression for the absolute statistical uncertainty of the efficiency in a bin for the case of weighted Monte Carlo simulation,

$$\delta\mathcal{E} = \sqrt{\frac{N_{gen} - 2N_{rec}}{N_{gen}^3} \sum_{i=1}^{N_{rec}} w_i^2 + \frac{N_{rec}^2}{N_{gen}^4} \sum_{j=1}^{N_{gen}} w_j^2}. \quad (3.6.2)$$

Meanwhile, according to Ref. [41], in the case of unweighted Monte Carlo simulation, the formula in Eq. (7.1.3) reduces to

$$\delta\tilde{\mathcal{E}} = \sqrt{\frac{N_{rec}(N_{gen} - N_{rec})}{N_{gen}^3}}, \text{ where } \tilde{\mathcal{E}} = \frac{N_{rec}}{N_{gen}}. \quad (3.6.3)$$

Figure 3.8 (a) shows the distribution of the relative efficiency uncertainty  $\delta\mathcal{E}/\mathcal{E}$  versus efficiency  $\mathcal{E}$  plotted taking the weights (see Eq. (7.1.3)) into account. In this plot the statistical effects turn out to be convoluted with the distribution of weights thus complicating the revealing of cells with unreliable efficiency. To isolate only the statistical effects, the distribution  $\delta\mathcal{E}/\tilde{\mathcal{E}}$  versus  $\tilde{\mathcal{E}}$ , which is produced ignoring the weights (see Eq. (3.6.3)), is plotted in the panel (b). As seen in this plot, the cells with high relative efficiency uncertainty are clustered along the horizontal stripes. This clustering originates from the fact that (if the weights are ignored) the efficiency is obtained by the division of two integer numbers, which reveals the bins with small statistics of the reconstructed events. These horizontal stripes, furthermore, contain many cells with unreliable extremely small efficiency. Therefore, the following criterion for the selection of cells with reliable efficiency is used  $\delta\tilde{\mathcal{E}}/\tilde{\mathcal{E}} < 0.3$ . This cut is shown in Fig. 3.8 (b) by the red horizontal line. All cells above this line were excluded from the analysis. The influence of this cut on the distribution  $\delta\mathcal{E}/\mathcal{E}$  (with the weights taken into account) is shown in Fig. 3.8 (c).

The number of reconstructed events in the revealed cells with unreliable efficiency is set to zero ( $N_{rec} = 0$ ). Then such a cell is ranked as an “empty cell” and, along with other empty cells, is subject to the filling procedure, which is described in Sect. 4.1.

The described above cut on the relative efficiency uncertainty directly impacts the cross section’s uncertainties. On the one hand, it eliminates the  $\Delta^5\tau$  bins with high relative efficiency uncertainty, thus reducing the total statistical uncertainty of the extracted cross sections (see Sect. 7.1). On the other hand, this cut increases the amount of empty cells, thus increasing the cross section’s model dependence and the uncertainty associated with it (see Sect. 7.2). The cut value is therefore chosen as a compromise between these two effects.

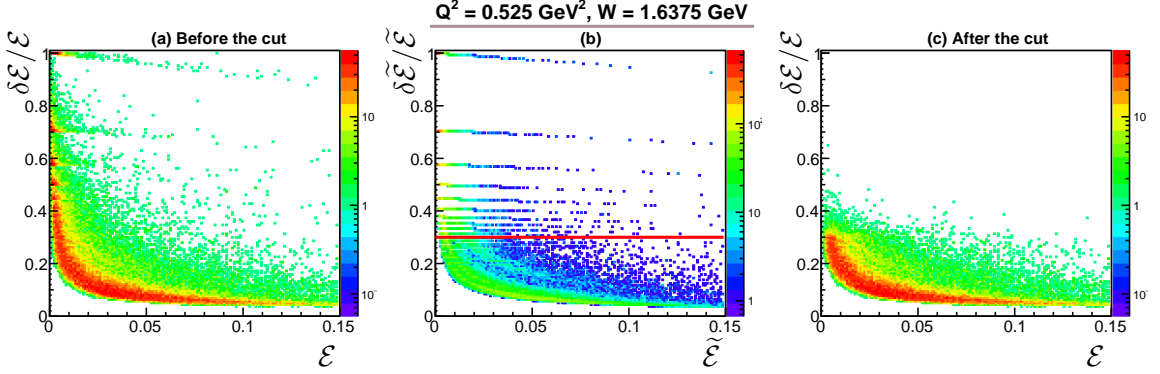


Figure 3.8: Distributions of the relative efficiency uncertainty versus efficiency (a) taking into account the weights (see Eq. (7.1.3)) and (b) ignoring them (see Eq. (3.6.3)). The cut that aims to select the cells with reliable efficiency is shown by the red horizontal line in panel (b). Panel (c) shows the influence of this cut on the distribution  $\delta\mathcal{E}/\mathcal{E}$  (with the weights taken into account). The distributions are provided for one particular  $\Delta W \Delta Q^2$  bin (with the central values specified in figure), and the color code represents the number of multi-dimensional cells within this bin. Note that the z-axis maximum for the plot (a) is set the same as for the plot (c).

1309     The idea of this cut is taken from the study [22, 23], which uses unweighted Monte Carlo  
 1310 simulation and therefore employs Eq. (3.6.3) to calculate the efficiency uncertainty. The  
 1311 study [22, 23] observed the similar cell clustering along horizontal stripes as that revealed in  
 1312 this analysis in the distributions of  $\delta\tilde{\mathcal{E}}/\tilde{\mathcal{E}}$  versus  $\tilde{\mathcal{E}}$  (produced ignoring the weights) and also  
 1313 set the cut at the position of 0.3.

1314     Note that in this particular analysis the formula (3.6.3) for the unweighted Monte Carlo  
 1315 is used only for selecting the bins with reliable efficiency, since it allows the pure statistical  
 1316 behavior of the efficiency uncertainty to be determined. For the estimation of the cross  
 1317 section's statistical uncertainty the weights are taken into account and the formula (7.1.3)  
 1318 is applied (see Sect. 7.1).

1319 **Chapter 4**

1320 **Corrections to the cross sections**

1321 This chapter gives the description of the corrections to the extracted cross sections in the  
1322 order they were applied.

1323 **4.1 Filling kinematic cells with zero acceptance**

1324 Due to blind areas in the geometrical coverage of the CLAS detector, some kinematic bins  
1325 of the double-pion production phase-space turned out to have zero acceptance. In such bins,  
1326 which are usually called empty cells, the cross section cannot be experimentally defined.  
1327 For the studies, which aim at extracting fully-differential cross sections (i.e. single-pion  
1328 production analyses), this is not a problem of great importance, since the cross section in  
1329 blind areas is just not reported. However, in the studies of double-pion production, where the  
1330 limited experimental statistics allows only single-differential cross sections to be extracted,  
1331 this issue becomes a point of special attention [17–19, 21–23]. The empty cells contribute to  
1332 the integrals in Eqs. (3.5.5) along with the other kinematic bins. Ignoring the contribution  
1333 from the empty cells leads to a systematic cross section underestimation and, therefore,  
1334 some assumptions for the empty cells’ content are needed. This situation causes some model  
1335 dependence of the final result.

1336 The map of the empty cells is determined using the Monte Carlo simulation. A cell  
1337 is treated as empty, if it contains generated events ( $N_{gen} > 0$ ), but does not contain any  
1338 reconstructed events ( $N_{rec} = 0$ ). The cells with unreliable efficiencies, revealed based on the  
1339 cut on the efficiency uncertainty (see Sect. 3.6), are also treated as empty. Empty cells should  
1340 not be confused with the cells that contain both generated and reconstructed events, but  
1341 do not contain experimental data, i.e. they appear due to the limited experiment duration,  
1342 which is taken into account via the normalization on the Faraday Cup charge, and therefore,  
1343 no model assumptions for them are needed.

1344 It is conventional practice in the studies of the double-pion production to fill the empty

1345 cells by means of the Monte Carlo event generator (usually the one that is used to evaluate  
 1346 the efficiency). The studies [15–19, 21] used GENEV [42] (the double-pion event generator  
 1347 based on the JM05 reaction model) for this purpose. The empty cells in these studies  
 1348 were filled with the generated events, which were subject to a special scaling procedure in  
 1349 order to match the experimental data in the regular (non-empty) cells. Meanwhile, the  
 1350 study [22, 23] used TWOPEG [36] for the empty cells filling. TWOPEG is the new double-  
 1351 pion event generator, which is based on the JM15 model and up to now provides the best  
 1352 cross section estimation in the kinematic region  $W < 2$  GeV and  $Q^2 < 1.3$  GeV $^2$ . Since  
 1353 TWOPEG is capable of providing the absolute cross section value for a given kinematic  
 1354 point, the study [22, 23] used the cross section estimated by TWOPEG as an assumption  
 1355 for the empty cells content.

1356 In this particular study the empty cells are filled by means of the TWOPEG-D event  
 1357 generator [26], which is the version of TWOPEG for moving protons. Although TWOPEG-D  
 1358 is also capable of providing the absolute cross section value, the empty cells in this study were  
 1359 nevertheless filled with the scaled generated events (as in Refs. [15–19, 21]). This method  
 1360 was chosen because TWOPEG-D assumes all events to be produced in the quasi-free regime  
 1361 (ignoring FSI) and therefore somewhat overestimates the quasi-free cross section.

1362 Thus, in this study empty multi-dimensional cells are filled with the Monte Carlo events  
 1363 generated by TWOPEG-D (following Refs. [15–19, 21]), relying on the cross section shape  
 1364 implemented in the generator. These generated events are subject to the scaling, which  
 1365 leaving the shape unchanged adjusts the empty cells content to the experimental yield in  
 1366 the regular (non-empty) cells. The scaling is performed individually in each  $\Delta W \Delta Q^2$  bin  
 1367 according to the integral yields of the experimental and simulated events in the non-empty  
 1368 cells within this bin. The number of events  $N_{model}$  that is assigned as a content for the empty  
 1369  $\Delta^5\tau$  cell located in the corresponding  $\Delta W \Delta Q^2$  bin is then estimated as

$$N_{model}(\Delta W, \Delta Q^2, \Delta^5\tau) = \frac{\mathcal{N}_{data}^{int}}{\mathcal{N}_{rec}^{int}} \cdot \mathbb{N}_{gen}(\Delta W, \Delta Q^2, \Delta^5\tau), \quad (4.1.1)$$

1370 where  $\mathbb{N}_{gen}$  is the weighted number of generated events in the corresponding multi-  
 1371 dimensional bin, while the fraction represents the integral scaling factor with  $\mathcal{N}_{data}^{int}$  and  
 1372  $\mathcal{N}_{rec}^{int}$  being the total number of experimental events (normalized by the FC charge) and  
 1373 the total number of reconstructed events in all non-empty  $\Delta^5\tau$  bins within the considered  
 1374  $\Delta W \Delta Q^2$  bin, respectively. These quantities are given by

$$\begin{aligned} \mathcal{N}_{data}^{int}(\Delta W, \Delta Q^2) &= \sum_{\substack{\text{All } \Delta^5\tau \\ \text{with } N_{rec} > 0}} \left[ \frac{N_{full}}{Q_{full}} - \frac{N_{empty}}{Q_{empty}} \right], \text{ and} \\ \mathcal{N}_{rec}^{int}(\Delta W, \Delta Q^2) &= \sum_{\substack{\text{All } \Delta^5\tau \\ \text{with } N_{rec} > 0}} \mathbb{N}_{rec}, \end{aligned} \quad (4.1.2)$$

1375 where  $\mathbb{N}_{rec}$  is the weighted number of reconstructed events in the corresponding  $\Delta^5\tau$  bin.

1376 For each empty  $\Delta W \Delta Q^2 \Delta^5\tau$  bin, the quantity given by Eq. (4.1.1) imitates the yield of  
 1377 experimental events normalized by the FC charge and corrected by the detector efficiency  
 1378 (see Eq. (3.5.1)). The cross section in the empty cells is then calculated as

$$\frac{d^7\sigma_e}{dW dQ^2 d^5\tau} = \frac{N_{model}}{\Delta W \cdot \Delta Q^2 \cdot \Delta^5\tau \cdot [\mathcal{L}]}, \quad (4.1.3)$$

1379 with  $N_{model}$  given by Eq. (4.1.1), and all other variables explained after Eq. (3.5.1). Note  
 1380 that the empty cells are filled before applying the correction factors  $R$  and  $\mathcal{F}$ .

1381 Figure 4.1 introduces the single-differential cross sections given by Eqs. (3.5.5) and  
 1382 (3.5.6)<sup>1</sup>. The empty squares correspond to the case when the contribution from the empty  
 1383 cells was ignored, and the black circles are for the case when that was taken into account in  
 1384 the way described above. The figure demonstrates a satisfactory small contribution from the  
 1385 empty cells (and therefore a small model dependence of the results). Only the edge points  
 1386 in the  $\theta$  distributions (middle row) reveal pronounced empty cell contributions due to the  
 1387 negligible/zero CLAS acceptance in the corresponding directions.

1388 Table 4.1 demonstrates the relative empty cell contribution to the integral cross sections  
 1389 for all reported ( $W, Q^2$ )-points<sup>1</sup>. Different shades of red correspond to different percentage  
 1390 ranges, i.e. the lightest shade corresponds to the contribution  $\leq 20\%$ , darker shade – from  
 1391 21% to 30%, and the darkest one shows the contribution  $> 30\%$ . As seen from the table,  
 1392 for most of the ( $W, Q^2$ )-points the contribution from the empty cells is kept on a low  
 1393 level of  $\sim 15\%$ , having a small rise at the low  $Q^2$  and high  $W$  boundaries, which originates  
 1394 from the momentum-dependent restrictions on the minimal and maximal polar angles of  
 1395 the scattered electron, respectively (see Sect. 2.3.1). Additionally, the rise of the empty  
 1396 cells contribution for small  $W \sim 1.3$  GeV is thought to be related to the fact that near the  
 1397 production threshold the hadrons carry small momentum and hence failed to be registered  
 1398 since (i) they are more likely bent to the detector holes, (ii) CLAS is not designed to register  
 1399 hadrons with a momentum less than a certain value (see e.g. Fig. 2.10), and (iii) the smaller  
 1400 the hadron velocity is, the more energy it loses in materials (Bragg peak). A similar rise of  
 1401 the empty cells contribution near the threshold was also observed in Refs. [17, 18, 22, 23],  
 1402 which are devoted to the double-pion electroproduction off the free proton.

1403 To account for the model dependence, the approach established for the previous studies  
 1404 of double-pion production cross sections is followed [19, 20, 22], i.e. the part of the  
 1405 single-differential cross section that came from the empty cells is assigned a 50% relative  
 1406 uncertainty. The corresponding absolute uncertainty  $\delta_{model}$  is then combined with the total  
 1407 statistical uncertainty, as was done in Refs. [19, 20, 22] (more details are in Sect. 7.1).

---

<sup>1</sup> Both Figure 4.1 and Table 4.1 are given for the cross sections, which (although being divided by the virtual photon flux) are neither corrected for the radiative effects (see Sect. 4.2) nor for the effects of the target motion (see Sect. 4.3).

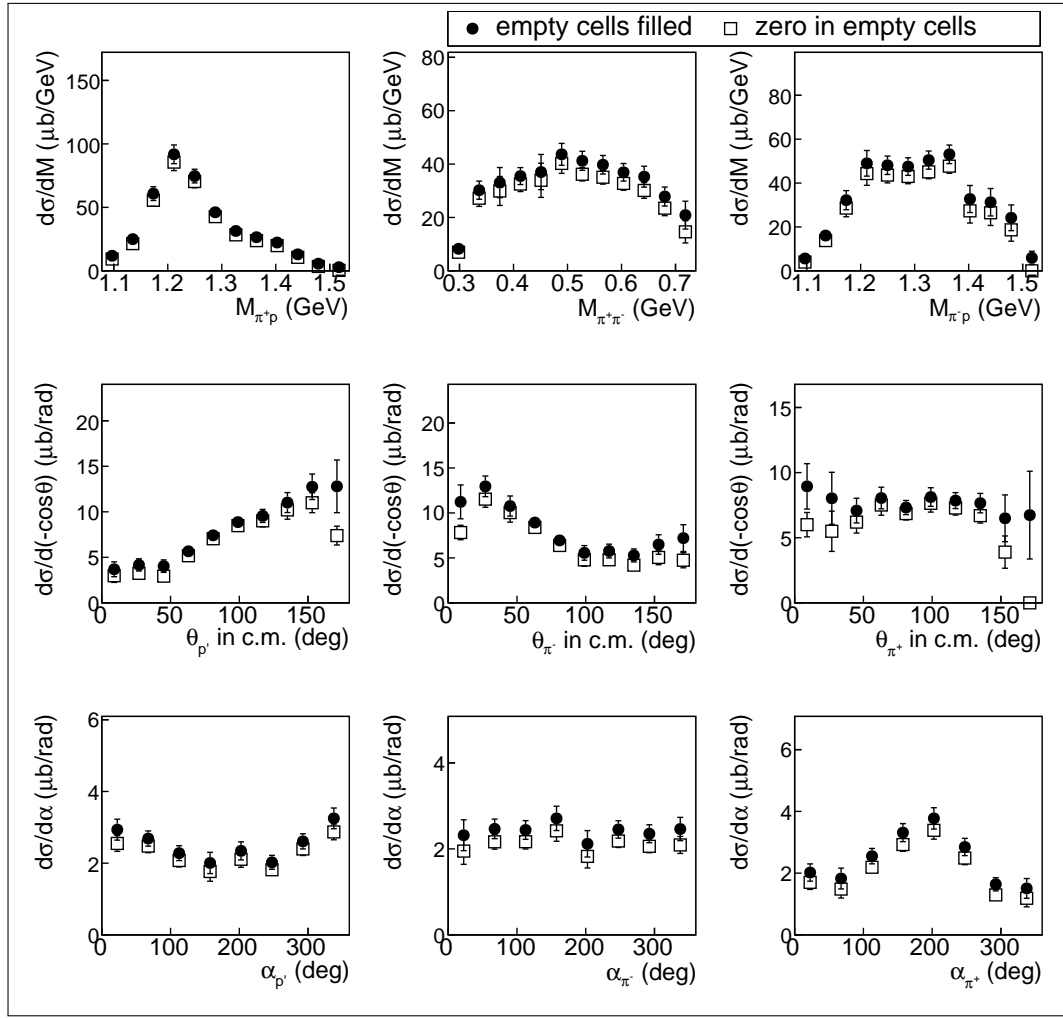


Figure 4.1: Extracted single-differential cross sections for the cases when the contribution from the empty cells was ignored (empty squares) and when it was taken into account (black circles). The former are reported with the uncertainty  $\delta_{\text{stat}}^{\text{tot}}$  given by Eq. (7.1.4), while the latter are with the uncertainty  $\delta_{\text{stat,mod}}^{\text{tot}}$  given by Eq. (7.4.1). All distributions are given for one particular bin in  $W$  and  $Q^2$  ( $W = 1.6375 \text{ GeV}$ ,  $Q^2 = 0.625 \text{ GeV}^2$ ).

Table 4.1: Relative empty cell contribution to the integral cross sections for all reported ( $W$ ,  $Q^2$ )-points. The columns correspond to the  $Q^2$  values in  $\text{GeV}^2$  and the rows to the  $W$  values in  $\text{GeV}$ . Different shades of red correspond to different percentage range, i.e. the lightest shade corresponds to the contribution  $\leq 20\%$ , darker shade – from 21% to 30%, and the darkest one shows the contribution  $> 30\%$ .

	0.425	0.475	0.525	0.575	0.625	0.675	0.725	0.775	0.825	0.875	0.925	0.975
1.3125	–	41	34	32	35	37	41	33	33	45	35	48
1.3375	–	28	28	27	26	28	31	32	33	35	33	35
1.3625	–	28	26	23	24	25	25	25	27	27	28	27
1.3875	–	21	19	18	17	19	19	18	18	21	23	21
1.4125	–	27	20	18	17	17	18	20	19	20	20	20
1.4375	–	23	17	17	14	14	14	17	15	15	16	18
1.4625	–	21	16	14	13	13	12	13	13	13	14	16
1.4875	–	24	18	15	14	14	13	13	15	15	15	16
1.5125	–	23	18	16	15	14	14	13	14	15	16	16
1.5375	–	23	19	16	16	14	14	14	14	17	18	15
1.5625	–	22	19	16	16	15	15	15	15	17	17	17
1.5875	–	23	18	17	20	15	15	17	16	18	17	–
1.6125	26	20	17	16	15	15	15	15	17	16	15	–
1.6375	26	19	17	16	14	16	14	16	17	16	–	–
1.6625	25	19	17	15	15	15	15	17	18	17	–	–
1.6875	24	20	17	16	15	15	16	19	18	–	–	–
1.7125	23	19	17	17	16	17	19	18	–	–	–	–
1.7375	23	20	17	17	17	18	19	–	–	–	–	–
1.7625	22	20	18	18	18	19	–	–	–	–	–	–
1.7875	21	19	18	18	–	–	–	–	–	–	–	–
1.8125	21	17	–	–	–	–	–	–	–	–	–	–

1408 **4.2 Radiative correction**

1409 The incoming and scattered electrons are subject to radiative effects, which means that  
1410 they can emit photons thus reducing their energy. However, in the experiment the infor-  
1411 mation on these emissions is not accessible, and one has to assume the electron energy to  
1412 be unchanged. Therefore, when extracting the cross sections, one assumes the energy of  
1413 the incoming/scattered electron to be greater/smaller than it actually was in the reaction.  
1414 This, in turn, leads to the systematic overestimation of the virtual photon energy with the  
1415 consequent overestimation<sup>2</sup> of  $W$ . As a result, the extracted cross section is assigned to the  
1416  $W$  value higher than the actual one. This distorts the measured  $W$  spectrum and leads to  
1417 its agglomeration in the high-lying region.

1418 The common way of handling this problem is to apply the radiative correction to the  
1419 extracted cross sections. In this study the radiative correction is performed using TWOPEG-  
1420 D [26], which is the event generator for the double-pion electroproduction that simulates  
1421 effects of the target motion. TWOPEG-D accounts for the radiative effects by means of the  
1422 well-known approach of Ref. [39], which is traditionally used for the radiative corrections  
1423 in the studies of double-pion electroproduction [15–19, 21–23]. In Ref. [39] the approach is  
1424 applied to the inclusive case, while in TWOPEG-D, the double-pion integrated cross sections  
1425 are used instead [26, 36].

1426 In the approach [26, 36, 39] the radiative photons are supposed to be emitted collinearly  
1427 either to the direction of the incoming or scattered electron (the so-called “peaking approx-  
1428 imation”). The calculation of the radiative cross section is split into two parts. The “soft”  
1429 part assumes the energy of the emitted radiative photon to be less than a certain minimal  
1430 value (10 MeV), while the “hard” part is for the photons with an energy greater than that  
1431 value. The “soft” part is evaluated explicitly, while for the calculation of the “hard” part,  
1432 an inclusive hadronic tensor is assumed. The latter assumption is however considered ade-  
1433 quate, especially taking into account that approaches that are capable of describing radiative  
1434 processes in exclusive double-pion electroproduction are not yet available.

1435 The radiative correction factor  $R$  in Eq. (3.5.1) is determined in the following way. The  
1436 double-pion events either with or without radiative effects are generated with TWOPEG-  
1437 D. Both radiated and non-radiated events are subjected to the smearing due to the Fermi  
1438 motion of the target. Then the ratio given by Eq. (4.2.1) is taken in each  $\Delta W \Delta Q^2$  bin.

$$R(\Delta W, \Delta Q^2) = \frac{N_{rad}}{N_{norad}}, \quad (4.2.1)$$

1439 where  $N_{rad}$  and  $N_{norad}$  are the weighted numbers of generated events in each  $\Delta W \Delta Q^2$  bin  
1440 with and without radiative effects, respectively. Note that neither  $N_{rad}$  nor  $N_{norad}$  are subject  
1441 to any cuts.

---

<sup>2</sup> The  $Q^2$  value is overestimated if the incoming electron emits and underestimated if the scattered electron emits. That is why the radiative effects do not significantly impact the  $Q^2$ -dependence of the cross section.

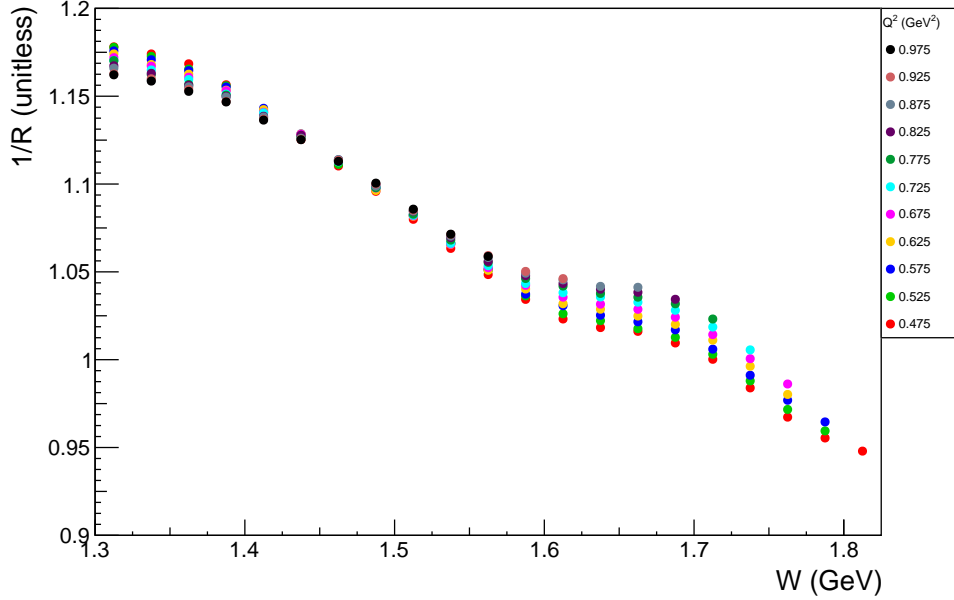


Figure 4.2: Reciprocal of the radiative correction factor ( $1/R$ ) as a function of  $W$  for different  $Q^2$  bins (see Eq. (4.2.1)).

This approach gives the correction factor  $R$  only as a function of  $W$  and  $Q^2$ , disregarding its dependence on the hadronic variables. However, the need to integrate the cross section at least over four hadronic variables (see Eq. (3.5.5)) considerably reduces the influence of the final state hadron kinematics on the radiative correction factor, thus justifying the applicability of the procedure [26, 36, 39].

The quantity  $1/R$  is plotted in Fig. 4.2 as a function of  $W$  for different  $Q^2$  bins. The uncertainties associated with the statistics of generated events are very small and therefore not seen in the plot<sup>3</sup>. Note that the correction factor introduced in Fig. 4.2 is slightly different from that given in Ref. [22] for the same beam energy of the free proton experiment ( $E_{beam} = 2.039 \text{ GeV}$ ). This difference comes from the fact that generated events in Eq. (4.2.1) are subjected to the smearing due to the Fermi motion of the target proton.

Once this correction is applied, the extracted cross sections are treated as non-radiated, but Fermi-smeared.

<sup>3</sup> The total of about  $2.5 \cdot 10^9$  either radiated or non-radiated events were generated in the investigated kinematic region for the calculation of the radiative correction factor.

## 1455 4.3 Unfolding the effects of the target motion

1456 The motion of the target proton in a deuterium nucleus introduces into this analysis some  
1457 specific issues that are not inherent for the previously conducted studies of the double-pion  
1458 cross sections [15–19, 21–23]. As was described in Sects. 2.4 and 3.1, the intention to use in  
1459 the analysis the  $\pi^-$  missing topology (that serves the purpose of the cross section extraction  
1460 best) leads inevitably to working under the target-at-rest-assumption. The latter, however,  
1461 not only complicates the selection of exclusive events (see Sect. 2.4), but also impacts the  
1462 extracted cross sections due to the following reasons.

- 1463 • One has to use the smeared reaction invariant mass  $W_{sm}$  for the cross section binning  
1464 (see Sect. 3.1). As a result, the extracted cross section is assigned to the  $W$  value  
1465 different from the actual one. This makes both integral and single-differential cross  
1466 sections to be distorted.
- 1467 • One has to use an approximate Lab to CMS transformation that ignores the target  
1468 motion (see Sect. 3.2). This approximation introduces some inaccuracy to the measured  
1469 angular ( $\theta$ ,  $\varphi$ , and  $\alpha$ ) distributions without having an impact on the invariant mass  
1470 distributions and  $W$  and  $Q^2$  cross section dependencies due to their Lorentz invariance.

1471 The former effect is thought to have a much greater impact on the cross section than  
1472 the latter. Thus, being folded with the aforementioned effects of the target motion, the  
1473 extracted cross sections are seeking the corresponding unfolding correction. This correction  
1474 is performed by means of two Monte Carlo event generators TWOPEG [36] and TWOPEG-  
1475 D [26]. TWOPEG is the event generator for the double-pion electroproduction off the free  
1476 proton that currently provides the best cross section estimation in the investigated kinematic  
1477 region. TWOPEG-D is the event generator for the same exclusive reaction but off the proton  
1478 that moves in the deuterium nucleus. This event generator was especially developed to be  
1479 used in the studies, where the experimental information of the target proton momentum is  
1480 inaccessible, and one is forced to work under the target-at-rest-assumption. TWOPEG-D  
1481 convolutes the double-pion cross section with effects of the target motion and thus imitates  
1482 the conditions of the experimental cross section extraction.

1483 To calculate the correction factor, two samples of double-pion events produced either off  
1484 the proton at rest and off the moving proton were generated (with TWOPEG and TWOPEG-  
1485 D, respectively). Both event generators provide the particle’s four-momenta written in the  
1486 Lab system and distribute events according to the corresponding electron-scattering cross  
1487 section. As the reaction invariant mass both samples use the value calculated from the  
1488 initial particles (see Eq. (3.1.1)), which for the “moving proton” events is calculated under  
1489 the target-at-rest-assumption (as was done for the cross section calculation). The generated  
1490 four-momenta are then subject to the transformation to the CMS. For both samples the  
1491 transformation is performed according to the procedure given in App. B for the case of

the proton at rest. For the “moving proton” sample, this approximation introduces in the event distributions the same inaccuracy as appears in the extracted cross sections. Then the kinematic variables are calculated and the generated events of both samples are binned in the same way as the extracted cross sections (see Sect. 3.4).

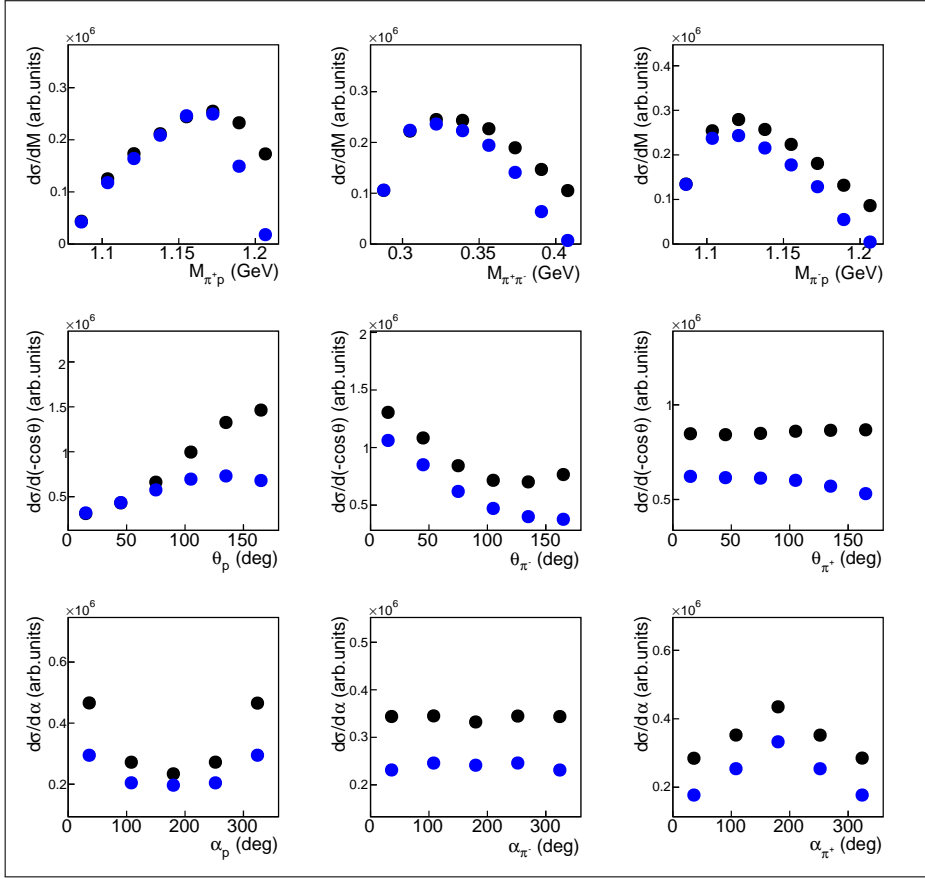


Figure 4.3: Single-differential distributions of generated double-pion events produced off the proton at rest (blue symbols) and off the moving proton (black symbols). The former were generated with TWOPEG [36] and the latter with TWOPEG-D [26]. The example is given for the particular  $\Delta W \Delta Q^2$  bin with the central point at  $W = 1.3375$  GeV and  $Q^2 = 0.475$  GeV $^2$ . As this bin is located near the threshold, the moving proton distributions (black symbols) have a high relative event excess comparing with the free proton distributions (blue symbols). See text for details.

Therefore, the distributions of events generated with TWOPEG-D acquire the same inaccuracies as the extracted cross sections, i.e. the value  $W_{sm}$  is used for the binning and the approximate Lab to CMS transformations are applied. The manifestation of these inaccuracies differs depending on various final state variables and has a strong  $W$ -dependence as Figs. 4.3 and 4.4 demonstrate. These figures show the single-differential distributions of  $N_{nofermi}$  (blue symbols) and  $N_{fermi}$  (black symbols), which are the weighted numbers of

events generated with TWOPEG and TWOPEG-D, respectively. In Fig. 4.3 these distributions are shown for a low  $W = 1.3375$  GeV, while in Fig. 4.4 they are shown for a higher  $W = 1.5625$  GeV. The uncertainties associated with the statistics of generated events are very small and therefore not seen in the plots<sup>4</sup>.

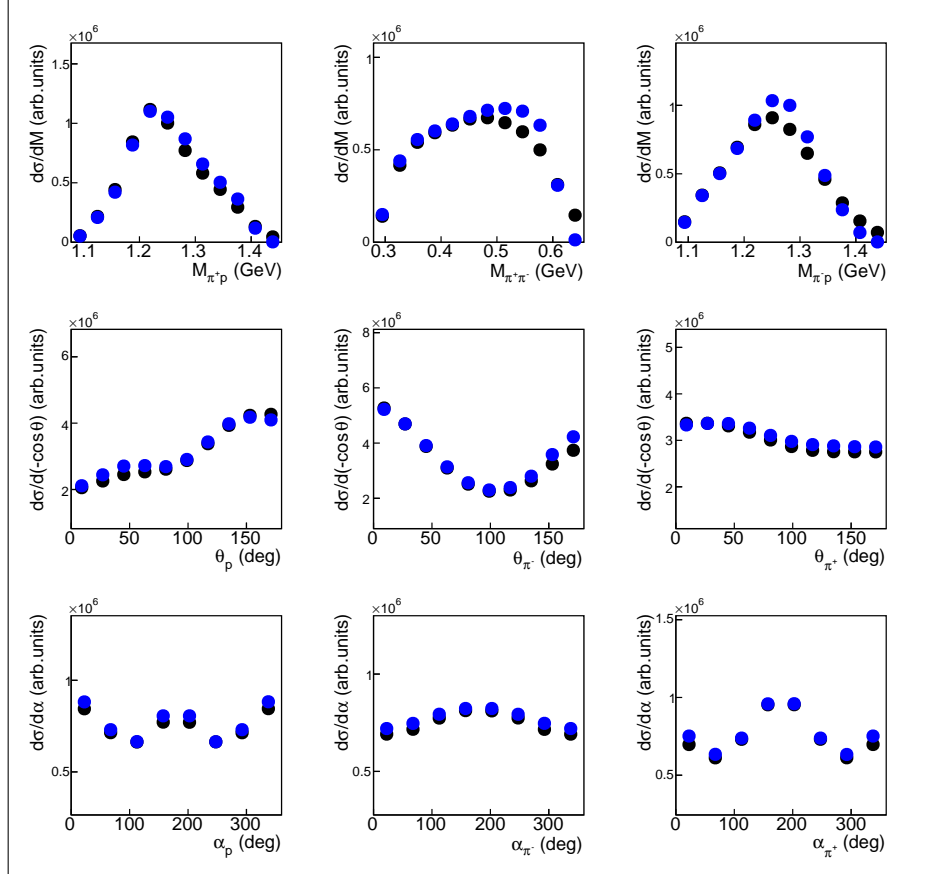


Figure 4.4: Single-differential distributions of generated double-pion events produced off the proton at rest (blue symbols) and off the moving proton (black symbols). The former were generated with TWOPEG [36] and the latter with TWOPEG-D [26]. The example is given for the particular  $\Delta W \Delta Q^2$  bin with the central point at  $W = 1.5625$  GeV and  $Q^2 = 0.475$  GeV $^2$ . As the bin is located in the peak region, the moving proton distributions (black symbols) have a small relative event deficit comparing with the free proton distributions (blue symbols). See text for details.

As seen from Figs. 4.3 and 4.4, the target motion considered under the itemized conditions listed above affects mostly the cross section near the threshold, while for higher  $W$  their impact is significantly less pronounced. This happens due to the following. Let's consider a particular  $W_{true}$  bin. As shown in Ref. [26], each value of  $W_{true}$  corresponds to a sequence

<sup>4</sup> For each event sample the total of about  $2.5 \cdot 10^{10}$  events were generated in the investigated kinematic region for the calculation of the correction factor.

1510 of  $W_{sm}$  values, which are symmetrically scattered in the vicinity of  $W_{true}$  with a spread of  
 1511 50-100 MeV. This leads to the fact that the same bin in  $W_{sm}$  has a different number of  
 1512 events compared to the  $W_{true}$  bin. This difference depends on the cross section behavior in  
 1513 the vicinity of 50-100 MeV of this bin. The cross section abruptly rises from the threshold  
 1514 with a strong convex nonlinearity, which smooths as  $W$  grows up to 1.4 GeV, and then turns  
 1515 to a concave nonlinearity forming the left slope of the resonance peak at 1.5 GeV. Then the  
 1516 cross section modestly increases and decreases several times changing its nonlinearity type.  
 1517 In any  $W_{true}$  subrange the cross section can be written as  $a + f(W)$ , where  $a = const$ , while  
 1518  $f(W)$  evolves from zero and determines the cross section nonlinearity within the subrange.  
 1519 Then the absolute variation in the event number in  $W_{sm}$  bin is determined solely by the  
 1520 nonlinearity of the function  $f(W)$ , i.e. convex nonlinearity leads to an event excess in the  
 1521 bin, while concave nonlinearity – to an event deficit. Hence, in the resonance peaks an event  
 1522 deficit is observed, while the region close to the threshold and the dip between the peaks have  
 1523 an event excess. However, the relative event variation depends on  $a$  and is higher for smaller  
 1524  $a$ . The smallest value of  $a$  is reached at the threshold ( $a = 0$ ), therefore the near-to-threshold  
 1525 subrange has the greatest relative variation of event number.

1526 Indeed, in Fig. 4.3, which is plotted for the  $W$  bin located close to the threshold, the  
 1527 moving proton distributions (black symbols) have a high relative event excess compared to  
 1528 the free proton distributions (blue symbols). Meanwhile, in Fig. 4.4, which is plotted for  
 1529 the  $W$  bin located at the peak region, the moving proton distributions (black symbols) have  
 1530 small relative event deficit comparing with the free proton distributions (blue symbols).

1531 For the low  $W$  region (as in Fig. 4.3) it is noteworthy that a very large relative difference  
 1532 between the free proton and the moving proton cross sections is observed for the right part  
 1533 of the invariant mass distributions. This happens due to the phase space broadening with  $W$   
 1534 that takes place for invariant masses (see App. C). The invariant mass distribution typically  
 1535 has a maximum in the middle and gradually goes to zero on both edges. The lower the  $W$   
 1536 value is, the narrower is the distribution width. As  $W$  grows, the distribution widens to  
 1537 the right and goes to zero farther away. Meanwhile, each bin in  $W_{sm}$  contains a mixture of  
 1538 events with the values of  $W_{true}$  spread within 50-100 MeV near this bin. For low  $W$  this  
 1539 spread is comparable with the total width of the invariant mass distribution. Therefore, the  
 1540 right distribution side acquired the event excess that comes from the same bins in invariant  
 1541 mass but located at higher  $W_{true}$  and hence having high cross sections.

1542 The unfolding correction is performed in each multi-dimensional bin of the double-pion  
 1543 production phase-space (see Sect. 3.3 as well as App. C), i.e. in each  $\Delta W \Delta Q^2 \Delta^5 \tau$  bin the  
 1544 cross section is divided by the correction factor  $\mathcal{F}$  (see Eq. (3.5.1)) that is calculated as

$$\mathcal{F}(\Delta W, \Delta Q^2, \Delta^5 \tau) = \frac{\mathbb{N}_{fermi}}{\mathbb{N}_{nofermi}}, \quad (4.3.1)$$

1545 where  $\mathbb{N}_{nofermi}$  and  $\mathbb{N}_{fermi}$  are the weighted numbers of generated double-pion events in the  
 1546  $\Delta W \Delta Q^2 \Delta^5 \tau$  bin produced off the proton at rest and off the moving proton, respectively.

1547 Both event samples were generated without radiative effects, since the correction factor  $\mathcal{F}$  is  
1548 applied to the cross sections that are already corrected for the radiative effects (see Sect. 4.2).

1549 The impact of the unfolding correction on the extracted integral cross sections is illus-  
1550 trated in Fig. 4.5, where the distributions before the correction are plotted in orange, while  
1551 the distributions after the correction are plotted in dark blue. The comparison is given for  
1552 two  $Q^2$  bins. As was expected, the correction causes a slight cross section increase in the  
1553 resonance peaks and a decrease near the threshold and in the dip between the peaks.

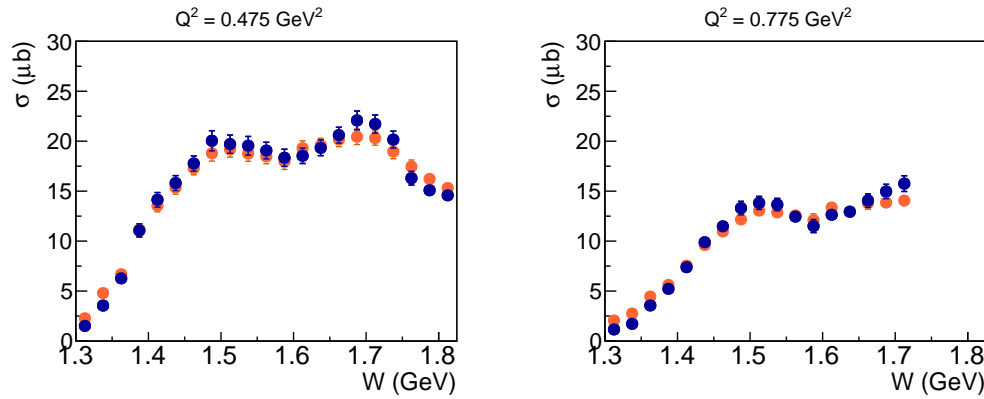


Figure 4.5: Impact of the unfolding correction on the extracted integral cross sections. The cross section before the correction is plotted in orange, while the cross section after the correction is plotted in dark blue (both are divided by the virtual photon flux). The comparison is given for two  $Q^2$  bins as specified above the plots.

1554 The value of the correction factor in Eq. (4.3.1) depends on both the free proton cross  
1555 sections and the model of the deuteron wave function that were employed in the event  
1556 generators. The former relies strongly on the JM model fit of the available data on double-  
1557 pion cross sections, while for the latter the Bonn model was used (see Refs. [26, 36] for  
1558 more detail). Therefore, the uncertainty of the extracted cross sections that comes from this  
1559 unfolding correction is attributed to the model dependence uncertainty and is discussed in  
1560 Sect. 7.2.

1561 Once corrected for the effects of the target motion and then divided by the virtual  
1562 photon flux, the cross section is treated as the true virtual photoproduction cross section  
1563 and is attributed to the central point of the corresponding  $\Delta W \Delta Q^2 \Delta^5 \tau$  bin.

## 1564 4.4 Correction for binning effects

1565 The cross section, extracted in bins of a finite size, is assigned to the central point of a  
1566 bin. On this way the cross sections acquire binning caused distortions and, therefore, are

1567 seeking the corresponding corrections. In this section, which is devoted to the binning effects,  
 1568 two separate binning issues are distinguished, i.e. (i) the specific issue of affecting the cross  
 1569 section value in the next to last point of the invariant mass distributions and (ii) the common  
 1570 binning issue that impacts the cross section value in any bin of finite size.

1571 Let's address the specific binning issue in the invariant mass distributions first. As shown  
 1572 in Sect. 3.4, the binning in invariant mass requires special attention due to the broadening  
 1573 of the reaction phase-space with  $W$  (see App. C) and the corresponding  $W$  dependence of  
 1574 the upper boundary of the invariant mass distributions (see Eq. (3.4.1)). This effect makes  
 1575 the upper boundary  $M_{upper}$  to be indistinct, since the cross section is calculated in a bin  
 1576  $W_{left} < W < W_{right}$ . To deal with this difficulty, the value of  $M_{upper}$  is calculated using  
 1577  $W_{center}$ , the center of the  $W$  bin. Then a specific arrangement of mass bins is used, which  
 1578 forces the last bin to be situated completely out of the boundaries given by Eq. (3.4.1) using  
 1579  $W_{center}$ . When integrating the cross section over the mass distribution, the events in the  
 1580 extra bin are included, but a cross section for this bin is not reported.

1581 Meanwhile, the cross section in the next to last bin (labeled as bin number  $N_{bins} - 1$ )  
 1582 should be treated carefully. This is best illustrated in Fig. 4.6, which shows schematically  
 1583 the event distribution in mass, ending in  $M_{upper}$  for three choices of  $W$  at  $W_{left}$  (dot-dashed),  
 1584  $W_{center}$  (solid) and  $W_{right}$  (dashed). The black points at  $M_{left}^{N_{bins}-1}$  and  $M_{right}^{N_{bins}-1}$  show the left  
 1585 and right boundaries of the next to last bin, respectively. In the next to last bin events with  
 1586  $W < W_{center}$  are distributed over a range, which is less than  $\Delta M$  defined by Eq. (3.4.2).  
 1587 However, when extracting the cross sections, the event yield was divided by the full bin  
 1588 width  $\Delta M$ , thus leading to an underestimation of the cross section.

1589 The correction for this effect was taken from Ref. [22, 23]. It was made using the  
 1590 TWOPEG double-pion event generator [36]. The correction factor to the cross section in  
 1591 the next to last bin is the ratio of the simulated cross sections calculated with fixed  $\Delta M$   
 1592 defined by Eq. (3.4.2) and with  $\widetilde{\Delta M} = W - m_{h_3} - M_{left}^{N_{bins}-1}$ , which was different for each  
 1593 generated event. This factor provides the correction to the cross section in the next to last  
 1594 bin that varied from  $\sim 5\%$  to  $\sim 10\%$ .

1595 Let's now address the common binning issue that impacts the cross section value in any  
 1596 bin of a finite size. Extracted in a finite bin, the cross section is subject to averaging within  
 1597 this bin. For instance, if there is a sharp peak in the middle of a bin, then the average value  
 1598 of the cross section in that bin will always be smaller than the peak value. Any non-linear  
 1599 behavior of the cross section will likely result in an offset of the obtained value. There are two  
 1600 methods of correcting this offset, i.e. (i) to correct the kinematic quantities associated with  
 1601 the bin and use the corrected values instead of the central values or (ii) to correct the cross  
 1602 section value in the center of the bin. Both these methods are widely used for the binning  
 1603 corrections. In the studies of double-pion cross sections, however, the second method has  
 1604 become conventional [17, 18, 22, 23]. Therefore, in this study the second method is chosen,  
 1605 in order to keep the initial binning over the kinematic variables and to facilitate the cross  
 1606 section comparison with the results obtained off the proton at rest [22, 23].

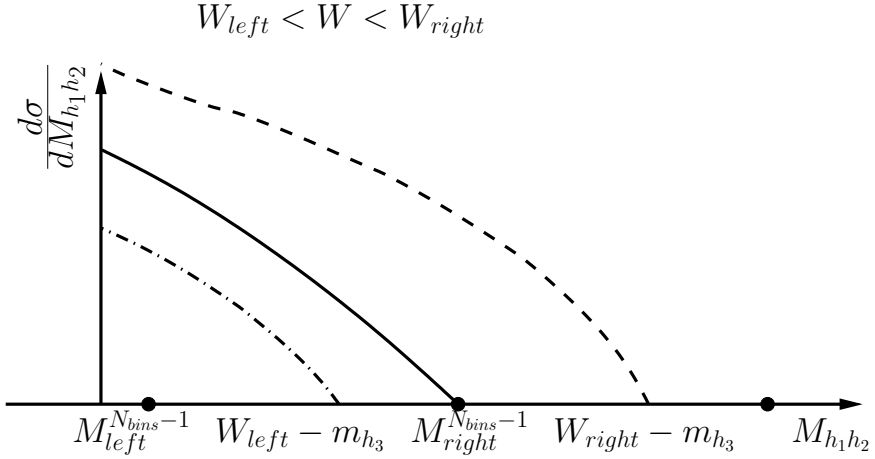


Figure 4.6: Schematic representation of the invariant mass distributions ending in  $M_{upper}$  calculated according to Eq. (3.4.1) for three choices of  $W$  at  $W_{left}$  (dot-dashed),  $W_{center}$  (solid) and  $W_{right}$  (dashed). The black points at  $M_{left}^{N_{bins}-1}$  and  $M_{right}^{N_{bins}-1}$  show the left and right boundaries of the next to last bin, respectively, while the remaining point marks the right boundary of the last mass bin.

In this study one-dimensional binning corrections are performed, i.e., the cross section dependence on each kinematic variable  $x$  is corrected individually (where  $x$  corresponds to  $W$ ,  $Q^2$ , and hadron variables). In any one-dimensional bin  $[x_{min}, x_{max}]$  the cross section value is multiplied by the correction factor  $C_{bin}$ . To estimate this factor some assumptions about the cross section behavior within the bin are needed, and hence, the cross section shape should be described by a continuous function  $f(x)$ . The multiplicative correction factor  $C_{bin}$  is then calculated in each bin  $[x_{min}, x_{max}]$  as

$$C_{bin} = \frac{f(x_{center})}{\int_{x_{min}}^{x_{max}} f(x) dx} , \quad (4.4.1)$$

where  $x_{center}$  is the central point of the  $[x_{min}, x_{max}]$  bin.

For the single-differential distributions a cubic spline approximation is chosen to continuously describe the cross section shape, as shown in Fig. 4.7. The black and red points in this figure are the cross sections before and after binning corrections, respectively, and the curves correspond to the spline approximation. For the invariant mass and  $\theta$  angular distributions the splines are forced to pass through the intermediate points that are obtained by averaging over two neighboring cross section points. This method reduces the splines sensitivity to accidental cross section fluctuations. Beside this, for the invariant mass distributions the splines are required to give zero at the distribution edges. For the  $\alpha$  angular distributions the splines are forced to pass through the points that are obtained by averaging

<sup>1624</sup> over two cross section points symmetrical with respect to  $\alpha = 180^\circ$ . This approach reflects  
<sup>1625</sup> the fact that after the integration over  $\varphi$ , the cross section must be symmetrical in the  $\alpha$   
<sup>1626</sup> angle (meanwhile, the extracted experimental distributions are slightly asymmetrical)<sup>5</sup>.

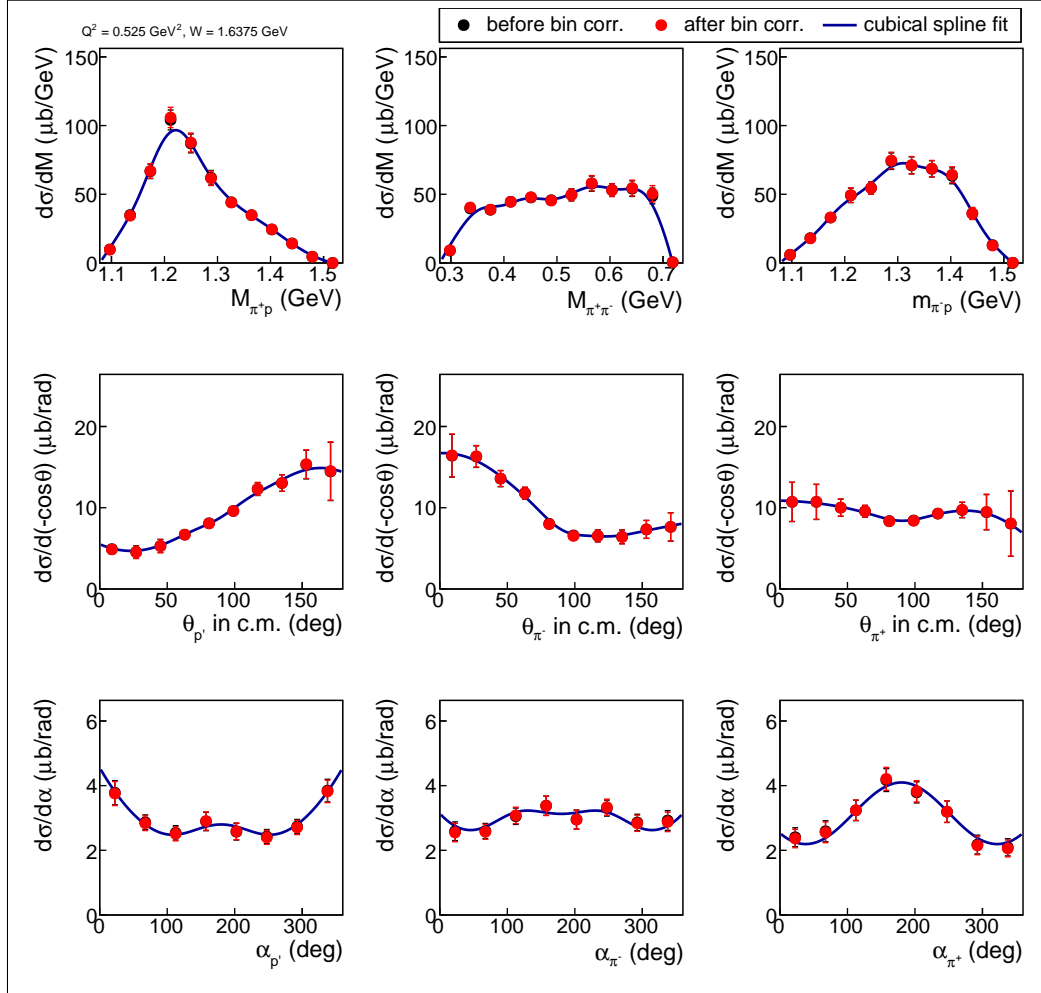


Figure 4.7: Single-differential cross sections as functions of the final hadron variables before (black points) and after (red points) the binning corrections. Curves represent a cubic spline approximation. The example is given for a particular  $\Delta W \Delta Q^2$  bin with the central point  $W = 1.6375$  GeV and  $Q^2 = 0.525$  GeV $^2$ .

<sup>1627</sup> The integral cross sections are subjected to individual corrections of the  $Q^2$  dependence  
<sup>1628</sup> inside the  $W$  bins and the  $W$  dependence inside the  $Q^2$  bins, as shown on the left and  
<sup>1629</sup> right plots of Fig. 4.8, respectively. In this figure black and red points represent the cross

---

<sup>5</sup> Although the  $\varphi$  distributions are not reported here, they were nevertheless extracted and added to the CLAS physics database [5]. The  $\varphi$  distributions were thus subjected to the binning correction with the same approach used for the  $\theta$  distributions.

1630 section values before and after binning corrections, respectively, while the curves correspond  
 1631 to the continuous cross section approximation. The latter are based on a second order  
 1632 polynomial fit of the  $Q^2$  distributions (left plot) and on a cubic spline approximation for  
 1633 the  $W$  distributions (right plot). The splines are forced to pass through the intermediate  
 1634 points that are obtained by averaging over two neighboring cross section points. In this way,  
 1635 the integral cross section value in each  $\Delta W \Delta Q^2$  bin acquires two multiplicative correction  
 1636 factors. The corrections obtained for the integral distributions are then propagated to the  
 1637 single-differential cross sections.

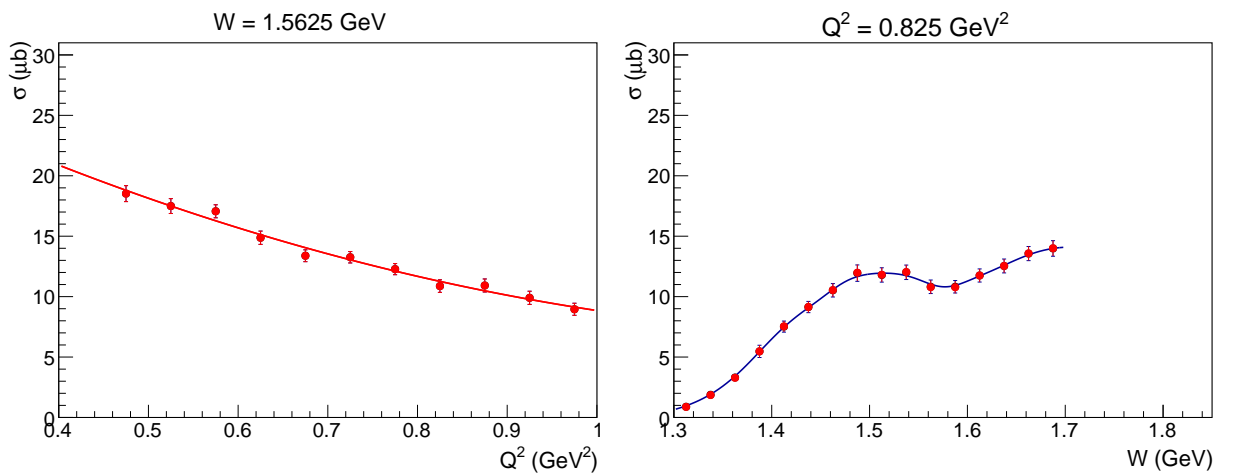


Figure 4.8:  $Q^2$  dependence (left plot) and the  $W$  dependence (right plot) of the integral cross sections before (black points) and after (red points) the binning corrections. The curves correspond to a second order polynomial fit for the left plot and a cubic spline approximation for the right one. Each distribution is plotted for one particular bin as specified above the plots.

1638 Since in this analysis a relatively fine binning in all kinematic variables is chosen (see  
 1639 Sect. 3.4), the effect of the binning corrections is almost insignificant. This is why in Figs. 4.7  
 1640 and 4.8 the black points (before the correction) are almost completely covered by the red  
 1641 ones (after the correction). For the  $Q^2$  dependences the correction factors are less than 1%  
 1642 in all bins, and for the  $W$  dependences they are  $\sim 2\%-3\%$  for the first two low  $W$  bins and  
 1643 less than 1% in all other bins. For the single-differential distributions, the corrections are on  
 1644 the level of 1%-2% for the majority of bins, but rise for some points (mostly at low  $W$ ) up  
 1645 to 5%-6%.

<sup>1646</sup> **Chapter 5**

<sup>1647</sup> **Other issues**

<sup>1648</sup> **5.1 The cross section dependence on the beam energy**

<sup>1649</sup> The phi-integrated virtual photoproduction cross section  $\sigma_v$  can be decomposed into the  
<sup>1650</sup> combination of the structure functions<sup>1</sup>,

$$\sigma_v = \sigma_T + \varepsilon_L \sigma_L \quad \text{with} \quad \varepsilon_L = \frac{Q^2}{\nu^2} \varepsilon_T, \quad (5.1.1)$$

<sup>1651</sup> where  $\sigma_T$  and  $\sigma_L$  are the transverse and longitudinal structure functions, respectively, while  
<sup>1652</sup>  $\varepsilon_L$  is the longitudinal polarization of the virtual photon with  $\varepsilon_T$  given by Eq. (3.5.4).

<sup>1653</sup> Being decomposed in this way, the cross section  $\sigma_v$  has a specific beam energy dependence,  
<sup>1654</sup> which is incorporated into the coefficient  $\varepsilon_L$ . The structure functions themselves, meanwhile,  
<sup>1655</sup> do not depend on the beam energy. A single experiment conducted with a certain beam  
<sup>1656</sup> energy allows for the extraction of  $\sigma_v$  as a whole without accessing the separate structure  
<sup>1657</sup> functions. Thus, the beam energy dependence turns out to be implicitly incorporated into  
<sup>1658</sup> the extracted cross sections.

<sup>1659</sup> Although the experiment is conducted with a fixed value of the laboratory beam energy,  
<sup>1660</sup> the actual energy of the incoming electron involved in the reaction turns out to alter and  
<sup>1661</sup> differ from the fixed laboratory value due to (i) the radiative effects that electrons undergo  
<sup>1662</sup> and (ii) the Fermi motion of the target proton. As a consequence, the extracted cross  
<sup>1663</sup> section cannot be associated with a distinct value of the electron beam energy, and this may  
<sup>1664</sup> complicate the interpretation of the results. Let's address these issues in more detail.

<sup>1665</sup> (i) The incoming and scattered electrons can emit photons thus reducing their energy. Due  
<sup>1666</sup> to the change of the incoming electron energy, the extracted cross sections correspond

---

<sup>1</sup> The full decomposition (for the case of the unpolarized electron beam) can be found e.g. in Refs. [3, 36].

1667 to the superposition of various beam energies. The correction due to this effect is  
1668 included into the procedure of radiative corrections (see Sect. 4.2).

1669 (ii) The experiment off the moving proton with fixed laboratory beam energy corresponds  
1670 to that off the proton at rest performed with varying effective beam energies [26].  
1671 As a result, the extracted cross sections off moving protons are convoluted with the  
1672 dependence of the quantity  $\varepsilon_L$  on the beam energy (see Eq. (5.1.1)). A study in  
1673 Ref. [26], however, proves that this effect has an insignificant influence on the cross  
1674 section. The correction due to this effect (which is negligible anyway) is automatically  
1675 included into the procedure of unfolding the effects of the target motion (see Sect. 4.3)<sup>2</sup>.

1676 Being corrected, the cross sections extracted in this analysis may be assigned to the  
1677 distinct value of the laboratory beam energy of  $E_{beam} = 2.039$  GeV.

## 1678 5.2 Off-shell effects

1679 The target proton is bound in the deuterium nucleus and thus undergoes nucleon-nucleon  
1680 interactions. The nucleon mass, however, is thought to be an interaction-dependent quantity,  
1681 i.e. the nucleon's physical mass in a nucleus is smaller than that of a free nucleon [14]. In  
1682 other words, the target proton bound in the deuteron is off-shell, which means that its  
1683 four-momentum squared is not equal to its mass squared.

1684 In the study [43], which aimed at  $\pi^-$  electroproduction off the neutron in deuterium, the  
1685 impact of the off-shell effects on the measured cross sections was shown to be marginal. In  
1686 this study the off-shell effects are ignored.

---

<sup>2</sup> Note that the radiative effects decrease the beam energy, while the Fermi motion leads to a symmetrical spread of the effective beam energy around the laboratory value.

# <sup>1687</sup> Chapter 6

## <sup>1688</sup> Normalization verification

<sup>1689</sup> To prove the credibility of an extracted observable, some well-established quantity is com-  
<sup>1690</sup> monly used as a reference point. For this purpose one can use already published measure-  
<sup>1691</sup> ments of this observable, if they exist in the desired kinematic region, but this usually is not  
<sup>1692</sup> the case. Alternatively, one can focus on some quantity, which can be reliably approximated  
<sup>1693</sup> in this kinematic region by a theoretical model or parameterization. This auxiliary quantity  
<sup>1694</sup> is then extracted from the analyzed dataset, and the comparison of the measured value with  
<sup>1695</sup> the approximated one allows the reliability of the main result to be judged.

<sup>1696</sup> For experiments off a free proton, the elastic cross section usually serves as such a ref-  
<sup>1697</sup> erence quantity as it can be approximated in a wide kinematic region by Peter Bosted  
<sup>1698</sup> parameterization with an excellent accuracy of a few percent, as Ref. [44] demonstrates (see  
<sup>1699</sup> App. B there). Therefore an agreement between the auxiliary measured elastic cross section  
<sup>1700</sup> with the parameterized one, if achieved indicates both the correct normalization of the main  
<sup>1701</sup> result and the trustworthy quality of the electron selection.

<sup>1702</sup> Meanwhile, for experiments off a deuterium target, the quasi-elastic cross section off  
<sup>1703</sup> nucleons can serve as the corresponding reference quantity. However, this observable, if  
<sup>1704</sup> compared with the elastic free proton cross section, is less understood and lacking the same  
<sup>1705</sup> quality of theoretical description [44]. Nonetheless, several techniques have been developed  
<sup>1706</sup> in this matter with the Bosted parameterization of the deuteron quasi-elastic peak being the  
<sup>1707</sup> most commonly used tool.

<sup>1708</sup> Ref. [44] gives some details on the performance of the Bosted parameterization of the  
<sup>1709</sup> deuteron quasi-elastic peak [45, 46] and tests its ability to describe experimental data by  
<sup>1710</sup> comparing the parameterized cross sections with published measurements [47–49]. This  
<sup>1711</sup> testing, being performed in the  $Q^2$  range from  $\sim 0.3 \text{ GeV}^2$  to  $\sim 4 \text{ GeV}^2$ , is of great importance  
<sup>1712</sup> for the current analysis as its  $Q^2$  coverage falls within this range.

<sup>1713</sup> As follows from Ref. [44], the Bosted parameterization in its default implementation  
<sup>1714</sup> systematically overestimates the measured integrals under the quasi-elastic peak and the

1715 overall description quality gradually decreases from several percent to almost 20% as  $Q^2$   
 1716 grows from 0.3 GeV $^2$  to 4 GeV $^2$ . The default implementation corresponds to the case when  
 1717 the nuclear scaling function is estimated using a PWIA calculation and the Paris deuteron  
 1718 wave function (see Refs. [45, 46] for details).

1719 Meanwhile, as also shown in Ref. [44], the Bosted parameterization in its alternative im-  
 1720 plementation systematically underestimates the corresponding integrals with the description  
 1721 quality gradually increasing from  $\sim 15\%$  to a few percent as  $Q^2$  grows from 0.3 GeV $^2$  to  
 1722 4 GeV $^2$ . The alternative implementation corresponds to the case when the nuclear scaling  
 1723 function is estimated according to the parameterization from Ref. [50] and is available with  
 1724 some minor modifications of the source code.

1725 Beside this, Ref. [44] describes a useful approximation formula for the cross section at  
 1726 the quasi-elastic peak, which came from Durand's theory [51]. This formula is of particular  
 1727 interest for this analysis, since it describes very nicely the experimental peak values in the  $Q^2$   
 1728 range from  $\sim 0.3$  GeV $^2$  to  $\sim 1.8$  GeV $^2$ . As shown in Ref. [44], the normalization of the cross  
 1729 section distributions of the Bosted parameterization to the values provided by this formula  
 1730 improves the data description quality in this  $Q^2$  range.

1731 Once we have acquired an impression of the performance and reliability of the param-  
 1732 eterizations currently available for the deuteron quasi-elastic peak, let's now estimate the  
 1733 quasi-elastic cross section from the analyzed dataset and then perform its comparison with  
 1734 the cross section approximated by various implementations of the Bosted parameterization.  
 1735 This investigation is carried out in the framework established in Ref. [44] and therefore, uses  
 1736 the same notations and color codes.

1737 To extract the cross section in the region of the quasi-elastic peak, the only particle that  
 1738 should be registered is the scattered electron. With the electron selection being exactly the  
 1739 same as for the double-pion cross section extraction, the quasi-elastic cross section is defined  
 1740 in each  $\Delta E' \Delta \theta_{e'}$  bin by

$$\frac{d\sigma_{exp}}{d\Omega dE'} = \frac{1}{2\pi} \cdot \frac{\left( \frac{N_{full}}{Q_{full}} - \frac{N_{empty}}{Q_{empty}} \right)}{\Delta E' \Delta(-\cos \theta_{e'})[\mathcal{L}]} \cdot \frac{N_{gen}}{N_{rec}}, \quad (6.1)$$

1741 where  $N_{full}$  and  $N_{empty}$  are the numbers of selected events inside the  $\Delta E' \Delta \theta_{e'}$  bin for runs  
 1742 with deuterium and empty target, respectively.  $N_{gen}$  and  $N_{rec}$  come from the Monte Carlo  
 1743 simulation and correspond to the numbers of generated and reconstructed quasi-elastic events  
 1744 inside the  $\Delta E' \Delta \theta_{e'}$  bin, respectively. The latter were subject to the same electron selection  
 1745 cuts as the experimental events. For the Monte Carlo simulation an event generator based  
 1746 on the measurements from Ref. [10] was used. The other variables are defined in the context  
 1747 of Eq. (3.5.1).

1748 The cross section calculated according to Eq. (6.1) is shown by the black symbols in  
 1749 Fig. 6.1 (note that it is the radiated cross section). The blue and green histograms in this  
 1750 figure correspond to the Bosted parameterization with the default and alternative methods of

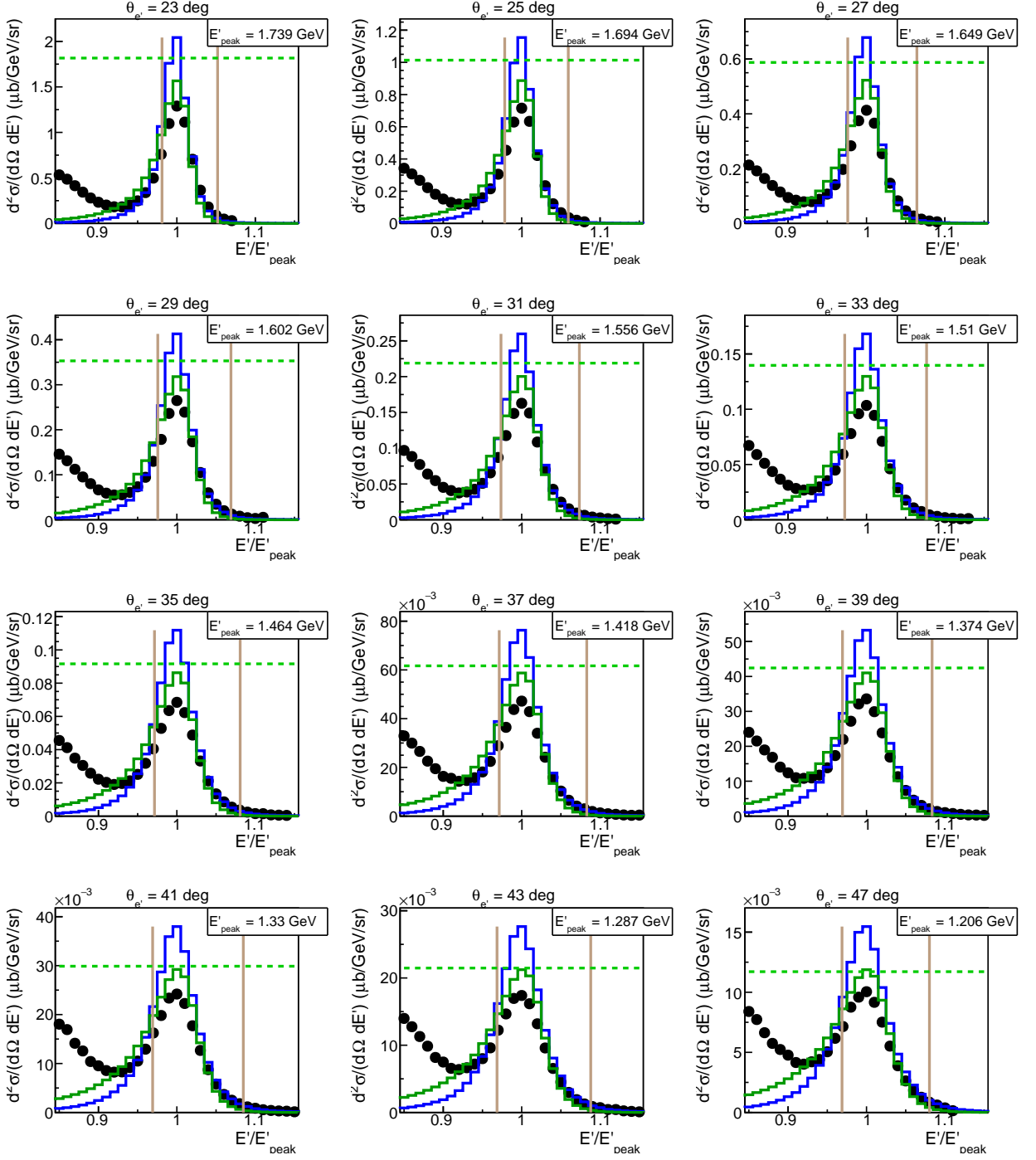


Figure 6.1: Black symbols correspond to the (radiated) cross section in the region of the quasi-elastic peak extracted from the analyzed dataset according to Eq. (6.1). The results of the Bosted parameterization [45, 46] are shown by the histograms. The blue histograms correspond to the default method to calculate the nuclear scaling function, while the green histograms to the alternative method. The green horizontal lines correspond to the peak values approximated by the formula described in Ref. [44]. The vertical lines correspond to the integration limits.

Table 6.1: Ratios of the experimental integrals under the quasi-elastic peak ( $\sigma_{exp}$ ) obtained from the analyzed dataset to those obtained from the Bosted parameterization [45, 46] with the nuclear scaling function calculated by the default ( $\sigma_{par}^1$ ) and alternative ( $\sigma_{par}^2$ ) methods. The index *norm* means that the parameterization histogram was scaled in a way that its maximum was equal to the prediction of the formula described in Ref. [44]. The dark-green shade stands for deviations  $\leq 5\%$ , light-green for 5%-10%, and light-red for more than 10%.

$\theta_{e'}$ , deg	$Q^2$ , GeV $^2$	$E'_{peak}$ , GeV	Left cut	$R$	$\sigma_{peak}^{peak}$ , $\mu b$	$\sigma_{exp}/\sigma_{par}^1$	$\sigma_{exp}/\sigma_{par}^1,_{norm}$	$\sigma_{exp}/\sigma_{par}^2$	$\sigma_{exp}/\sigma_{par}^2,_{norm}$
23	0.56	1.739	0.9811	0.8222	1.817E0	0.91	1.03	1.13	0.98
25	0.65	1.694	0.9784	0.8280	1.014E0	0.89	1.02	1.10	0.96
27	0.73	1.649	0.9761	0.8325	5.876E-1	0.87	1.00	1.07	0.95
29	0.82	1.602	0.9757	0.8324	3.531E-1	0.89	1.04	1.10	0.99
31	0.91	1.556	0.9736	0.8362	2.188E-1	0.87	1.03	1.07	0.98
33	0.99	1.51	0.9722	0.8384	1.397E-1	0.85	1.02	1.05	0.97
35	1.08	1.464	0.9715	0.8394	9.162E-2	0.84	1.02	1.04	0.98
37	1.17	1.418	0.9714	0.8390	6.167E-2	0.83	1.03	1.04	0.99
39	1.25	1.374	0.9694	0.8427	4.244E-2	0.83	1.04	1.04	1.00
41	1.33	1.33	0.9691	0.8428	2.988E-2	0.84	1.07	1.05	1.03
43	1.41	1.287	0.9686	0.8436	2.147E-2	0.83	1.07	1.04	1.03
45	1.49	1.246	0.9680	0.8444	1.571E-2	0.83	1.09	1.04	1.04
47	1.56	1.206	0.9688	0.8427	1.171E-2	0.83	1.10	1.04	1.05

1751 calculating the nuclear scaling function, respectively. The green horizontal lines correspond  
1752 to the prediction of the peak value given by the aforementioned approximation formula.

1753 Since the experimental cross section is radiated, while the parameterized cross section is  
1754 not, their visual comparison loses informativeness. To judge more definitely the agreement  
1755 of the measurement with the parameterization, the corresponding integrals under the quasi-  
1756 elastic peak were compared. The distributions were integrated within the limits shown by  
1757 the vertical lines in Fig. 6.1. To determine the positions of these limits, the procedure  
1758 suggested in Ref. [44] was used. First, the quasi-elastic peaks in the experimental spectra  
1759 were fit by Gaussians with polynomial background. Then the values  $\mu - \sigma$  and  $\mu + 3\sigma$   
1760 were set as the left and right integration limits, respectively, with  $\mu$  and  $\sigma$  being the mean  
1761 value and the standard deviation of the corresponding Gaussian function. The integration  
1762 limits were chosen to be asymmetrical in order to minimize the inelastic background under  
1763 the quasi-elastic peak. This procedure of obtaining the integration limits allows to achieve  
1764 consistency among all plots, since the width of the quasi-elastic peak and its proximity to  
1765 the inelastic part of the spectrum depend on the kinematics.

1766 The experimental integrated cross sections were divided by the radiative correction factors  
1767 ( $R$ ), which were calculated in each  $\theta_{e'}$  bin according to the Mo&Tsai approach [39]. These  
1768 correction factors are listed in Tab. 6.1 together with the positions of the corresponding left  
1769 integration limits. The peak cross section values given by the approximation formula are also  
1770 given there. The last four columns contain the values of the ratio of the experimental integral  
1771 under the quasi-elastic peak ( $\sigma_{exp}$ ) to that obtained from the Bosted parameterization with  
1772 the nuclear scaling function calculated by the default ( $\sigma_{par}^1$ ) and alternative ( $\sigma_{par}^2$ ) methods.  
1773 The index *norm* indicates that the parameterization histogram was scaled in a way that its  
1774 maximum is equal to the prediction of the considered approximation formula. The cells'  
1775 coloring is the same as for Tab. 1 in Ref. [44], i.e. the dark-green shade stands for deviations  
1776  $\leq 5\%$ , light-green for 5%-10%, and light-red for more than 10%.

1777 The ratios of the experimental integrals to the parameterized ones are also shown in  
1778 Fig. 6.2 as a function of the polar angle of the scattered electron ( $\theta_{e'}$ ). The left side corre-  
1779 sponds to the case, when the nuclear scaling function was calculated by the default method  
1780 (blue symbols), while for the right side it was calculated by the alternative method (green  
1781 symbols). The top row stands for the unscaled parameterization histograms, while for the  
1782 bottom row they were scaled to the peak value given by the approximation formula.

1783 As seen from both Tab. 6.1 and Fig. 6.2, the measured integrals under the quasi-elastic  
1784 peak were found to be lower than the values given by the Bosted parameterization in its  
1785 default implementation and their difference increases from  $\sim 10\%$  to  $\sim 15\%$  as  $Q^2$  grows.  
1786 The measured integrals were also found to be higher than the values given by the Bosted  
1787 parameterization in its alternative implementation with the difference decreasing with  $Q^2$   
1788 from  $\sim 10\%$  to  $\sim 5\%$ . Meanwhile, if the parameterization histograms are scaled to the peak  
1789 values predicted by the formula described in Ref. [44], the corresponding ratio stays in the  
1790 vicinity of unity with a reasonable deviation for both options of scaling function calculation.

1791 This result is fully consistent with the conclusion made in Ref. [44] regarding the ability  
 1792 of the Bosted parameterization to describe experimental measurements in this kinematic  
 1793 region. The deviations of the measured integrals from their parameterized values revealed in  
 1794 this analysis and the  $Q^2$  behavior of those deviations are almost exactly the same as those  
 1795 found in Ref. [44] for already established measurements.

1796 Thus, one can conclude that the quality of agreement between the quasi-elastic cross  
 1797 section estimated in this analysis with the Bosted parameterization [45, 46] is the same  
 1798 as was observed for other published measurements. This, in turn, indicates that in this  
 1799 particular analysis, both the electron selection and overall cross section normalization are  
 1800 under control.

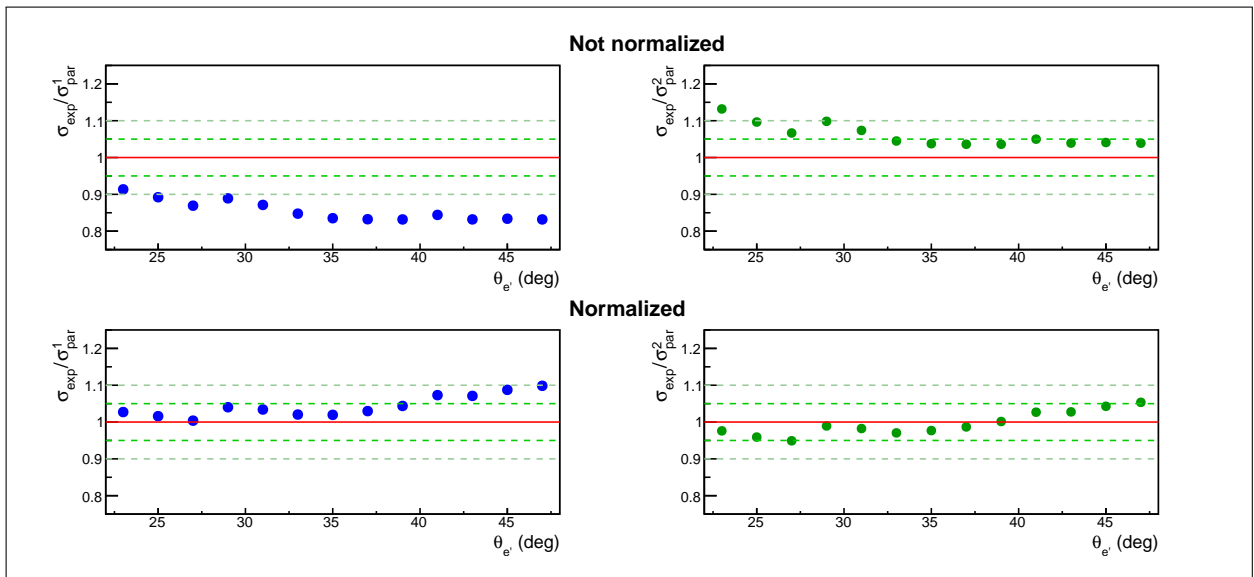


Figure 6.2: Ratios of the experimental integral under the quasi-elastic peak to the parameterized one as a function of the angle  $\theta_{e'}$ . The left side corresponds to the case, when the nuclear scaling function was calculated by the default method (blue symbols), while for the right side it was calculated by the alternative method (green symbols). The top row stands for the unscaled parameterized histograms, while for the bottom row, they were scaled to the peak value approximated by the formula described in Ref. [44]. The red solid line marks the position of unity. The dark-green dashed lines mark the deviation of 5%, while the light-green ones show the deviation of 10%.

1801 The value of the uncertainty due to normalization and electron identification is then  
 1802 estimated considering the following arguments.

- 1803 • as shown in this Chapter, the quasi-elastic cross section extracted from the current  
 1804 dataset have the same quality of agreement with the Bosted parameterization as other  
 1805 published measurements demonstrate [44];

- 1806 • as follows from Tab. 6.1 and Fig. 6.2, one can achieve a good  $\sim 5\%$  agreement between  
1807 the measured and parameterized values of the quasi-elastic cross sections when the  
1808 parameterized distributions are normalized to the peak values approximated by the  
1809 formula that was proven to describe well the experimental peak cross sections in this  
1810 kinematic region [44];
- 1811 • as shown in Refs. [22, 23], the elastic cross section off protons estimated from the  
1812 same “e1e” run period (as it included both hydrogen and deuterium target runs in the  
1813 same experimental configuration) agrees within  $\sim 3\%$  with the corresponding Bosted  
1814 parameterization. The latter, meanwhile, employs the same empirical fit of the nucleon  
1815 electromagnetic form factors as the Bosted parameterization of the quasi-elastic cross  
1816 section off deuteron used in the current study [52].

1817 Taking these facts into account, a 5% global uncertainty is assigned to the extracted  
1818 double-pion cross sections due to potential inaccuracies in the normalization and electron  
1819 selection.

<sub>1820</sub> **Chapter 7**

<sub>1821</sub> **Cross section uncertainties**

<sub>1822</sub> In this study (like in other studies of the double-pion cross sections [15–19, 21–23]) three  
<sub>1823</sub> separate types of the cross section uncertainties are considered, i.e. statistical uncertainty,  
<sub>1824</sub> uncertainty due to the model dependence, and systematic uncertainty. The recipe for esti-  
<sub>1825</sub> mating the uncertainty of each type is given below.

<sub>1826</sub> **7.1 Statistical uncertainties**

<sub>1827</sub> The limited statistics of both the experimental data and the Monte Carlo simulation are  
<sub>1828</sub> the two sources of statistical fluctuations of the extracted cross sections. The cut on the  
<sub>1829</sub> efficiency uncertainty described in Sec. 3.6 was chosen in a way that the latter source gives  
<sub>1830</sub> a minor contribution to the total statistical uncertainty.

<sub>1831</sub> The statistical uncertainty to the five-fold differential virtual photoproduction cross sec-  
<sub>1832</sub> tion is calculated individually in each non-empty multi-dimensional  $\Delta^5\tau$  bin as described  
<sub>1833</sub> below.

<sub>1834</sub> The absolute statistical uncertainty due to the limited statistics of the experimental data  
<sub>1835</sub> is calculated in the non-empty bins as<sup>1</sup>

$$\delta_{\text{stat}}^{\text{exp}}(\Delta^5\tau) = \frac{1}{\mathcal{E} \cdot R \cdot \mathcal{F} \cdot \Gamma_v} \cdot \sqrt{\left( \frac{N_{\text{full}}}{Q_{\text{full}}^2} + \frac{N_{\text{empty}}}{Q_{\text{empty}}^2} \right)} \cdot \frac{\Delta W \cdot \Delta Q^2 \cdot \Delta^5\tau \cdot \mathcal{L}}, \quad (7.1.1)$$

<sub>1836</sub> where  $\Gamma_v$  is the virtual photon flux given by Eq. (3.5.3), while the other ingredients are  
<sub>1837</sub> explained after Eq. (3.5.1).

<sub>1838</sub> The absolute uncertainty due to the limited Monte Carlo statistics is estimated in the

---

<sup>1</sup> See Eq. (D.1) in App. D.

1839 non-empty bins as<sup>2</sup>

$$\delta_{\text{stat}}^{\text{MC}}(\Delta^5\tau) = \frac{d^5\sigma_v}{d^5\tau} \left( \frac{\delta\mathcal{E}}{\mathcal{E}} \right), \quad (7.1.2)$$

1840 where  $\frac{d^5\sigma_v}{d^5\tau}$  is the virtual photoproduction cross section given by Eq. (3.5.2),  $\mathcal{E}$  is the efficiency  
1841 inside the multi-dimensional bin defined by Eq. (3.6.1), while  $\delta\mathcal{E}$  is its absolute statistical  
1842 uncertainty.

1843 Meanwhile, the calculation of the efficiency uncertainty  $\delta\mathcal{E}$  is not straightforward and  
1844 needs special attention, since (i)  $N_{\text{gen}}$  and  $N_{\text{rec}}$  in Eq. (3.6.1) are not independent and (ii)  
1845 Monte Carlo events in this equation are subject to weighting. Therefore, the special approach  
1846 described in Ref. [41] was used for this purpose. Neglecting the event migration between the  
1847 bins, this approach gives the following expression for the absolute statistical uncertainty of  
1848 the efficiency in a bin for the case of weighted Monte Carlo simulation,

$$\delta\mathcal{E}(\Delta^5\tau) = \sqrt{\frac{\mathbb{N}_{\text{gen}} - 2\mathbb{N}_{\text{rec}}}{\mathbb{N}_{\text{gen}}^3} \sum_{i=1}^{N_{\text{rec}}} w_i^2 + \frac{\mathbb{N}_{\text{rec}}^2}{\mathbb{N}_{\text{gen}}^4} \sum_{j=1}^{N_{\text{gen}}} w_j^2}, \quad (7.1.3)$$

1849 where  $N_{\text{gen}}$  and  $N_{\text{rec}}$  are the numbers of the generated and reconstructed Monte Carlo events  
1850 inside the multi-dimensional bin, respectively,  $\mathbb{N}_{\text{gen}}$  and  $\mathbb{N}_{\text{rec}}$  are the corresponding weighted  
1851 event numbers, while  $w$  is a weight of an individual event.

1852 The two parts of the statistical uncertainty given by Eqs. (7.1.1) and (7.1.2) are combined  
1853 quadratically into the total absolute statistical uncertainty in each non-empty  $\Delta^5\tau$  bin<sup>3</sup>,

$$\delta_{\text{stat}}^{\text{tot}}(\Delta^5\tau) = \sqrt{(\delta_{\text{stat}}^{\text{exp}})^2 + (\delta_{\text{stat}}^{\text{MC}})^2}. \quad (7.1.4)$$

1854 The cross section assigned to the empty  $\Delta^5\tau$  cells (see Eq. (4.1.3)) acquires zero statistical  
1855 uncertainty.

1856 For the extracted single-differential cross sections the statistical uncertainty  $\delta_{\text{stat}}^{\text{tot}}(\Delta X)$   
1857 (where  $X$  is one of the final state variables, i.e.  $M_{h_1 h_2}$ ,  $M_{h_2 h_3}$ ,  $\theta_{h_1}$ ,  $\alpha_{h_1}$ ) is obtained from the  
1858 uncertainties  $\delta_{\text{stat}}^{\text{tot}}(\Delta^5\tau)$  of the five-fold differential cross sections according to the standard  
1859 error propagation rules.

---

<sup>2</sup>See Eq. (D.2) in App. D.

<sup>3</sup>The THnSparse root histograms offer an easy way of dealing with the uncertainties. Each multi-dimensional bin of the histograms with the experimental data acquires the absolute uncertainty  $\sqrt{N_{\text{full}}}$  and  $\sqrt{N_{\text{empty}}}$  for full and empty target runs, respectively. The efficiency histograms get the uncertainty  $\delta\mathcal{E}(\Delta^5\tau)$  given by Eq. (7.1.3). Then the uncertainty automatically propagates upon all manipulations with these histograms (addition, division, scaling).

1860 **7.2 Model dependent uncertainties**

1861 In the studies of the double-pion cross sections off the free proton [15–19, 21–23], the un-  
1862 certainty of the model dependence is commonly treated as a unique uncertainty type and is  
1863 associated with the filling of the empty cells. In this analysis one more source of the cross  
1864 section model dependence had to be considered, which is unfolding the effects of the target  
1865 motion. These two sources give comparable uncertainties only for the two lowest  $W$  bins,  
1866 while for the other bins the dominant part of the model dependent uncertainty comes from  
1867 the filling of the empty cells.

1868 Both the contribution from the empty cells and the value of the unfolding correction vary  
1869 greatly (from completely insignificant to considerable) for different final state variable bins.  
1870 Therefore, it is convenient to estimate the model dependent uncertainties in each  $\Delta X$  bin of  
1871 the single-differential cross sections (where  $X$  is one of the final state variables introduced  
1872 in Sect. 3.3).

1873 **7.2.1 Uncertainty due to the empty cells filling**

1874 During the empty cell filling the extracted cross sections acquire a moderate model depen-  
1875 dence (see Sect. 4.1). Once the empty cells are filled, the part of the single-differential cross  
1876 section that came from the empty cells is assigned a 50% relative uncertainty<sup>4</sup> (see Sect. 4.1).  
1877 The absolute cross section uncertainty  $\tilde{\delta}_{\text{model}}^{\text{cells}}(\Delta X)$  is hence given by

$$\tilde{\delta}_{\text{model}}^{\text{cells}}(\Delta X) = \frac{1}{2} \left( \left[ \frac{d\sigma}{dX} \right]_{\text{filled}} - \left[ \frac{d\sigma}{dX} \right]_{\text{not filled}} \right), \quad (7.2.1)$$

1878 where the parentheses contain the difference between the cross section values calculated with  
1879 the empty cell contributions (“filled”) and without them (“not filled”).

1880 The corresponding relative uncertainty  $\varepsilon_{\text{model}}^{\text{cells}}(\Delta X)$  is in turn given by

$$\varepsilon_{\text{model}}^{\text{cells}}(\Delta X) = \frac{\tilde{\delta}_{\text{model}}^{\text{cells}}}{\left[ \frac{d\sigma}{dX} \right]_{\text{filled}}}. \quad (7.2.2)$$

1881 After the filling of the empty cells the cross section is subject to several subsequent  
1882 manipulations, i.e. virtual photon flux normalization, radiative correction, and unfolding  
1883 the effects of initial proton motion. Along this path the absolute uncertainty  $\tilde{\delta}_{\text{model}}^{\text{cells}}(\Delta X)$  is  
1884 propagated in such a way as to keep the relative uncertainty  $\varepsilon_{\text{model}}^{\text{cells}}(\Delta X)$  in each  $\Delta X$  bin of  
1885 the single-differential distribution unchanged.

---

<sup>4</sup>This way to estimate this uncertainty, although being rather conservative, has become conventional for the studies of double-pion production cross sections [19, 20, 22].

1886 Therefore, the absolute uncertainty  $\delta_{\text{model}}^{\text{cells}}(\Delta X)$  for the final single-differential distributions is obtained by  
 1887

$$\delta_{\text{model}}^{\text{cells}}(\Delta X) = \left[ \frac{d\sigma_v}{dX} \right]_{\text{final}} \cdot \varepsilon_{\text{model}}^{\text{cells}}, \quad (7.2.3)$$

1888 with the relative uncertainty  $\varepsilon_{\text{model}}^{\text{cells}}$  given by Eq. (7.2.2) and the single-differential cross  
 1889 section determined according to Eq. (3.5.5).

## 1890 7.2.2 Uncertainty due to unfolding the effects of target motion

1891 In this study the cross sections are subjected to one extra correction compared to the cross  
 1892 sections extracted off the free proton [15–19, 21–23], i.e. unfolding the effects of initial proton  
 1893 motion. The potential inaccuracies due to this procedure are also attributed to the model  
 1894 dependent uncertainty, since the procedure is based on (i) the free proton cross sections  
 1895 taken from the model JM and (ii) the model of the deuteron wave function, which was the  
 1896 Bonn model (see Sect. 4.3 for more detail).

1897 For each  $\Delta X$  bin of the single-differential distributions the relative uncertainty due to  
 1898 the unfolding procedure was estimated by<sup>5</sup>

$$\varepsilon_{\text{model}}^{\text{unfold}}(\Delta X) = \left| \frac{\left[ \frac{d\sigma}{dX} \right]_{\text{folded}} - \left[ \frac{d\sigma}{dX} \right]_{\text{unfolded}}}{\left[ \frac{d\sigma}{dX} \right]_{\text{folded}} + \left[ \frac{d\sigma}{dX} \right]_{\text{unfolded}}} \right|. \quad (7.2.4)$$

1899 The corresponding absolute uncertainty is then given by

$$\delta_{\text{model}}^{\text{unfold}}(\Delta X) = \left[ \frac{d\sigma_v}{dX} \right]_{\text{final}} \cdot \varepsilon_{\text{model}}^{\text{unfold}}. \quad (7.2.5)$$

## 1900 7.3 Systematic uncertainties

1901 The systematic uncertainty of the extracted cross sections is estimated in each bin in  $W$  and  
 1902  $Q^2$ . As in the previous studies of the double-pion production cross sections [15–19, 21–23],  
 1903 the dependence of the systematic uncertainty on the hadronic variables is not investigated.

1904 The following sources are considered to contribute to the total systematic uncertainty of  
 1905 the extracted cross sections.

---

<sup>5</sup> Although the relative uncertainty due to empty cell filling can also be estimated in this way, it was decided to calculate it according to Eq. (7.2.2) to observe consistency with the free proton results [22].

1906 **Normalization and electron identification**

1907 The presence of quasi-elastic events in the dataset advantages the verification of both the  
1908 overall cross section normalization and the quality of the electron selection. The former  
1909 may lack accuracy due to potential miscalibrations of the Faraday cup, fluctuations in the  
1910 target density, deviations of the beam current and position, inaccuracies in determining  
1911 the DAQ live-time as well as imprecise knowledge of other “luminosity ingredients” such as  
1912 target length or the density of liquid deuterium (see Eq. (3.5.1)). Meanwhile, the quality of  
1913 the electron selection may suffer from potential miscalibrations of different detector parts,  
1914 inaccuracies in the electron tracking and identification as well as uncertainties of the cuts  
1915 and corrections involved in the electron selection.

1916 To verify the correct cross section normalization and the quality of the electron selection,  
1917 the study [22, 23] (which is the study of double-pion cross sections off the free proton in  
1918 the same kinematic region) estimates the elastic cross section and then compares it with  
1919 the Bosted parameterization [52]. This comparison revealed a 3% agreement between the  
1920 experimental and parameterized cross sections that allowed to assign a 3% global uncertainty  
1921 to the extracted double-pion cross sections due to inaccuracies in the normalization and  
1922 electron selection.

1923 To achieve the same goals in the current analysis, the quasi-elastic cross section was  
1924 estimated and then compared with the Bosted parameterization of the quasi-elastic cross  
1925 section off the deuteron [45, 46] (see Sect. 6 for details). This comparison allows to claim a  
1926 5% agreement between the experimental and parameterized cross sections and, therefore, to  
1927 assign a 5% global uncertainty to the extracted double-pion cross sections due to inaccuracies  
1928 in the normalization and electron selection.

1929 **Integration over three sets of final hadron variables**

1930 According to Sect. 3.3, the cross sections are extracted in three sets of the kinematic variables.  
1931 The integral cross sections are found to slightly differ among the sets due to the different  
1932 data and efficiency propagation to various kinematic grids. As a final result, the integral  
1933 cross sections averaged (as an arithmetic mean) over these three grids are reported. The  
1934 standard error of the mean is interpreted as a systematic uncertainty (which is calculated  
1935 according to Eq. (D.4) in App. D). The single-differential cross sections and the uncertainty  
1936  $\delta_{\text{stat,mod}}^{\text{tot}}$  are scaled to the mean integral value.

1937 Since different variable sets correspond to different registered final hadrons (and, there-  
1938 fore, to different combinations of the hadron cuts), this systematic error includes the error  
1939 due to the shapes of the hadron cuts that are used in the analysis. The average value of this  
1940 uncertainty among all  $W$  and  $Q^2$  bins is 1.6%. However, the error is larger in the first two  
1941  $W$  bins (with the maximum of 9.5% achieved in the first  $W$  bin at  $Q^2 = 0.675 \text{ GeV}^2$ ), which  
1942 being located near the reaction threshold, correspond to low momenta of the final hadrons.

1943 **Relative efficiency uncertainty cut**

1944 The cut on the relative efficiency uncertainty directly impacts both the cross section value  
1945 and the cross section uncertainties, since it excludes entire kinematic cells from further  
1946 consideration (see Sect. 3.6). This cut, therefore, reduces the total statistical uncertainty  
1947 and increases the model dependent uncertainty, and a cut value  $\delta\tilde{\mathcal{E}}/\tilde{\mathcal{E}} = 0.3$  is chosen as  
1948 a compromise between these two effects. To estimate the systematic effect of the cut, the  
1949 integral cross sections were also calculated for the cut values 0.25 and 0.35. As a final result,  
1950 the arithmetic mean of the integral cross sections for these three cut values is reported, and  
1951 the standard error of the mean is interpreted as a systematic uncertainty (which is calculated  
1952 according to Eq. (D.4) in App. D). The single-differential cross sections and the uncertainty  
1953  $\delta_{\text{stat,mod}}^{\text{tot}}$  are reported for the cut value 0.3, being scaled to the mean integral value.

1954 The systematic effect of the relative efficiency uncertainty cut is estimated for each bin  
1955 in  $W$  and  $Q^2$  individually and is found to be minor, i.e. the average uncertainty value is  
1956 0.8%. Taking into account that the cut on the relative efficiency uncertainty impacts directly  
1957 the amount of empty cells, the revealed small uncertainty associated with this cut indicates  
1958 that the procedure of the empty cell filling is well under control and that the cross section  
1959 inaccuracy caused by the corresponding model dependence is not significant.

1960 **Correction due to FSI-background admixture**

1961 One more part of the systematic uncertainties comes from the effective correction due to  
1962 FSI-background admixture. This correction is performed for the experimental events in the  
1963  $\pi^-$  missing topology and described in Sect. 2.4.2. The fit shown in Fig. 2.33 (as well as the  
1964 corresponding correction factor given by Eq. (2.4.2)) turned out to be slightly dependent on  
1965 the histogram binning. To account for this uncertainty, the correction factor is estimated  
1966 for five different histogram bin sizes, and the arithmetic mean of these five individual values  
1967 is used for the correction (for each bin in  $W$ ). The absolute uncertainty of the resulting cor-  
1968 rection factor is estimated as a standard error of the mean (which is calculated according to  
1969 Eq. (D.4) in App. D). The corresponding cross section uncertainty is estimated by Eq. (D.3),  
1970 where the quantity  $a$  includes the number of events from the  $\pi^-$  missing topology, while  $c$   
1971 in the denominator includes the efficiency estimated for both topologies.

1972 The systematic effect of the FSI-background correction is estimated for each bin in  $W$   
1973 and  $Q^2$  where the correction is applied. For such bins, the average value of the relative  
1974 systematic uncertainty is 0.4%, which is rather marginal.

<sub>1975</sub> **Radiative corrections**

<sub>1976</sub> As a common practice in studies of the double-pion cross sections with CLAS [15–19, 21–  
<sub>1977</sub> 23], a 5% global uncertainty is assigned to the cross section due to the inclusive radiative  
<sub>1978</sub> correction procedure (see Sect. 4.2).

<sub>1979</sub> **Summary of the systematic uncertainties**

<sub>1980</sub> The average values of integral systematic errors with their sources are presented in Tab. 7.1.  
<sub>1981</sub> The uncertainties due to these sources were summed up in quadrature in each  $W$  and  $Q^2$   
<sub>1982</sub> bin to obtain the total systematic uncertainty for the integral cross sections. The common  
<sub>1983</sub> value of the total systematic uncertainty in the bin is  $\sim 7\%$  (it is, however, higher near the  
<sub>1984</sub> threshold).

Table 7.1: Average values of integral systematic uncertainties.

Source	Average value
Normalization and electron identification	5%
Integration over three sets of hadron variables	1.7%
Relative efficiency uncertainty cut	0.6%
Correction due to FSI-background admixture	0.4%
Radiative corrections	5%
<b>Total</b>	<b>7.4%</b>

<sub>1985</sub> **7.4 Summary for the cross section uncertainties**

<sub>1986</sub> Finally, the model dependent uncertainties  $\delta_{\text{model}}^{\text{cells}}(\Delta X)$  and  $\delta_{\text{model}}^{\text{unfold}}(\Delta X)$  defined by Eq. (7.2.3)  
<sub>1987</sub> and Eq. (7.2.5), respectively, are combined with the total statistical uncertainty  $\delta_{\text{stat}}^{\text{tot}}(\Delta X)$   
<sub>1988</sub> defined in Sect. 7.1 as the following.

$$\delta_{\text{stat,mod}}^{\text{tot}}(\Delta X) = \sqrt{(\delta_{\text{stat}}^{\text{tot}})^2 + (\delta_{\text{model}}^{\text{cells}})^2 + (\delta_{\text{model}}^{\text{unfold}})^2}. \quad (7.4.1)$$

<sub>1989</sub> The extracted cross sections are reported with the uncertainty  $\delta_{\text{stat,mod}}^{\text{tot}}$ , which for the  
<sub>1990</sub> single-differential distributions is given by Eq. (7.4.1), while for the integral cross sections is

1991 obtained from the uncertainty of the single-differential distributions according to the stan-  
1992 dard error propagation rules<sup>6</sup>. For the majority of ( $W$ ,  $Q^2$ ) points of the integral cross  
1993 sections the uncertainty  $\delta_{\text{stat,mod}}^{\text{tot}}$  stays on a level of  $\sim 4\%-6\%$ .

1994 It should be mentioned that to combine the statistical uncertainty with the uncertainty  
1995 of the model dependence and to report the final cross sections with the resulting uncer-  
1996 tainty  $\delta_{\text{stat,mod}}^{\text{tot}}$  have become conventional for the studies of double-pion production cross  
1997 sections [15–19, 21–23].

1998 In addition to the uncertainty  $\delta_{\text{stat,mod}}^{\text{tot}}$ , for the integral cross sections the total systematic  
1999 uncertainty is also reported as a separate quantity. If necessary, the relative systematic  
2000 uncertainty in each  $W$  and  $Q^2$  bin can be propagated as a global factor to the corresponding  
2001 single-differential distributions.

2002 In this study the uncertainty  $\delta_{\text{stat,mod}}^{\text{tot}}$  is less than the total systematic uncertainty for the  
2003 majority of ( $W$ ,  $Q^2$ ) points, exceeding it only near the threshold (for  $W \lesssim 1.4$  GeV). This  
2004 happens because the former rises close to the threshold due to small experimental statistics,  
2005 large contribution of the empty cells (see Sect. 4.1), and pronounced impact of the unfolding  
2006 correction (see Sect. 4.3).

---

<sup>6</sup> Note that for the integral cross sections the value of  $\delta_{\text{stat,mod}}^{\text{tot}}$  was averaged (as arithmetic mean) among the three sets of final hadron variables.

2007 **Chapter 8**

2008 **Results and conclusion**

2009 As a result of this study, the integral and single-differential cross sections of the reaction  
2010  $\gamma_v p(n) \rightarrow p'(n')\pi^+\pi^-$  in the kinematic region of invariant mass  $W$  from 1.3 GeV to 1.825 GeV  
2011 and photon virtuality  $Q^2$  from 0.4 GeV $^2$  to 1 GeV $^2$  were obtained. The cross sections  
2012 were extracted in the quasi-free regime, which means that FSI-background admixture in the  
2013 analyzed event sample was decreased as much as was possible and left on a level comparable  
2014 with that in the free proton cross sections.

2015 Figure 8.1 shows the  $W$  dependences of the extracted integral cross sections in various  
2016 bins in  $Q^2$ , while Figure 8.3 shows their  $Q^2$  dependences in various bins in  $W$ . The red  
2017 shadowed area for each point is the total cross section uncertainty, which is the uncertainty  
2018  $\delta_{\text{stat,mod}}^{\text{tot}}$  (see Sect. 7.2) summed up in quadrature with the total systematic uncertainty (see  
2019 Sect. 7.3). The error bars correspond to the uncertainty  $\delta_{\text{stat,mod}}^{\text{tot}}$  only, which for most of the  
2020 points is smaller than the symbol size.

2021 For each integral ( $W, Q^2$ ) point nine single-differential cross sections are reported<sup>1</sup>. They  
2022 are presented in App. F with the uncertainty  $\delta_{\text{stat,mod}}^{\text{tot}}$  shown by error bars. Once the analysis  
2023 is approved, the whole set of the extracted cross sections (both integral and single-differential)  
2024 will be available in the CLAS physics database [5].

2025 After approval the cross sections will be subject to further physical interpretation, which  
2026 includes as an important step the comparison with the double-pion cross sections off the  
2027 free proton recently extracted from CLAS data [22, 23]. These cross sections were obtained  
2028 in the same experimental configuration (including beam energy and target setup) as the  
2029 cross sections of this study. Both measurements have, therefore, similar inherent systematic  
2030 inaccuracies. Moreover, the cross sections of both sets, being obtained in the same kine-

---

1 Note that FSI-background admixture left after the exclusivity cut in the  $\pi^-$ -missing topology (see Sect. 2.4.2), being corrected only in integral sense, may potentially impact the shape of extracted single-differential distributions (mostly angular). However, since this admixture is present only for events from the  $\pi^-$ -missing topology for  $W > 1.4875$  GeV and stays on the level of 3-7%, its impact is not thought to be discernible against the total cross section uncertainty.

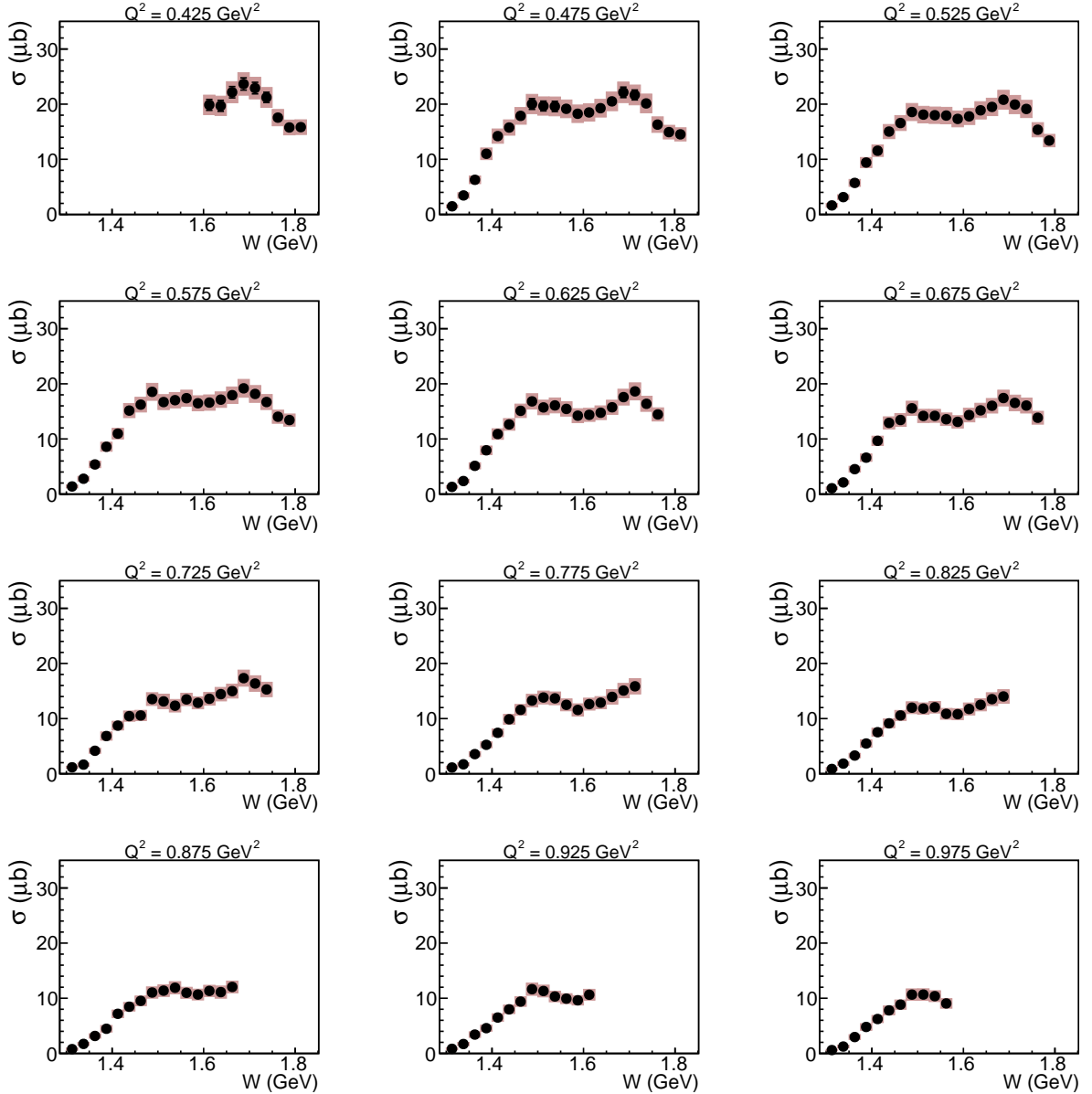


Figure 8.1:  $W$  dependences of the extracted integral cross sections in various bins in  $Q^2$ . The pink shadowed area for each point is the total cross section uncertainty, which is the uncertainty  $\delta_{\text{stat,mod}}^{\text{tot}}$  (see Sect. 7.2) summed up in quadrature with the total systematic uncertainty (see Sect. 7.3). The error bars that correspond to the uncertainty  $\delta_{\text{stat,mod}}^{\text{tot}}$  only, are smaller than the symbol size.

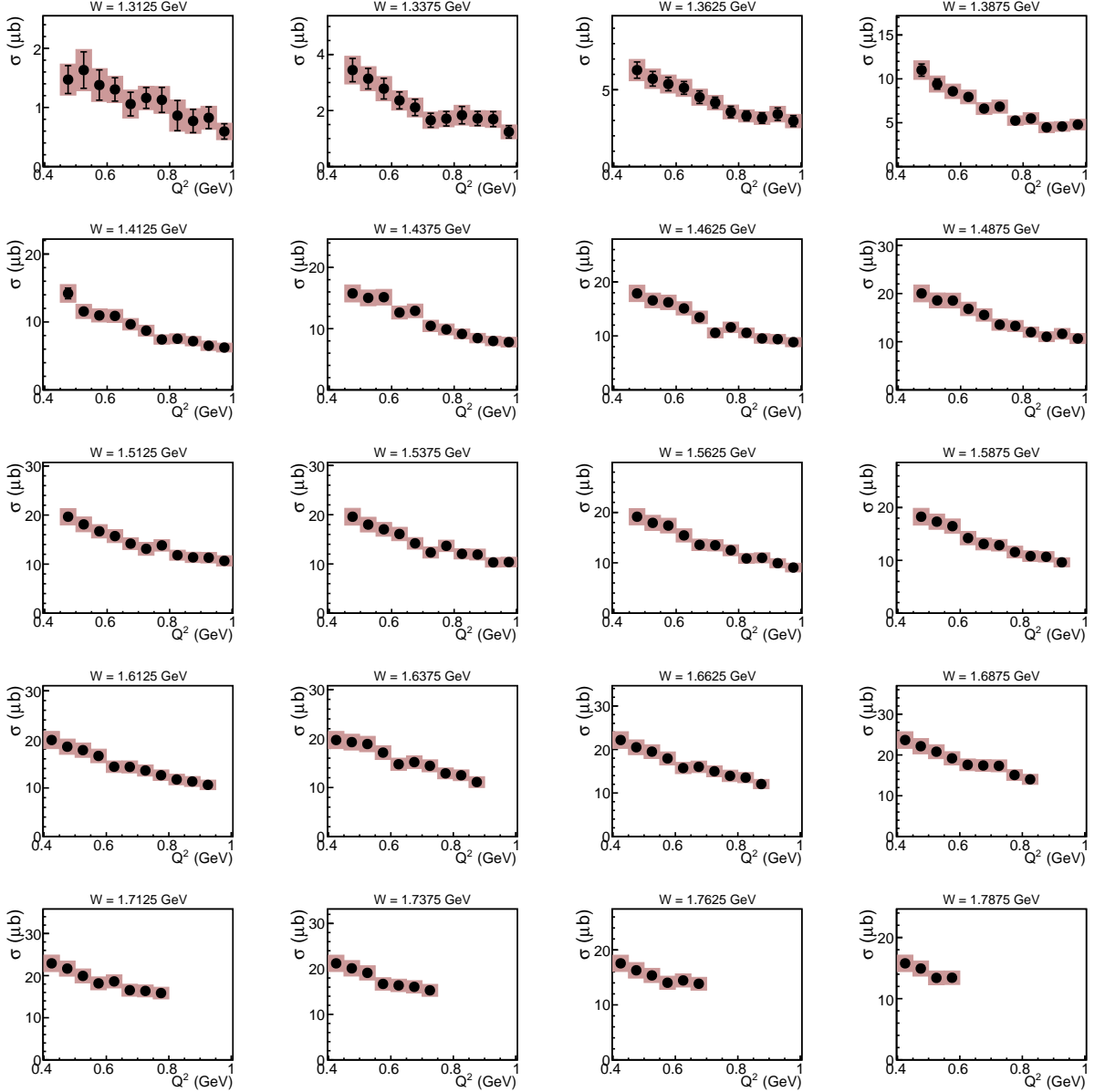


Figure 8.2:  $Q^2$  dependences of the extracted integral cross sections in various bins in  $W$ . The pink shadowed area for each point is the total cross section uncertainty, which is the uncertainty  $\delta_{\text{stat,mod}}^{\text{tot}}$  (see Sect. 7.2) summed up in quadrature with the total systematic uncertainty (see Sect. 7.3). The error bars that correspond to the uncertainty  $\delta_{\text{stat,mod}}^{\text{tot}}$  only, are smaller than the symbol size.

2031 matic region, have identical binning in the kinematic variables that advantages their direct  
 2032 comparison. This comparison hence provides the experimentally best possible opportunity  
 2033 to investigate the differences and alterations (including possible in-medium modifications)  
 2034 that occur in the exclusive reaction off the bound proton in comparison with that off the  
 2035 free proton.

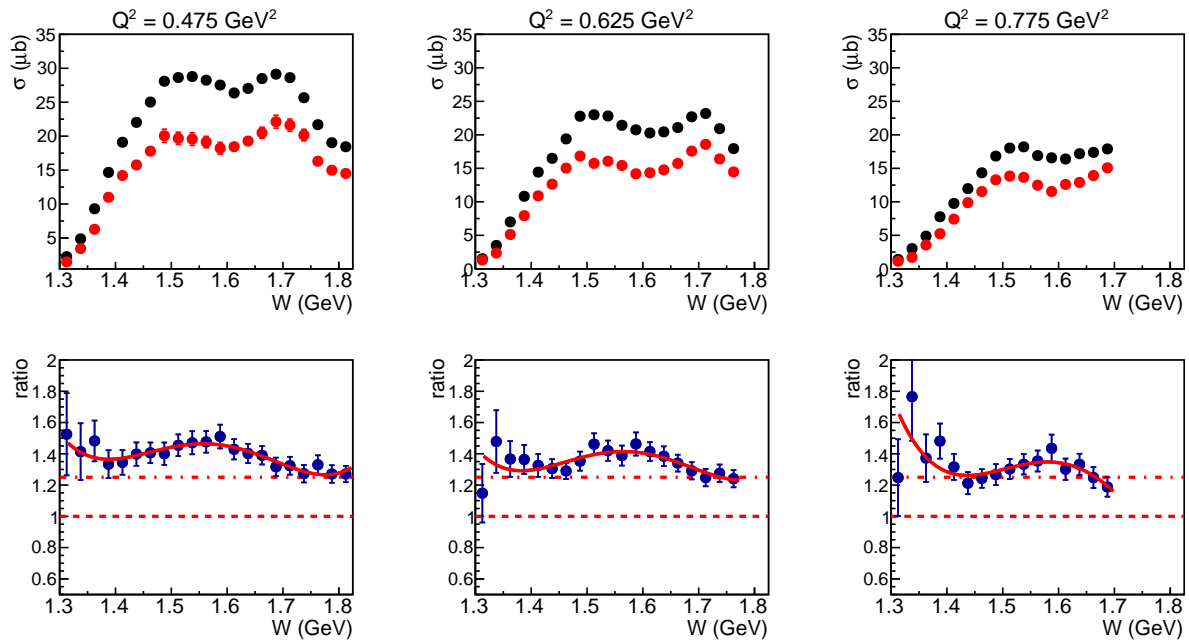


Figure 8.3: Comparison between integral cross sections obtained in this analysis (red symbols) and those obtained off the free proton [22, 23] (black symbols) shown for three typical equidistant  $Q^2$  bins specified in the plots. The cross sections from both studies are given with the uncertainties  $\delta_{\text{stat,mod}}^{\text{tot}}$  only (shown by error bars), while systematic effects are assumed to be identical and are hence ignored. The bottom row of Fig. 8.3 shows the ratio of the corresponding distributions from the top row together with its preliminary fit by the fifth order polynomial. The dashed line marks the position of unity, while the dash-dotted line shows the value of 1.25.

2036 The top row of Fig. 8.3 shows some example plots, which demonstrate the difference  
 2037 between integral cross sections obtained in this analysis (red symbols) and their free proton  
 2038 analogue from Ref. [22, 23] (black symbols). The comparison shown here is given for three  
 2039 typical equidistant  $Q^2$  bins specified in the plots. The cross sections from both studies are  
 2040 given with the uncertainties  $\delta_{\text{stat,mod}}^{\text{tot}}$  only (shown by error bars), while systematic effects are  
 2041 assumed to be identical and are hence ignored. The bottom row of Fig. 8.3 shows the ratio  
 2042 of the corresponding distributions from the top row together with its preliminary fit by the  
 2043 fifth order polynomial.

2044 The examples shown in Fig. 8.3 indicate a pronounced difference between the free proton  
 2045 cross section and its quasi-free analogue measured off the proton bound in deuterium. This

2046 difference, which is thought to be attributed mainly to the FSI effects, is seeking a detailed  
2047 investigation and physical interpretation including the study of its dependence on various  
2048 kinematic variables. This activity will eventually shed light on the processes that occur in  
2049 the deuteron, such as FSI and in-medium effects.

2050 Further physical discussions and interpretations of the obtained results are left for the  
2051 PhD thesis (which is in preparation) and a future publication on the subject.

2052 It is also noteworthy that during this study a sophisticated analysis framework was  
2053 elaborated that includes the tools for data processing and cross section calculation. This  
2054 framework, which is partially based on the achievements of the study [22, 23], might be  
2055 of use for future studies including the upcoming analysis of new CLAS12 data. Therefore,  
2056 the data analysis procedure and the links to the codes of programs and scripts are given in  
2057 App. E.

# 2058 Appendices

## 2059 Appendix A: Features of missing mass distributions

2060 Let's consider the double-pion electroproduction off the free proton  $ep \rightarrow e'p'\pi^+\pi^-$  and  
 2061 define the following missing quantities,

$$\begin{aligned} M_{X[0]}^2 &= [P_{X[0]}^\mu]^2 = [P_e^\mu + P_p^\mu - P_{e'}^\mu - P_{p'}^\mu - P_{\pi^+}^\mu - P_{\pi^-}^\mu]^2, \\ M_{X[\pi^-]}^2 &= [P_{X[\pi^-]}^\mu]^2 = [P_e^\mu + P_p^\mu - P_{e'}^\mu - P_{p'}^\mu - P_{\pi^+}^\mu]^2, \end{aligned} \quad (\text{A.1})$$

2062 where  $P_{X[0]}^\mu$  and  $P_{X[\pi^-]}^\mu$  are the corresponding missing four-vectors, while  $P_i^\mu$  is the four-momentum of the particle  $i$ .

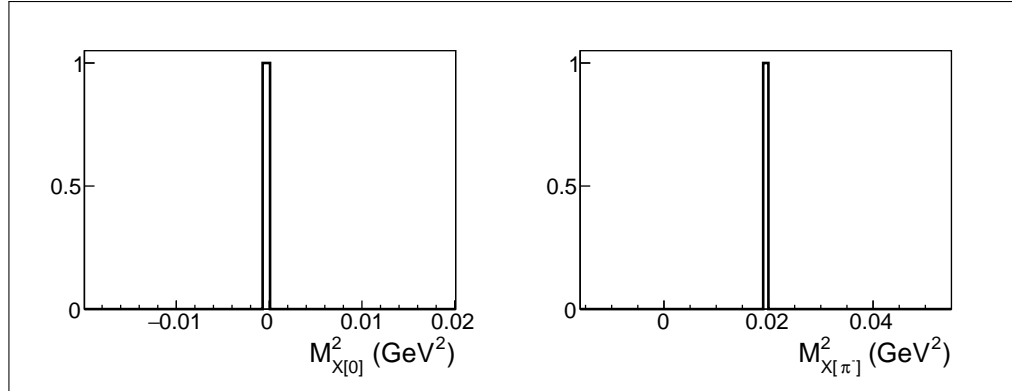


Figure A.1: Quantities  $M_{X[0]}^2$  (left) and  $M_{X[\pi^-]}^2$  (right).

2063 Let's firstly assume that (i) all events in the sample correspond to the reaction  $ep \rightarrow$   
 2064  $e'p'\pi^+\pi^-$ , (ii) all four-momenta are defined exactly without any resolution uncertainty, and  
 2065 (iii) neither radiative effects nor FSI occur. Then<sup>1</sup>

$$M_{X[0]}^2 = 0 \quad \text{and} \quad M_{X[\pi^-]}^2 = [P_{\pi^-}^\mu]^2 = m_\pi^2, \quad (\text{A.2})$$

<sup>1</sup> Note that for the quantity  $M_{X[0]}^2$  the missing four-vector in the square brackets in Eqs. (A.1) is equal to zero componentwise, which means that the energy and each momentum component are equal to zero.

which means that both  $M_{X[0]}^2$  and  $M_{X[\pi^-]}^2$  form a discrete narrow peak at the position of zero and  $m_\pi^2$ , respectively, as Fig. A.1 demonstrates<sup>2</sup>.

Now let's trace the impact of different effects on the missing mass distributions.

## Radiative effects

Let's calculate the quantities  $M_{X[0]}^2$  and  $M_{X[\pi^-]}^2$  assuming that either the incoming or scattered electron can emit a radiative photon, and (if the emission occurs)  $P_e^\mu/P_{e'}^\mu$  in Eqs. (A.1) is the four-momentum of the incoming/scattered electron determined before/after the emission, respectively. Then for events with the photon emission

$$\begin{aligned} M_{X[0]}^2 &= [P_\gamma^\mu]^2 = 0 \quad \text{and} \\ M_{X[\pi^-]}^2 &= [P_{\pi^-}^\mu + P_\gamma^\mu]^2 = [P_{\pi^-}^\mu]^2 + [P_\gamma^\mu]^2 + 2(P_{\pi^-}^\mu \cdot P_\gamma^\mu) = \\ &= m_\pi^2 + 2(E_{\pi^-} - E_\gamma - (\vec{p}_{\pi^-} \cdot \vec{p}_\gamma)) = \\ &= m_\pi^2 + 2(E_{\pi^-} - E_\gamma - |\vec{p}_{\pi^-}|E_\gamma \cos\beta) = \\ &= m_\pi^2 + 2E_\gamma(E_{\pi^-} - |\vec{p}_{\pi^-}| \cos\beta) > m_\pi^2, \end{aligned} \quad (\text{A.3})$$

where  $\beta$  corresponds to the angle between the  $\pi^-$  and the emitted radiative photon.

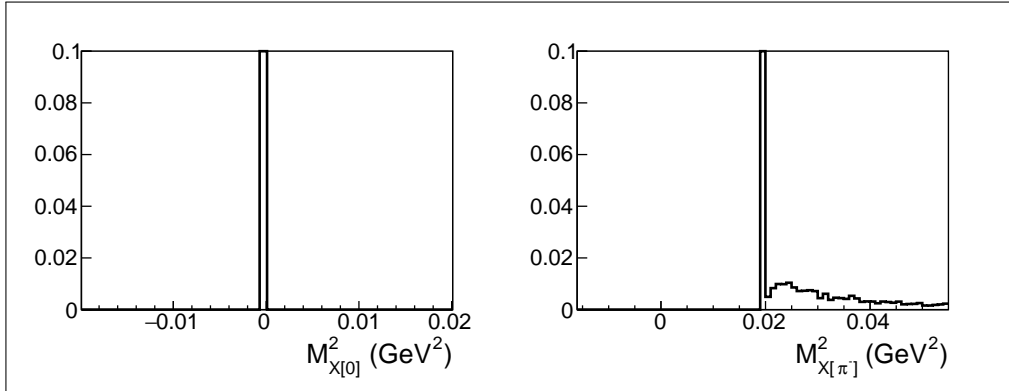


Figure A.2: Impact of radiative effects on  $M_{X[0]}^2$  (left) and  $M_{X[\pi^-]}^2$  (right). Both distributions are zoomed in onto small  $y$  to make the impact of the radiative effects visible.

As follows from Eqs. (A.3), the quantity  $M_{X[0]}^2$  feels no impact of the radiative photon emission<sup>3</sup>, while the quantity  $M_{X[\pi^-]}^2$  acquires a right-side tail, which is demonstrated in Fig. A.2.

<sup>2</sup> All histograms in this Appendix are filled with events generated with TWOPEG [36] for  $E_{beam} = 2.039$  GeV,  $1.4 \text{ GeV} < W < 1.8 \text{ GeV}$  and  $0.4 \text{ GeV}^2 < Q^2 < 0.6 \text{ GeV}^2$  (unless specified otherwise). All distributions are normalized in a way that the maxima of the main peaks are equal to one.

<sup>3</sup> Note that for the quantity  $M_{X[0]}^2$  the missing four-vector in the square brackets in Eqs. (A.1) is the four-momentum of the radiative photon, which is not equal to zero componentwise. However, being massless, the photon has the energy equal to its momentum magnitude, which gives zero upon the calculation of  $M_{X[0]}^2$ . Thus the zero value of  $M_{X[0]}^2$  has a different nature for events with and without radiative effects.

2079 **Admixture from other channels**

2080 Let's assume that some events in the sample correspond to the background channel with  
 2081 greater amount of final state particles, i.e.  $ep \rightarrow e'p'\pi^+\pi^-x$ . Then for the background events  
 2082

$$M_{X[0]}^2 = [P_x^\mu]^2 = m_x^2 > 0 \text{ and}$$

$$\begin{aligned} M_{X[\pi^-]}^2 &= [P_{\pi^-}^\mu + P_x^\mu]^2 = [P_{\pi^-}^\mu]^2 + [P_x^\mu]^2 + 2(P_{\pi^-}^\mu \cdot P_x^\mu) = \\ &= m_\pi^2 + m_x^2 + 2(E_{\pi^-} - E_x - (\vec{p}_{\pi^-} \cdot \vec{p}_x)) > \\ &> m_\pi^2 + m_x^2 + 2m_\pi m_x > m_\pi^2, \end{aligned} \quad (\text{A.4})$$

2083 which means that background events form an additional right-side peak well-separated from  
 2084 the main one by  $m_x^2$  and  $m_x^2 + 2m_\pi m_x$  for  $M_{X[0]}^2$  and  $M_{X[\pi^-]}^2$ , respectively.

2085 This situation is illustrated in Fig. A.3 for the case when the background channel is  
 2086  $ep \rightarrow e'p'\pi^+\pi^-\pi^0$ .

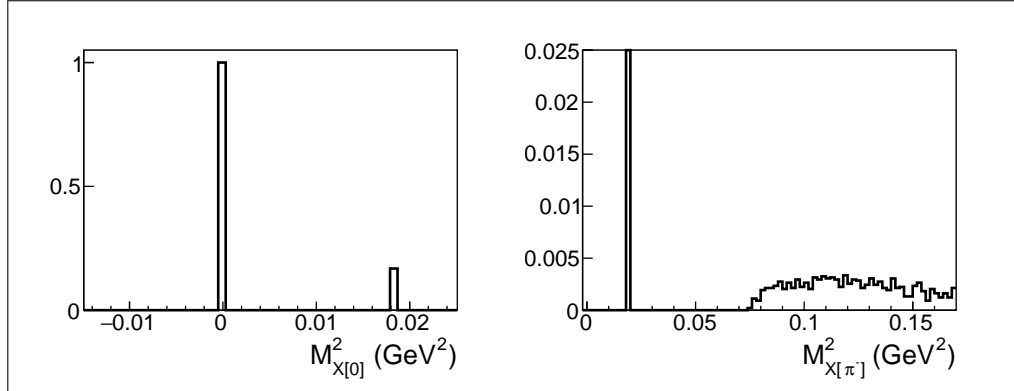


Figure A.3: Quantities  $M_{X[0]}^2$  (left) and  $M_{X[\pi^-]}^2$  (right) plotted for the case when the event sample has an admixture from the background channel  $ep \rightarrow e'p'\pi^+\pi^-\pi^0$ . The discrete right peak (in the left plot) and the right-side structure (in the right plot), both well-separated from the main peak, correspond to the background events. The right plot is zoomed in onto small  $y$ . The plots are produced by means of the GENEV event generator [42] for  $E_{beam} = 2.039$  GeV,  $1.4 \text{ GeV} < W < 1.8 \text{ GeV}$  and  $0.4 \text{ GeV}^2 < Q^2 < 0.6 \text{ GeV}^2$ .

2087 **Detector resolution**

2088 Let's now assume that for all events in the sample the particle four-momenta  $P_i^\mu$  in Eqs. (A.1)  
 2089 are determined with the uncertainty of the detector resolution and then estimate the resulting  
 2090 uncertainties of the missing mass distributions.

2091 The missing quantity  $M_X^2$  can be written in the following way,

$$\begin{aligned} M_X^2 &= (E_X)^2 - (p_X^x)^2 - (p_X^y)^2 - (p_X^z)^2 = \\ &= \left( \sum_i \pm \sqrt{m_i^2 + p_i^2} \right)^2 - \left( \sum_i \pm p_i^x \right)^2 - \left( \sum_i \pm p_i^y \right)^2 - \left( \sum_i \pm p_i^z \right)^2, \end{aligned} \quad (\text{A.5})$$

where  $E_X$  and  $p_X^j$  ( $j = x, y, z$ ) are the energy and momentum components of the missing four-vector, while  $m_i$ ,  $E_i$ , and  $p_i^j$  are the mass, energy, and momentum components of the individual particles with the index  $i$  running over all particles involved in the missing mass calculation (see Eqs. (A.1)). For the  $\pm$  sign the plus is taken for the initial particles ( $e$  and  $p$ ) and the minus for the final particles.

Then let's estimate the uncertainties of the quantities  $E_X$  and  $p_X^j$  through the corresponding uncertainties for the individual particles. The absolute uncertainties for the energy components  $E_X$  are given by

$$\begin{aligned}\Delta E_{X[0]} &= \sqrt{(\Delta E_{e'})^2 + (\Delta E_{p'})^2 + (\Delta E_{\pi^+})^2 + (\Delta E_{\pi^-})^2} = \\ &= \sqrt{(\Delta p_{e'})^2 + (p_{p'}/E_{p'})^2 (\Delta p_{p'})^2 + (p_{\pi^+}/E_{\pi^+})^2 (\Delta p_{\pi^+})^2 + (p_{\pi^-}/E_{\pi^-})^2 (\Delta p_{\pi^-})^2}, \\ \Delta E_{X[\pi^-]} &= \sqrt{(\Delta E_{e'})^2 + (\Delta E_{p'})^2 + (\Delta E_{\pi^+})^2} = \\ &= \sqrt{(\Delta p_{e'})^2 + (p_{p'}/E_{p'})^2 (\Delta p_{p'})^2 + (p_{\pi^+}/E_{\pi^+})^2 (\Delta p_{\pi^+})^2},\end{aligned}\quad (\text{A.6})$$

where  $\Delta p_i$  is the uncertainty of the momentum magnitude for the particle  $i$ , which comes from the momentum resolution of Drift Chambers (where the momentum magnitude is supposed to be measured).

The absolute uncertainties for the momentum components  $p_X^j$  are in turn

$$\begin{aligned}\Delta p_{X[0]}^j &= \sqrt{(\Delta p_{e'}^j)^2 + (\Delta p_{p'}^j)^2 + (\Delta p_{\pi^+}^j)^2 + (\Delta p_{\pi^-}^j)^2}, \\ \Delta p_{X[\pi^-]}^j &= \sqrt{(\Delta p_{e'}^j)^2 + (\Delta p_{p'}^j)^2 + (\Delta p_{\pi^+}^j)^2},\end{aligned}\quad (\text{A.7})$$

where  $\Delta p_i^j$  are the uncertainties of the  $j$ -components of the particle's three-momenta ( $j = x, y, z$ ), which come from both the momentum magnitude resolution and the spatial angular resolution of Drift Chambers.

As follows from Eqs. (A.6) and (A.7),  $p_{X[0]}^j$  and  $E_{X[0]}$  acquire larger absolute uncertainties than  $p_{X[\pi^-]}^j$  and  $E_{X[\pi^-]}$ , respectively, as they include extra terms associated with uncertainties of the registration of an additional particle (the  $\pi^-$  in this case).

Now let's estimate the absolute uncertainties of the corresponding missing masses.

$$\begin{aligned}\Delta M_{X[0]}^2 &= \sqrt{(2E_{X[0]}\Delta E_{X[0]})^2 + \sum_{j=x, y, z} \left(2p_{X[0]}^j\Delta p_{X[0]}^j\right)^2} \\ \Delta M_{X[\pi^-]}^2 &= \sqrt{(2E_{X[\pi^-]}\Delta E_{X[\pi^-]})^2 + \sum_{j=x, y, z} \left(2p_{X[\pi^-]}^j\Delta p_{X[\pi^-]}^j\right)^2}\end{aligned}\quad (\text{A.8})$$

In Eqs. (A.8) the quantities  $\Delta E_{X[0]}$ ,  $\Delta p_{X[0]}^j$  and  $\Delta E_{X[\pi^-]}$ ,  $\Delta p_{X[\pi^-]}^j$  are respectively com-

2112 parable, though (as was shown above) the former is systematically large than the latter.  
 2113 Meanwhile, both  $E_{X[0]}$  and  $p_{X[0]}^j$  are very close to zero, while both  $E_{X[\pi^-]}$  and  $p_{X[\pi^-]}$  are  
 2114 non-zero. As a consequence, the quantity  $\Delta M_{X[0]}^2$  acquires smaller absolute uncertainty  
 2115 value than  $\Delta M_{X[\pi^-]}^2$ . This is, however, not the case for their relative uncertainties, since (in  
 2116 contrast with  $M_{X[\pi^-]}^2$ ) the quantity  $M_{X[0]}^2$  is extremely close to zero.

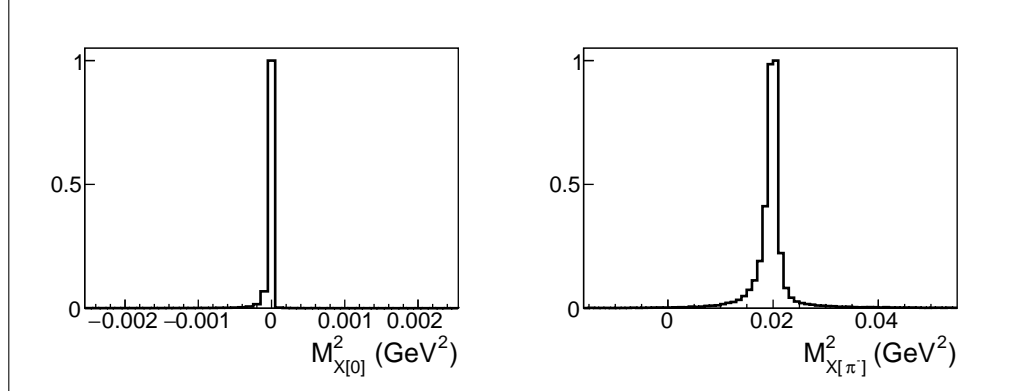


Figure A.4: Impact of the detector resolution on  $M_{X[0]}^2$  (left) and  $M_{X[\pi^-]}^2$  (right). The distribution of  $M_{X[0]}^2$  is zoomed in on  $x$  to demonstrate the disturbances.

2117 This impact of the detector resolution<sup>4</sup> on  $M_{X[0]}^2$  and  $M_{X[\pi^-]}^2$  is demonstrated in Fig. A.4,  
 2118 where  $M_{X[0]}^2$  is shown to be visually very narrow with slight disturbances, while  $M_{X[\pi^-]}^2$   
 2119 acquires perceptible smearing.

## 2120 Final state interactions

2121 Let's estimate the quantities  $M_{X[0]}^2$  and  $M_{X[\pi^-]}^2$  considering the change of the final hadron  
 2122 momenta as in the case of FSI. To simplify the estimation, let's assume the following: (i) for  
 2123 each event only one final state hadron is affected<sup>5</sup>, (ii) the type of the affected hadron is the  
 2124 same among all events in the sample, (iii) FSI are limited to the change of the momentum  
 2125 magnitude of the affected hadron as  $p'_h = \varepsilon p_h$ , and (iv) such momentum modification occurs  
 2126 in all events in the sample. Then

$$\begin{aligned} M_{X[0]}^2 &= [P_h^\mu - P_h'^\mu]^2 = [P_h^\mu]^2 + [P_h'^\mu]^2 - 2(P_h^\mu \cdot P_h'^\mu) = \\ &= 2m^2 - 2(EE' - (\vec{p} \cdot \vec{p}')) = \\ &= 2m^2 - 2(\sqrt{m^2 + p^2}\sqrt{m^2 + \varepsilon^2 p^2} - \varepsilon p^2), \end{aligned} \quad (\text{A.9})$$

2127 where  $m$  and  $p$  are the mass and the momentum magnitude of the affected hadron.

2128 The final expression in Eq. (A.9) is always less than zero regardless of both the value of  
 2129  $\varepsilon$  and hadron kinematics, as the comparison below demonstrates.

<sup>4</sup> To produce this plot, generated events were reconstructed via CLAS reconstruction software.

<sup>5</sup> This imitates the interaction with the remaining neutron for the case of deuteron target.

$$\begin{aligned}
& 2m^2 - 2(\sqrt{m^2 + p^2}\sqrt{m^2 + \varepsilon^2 p^2} - \varepsilon p^2) \wedge 0 \\
& m^2 - \sqrt{m^2 + p^2}\sqrt{m^2 + \varepsilon^2 p^2} + \varepsilon p^2 \wedge 0 \\
& \quad m^2 + \varepsilon p^2 \wedge \sqrt{m^2 + p^2}\sqrt{m^2 + \varepsilon^2 p^2} \\
& \quad m^4 + \varepsilon^2 p^4 + 2m^2 \varepsilon p^2 \wedge m^4 + p^2 m^2 + m^2 \varepsilon^2 p^2 + \varepsilon^2 p^4 \\
& \quad 2m^2 \varepsilon p^2 \wedge p^2 m^2 + m^2 \varepsilon^2 p^2 \\
& \quad 0 \wedge p^2 m^2 (\varepsilon^2 - 2\varepsilon + 1) \\
& \quad 0 < p^2 m^2 (\varepsilon - 1)^2
\end{aligned} \tag{A.10}$$

2130 The quantity  $M_{X[\pi^-]}^2$  in turn can be written as

$$\begin{aligned}
M_{X[\pi^-]}^2 &= [P_{\pi^-}^\mu + P_h^\mu - P'_h]{}^2 = \\
&= [P_{\pi^-}^\mu]^2 + [P_h^\mu - P'_h]{}^2 + 2P_{\pi^-}^\mu(P_h^\mu - P'_h) = \\
&= m_\pi^2 + M_{X[0]}^2 + 2\{E_{\pi^-}(E_h - E'_h) - (\vec{p}_{\pi^-} \cdot \vec{p}_h)(1 - \varepsilon)\},
\end{aligned} \tag{A.11}$$

2131 which can be either greater or smaller than zero depending on the value of  $\varepsilon$  and kinematics.

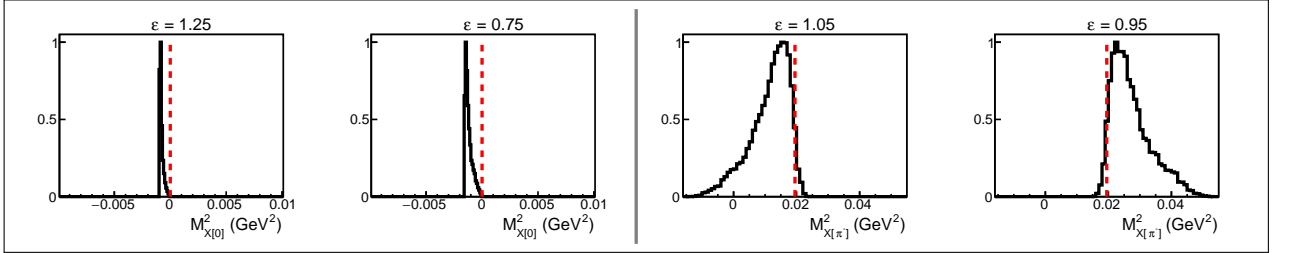


Figure A.5: Quantities  $M_{X[0]}^2$  (left side) and  $M_{X[\pi^-]}^2$  (right side) plotted assuming the change of the  $\pi^+$  momentum magnitude as  $p'_{\pi^+} = \varepsilon p_{\pi^+}$ . Red dashed lines mark the position of zero and pion mass squared, respectively.

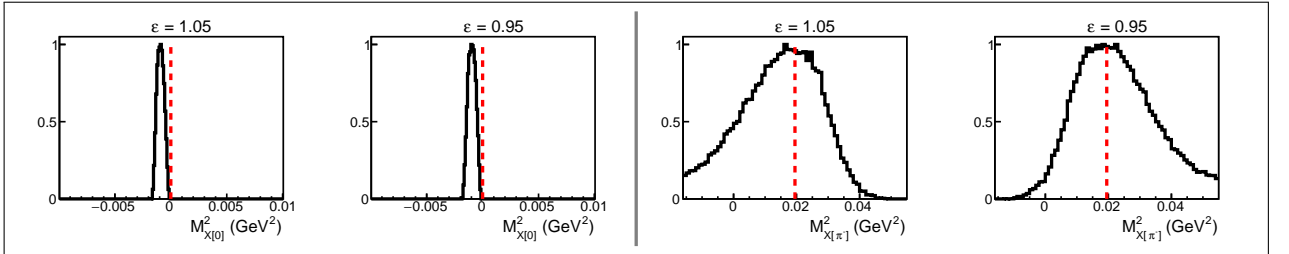


Figure A.6: Quantities  $M_{X[0]}^2$  (left side) and  $M_{X[\pi^-]}^2$  (right side) plotted assuming the change of the momentum magnitude of the final proton as  $p'_{p'} = \varepsilon p_{p'}$ . Red dashed lines mark the position of zero and pion mass squared, respectively.

2132 Figure A.5 shows the distributions of  $M_{X[0]}^2$  and  $M_{X[\pi^-]}^2$  for the case, when all positive  
2133 pions change their momenta as  $p'_{\pi^+} = \varepsilon p_{\pi^+}$ . The quantity  $M_{X[0]}^2$  (left side) is plotted for  
2134 the sizable values of  $\varepsilon$  ( $\varepsilon = 1.25$  and  $\varepsilon = 0.75$ ), since it turns out to be rather insensitive

2135 to the change of pion momenta. The quantity  $M_{X[\pi^-]}^2$  (right side), being in contrast rather  
 2136 sensitive to the  $\pi^+$  momentum change, is plotted for  $\varepsilon = 1.05$  and  $\varepsilon = 0.95$ .

2137 Figure A.6 shows the distributions of  $M_{X[0]}^2$  and  $M_{X[\pi^-]}^2$  for the case, when all final protons  
 2138 change their momenta as  $p'_{p'} = \varepsilon p_{p'}$ . Both  $M_{X[0]}^2$  (left side) and  $M_{X[\pi^-]}^2$  (right side) turn out  
 2139 to be sensitive to the proton momentum change and therefore are plotted for  $\varepsilon = 1.05$  and  
 2140  $\varepsilon = 0.95$ .

## 2141 **Appendix B: Lab to CMS transformation for the proton 2142 at rest case**

2143 Here the procedure of the Lab to CMS transformation for an electroproduction experiment  
 2144 off the proton at rest (bottom left illustration in Fig. 3.2) is described [22]. In this case the  
 2145 CMS axis orientation is different for each reaction event and is specified by the direction of  
 2146 the scattered electron. The transformation from Lab to CMS includes the following steps<sup>1</sup>:

2147 A. The  $xy$ -plane of the Lab system is rotated around the  $z$ -axis (given by the incom-  
 2148 ing electron direction) to make the  $x$ -axis lying in the electron scattering plane (see  
 2149 Fig. A.7). This rotation transforms the four-momentum as  $P' = P \cdot R_1(\varphi_{e'})$ , with

$$R_1(\varphi_{e'}) = \begin{pmatrix} \cos \varphi_{e'} & -\sin \varphi_{e'} & 0 & 0 \\ \sin \varphi_{e'} & \cos \varphi_{e'} & 0 & 0 \\ 0 & 0 & 1 & 0 \\ 0 & 0 & 0 & 1 \end{pmatrix}, \quad (\text{B.1})$$

2150 where  $\varphi_{e'}$  is the azimuthal angle of the scattered electron.

2151 After this rotation  $\varphi_{e'} = 0$ , while  $\varphi_{\gamma_v} = \pi$  with respect to the intermediate reference  
 2152 frame.

2153 B. The Lab system is then rotated to align the  $z$ -axis with the virtual photon direction.  
 2154 The four-momentum transformation for this rotation is given by  $P'' = P' \cdot R_2(\theta_{\gamma_v})$ ,  
 2155 with

$$R_2(\theta_{\gamma_v}) = \begin{pmatrix} \cos \theta_{\gamma_v} & 0 & -\sin \theta_{\gamma_v} & 0 \\ 0 & 1 & 0 & 0 \\ \sin \theta_{\gamma_v} & 0 & \cos \theta_{\gamma_v} & 0 \\ 0 & 0 & 0 & 1 \end{pmatrix}, \quad (\text{B.2})$$

---

<sup>1</sup> In all derivations the energy is assumed to be the last component of the four-momentum and the four-momentum to be a row vector.

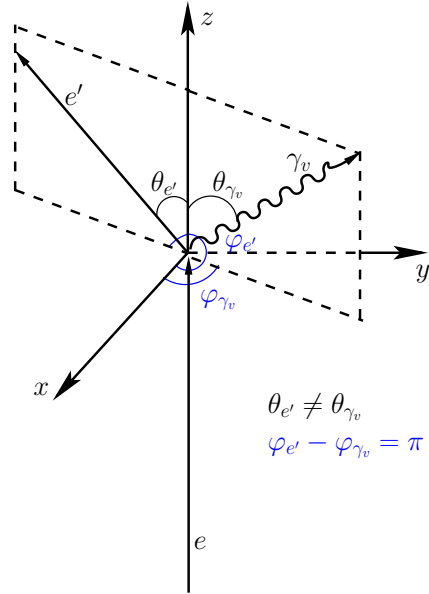


Figure A.7: Virtual photon and scattered electron angles  $\theta$  and  $\varphi$  in the Lab frame for the proton at rest experiment.

2156 where  $\theta_{\gamma_v}$  is the polar angle of the virtual photon<sup>2</sup>.

2157 C. Finally, a boost into the CM frame of the *virtual photon – initial proton* system is  
2158 performed. It is given by the formula  $P''' = P'' \cdot R_3(\beta)$ , with

$$R_3(\beta) = \begin{pmatrix} 1 & 0 & 0 & 0 \\ 0 & 1 & 0 & 0 \\ 0 & 0 & \gamma & -\gamma\beta \\ 0 & 0 & -\gamma\beta & \gamma \end{pmatrix}, \quad \beta = \frac{|\vec{q}|}{E_\gamma + m_{proton}} = \frac{\sqrt{E_\gamma^2 + Q^2}}{E_\gamma + m_{proton}}, \quad \gamma = \frac{1}{\sqrt{1 - \beta^2}}, \quad (B.3)$$

2159 where  $|\vec{q}|$  is the magnitude of the three-vector of the virtual photon and  $\beta$  the mag-  
2160 nitude and  $z$ -component of the three-vector<sup>3</sup>  $\vec{\beta} = (0, 0, \beta)$ .

<sup>2</sup> Using embedded ROOT functions, both rotations can be coded using the unit vectors TVector3  $uz = P4\_gamma.Vect().Unit()$  and TVector3  $ux = (P4\_EL.Vect().Cross(P4\_ELP.Vect())).Unit()$ , where P4\_gamma, P4\_EL, and P4\_ELP are the four-momenta of the virtual photon, initial and final electrons, respectively. The axis vector  $ux$  needs to be rotated according to  $ux.Rotate(3.*M_PI/2,uz)$ . Finally the rotation is defined as  $rot.SetZAxis(uz,ux).Invert()$  and needs to be applied to the four-momentum (P4) of each particle:  $P4.Transform(rot)$ .

<sup>3</sup> Note: if you use the ROOT function .Boost, you should change the sign of the  $z$ -component of  $\beta$ -vector as  $.Boost(0,0,-\beta)$ .

## 2161 Appendix C: The reaction phase-space

2162 The phase-space of the reaction  $ep \rightarrow e'p'\pi^+\pi^-$  is determined by seven kinematic variables,  
 2163 i.e.  $W$ ,  $Q^2$ ,  $M_{h_1h_2}$ ,  $M_{h_2h_3}$ ,  $\theta_{h_1}$ ,  $\varphi_{h_1}$ , and  $\alpha_{h_1}$  (see Sect. 3.3 for details). The kinematic coverage  
 2164 for various variables has the following specificities.

- 2165 • In the  $W$  and  $Q^2$  variables it depends on the electron beam energy and experimental  
 2166 conditions and is fixed for a particular experiment.
- 2167 • The angular variables  $\theta_{h_1}$ ,  $\varphi_{h_1}$ , and  $\alpha_{h_1}$  vary in the fixed limits of  $[0, \pi]$ ,  $[0, 2\pi]$ , and  
 2168  $[0, 2\pi]$ , respectively.
- 2169 • In the invariant masses  $M_{h_1h_2}$  and  $M_{h_2h_3}$  the coverage depends on  $W$  and broadens as  
 2170  $W$  grows.

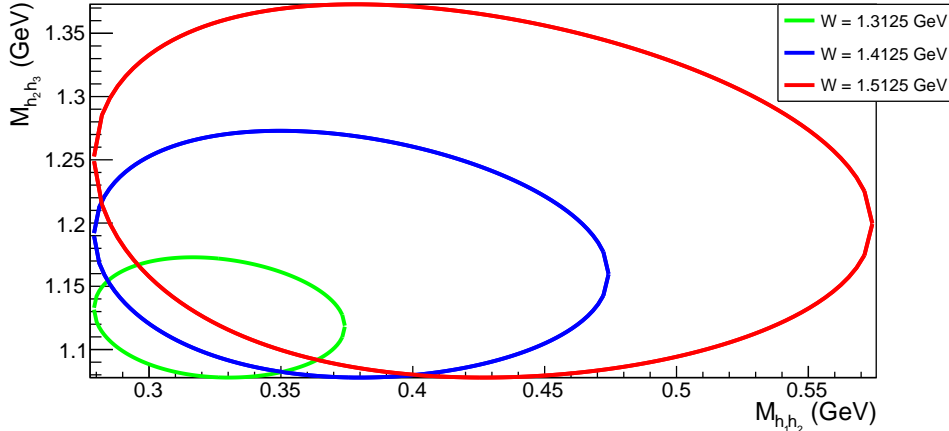


Figure A.8: Boundary of the  $M_{h_2h_3}$  versus  $M_{h_1h_2}$  distribution for several distinct values of  $W$  specified in the plot.

2171 The shape of the reaction phase-space in the invariant masses is determined by the  
 2172 condition  $B(M_{h_1h_2}^2, M_{h_2h_3}^2, W^2, m_{h_2}^2, m_{h_1}^2, m_{h_3}^2) = 0$ , where  $B(x, y, z, u, v, w)$  is the Byckling  
 2173 function [38] given by

$$B(x, y, z, u, v, w) = x^2y + xy^2 + z^2u + zu^2 + v^2w + vw^2 + \\ xzw + xuv + yzv + yuw - xy(z + u + v + w) - \\ zu(x + y + v + w) - vw(x + y + z + u). \quad (C.1)$$

2174 Figure A.8 shows the boundary of the  $M_{h_2h_3}$  versus  $M_{h_1h_2}$  distribution for several values  
 2175 of  $W$  specified in the plot and visually demonstrates the effect of the phase-space broadening  
 2176 with the increase of  $W$ .

## 2177 Appendix D: Uncertainties for indirect measurements

2178 Some useful examples of the error propagation for indirect measurements are described here.  
 2179 In these examples one assumes that  $a > 0$ ,  $b > 0$ , and  $c > 0$ .

- 2180 • If independent variables  $x_1$  and  $x_2$  have absolute uncertainties  $\Delta x_1$  and  $\Delta x_2$ , respectively,  
 2181 then the absolute uncertainty of the variable  $y = c\left(\frac{x_1}{a} - \frac{x_2}{b}\right)$  is

$$\Delta y = c \sqrt{\left(\frac{\Delta x_1}{a}\right)^2 + \left(\frac{\Delta x_2}{b}\right)^2}. \quad (\text{D.1})$$

- 2182 • If the variable  $x$  has an absolute uncertainty  $\Delta x$ , then the absolute uncertainty of the  
 2183 variable  $y = \frac{a}{x}$  is

$$\Delta y = \frac{a}{x^2} \cdot \Delta x = y \cdot \frac{\Delta x}{x}. \quad (\text{D.2})$$

- 2184 • If the variable  $x$  has an absolute uncertainty  $\Delta x$ , then the absolute uncertainty of the  
 2185 variable  $y = \frac{ax+b}{c}$  is

$$\Delta y = \frac{a \cdot \Delta x}{c}. \quad (\text{D.3})$$

- 2186 • If there is a set of measurements  $x_1, x_2, \dots, x_n$  with the arithmetic mean  $\bar{x}$ , then the  
 2187 absolute standard error of the arithmetic mean is

$$\Delta \bar{x} = \sqrt{\frac{\sum_{i=1}^n (x_i - \bar{x})^2}{n \cdot (n - 1)}}. \quad (\text{D.4})$$

## 2188 Appendix E: Analysis procedure and code availability

2189 The following files are used as an input for the analysis.

- 2190 • 1989 files with full target runs stored at  
2191    /mss/clas/e1e/production/pass1/h10/
- 2192 • 14 files with empty target runs stored at  
2193    /mss/clas/e1e/production/pass1/h10emptarg\_d/
- 2194 • 165625 files with the Monte Carlo simulation. They are stored at  
2195    /mss/clas/e1e/production/simulation\_2pi/sim\_skorodum\_Aug2016/nt10\*

2196 All these files contain “h10” ROOT ntuples. They were converted from HBOOK outputs  
2197 of nt10maker (which is a part of CLAS software) using the “h2root” utility.

2198 The scripts used for performing the Monte Carlo simulation, which incorporate the in-  
2199 formation on the simulation/reconstruction parameters used in this analysis, can be found  
2200 here [https://github.com/skorodumina/CLAS6\\_sim\\_rec\\_sequence](https://github.com/skorodumina/CLAS6_sim_rec_sequence).

2201 To speed up the analysis process, the specified above files are converted to reduced “t21”  
2202 ROOT ntuples, which contain only those variables that are used in the analysis (the conver-  
2203 sion program is available at [https://github.com/skorodumina/converter\\_clas6.git](https://github.com/skorodumina/converter_clas6.git)).  
2204 After the conversion one is left with

- 2205 • 284 files with full target runs stored at  
2206    /mss/home/skorodum/e1e/data\_2pi\_conv\_2July2018/
- 2207 • 1 file with empty target runs, i.e.  
2208    /mss/home/skorodum/e1e/out\_conv\_empty\_2pi\_2July2018.root
- 2209 • 33125 files with the simulation. They are stored at /mss/clas/e1e/production/  
2210    simulation\_2pi/sim\_skorodum\_Aug2016/converted\_July2018\_cc\_ok/

2211 For further calculations the double-pion analysis program is used (it is available at  
2212 [https://github.com/skorodumina/two\\_pi\\_analysis\\_code.git](https://github.com/skorodumina/two_pi_analysis_code.git)). This program outputs  
2213 the root file with multi-dimensional histograms.

2214 For the experimental data this process is rather simple:

- 2215 • 284 full target files are fed to the double-pion analysis program at once.
- 2216 • 1 empty target file is fed to the same program.
- 2217 • Both outputs for full and empty target runs are processed with the corresponding  
2218 script to combine the topologies. This results in the output file *out\_data.root*.

2219 For the Monte Carlo simulation the process is more complicated.

- 2220 • 33125 files with the simulation are processed on batch farms with the double-pion  
2221 analysis program to produce 1325 output files with multi-dimensional histograms.
- 2222 • These 1325 files are then processed with the corresponding scripts. As a result one has  
2223 three sets of 53 files each. Files within each set contain multi-dimensional histograms  
2224 filled with  $\sigma$ ,  $\sigma^2$ , or 1.

- 2225     ● Then 53 files within each set are combined by the ROOT utility “hadd” into three  
2226       resulting files.  
2227     ● The three files are processed with the corresponding scripts (which either combine  
2228       topologies and/or calculate efficiency) with the three resulting outputs.  
2229     ● These three outputs are combined (with “hadd”) to form the output *out\_sim.root*.

2230     Then the script that performs the cross section calculation is used. This script is located  
2231     at [https://github.com/skorodumina/twopi\\_crsect\\_calc.git](https://github.com/skorodumina/twopi_crsect_calc.git) together with the afore-  
2232     mentioned scripts. The program for unfolding the effects of the target motion is also located  
2233     there (it is needed to produce the root file with the Fermi correction factor).

2234     The script for the cross section calculation uses as inputs the files *out\_data.root*,  
2235     *out\_sim.root* and the file with the Fermi correction factor (all of them are introduced above).  
2236     The script processes the multi-dimensional histograms from the input files and performs the  
2237     cross section calculation that includes the empty target subtraction, normalization to the  
2238     luminosity and the virtual photon flux, filling the empty cells, radiative corrections, and  
2239     unfolding the effects of the initial proton motion. Beside this, the script also calculates  
2240     the cross section uncertainty  $\delta_{\text{stat,mod}}^{\text{tot}}$ . The single-differential and integral cross sections are  
2241     finally output to the root file.

2242     Once the cross section is extracted, it is then subject to several final manipula-  
2243     tions (i.e. binning corrections, averaging, and estimating the systematic uncertainties),  
2244     which are performed by means of the corresponding scripts. They are also available at  
2245     [https://github.com/skorodumina/twopi\\_crsect\\_calc.git](https://github.com/skorodumina/twopi_crsect_calc.git).

2246     The majority of codes introduced here are provided with their own README files, which  
2247     are intended to clarify other details of the code performance.

## 2248 Appendix F: Measured single-differential cross sections

2249 This Appendix contains the full set of single-differential cross sections measured in the current  
 2250 analysis. The cross sections are reported with the uncertainty  $\delta_{\text{stat,mod}}^{\text{tot}}$  shown by error  
 2251 bars (see Sect. 7.2.2). The central point of the corresponding  $W$  and  $Q^2$  bin is specified  
 2252 in each figure together with the value of the relative integral systematic uncertainty (see  
 2253 Sect. 7.3) that can be propagated as a global factor to the corresponding single-differential  
 2254 cross sections.

2255 Note that the invariant mass distributions are shown in the range from  $M_{\text{lower}}$  to  $M_{\text{upper}}$ ,  
 2256 both given by Eq. (3.4.1) with the latter calculated using the central value of the  $W$  bin.  
 2257 One, therefore, should take into consideration that the cross section in invariant mass is  
 2258 equal to zero on both sides of the range. Also note that the invariant mass distributions  
 2259 contain one bin less than specified in Tab. 3.1, since the cross section in the last mass bins is  
 2260 not reported. This happens due to the special arrangement of mass bins used in the analysis,  
 2261 which forces the last bin to be situated out of the specified range (see Sect. 3.4 for details).

2262 It is also noteworthy that  $\alpha$  angular distributions of the double-pion cross sections should  
 2263 be symmetrical with respect to  $\alpha = 180^\circ$ , when integrated over  $\varphi$ . However, the experimen-  
 2264 tally measured  $\alpha$  distributions acquire some asymmetry. To judge more quantitatively the  
 2265 asymmetry degree, the average asymmetry factor was estimated for each extracted  $\alpha$  distri-  
 2266 bution as

$$\text{asym} = \frac{1}{\text{int}[n/2]} \sum_{i=1}^{\text{int}[n/2]} \left| 1 - \frac{2\sigma_i}{\sigma_i + \sigma_{n-i}} \right|, \quad (\text{F.1})$$

2267 where  $n$  is the number of bins in the distribution and  $\sigma_i$  the cross section value in the bin  $i$ .

2268 The average asymmetry factor estimated by Eq. (F.1) is specified in the plots for each  
 2269  $\alpha$  distribution to facilitate visual judgement of the distribution's shape and its inherent  
 2270 systematic inaccuracy.

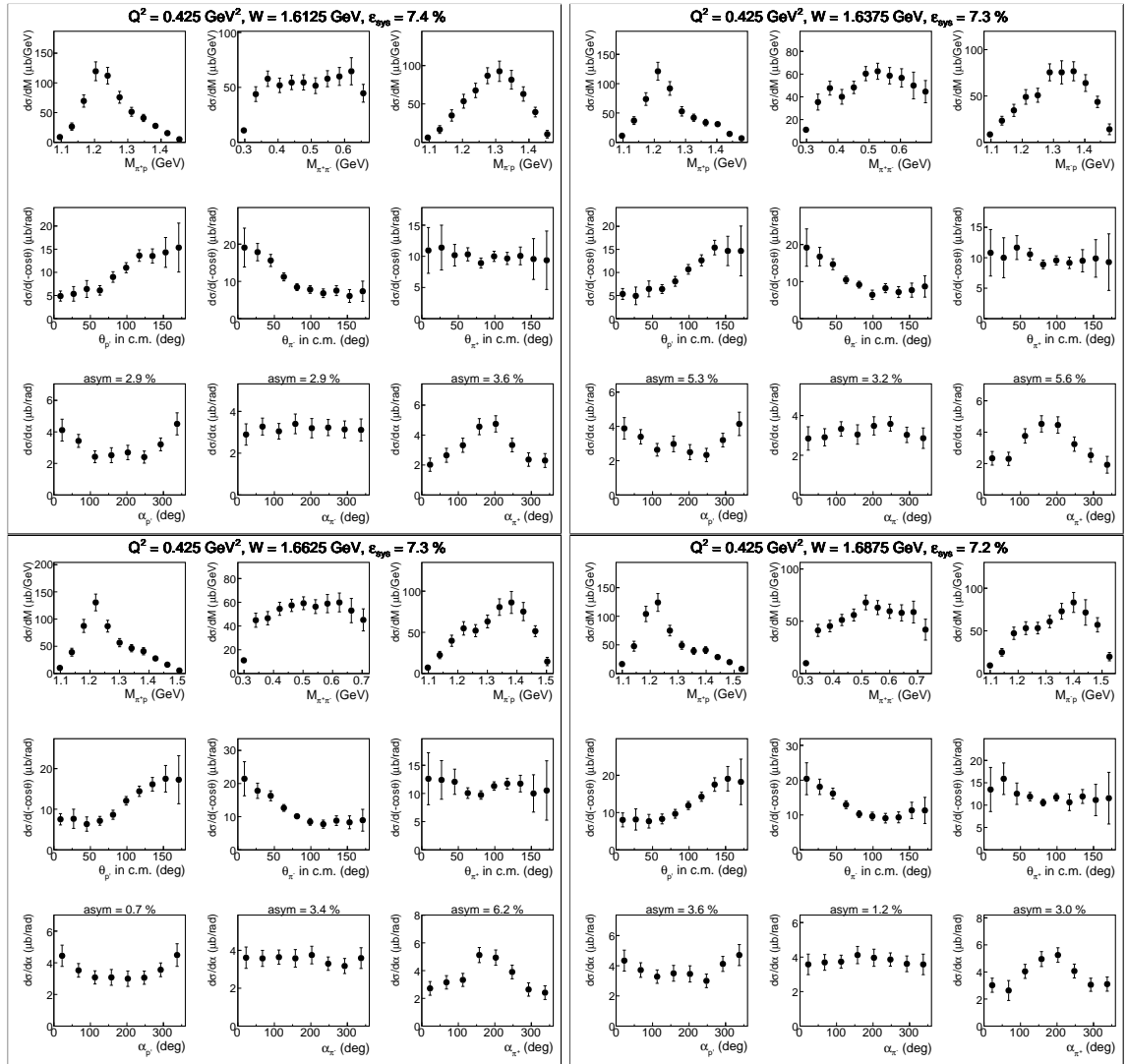


Figure A.9:

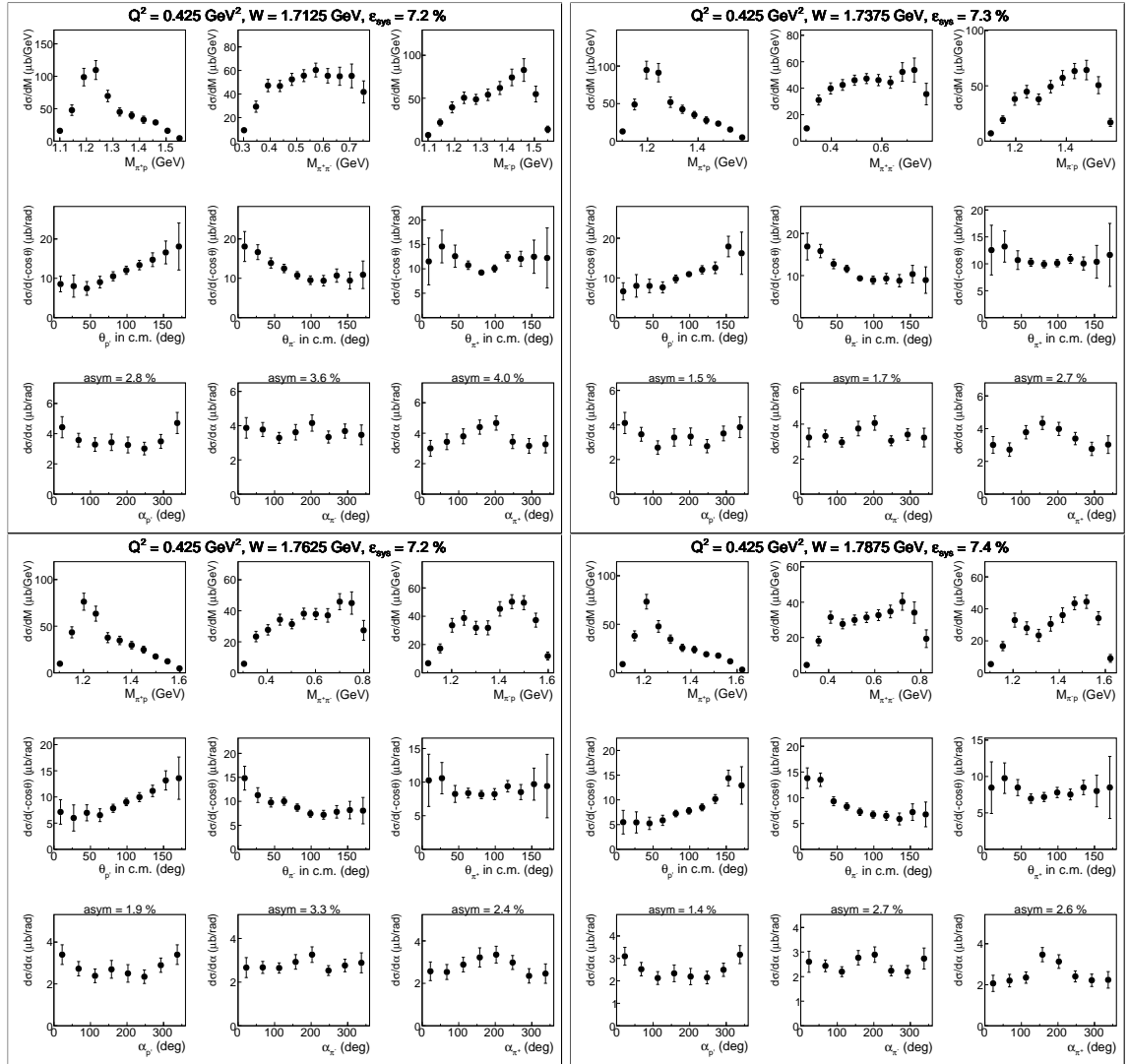


Figure A.10:

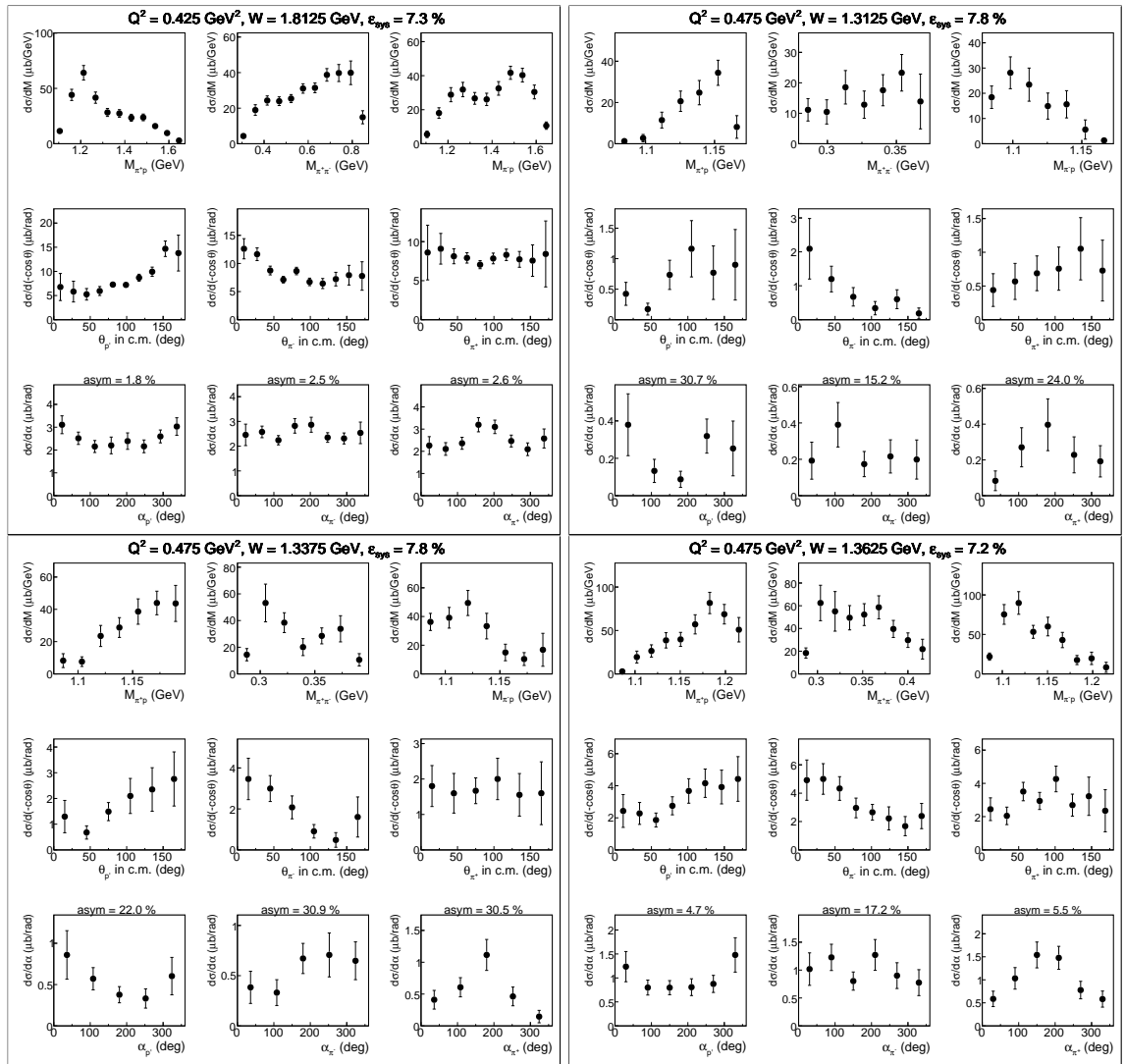


Figure A.11:

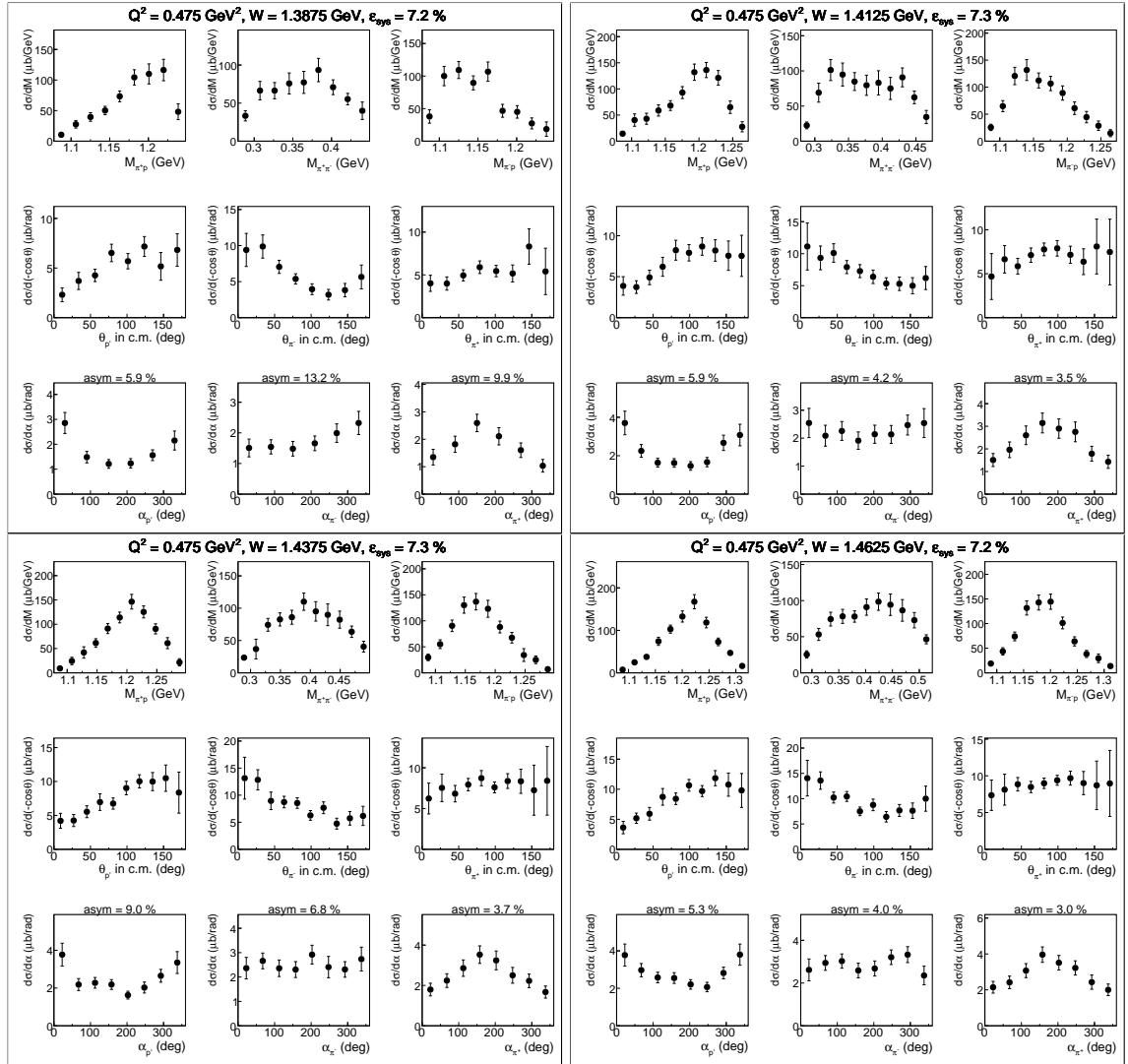


Figure A.12:

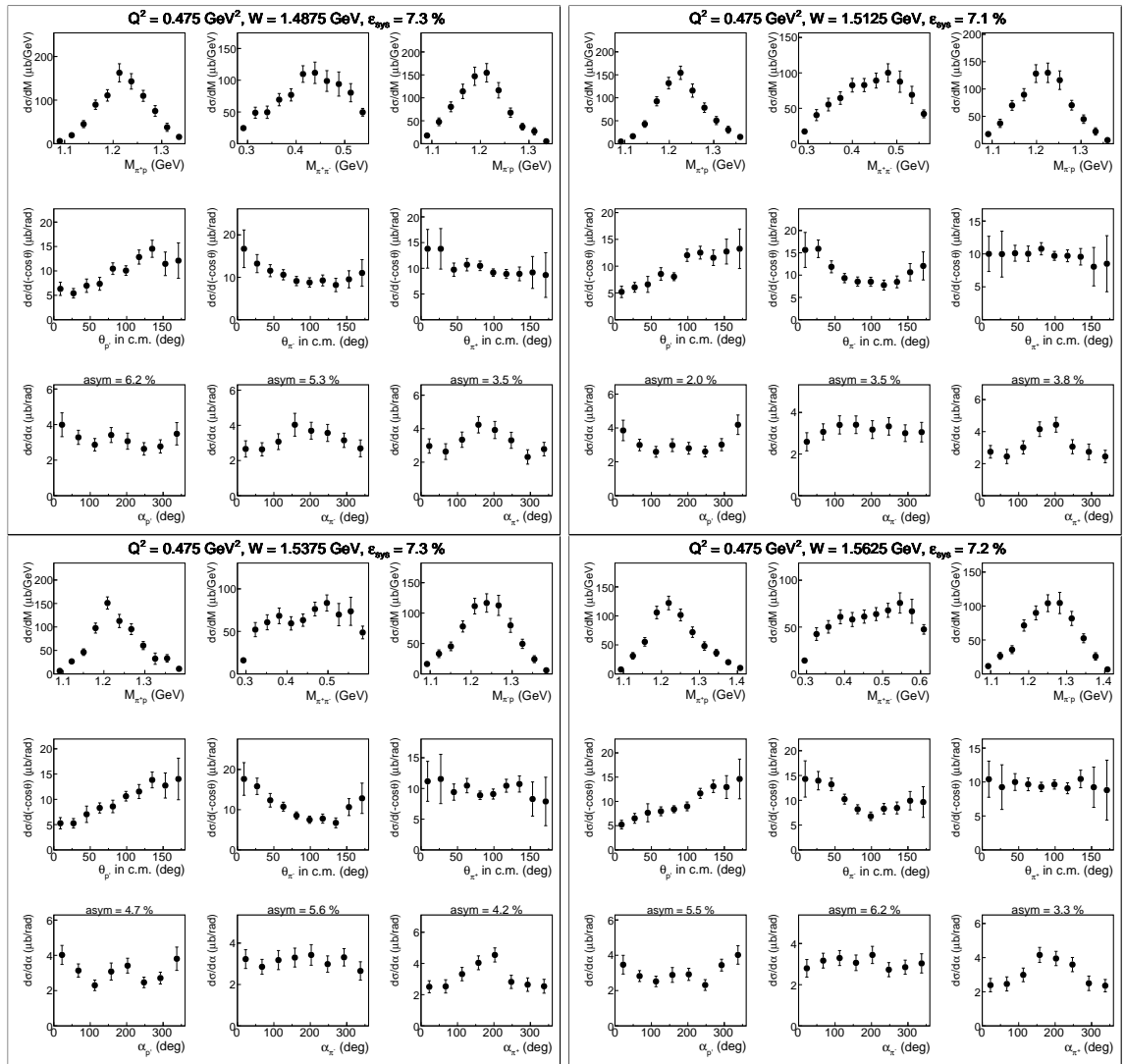


Figure A.13:

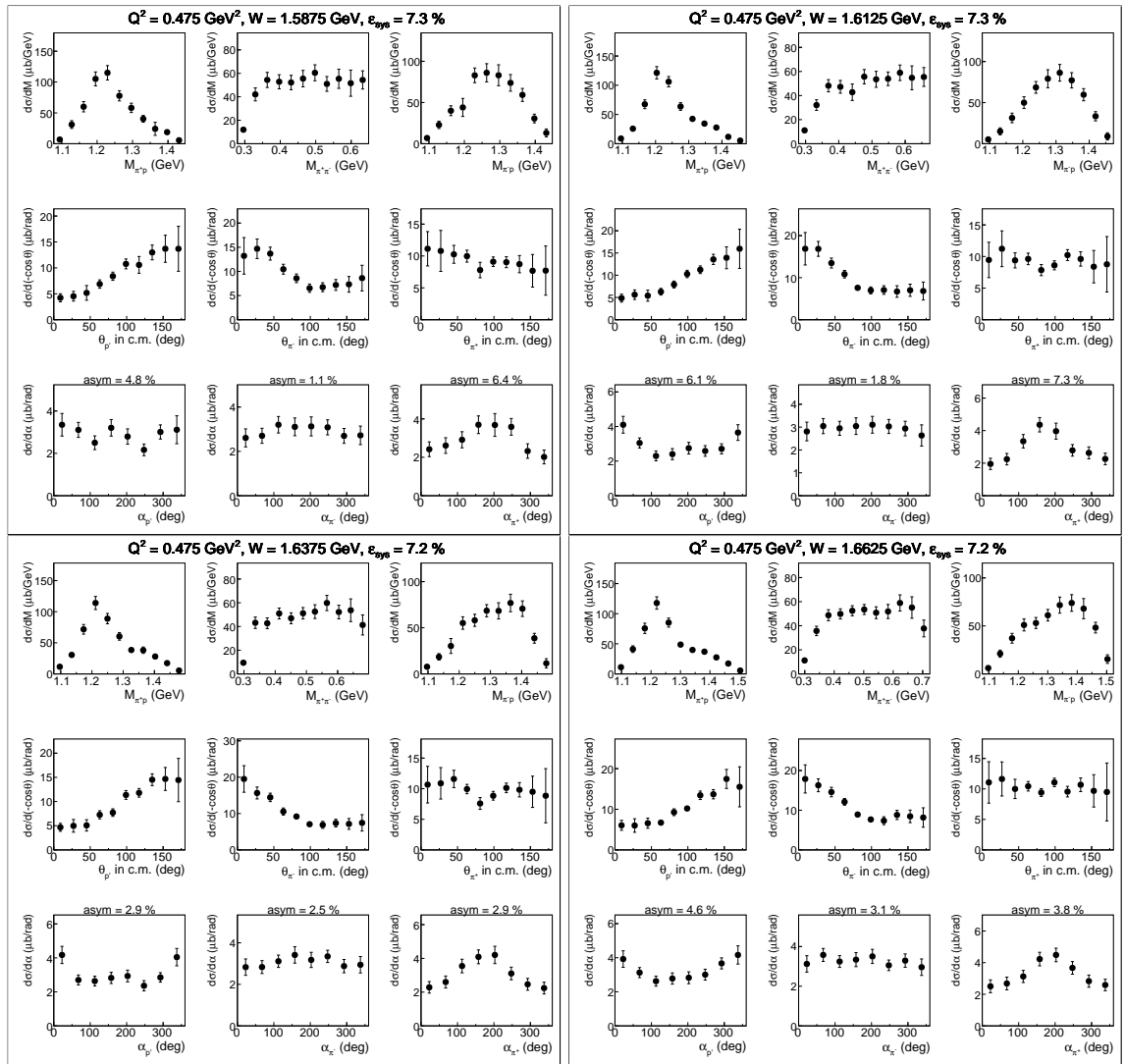


Figure A.14:

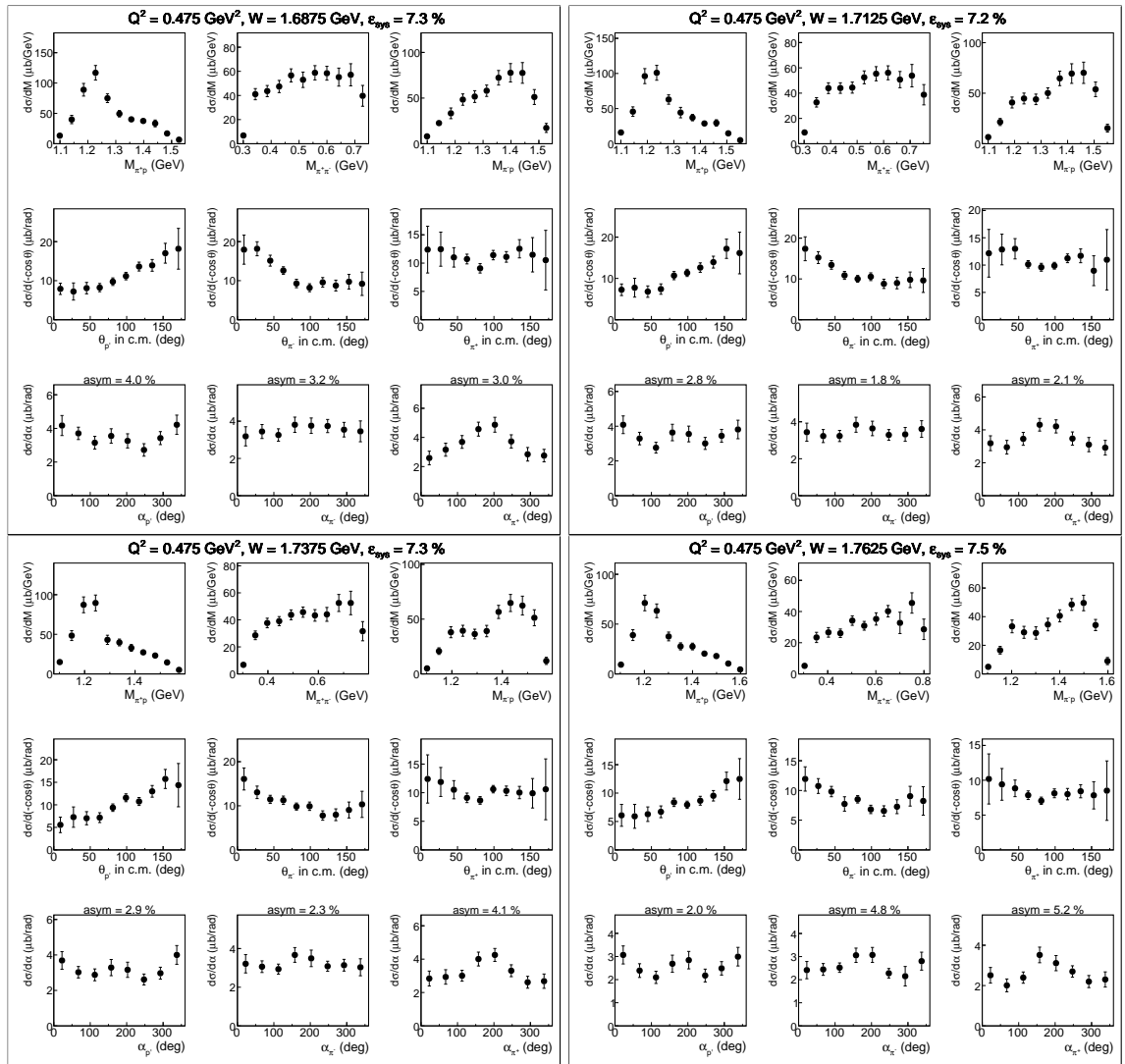


Figure A.15:

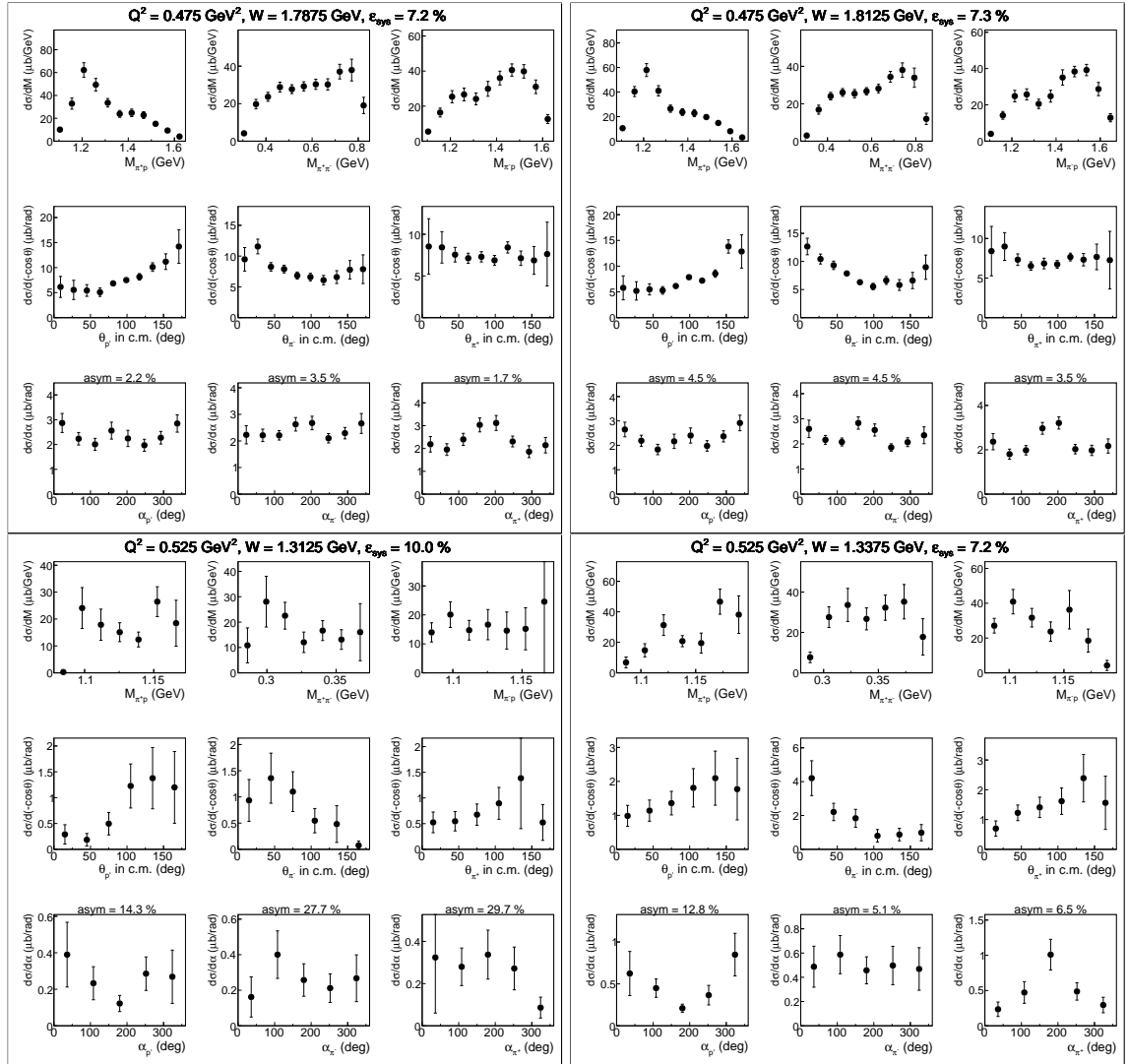


Figure A.16:

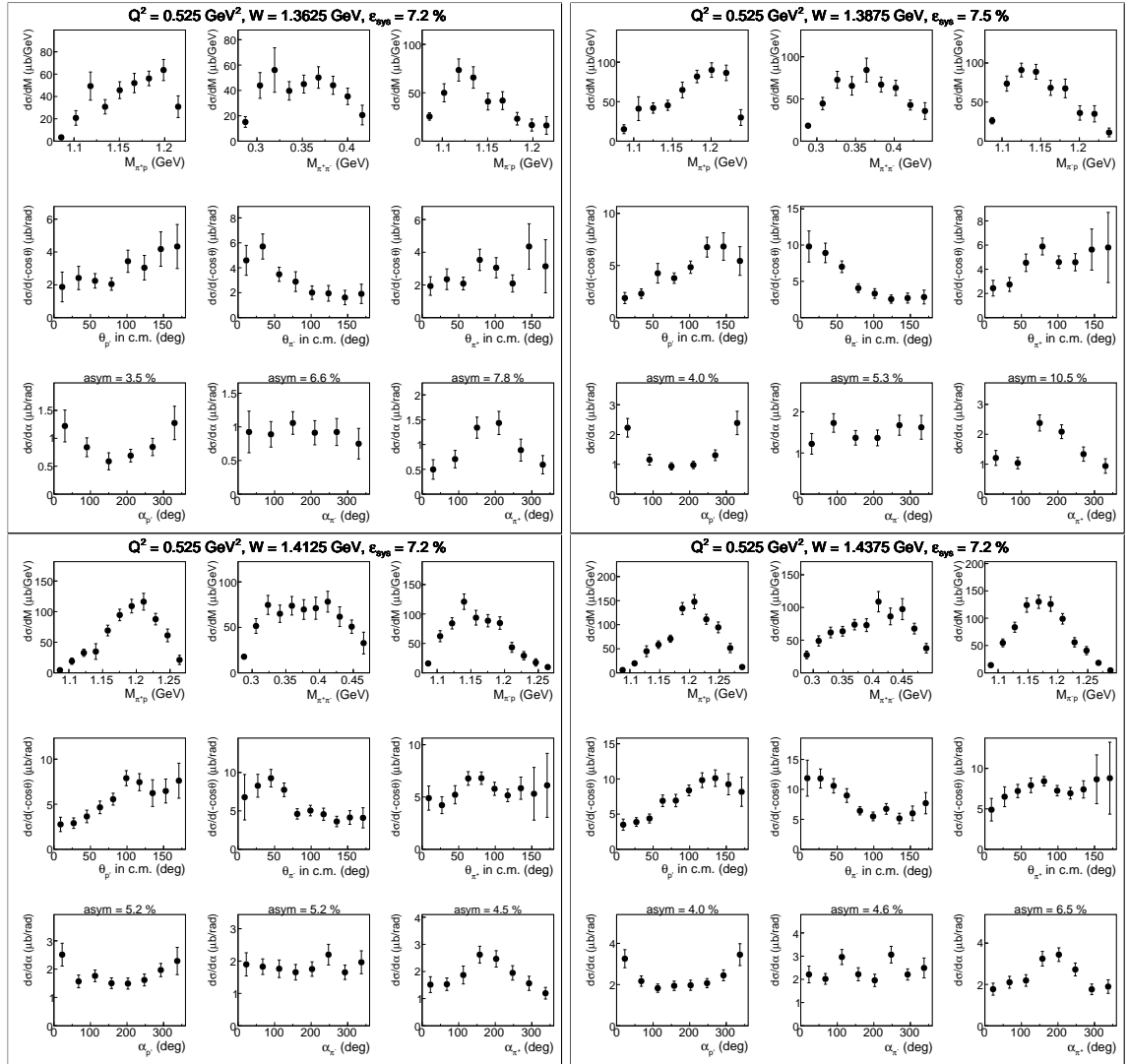


Figure A.17:

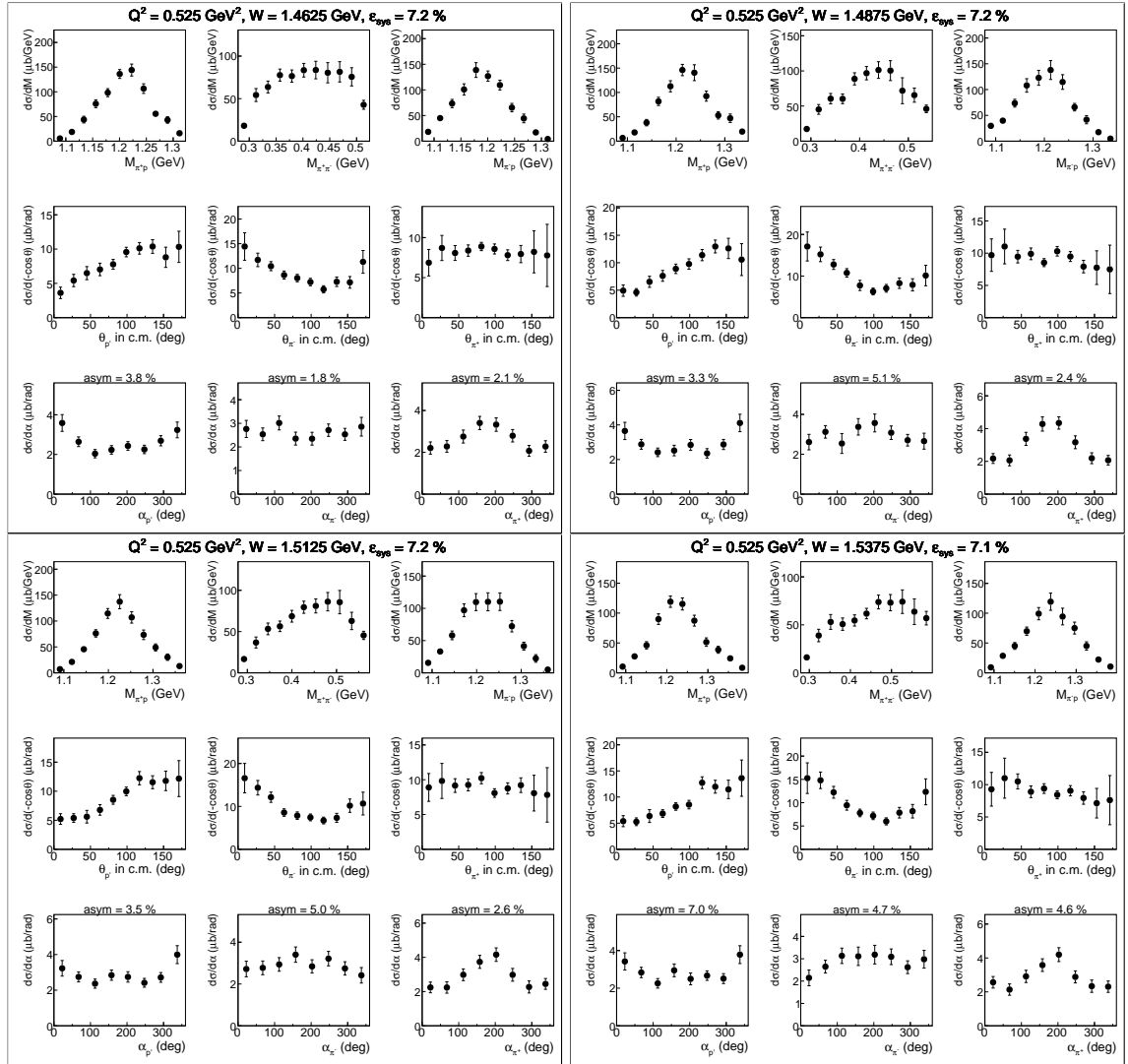


Figure A.18:

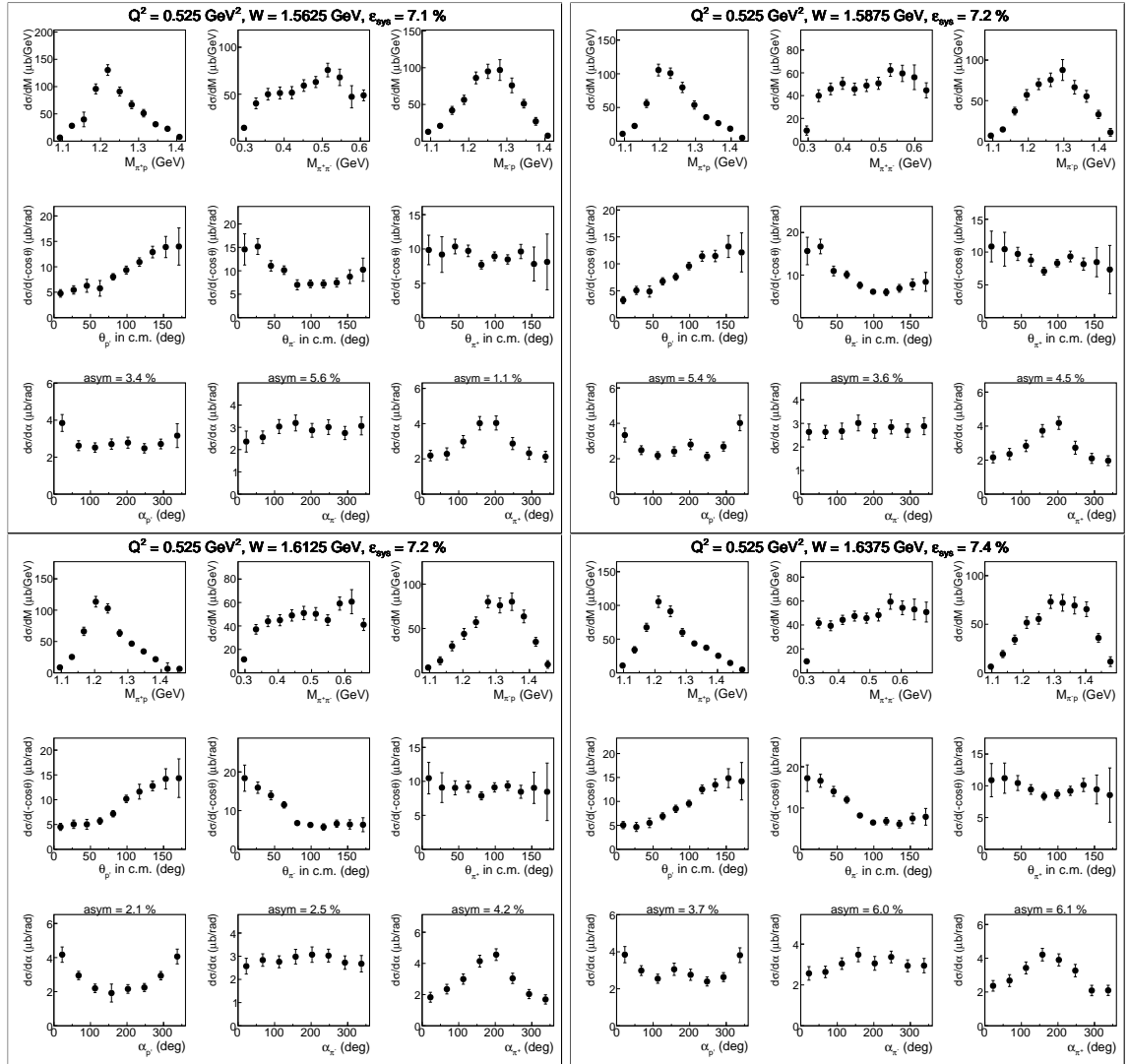


Figure A.19:

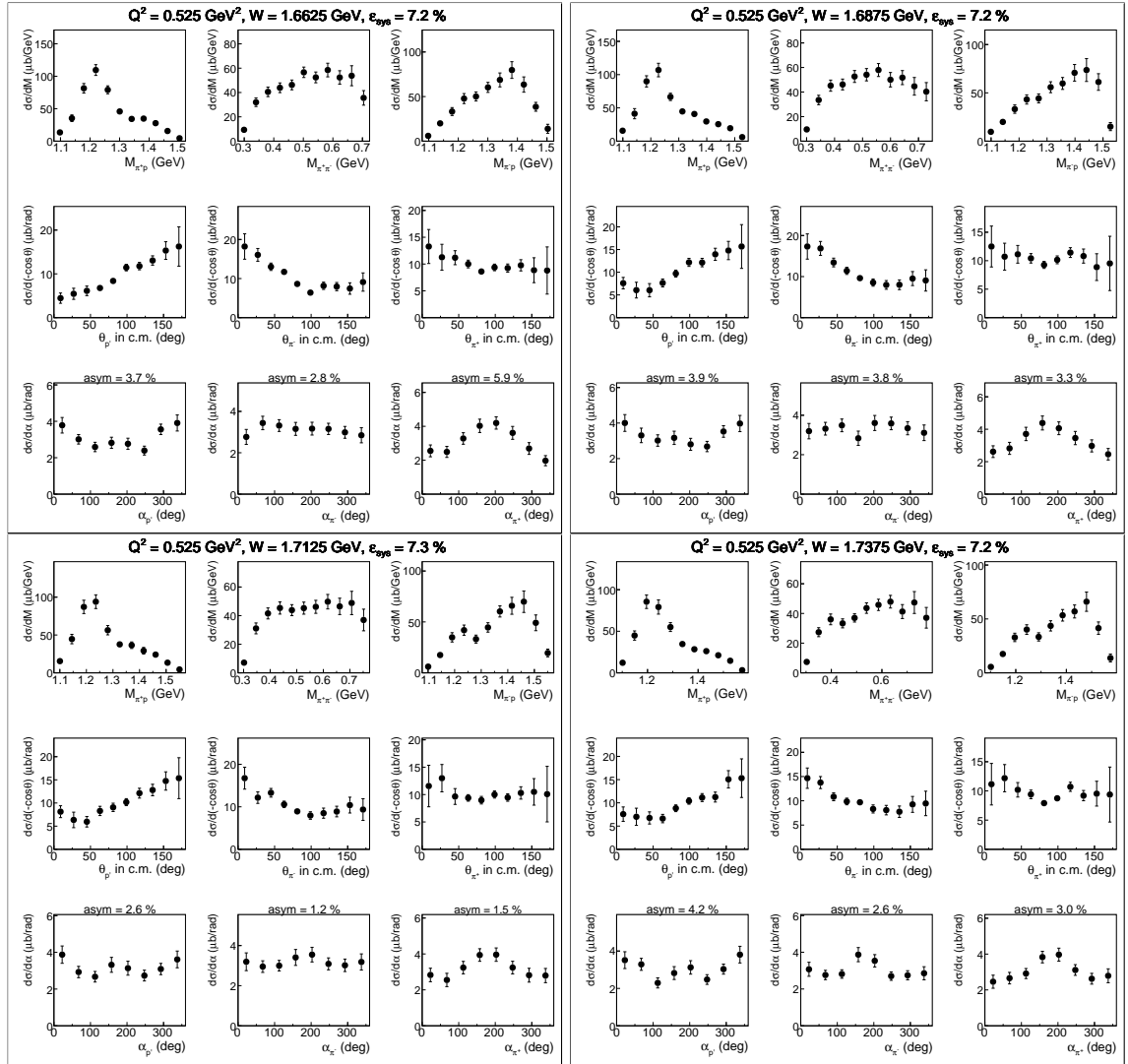


Figure A.20:

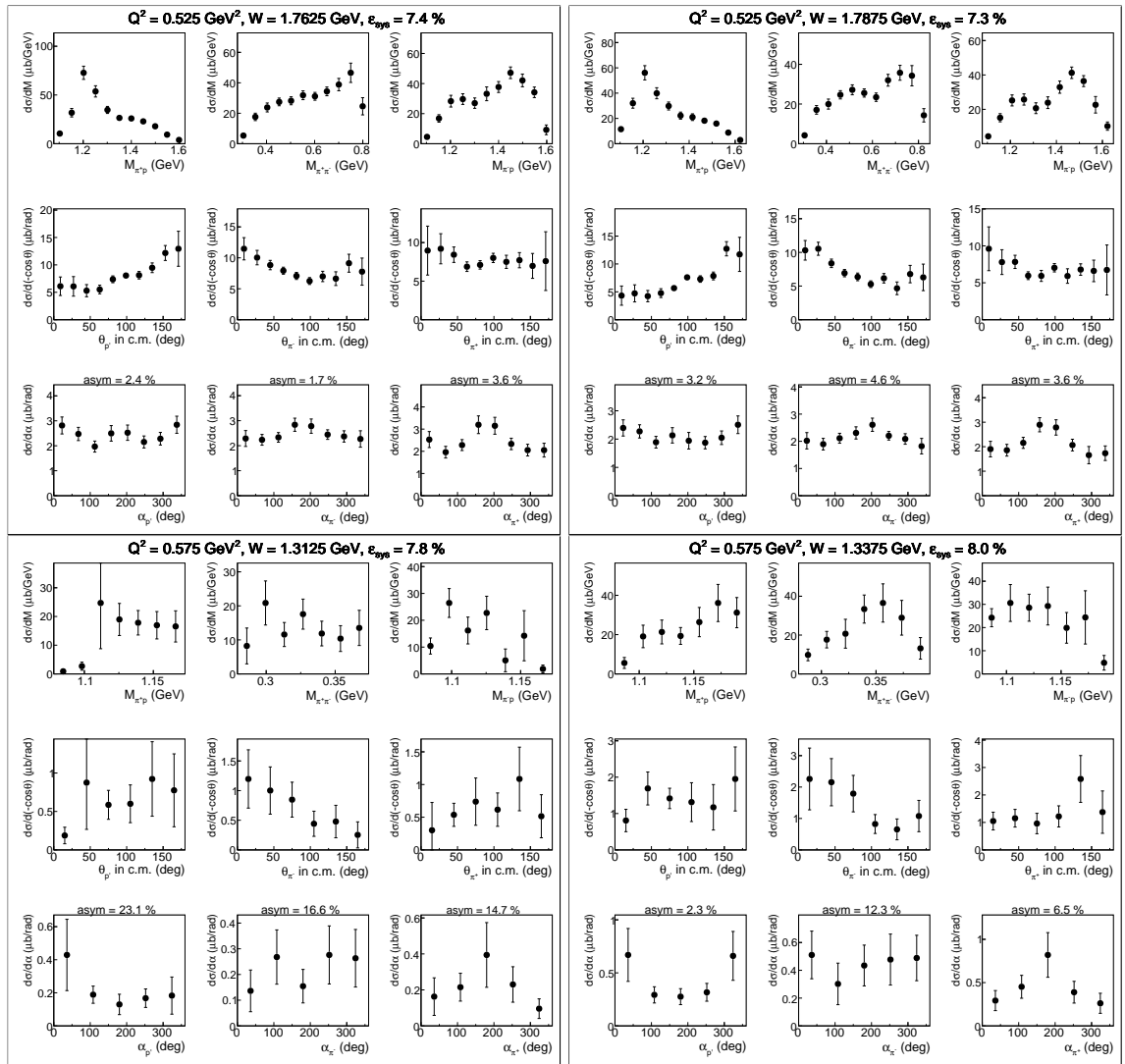


Figure A.21:

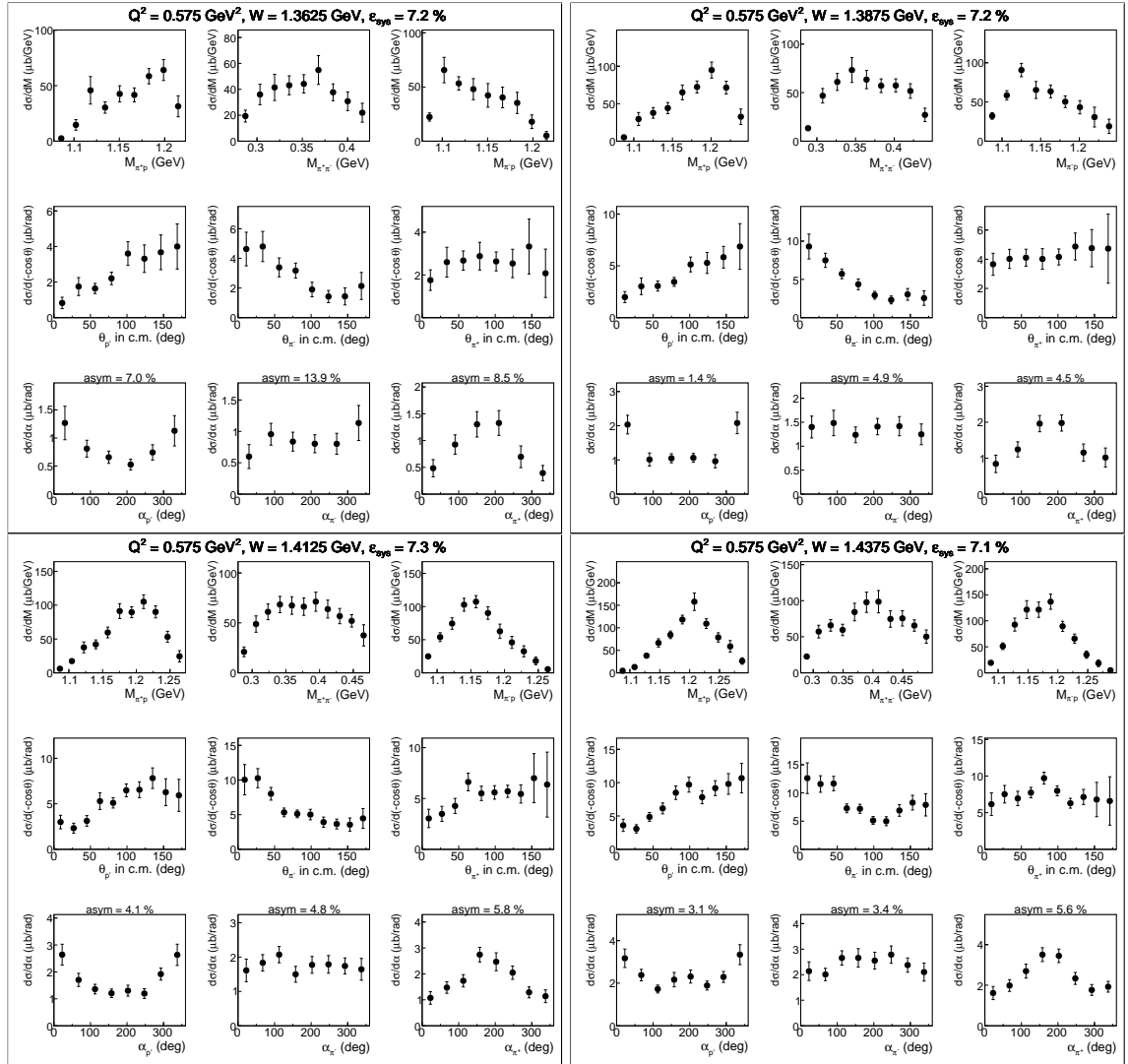


Figure A.22:

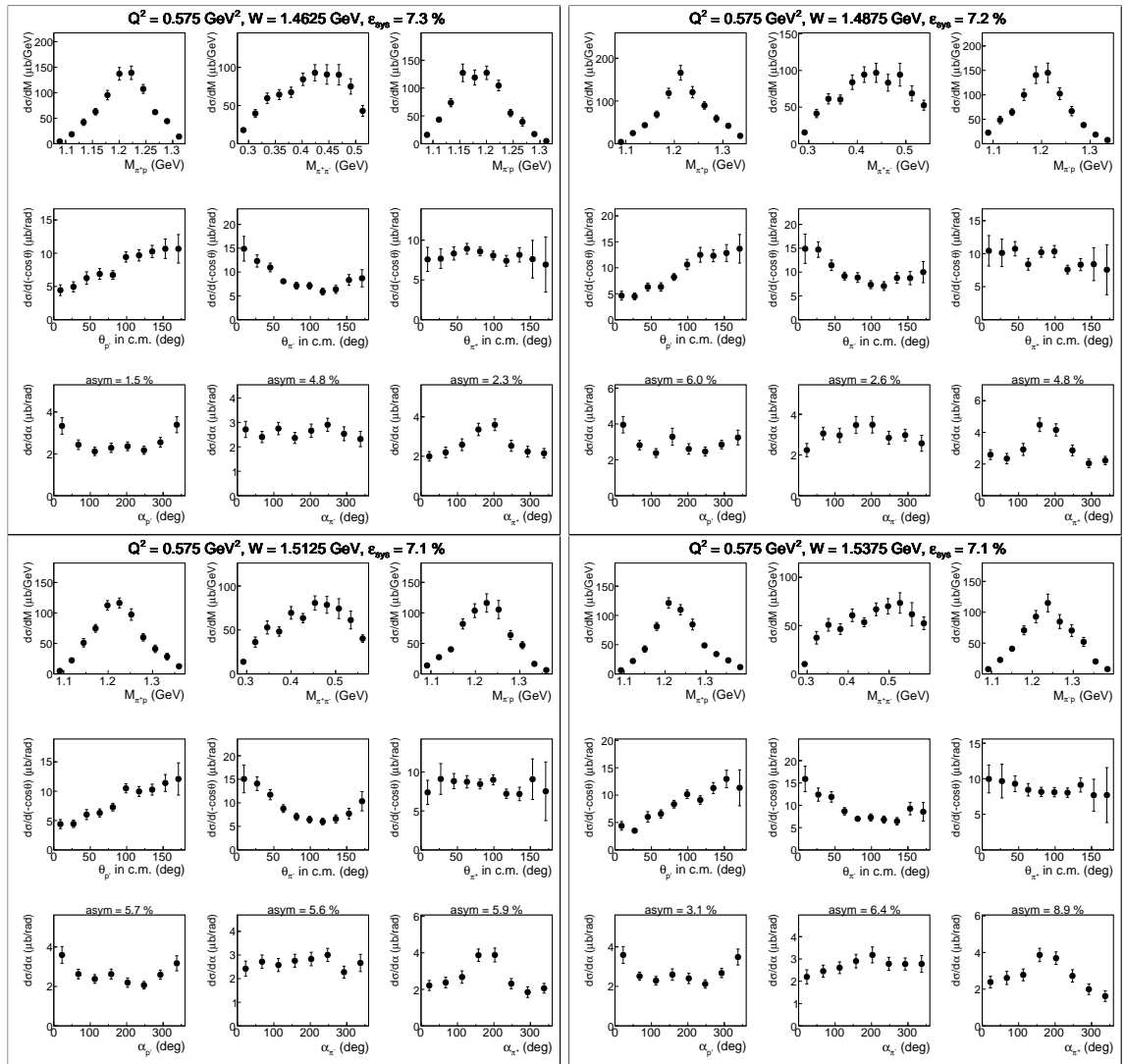


Figure A.23:

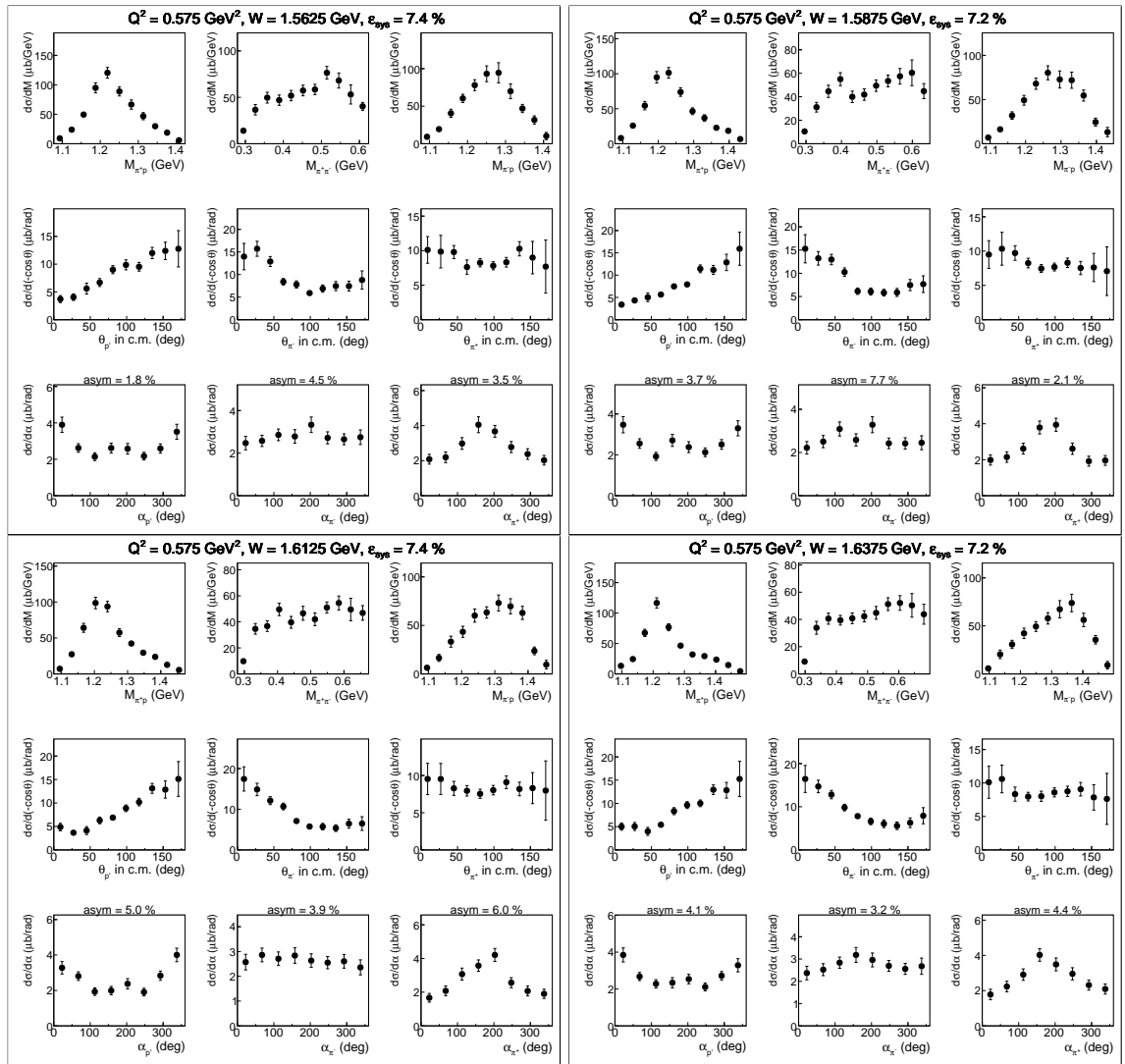


Figure A.24:

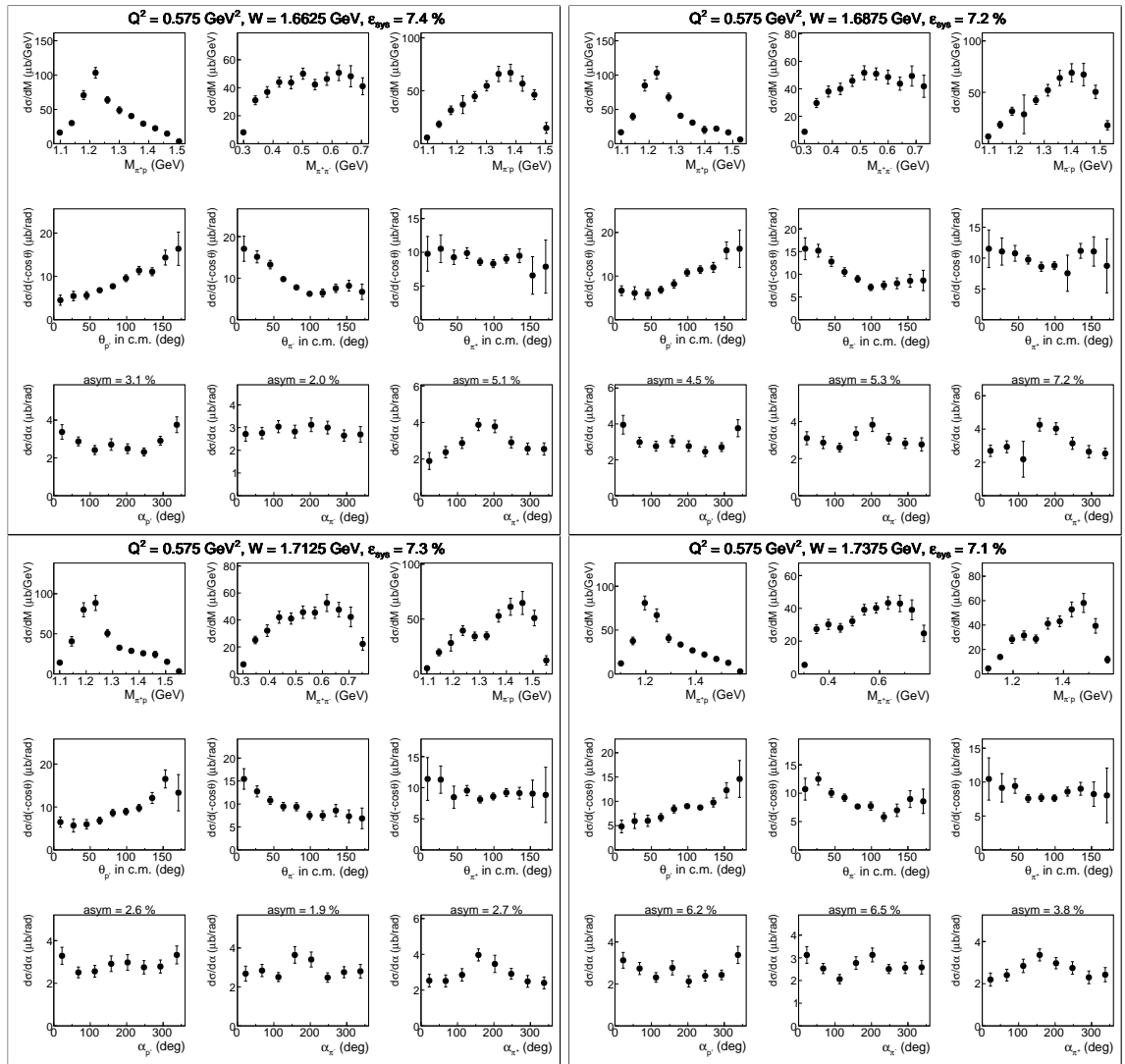


Figure A.25:

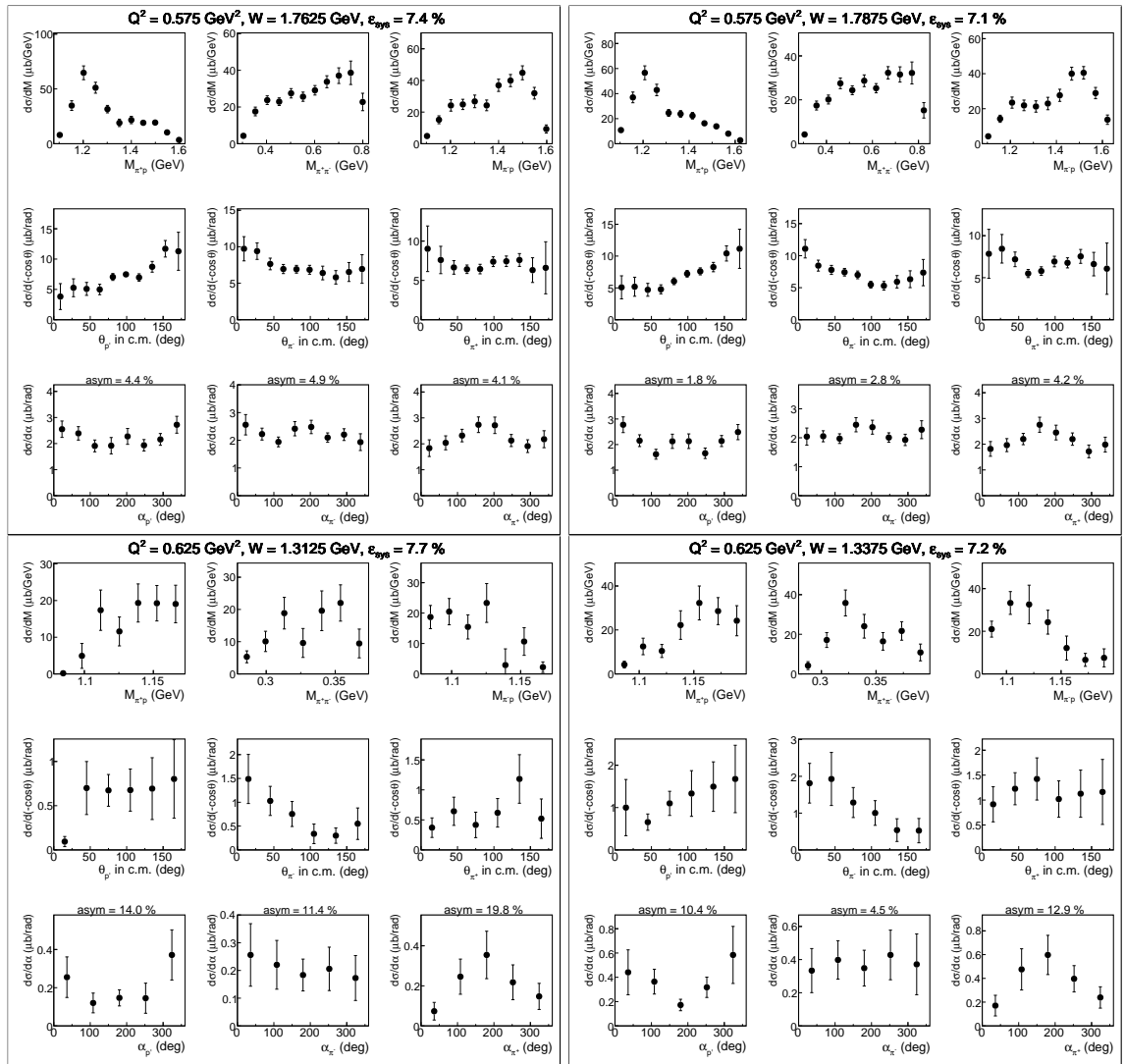


Figure A.26:

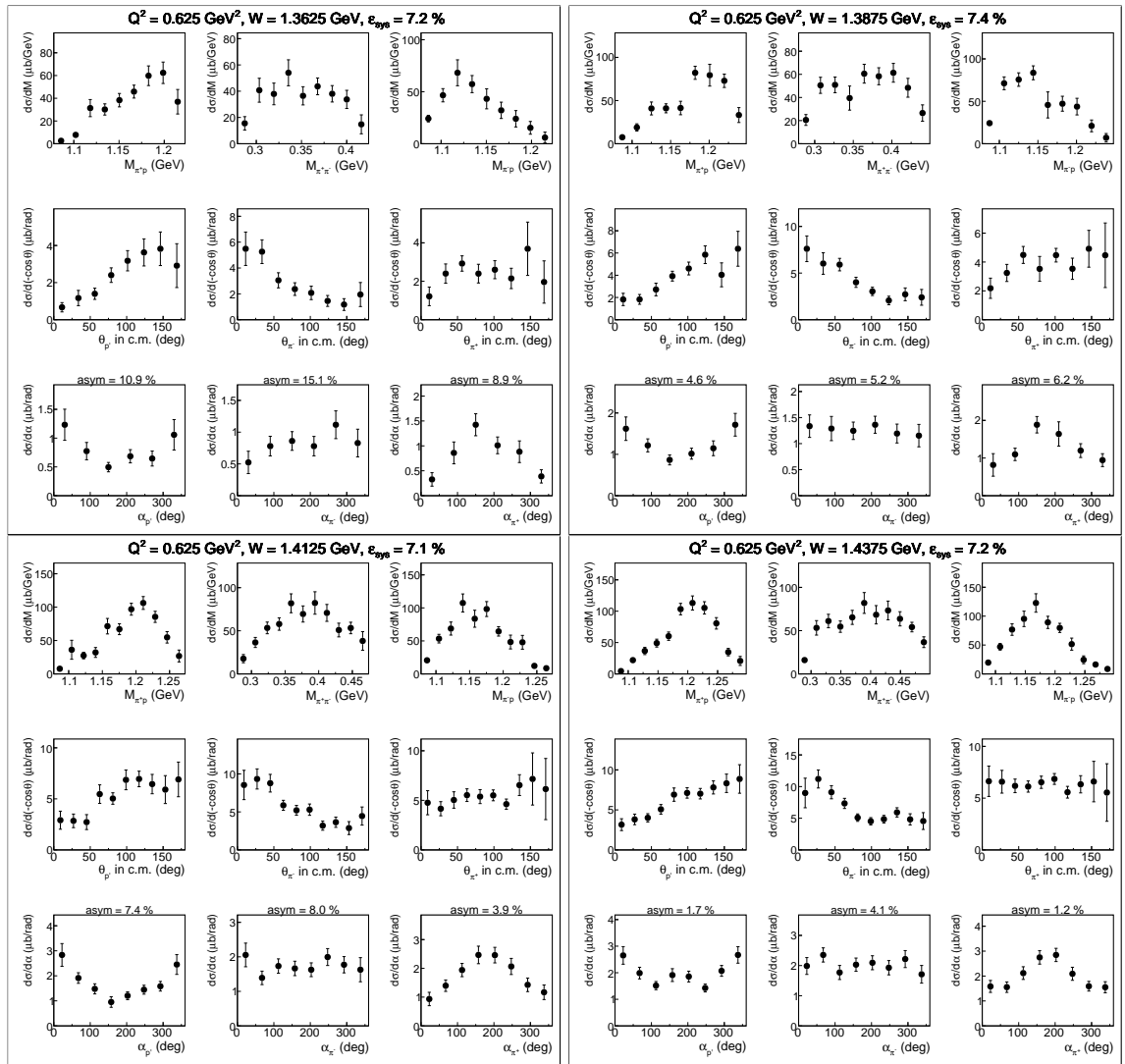


Figure A.27:

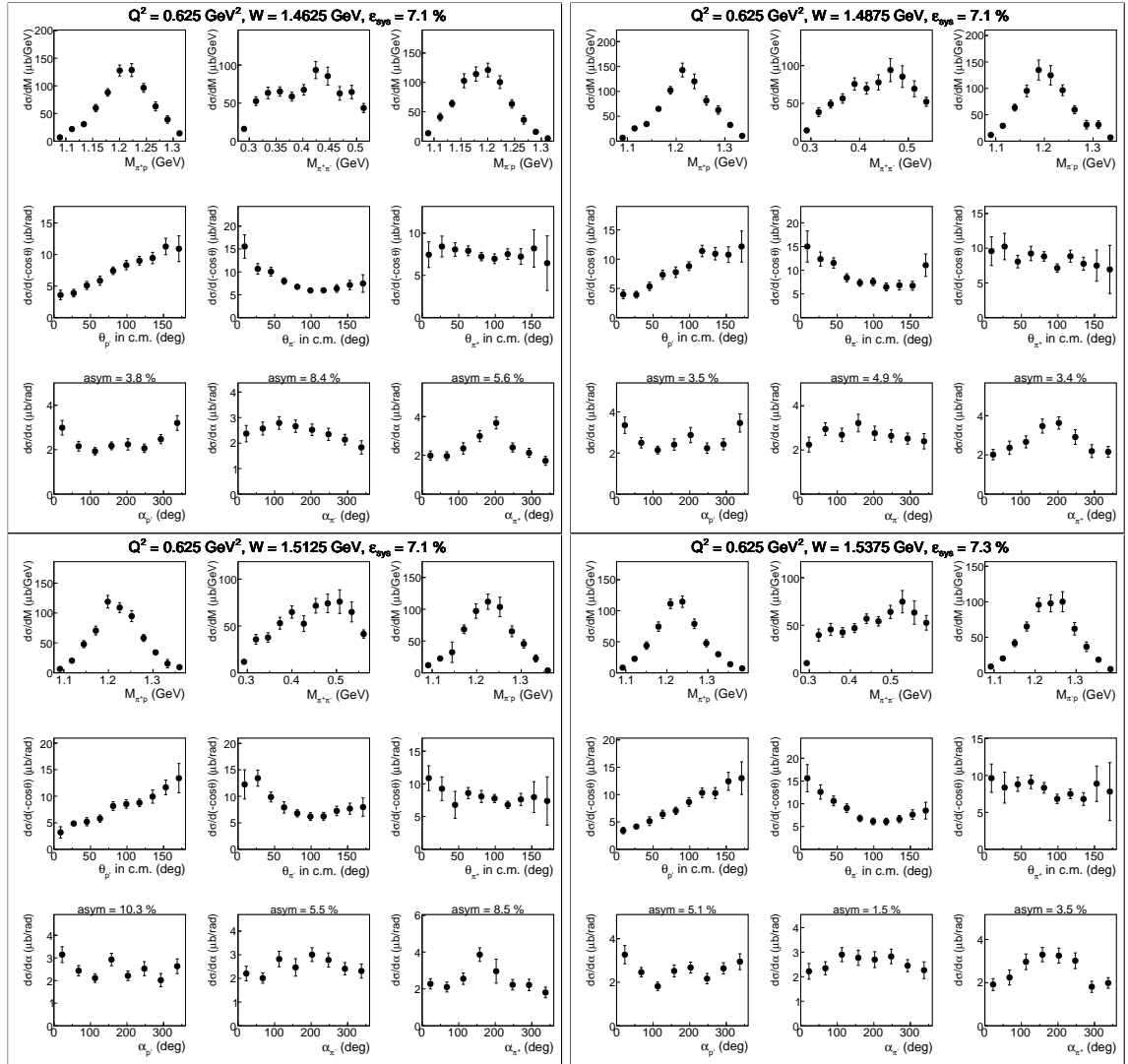


Figure A.28:

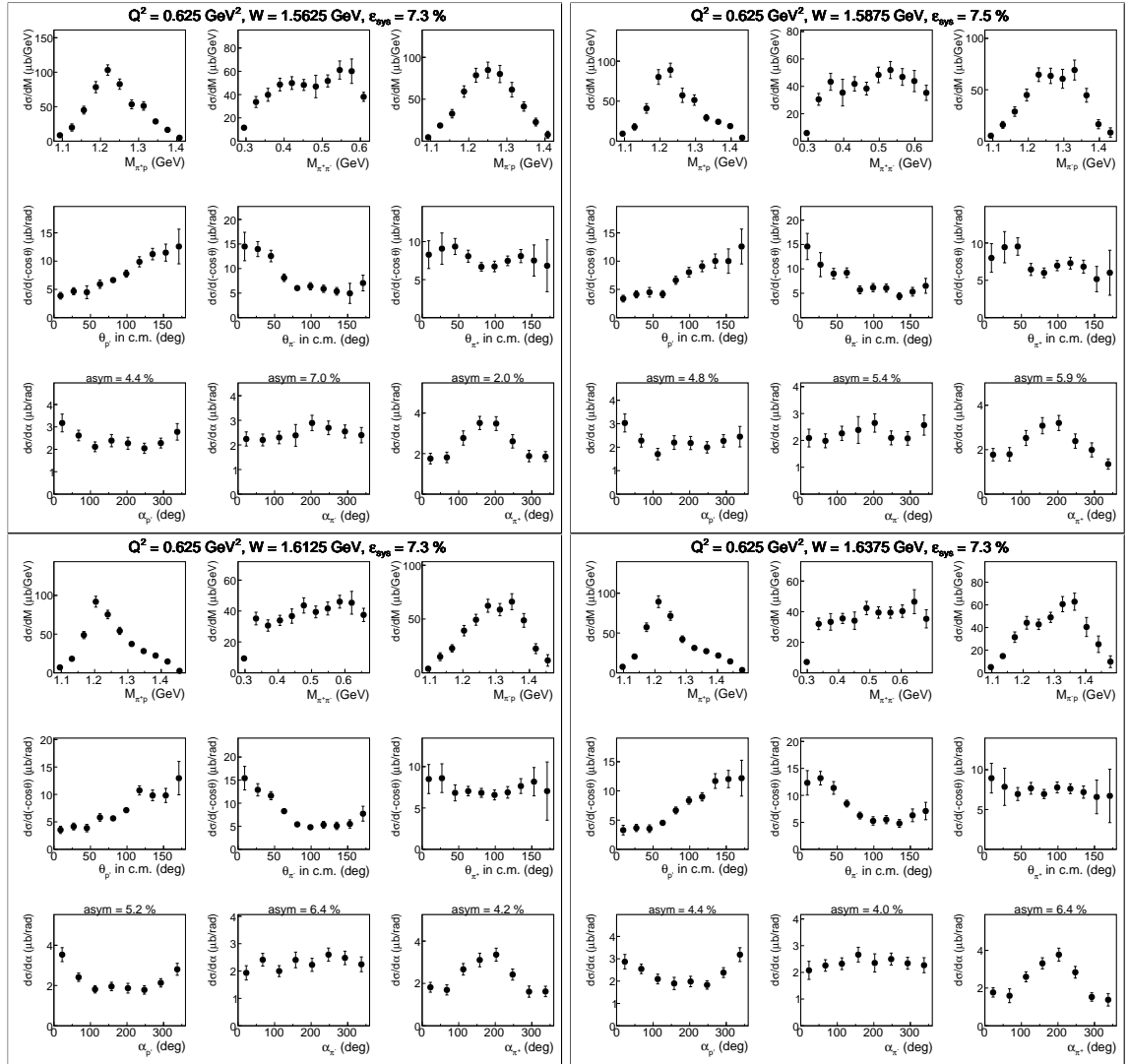


Figure A.29:

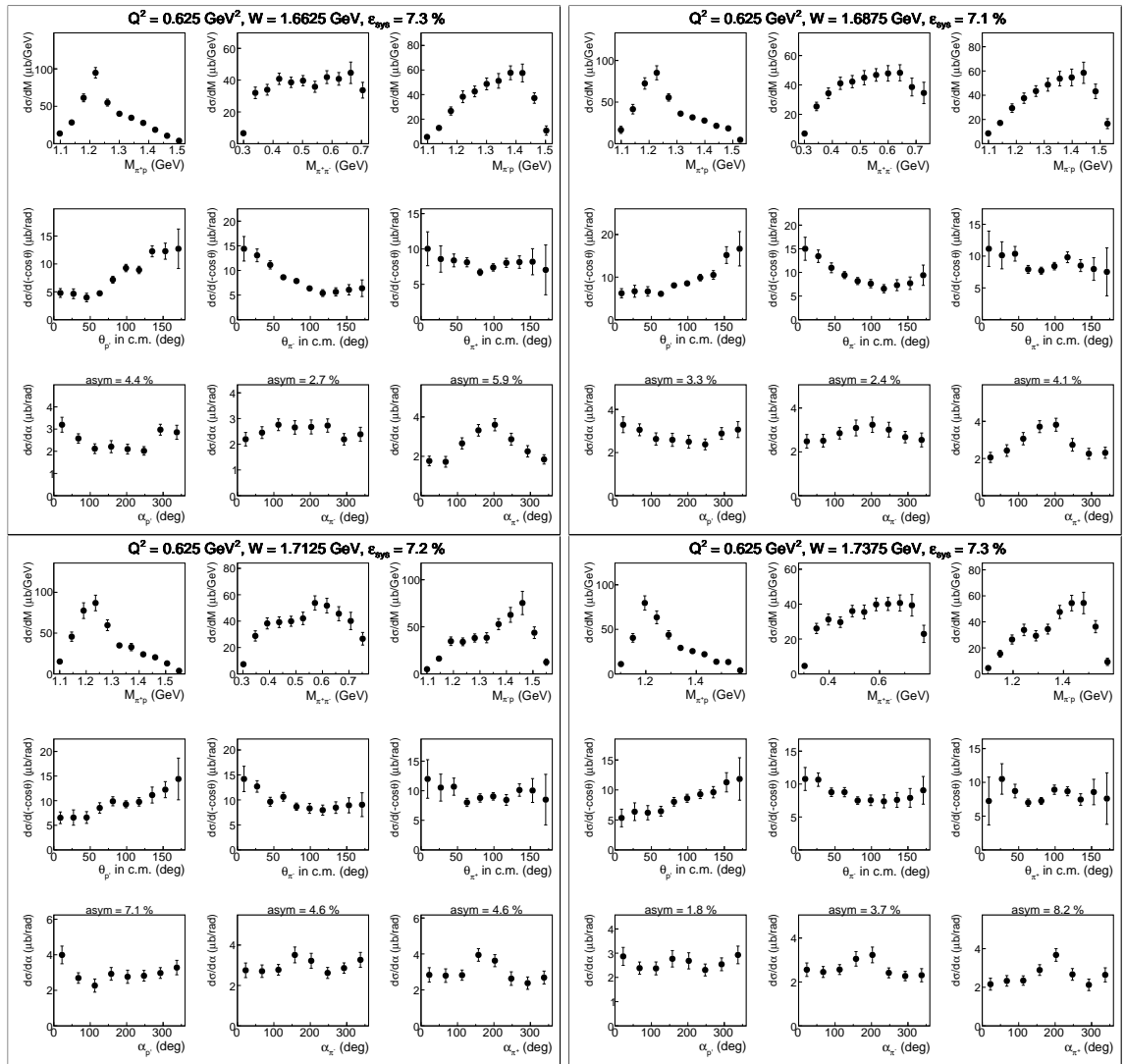


Figure A.30:

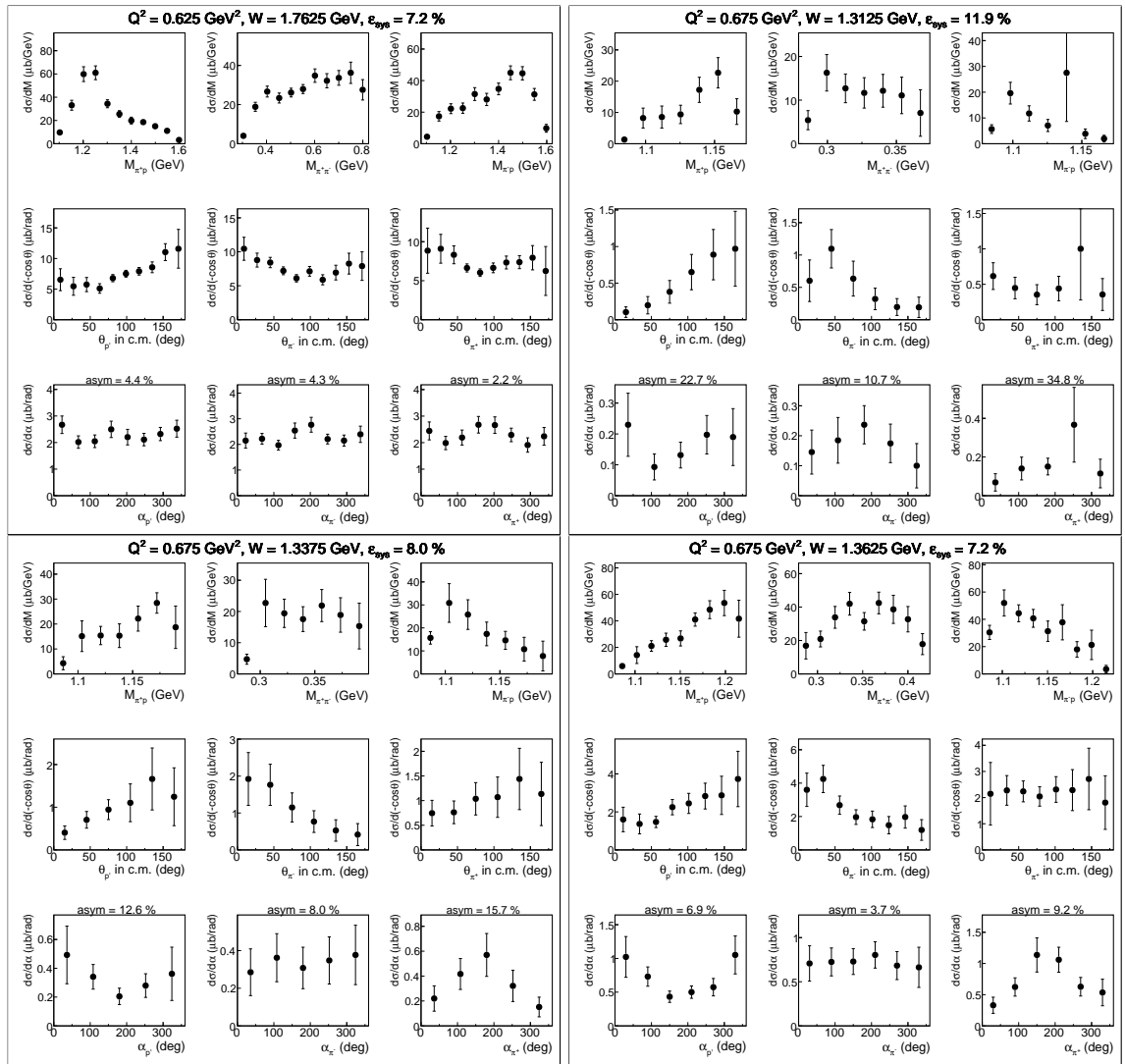


Figure A.31:

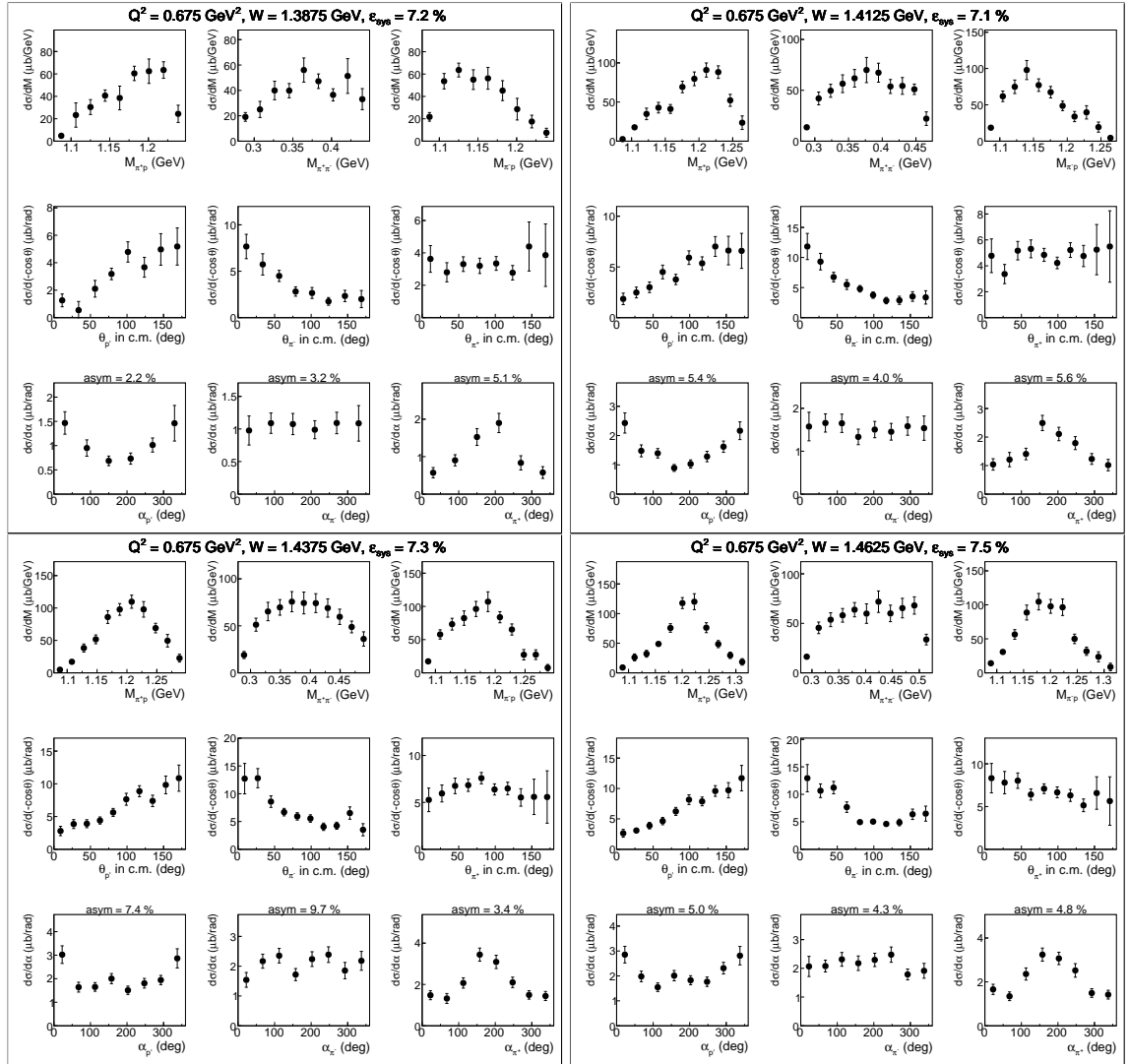


Figure A.32:

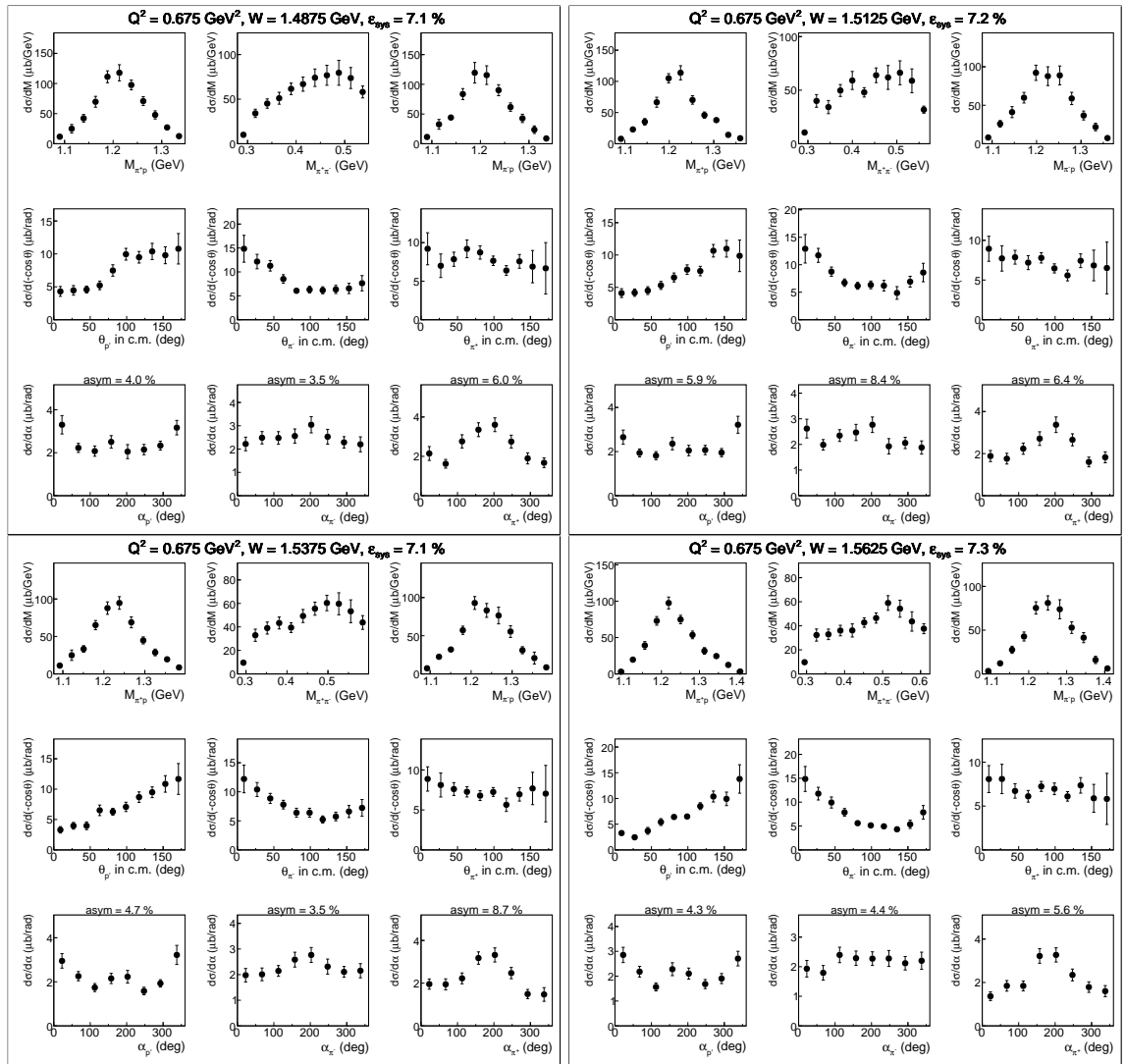


Figure A.33:

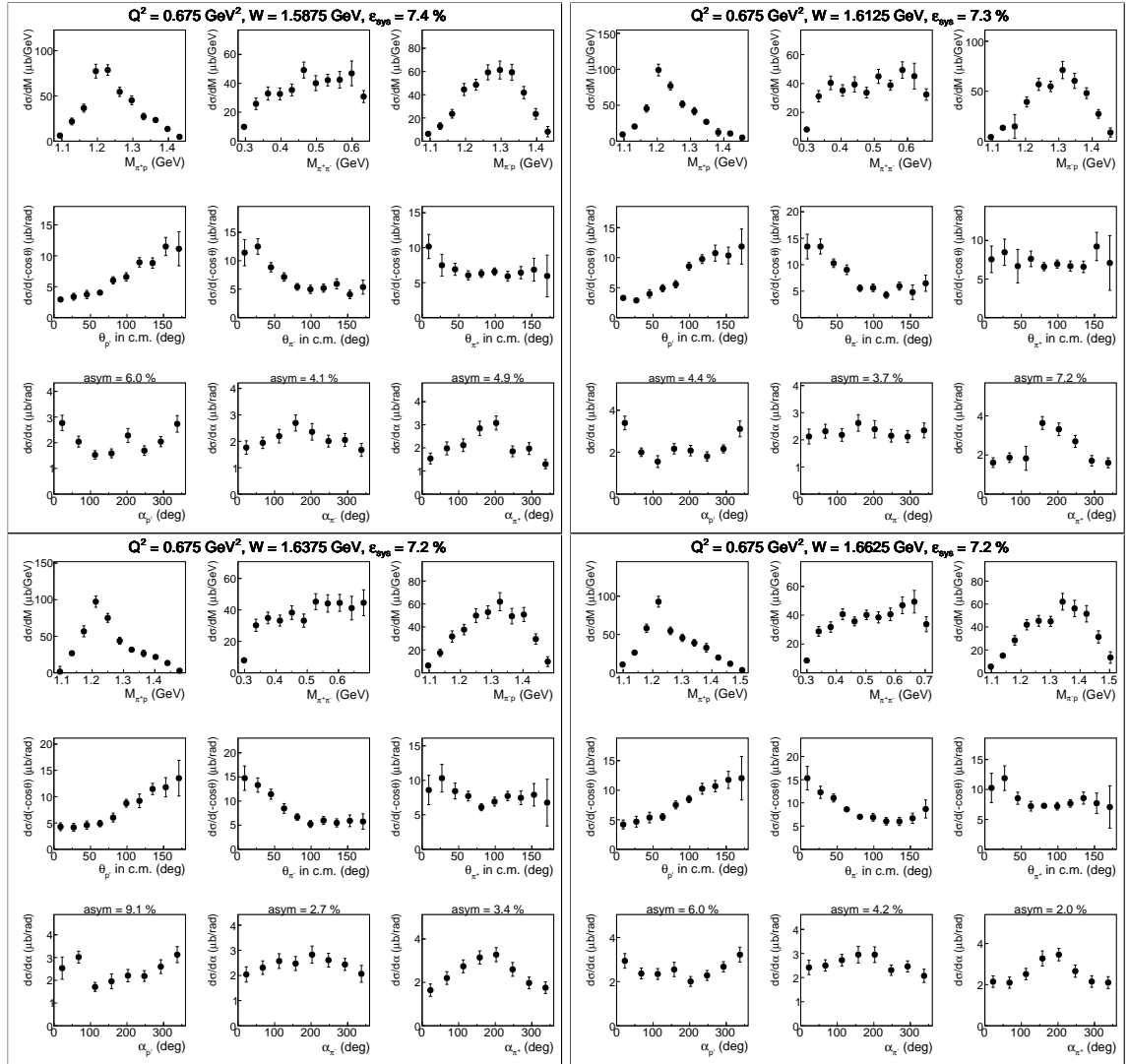


Figure A.34:

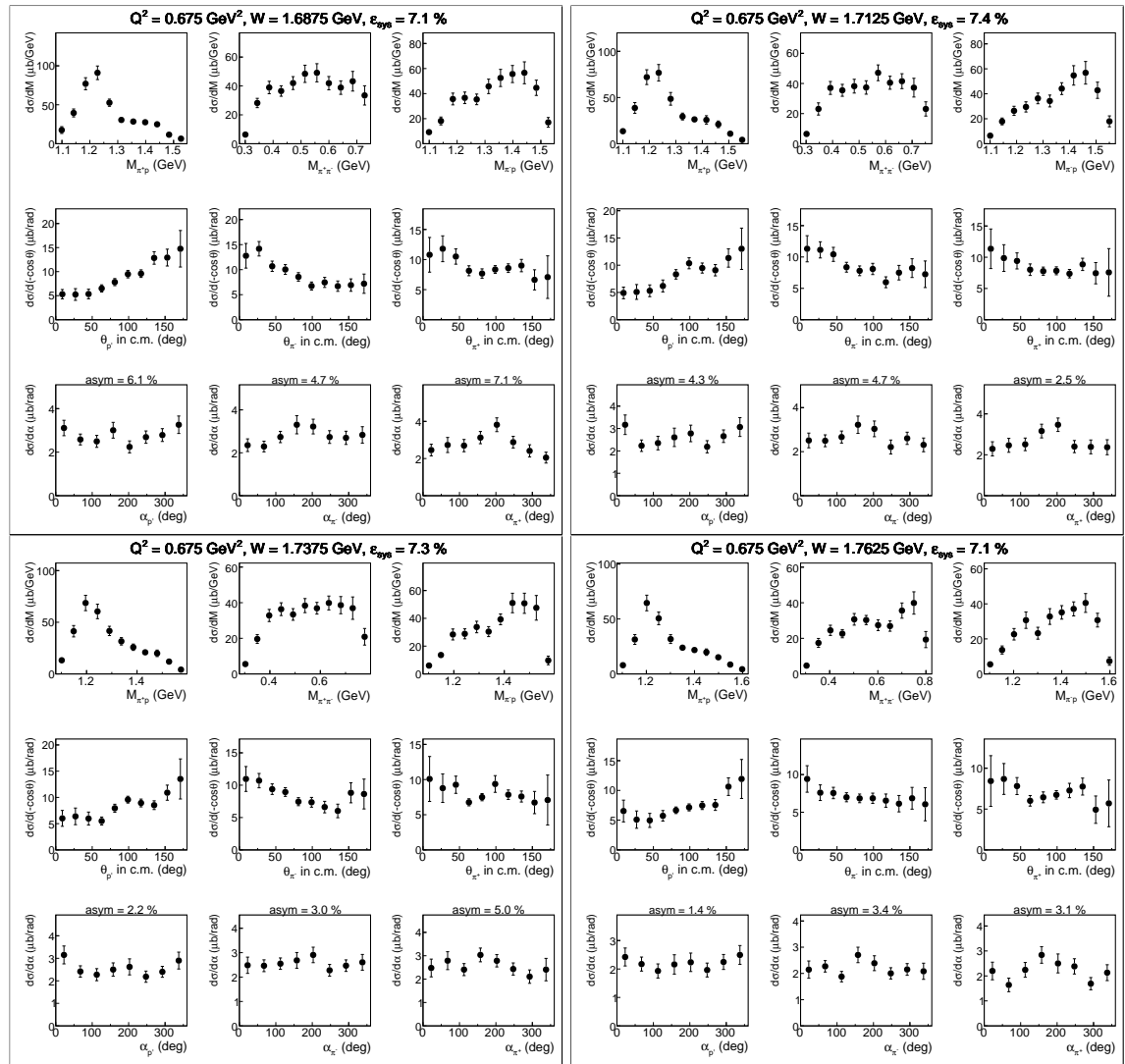


Figure A.35:

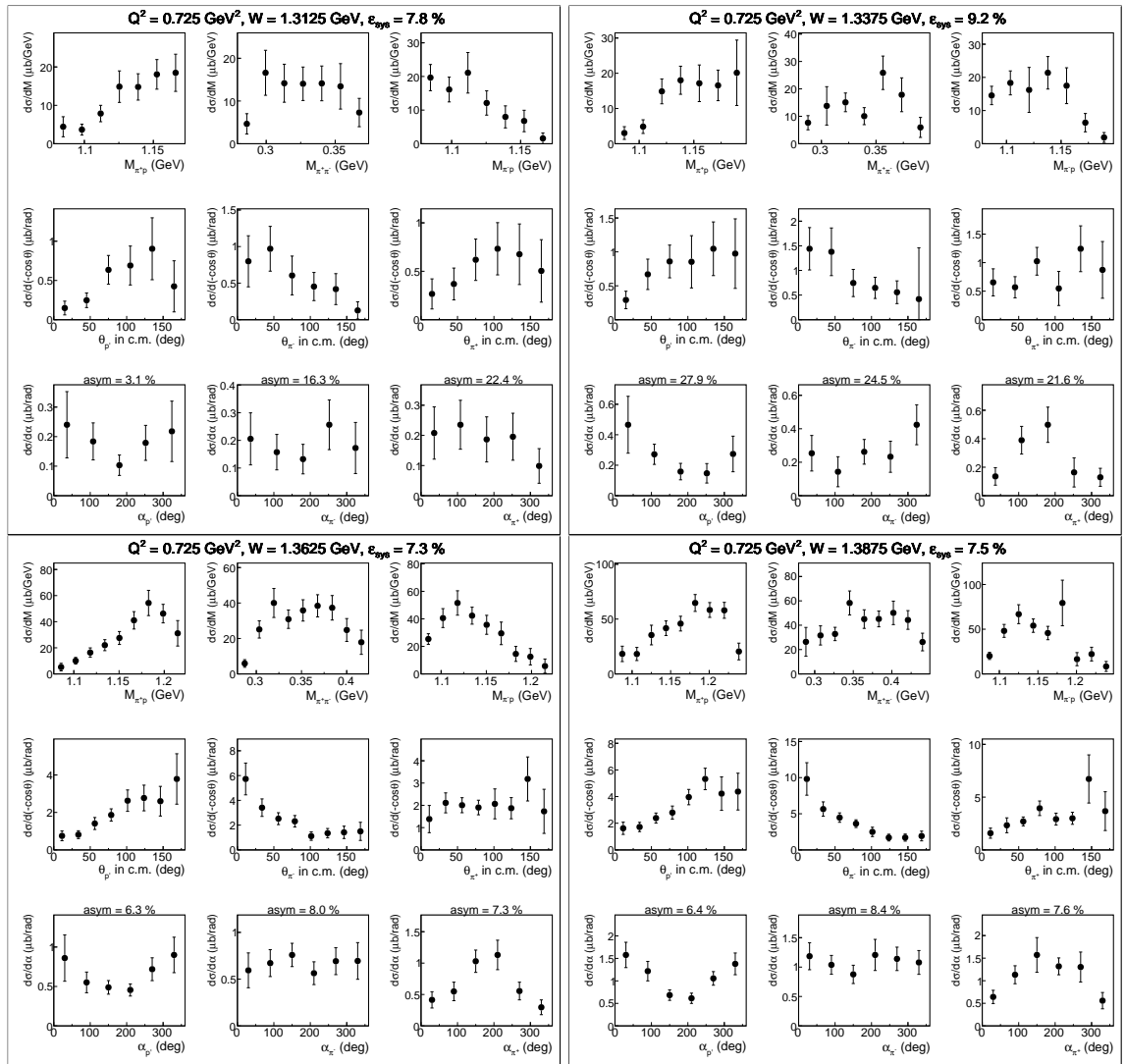


Figure A.36:

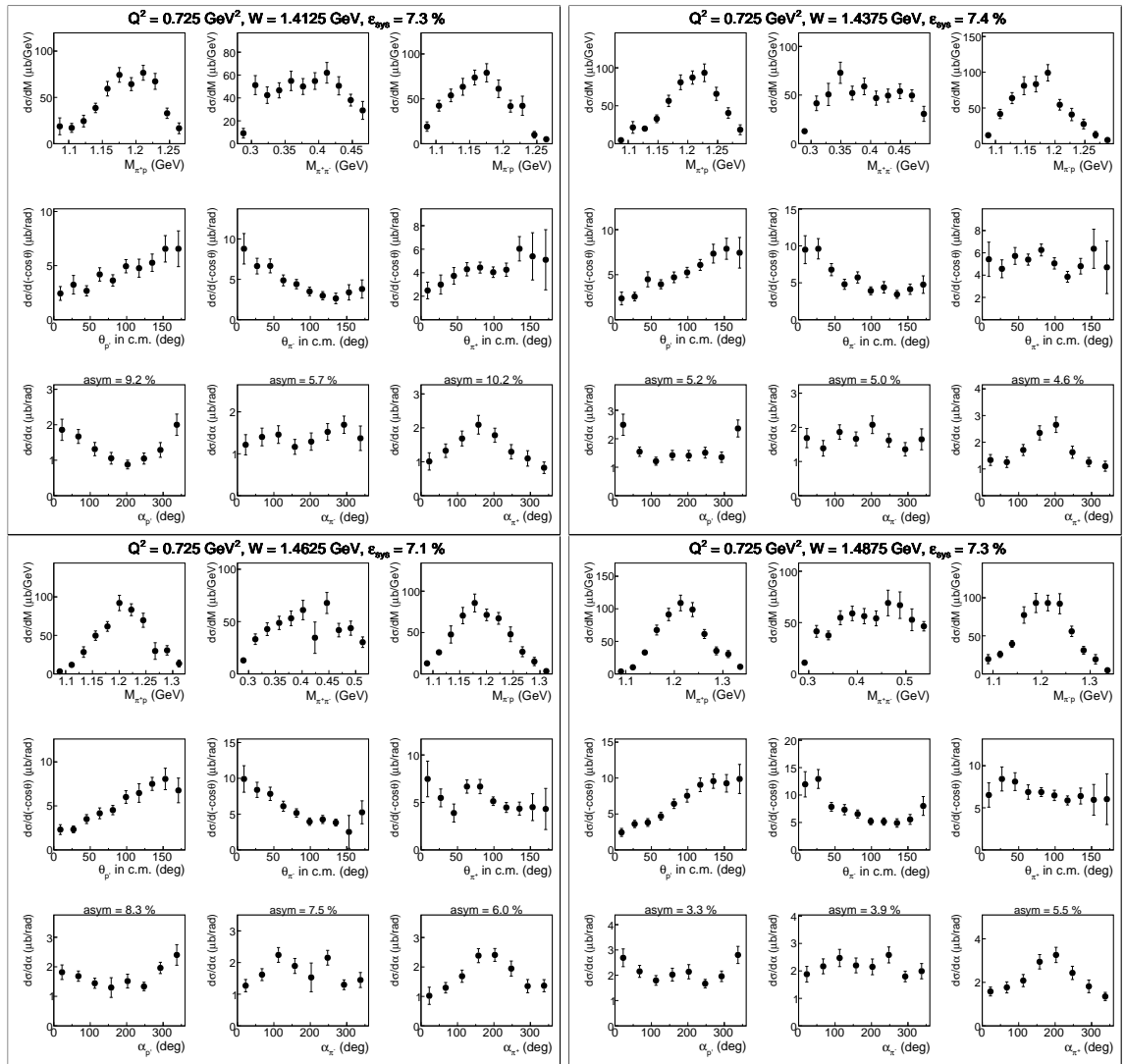


Figure A.37:

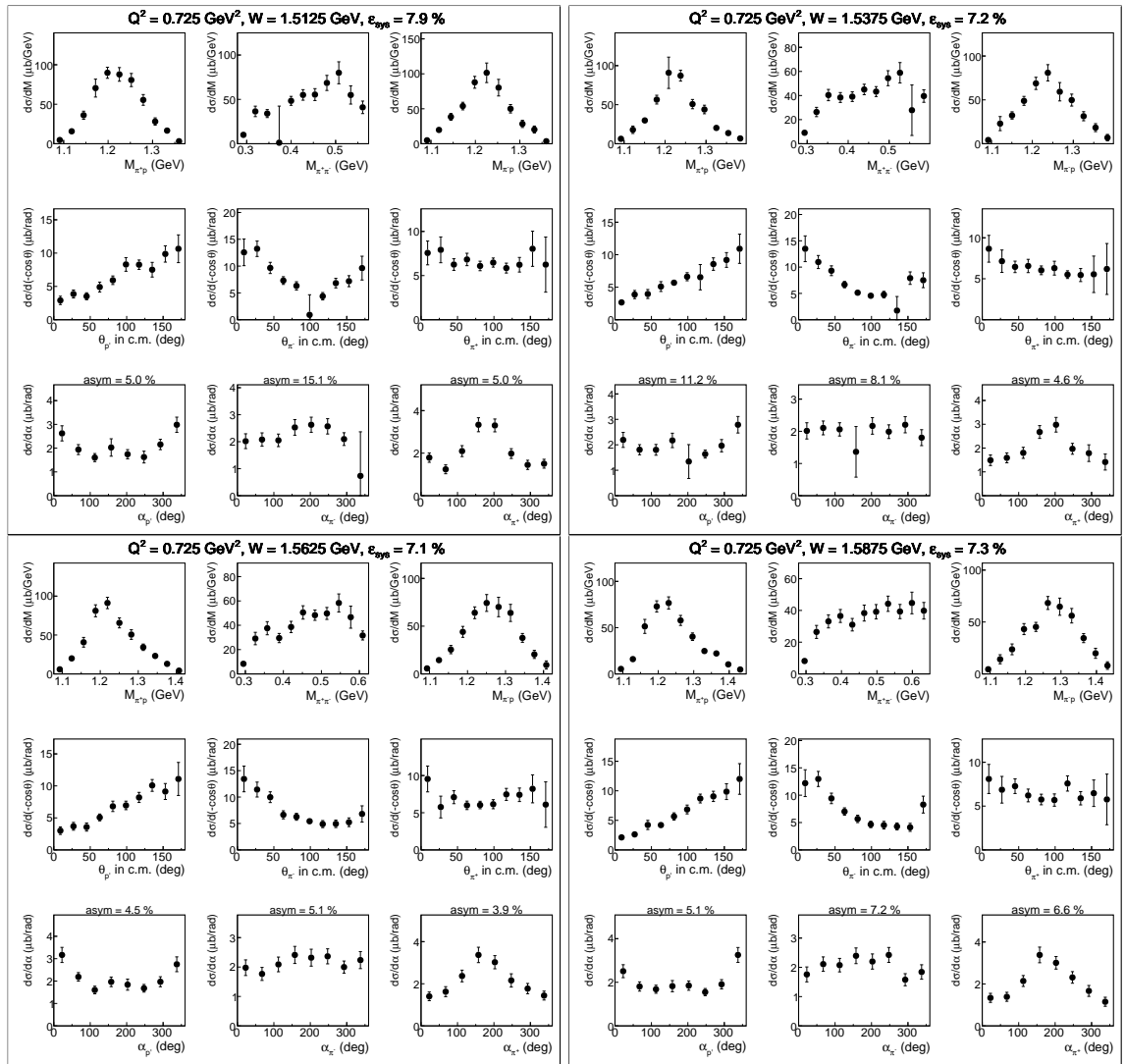


Figure A.38:

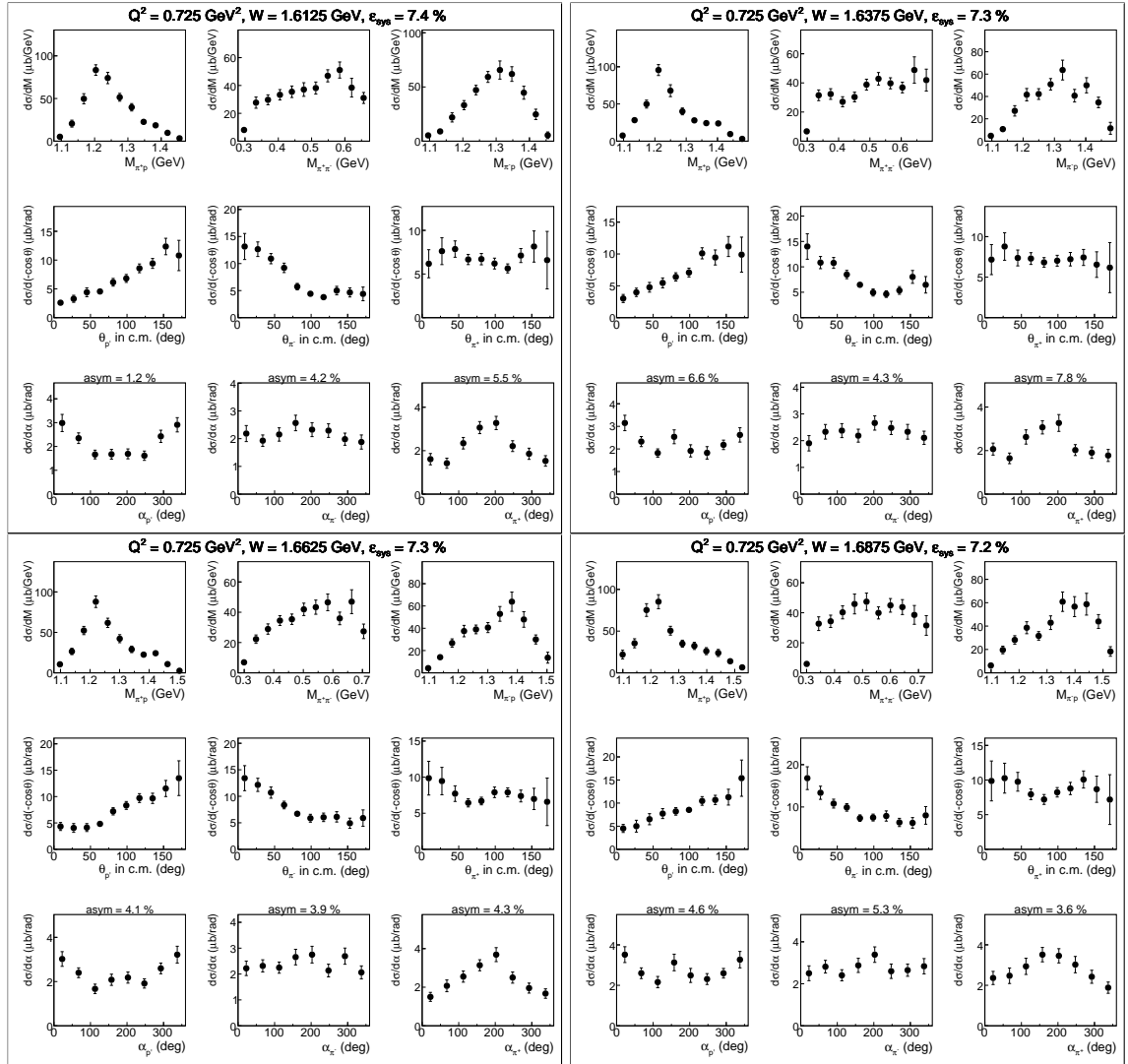


Figure A.39:

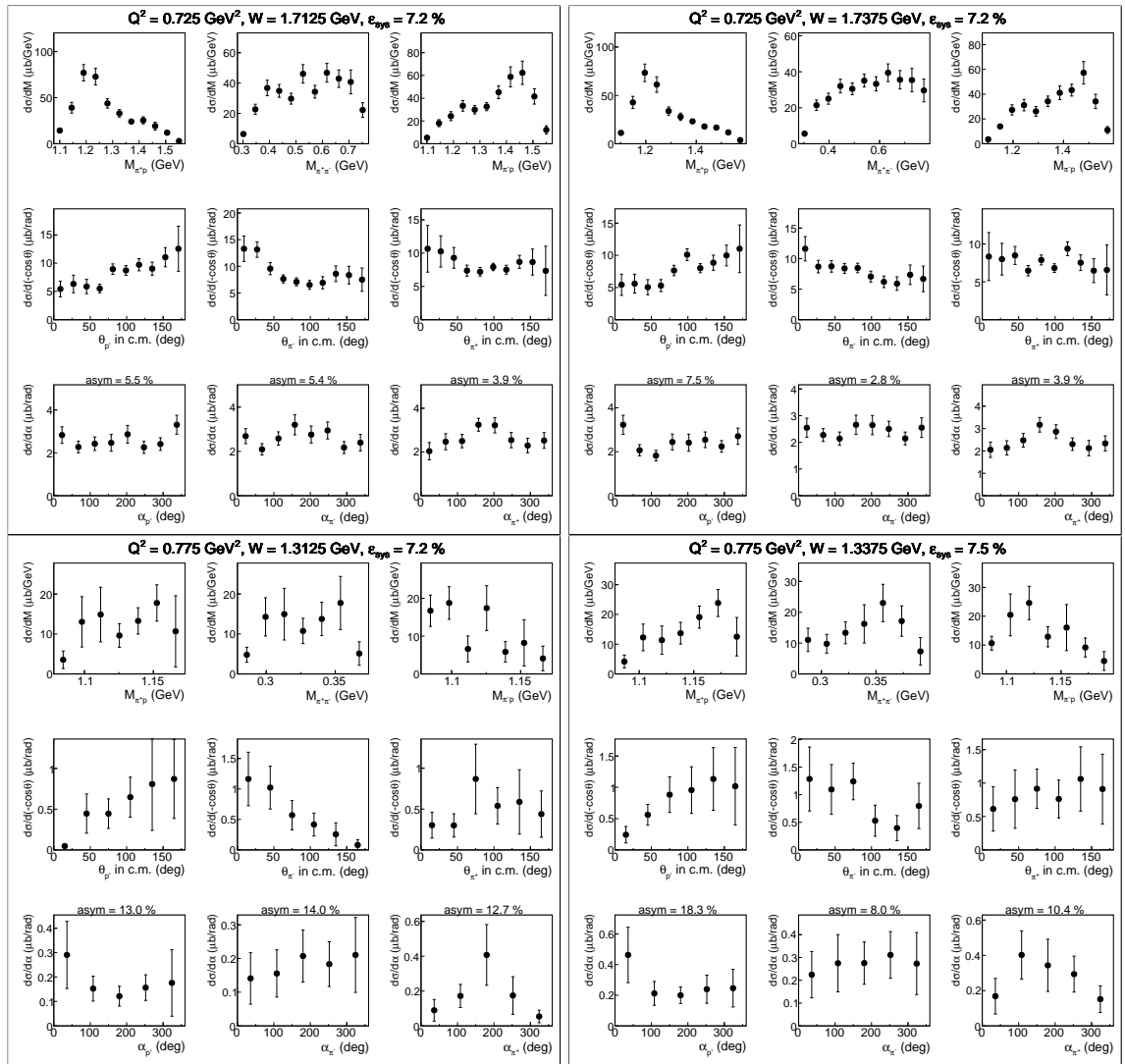


Figure A.40:

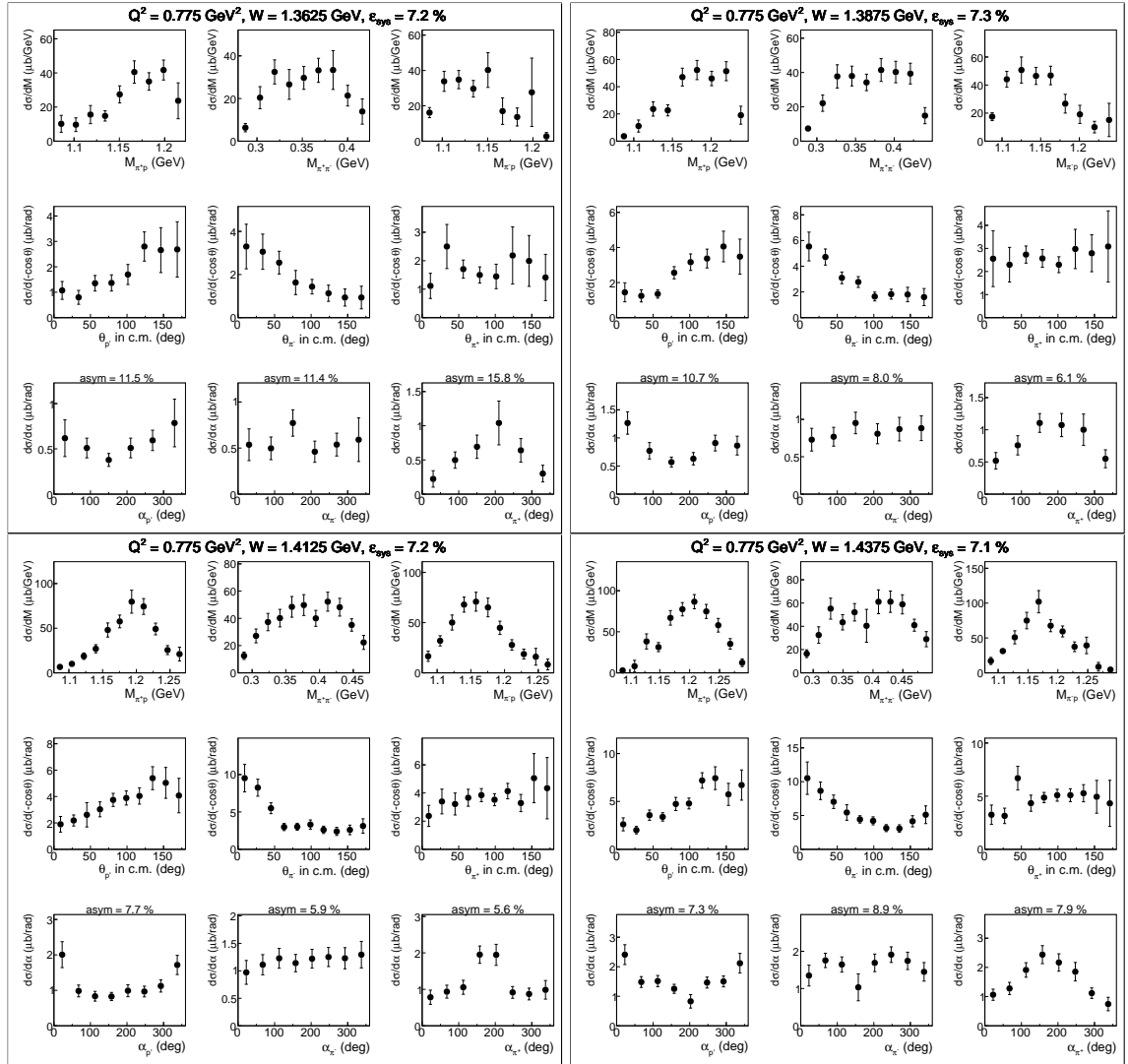


Figure A.41:

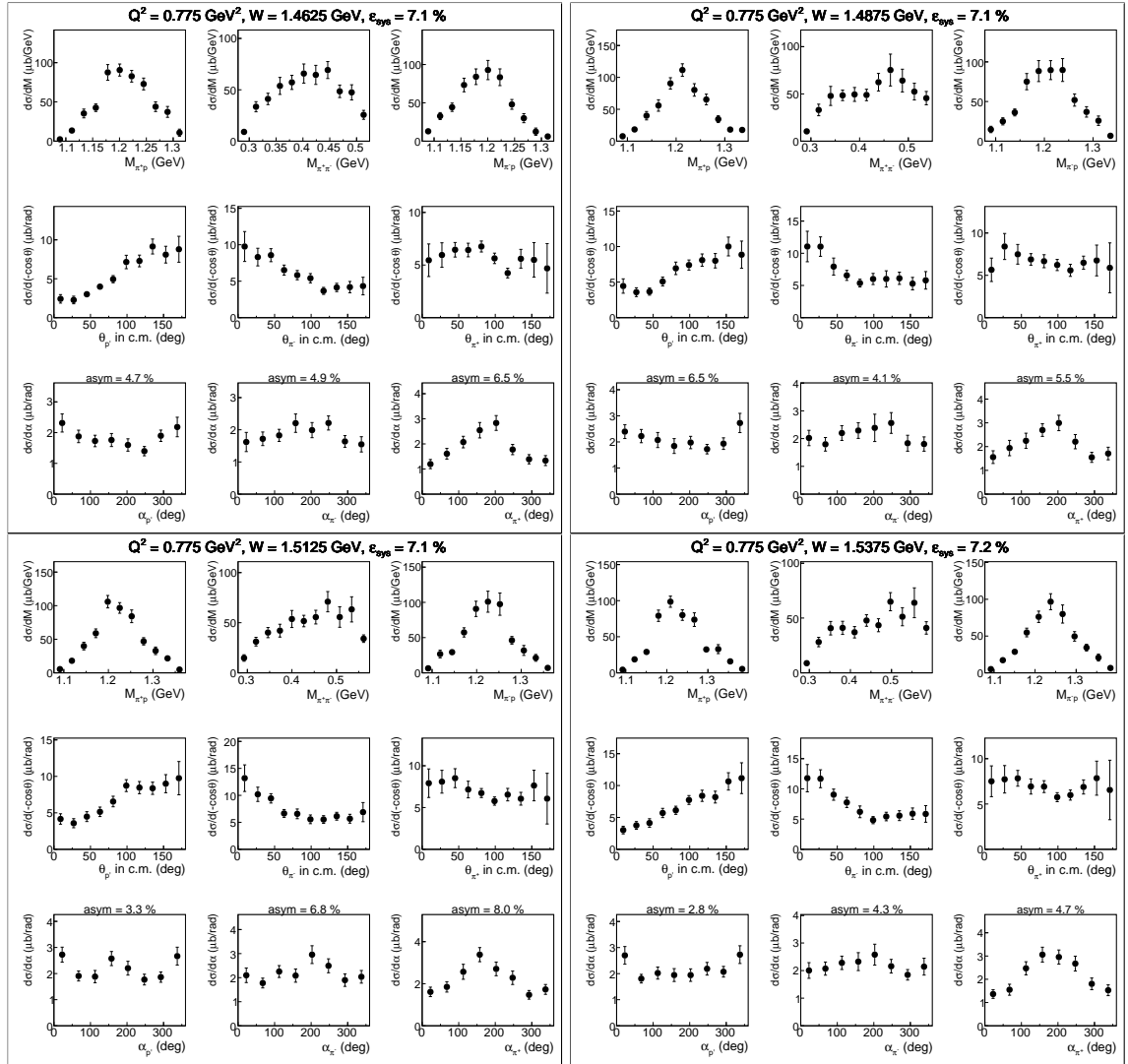


Figure A.42:

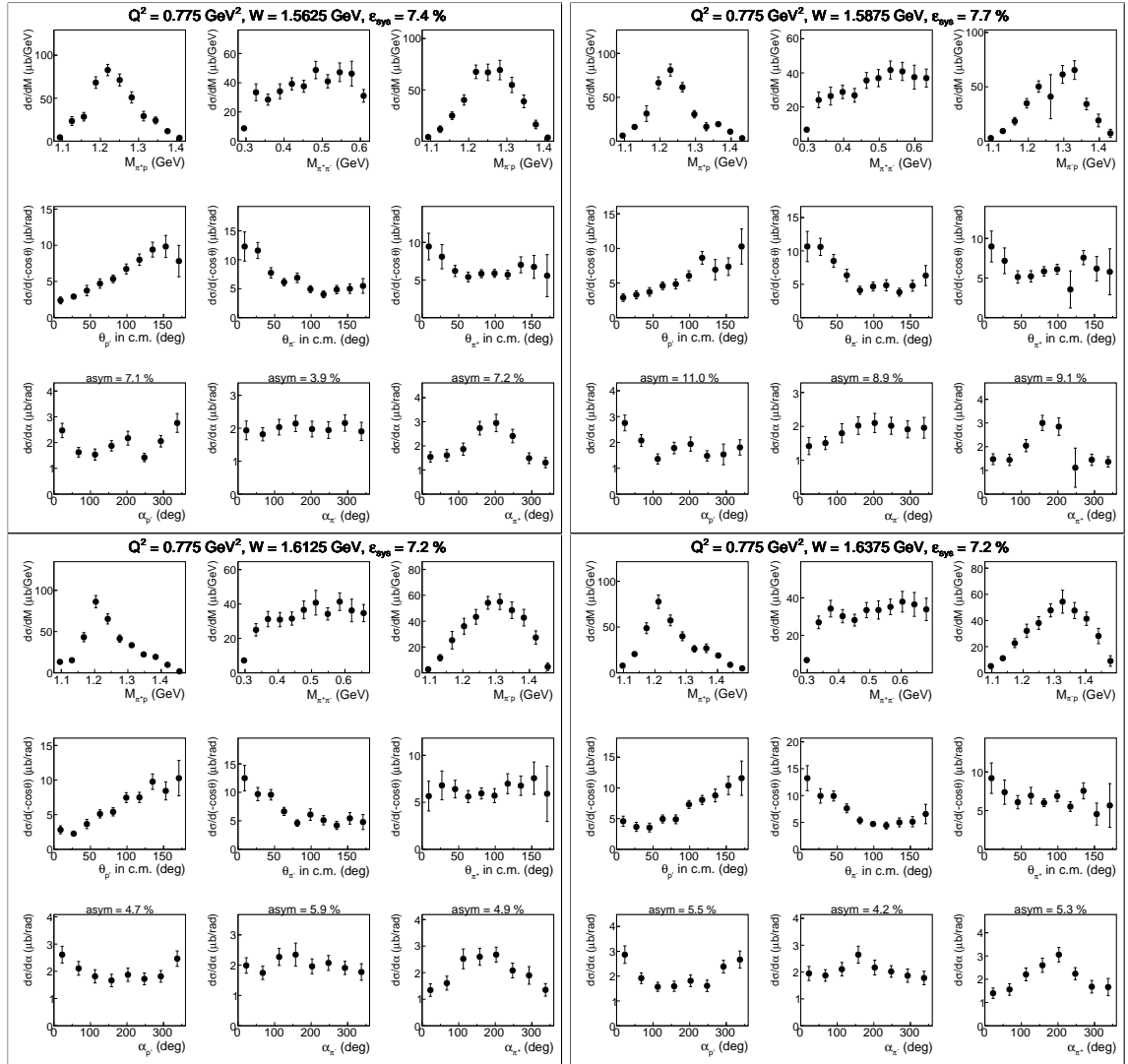


Figure A.43:

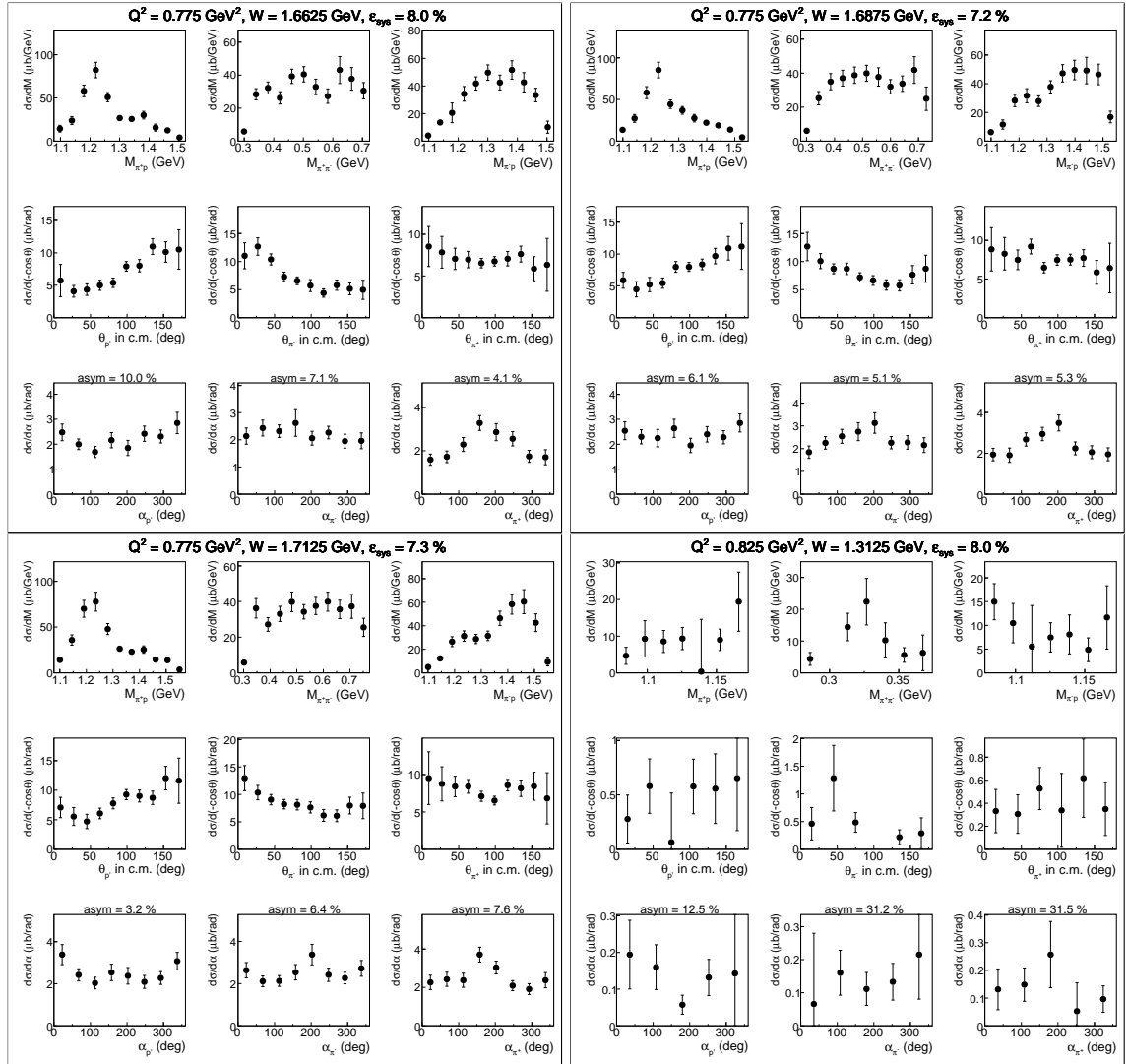


Figure A.44:

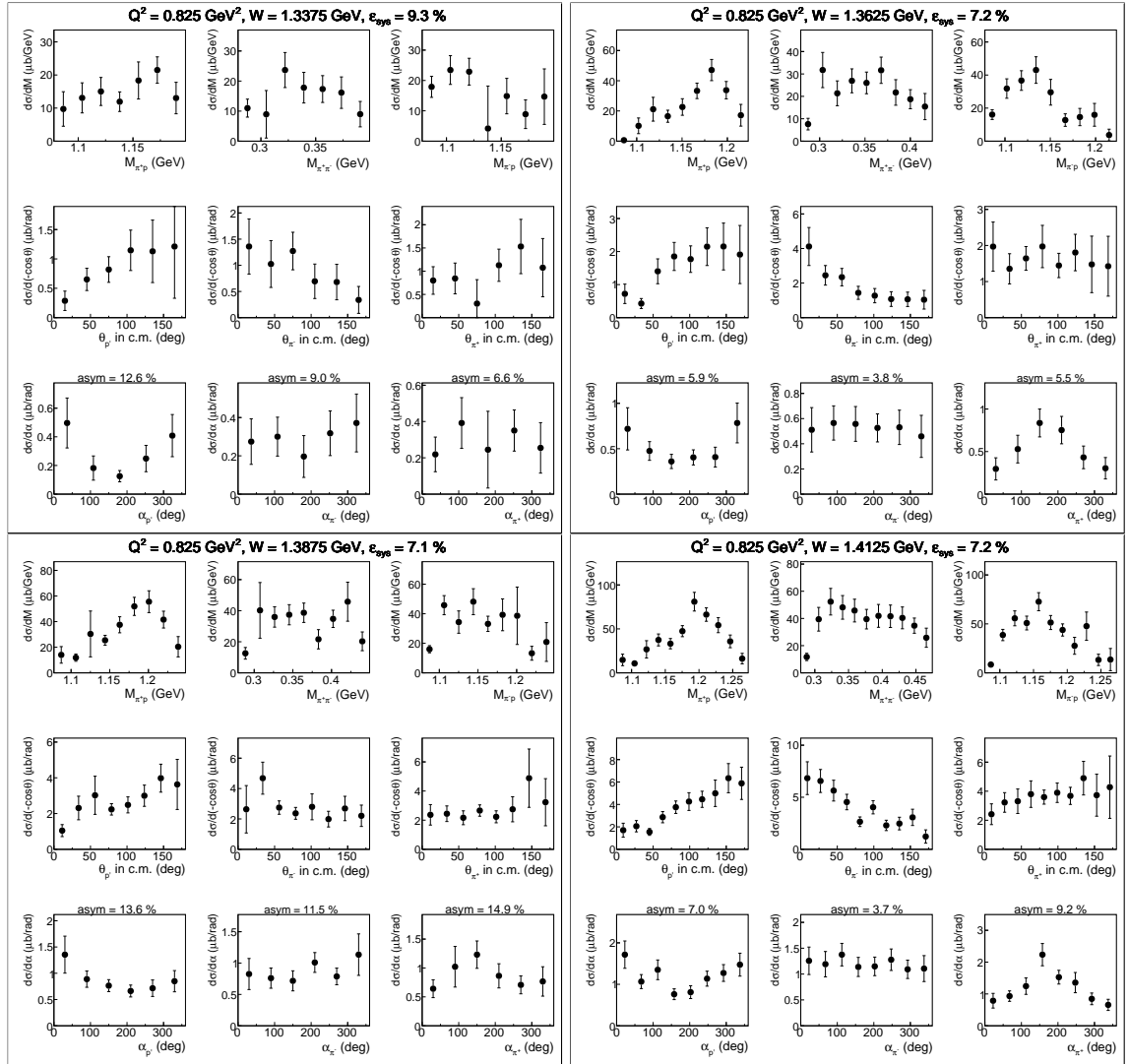


Figure A.45:

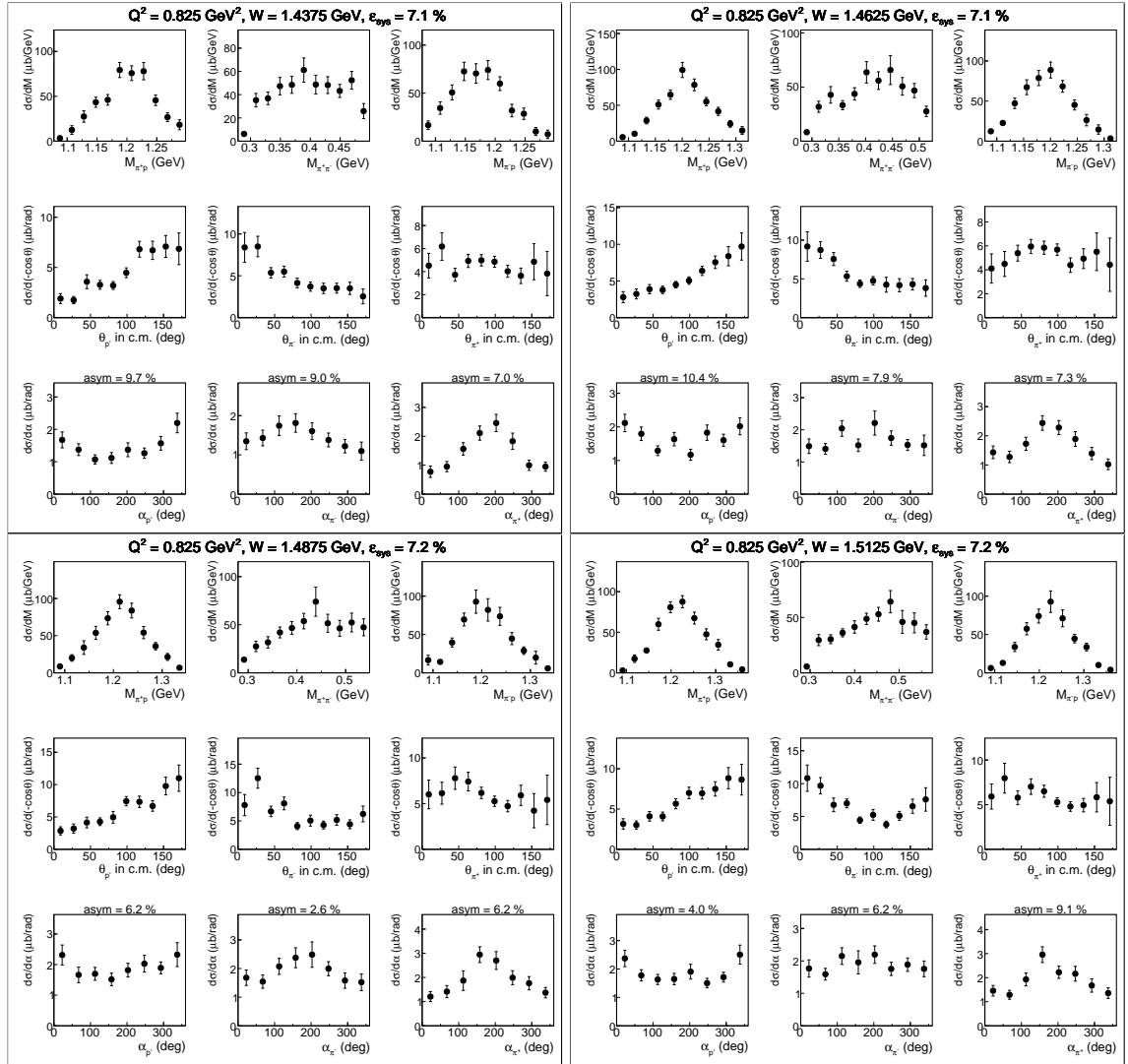


Figure A.46:

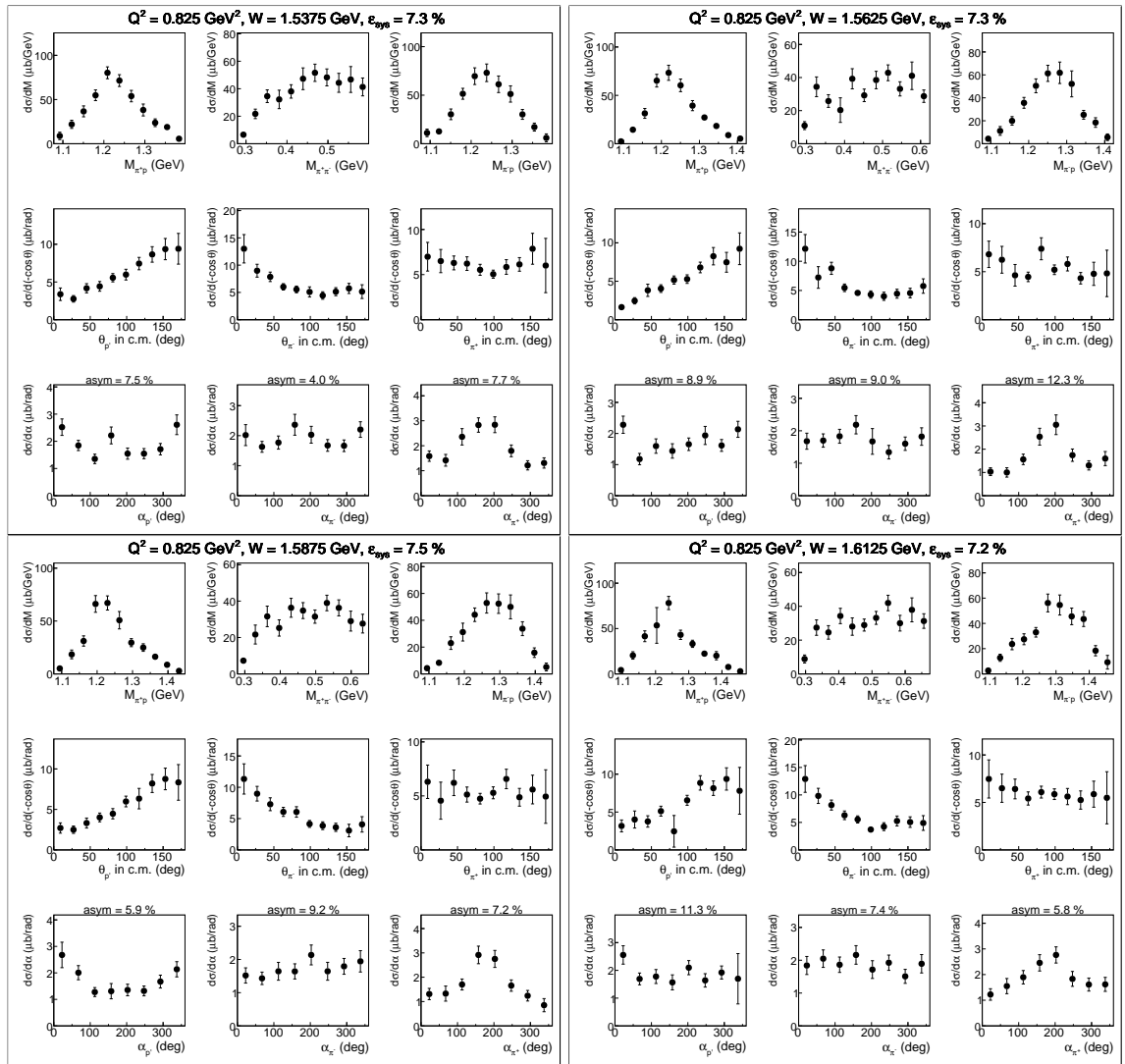


Figure A.47:

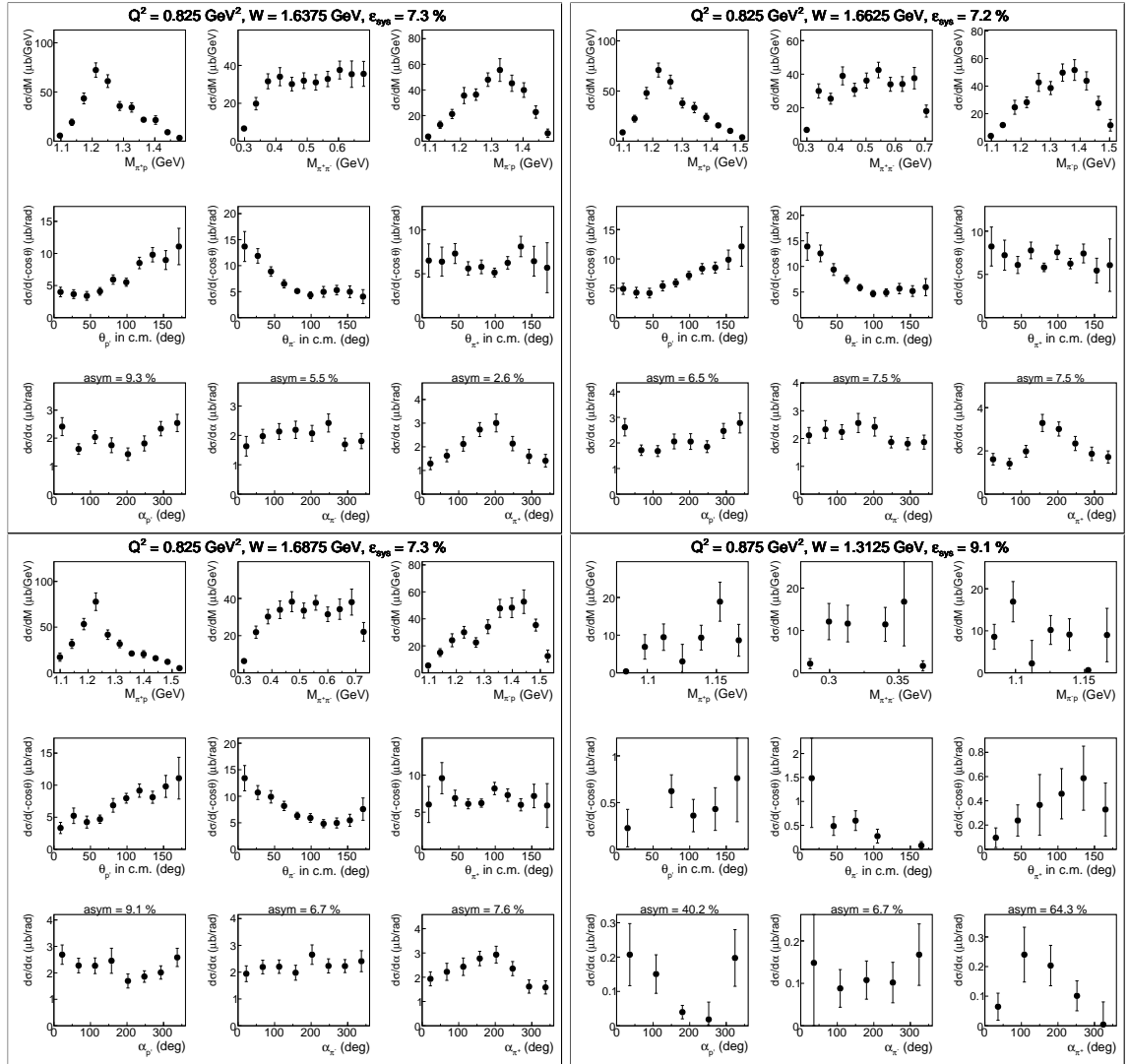


Figure A.48:

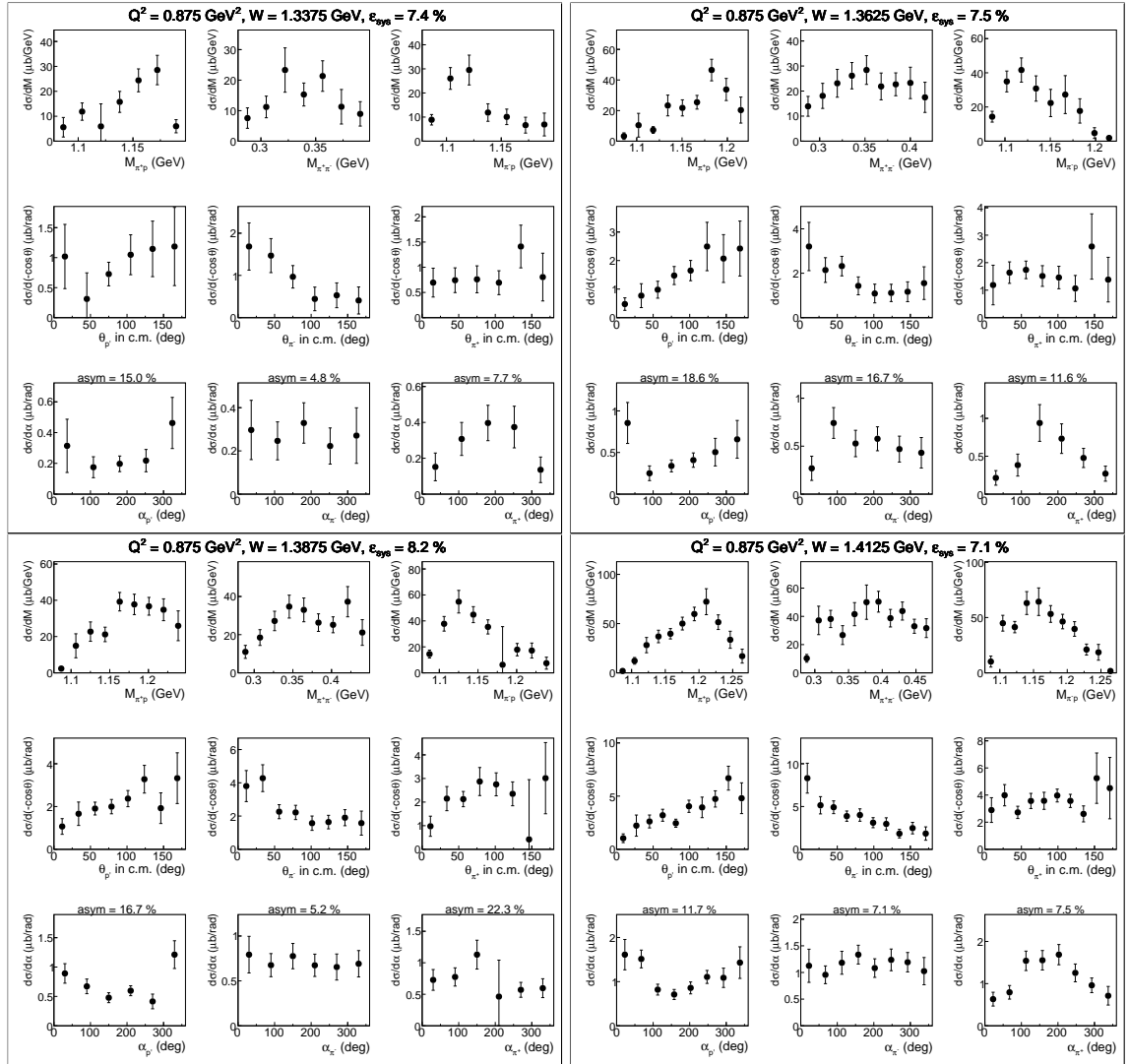


Figure A.49:

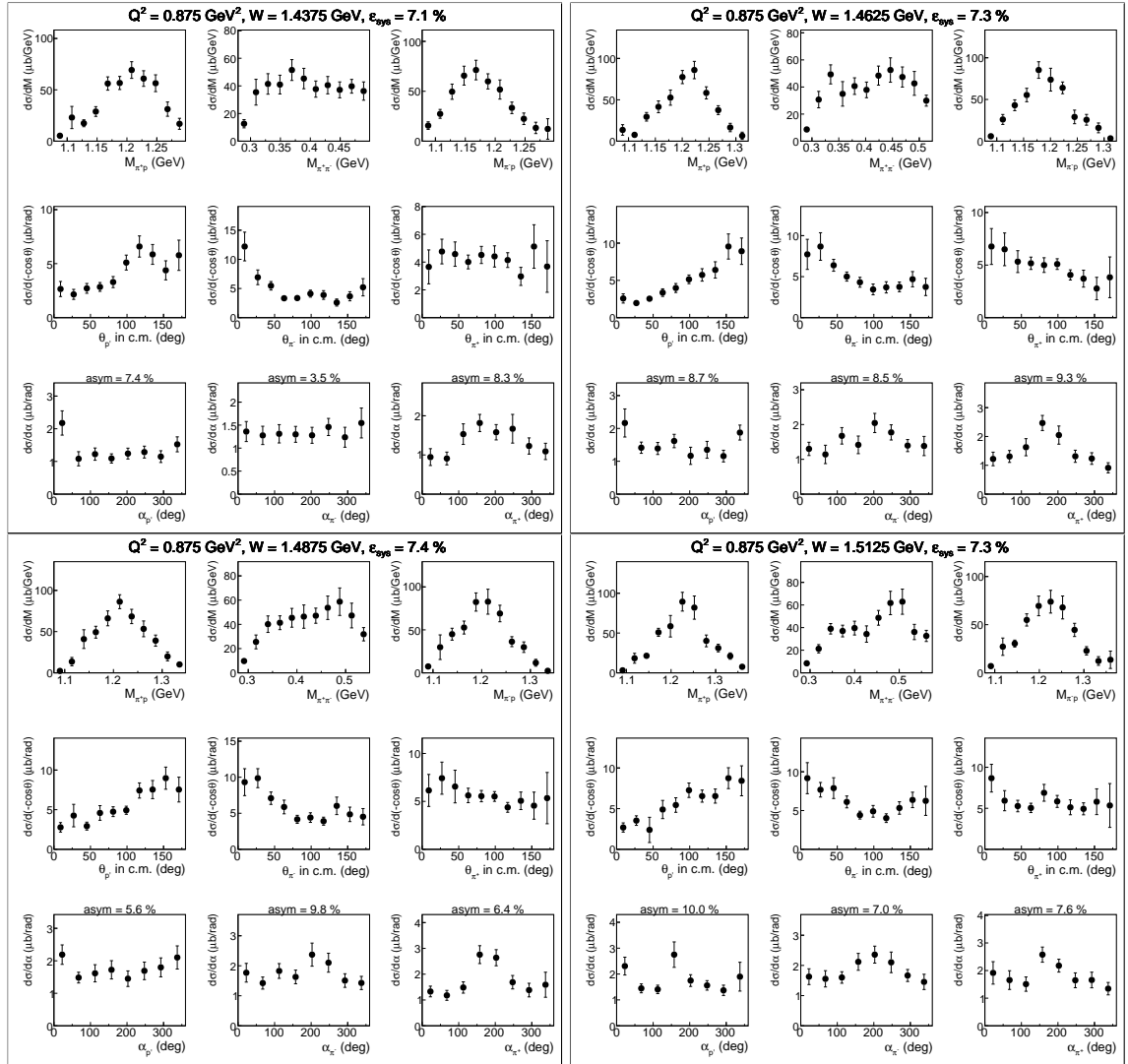


Figure A.50:

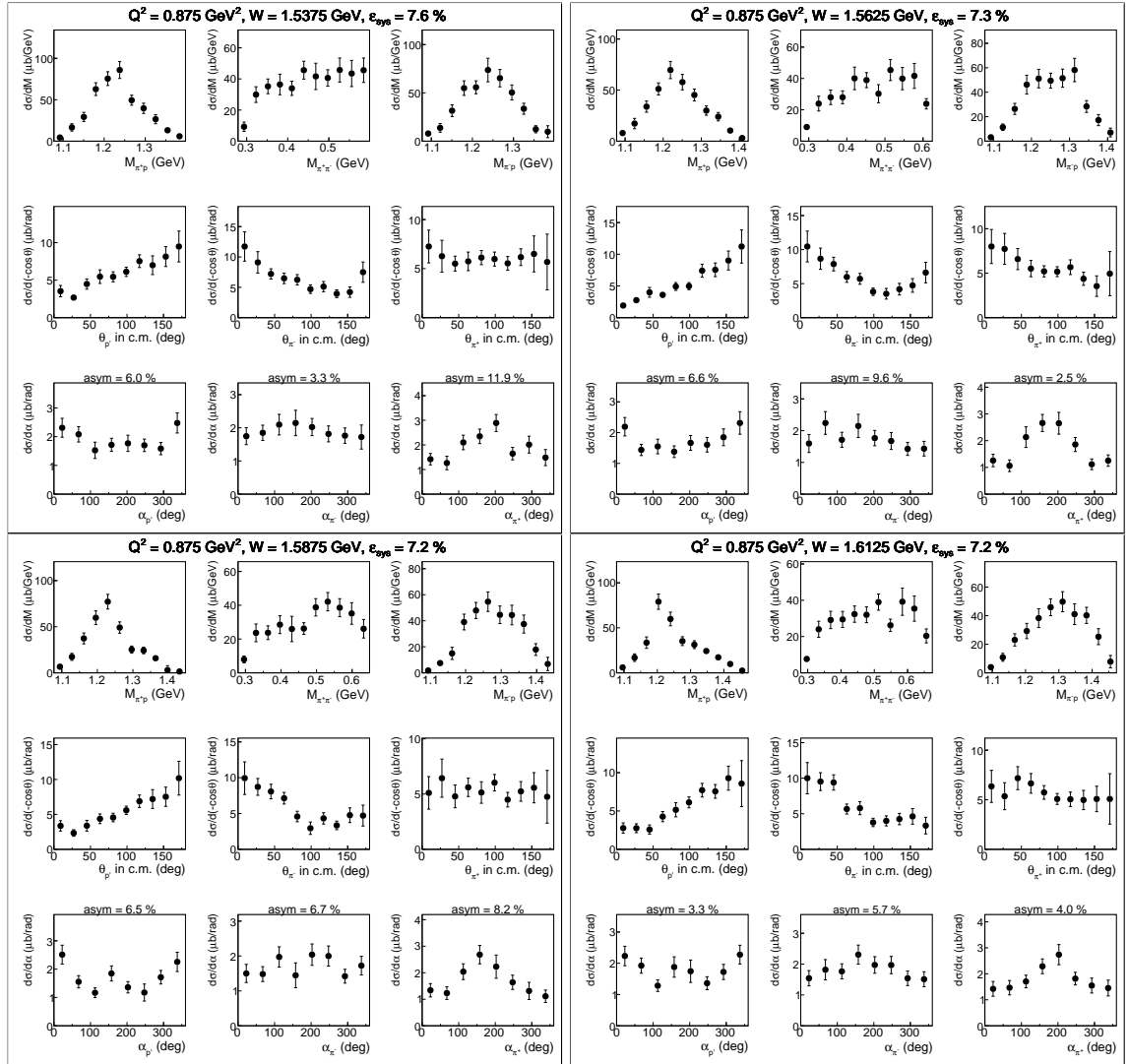


Figure A.51:

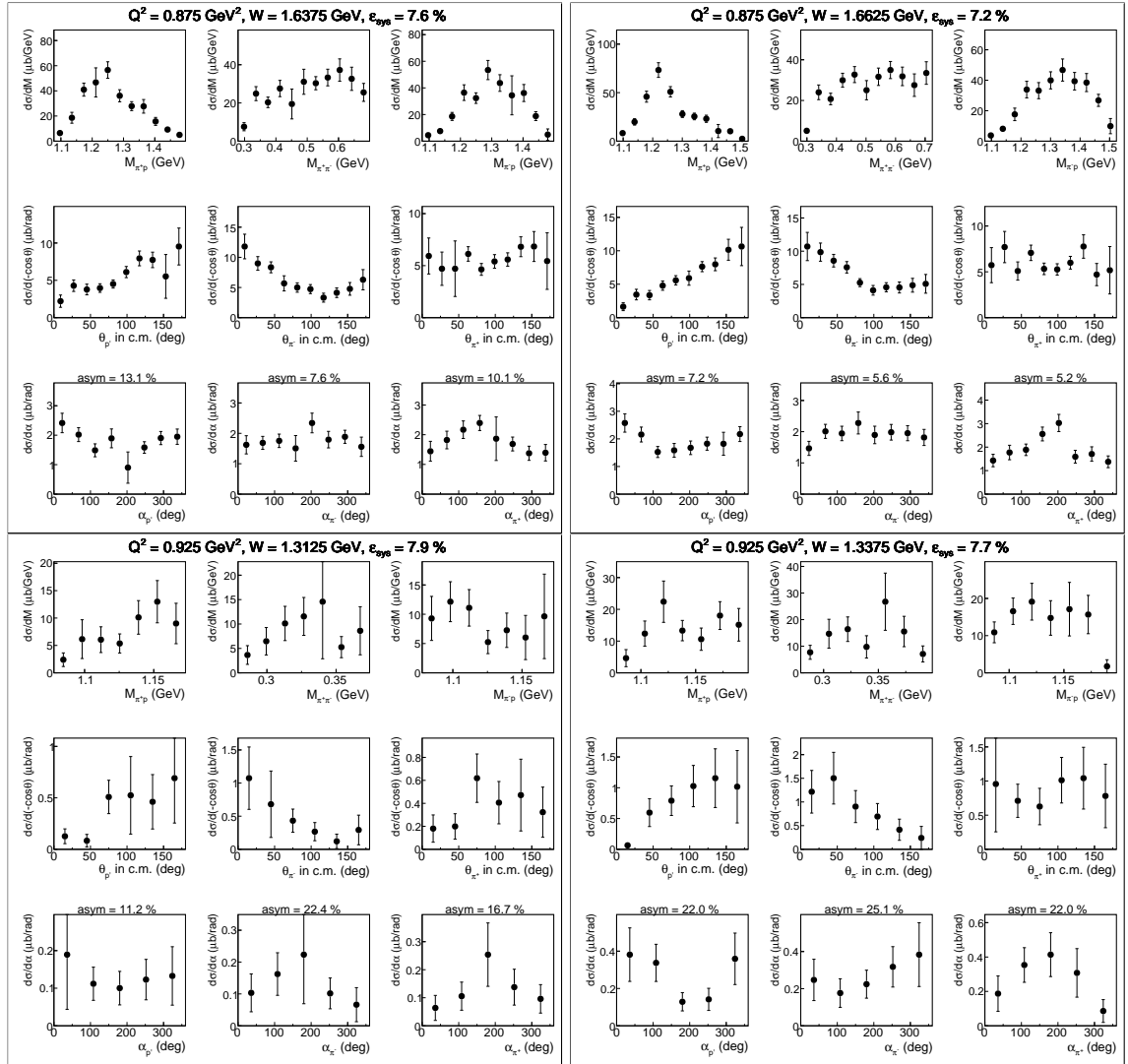


Figure A.52:

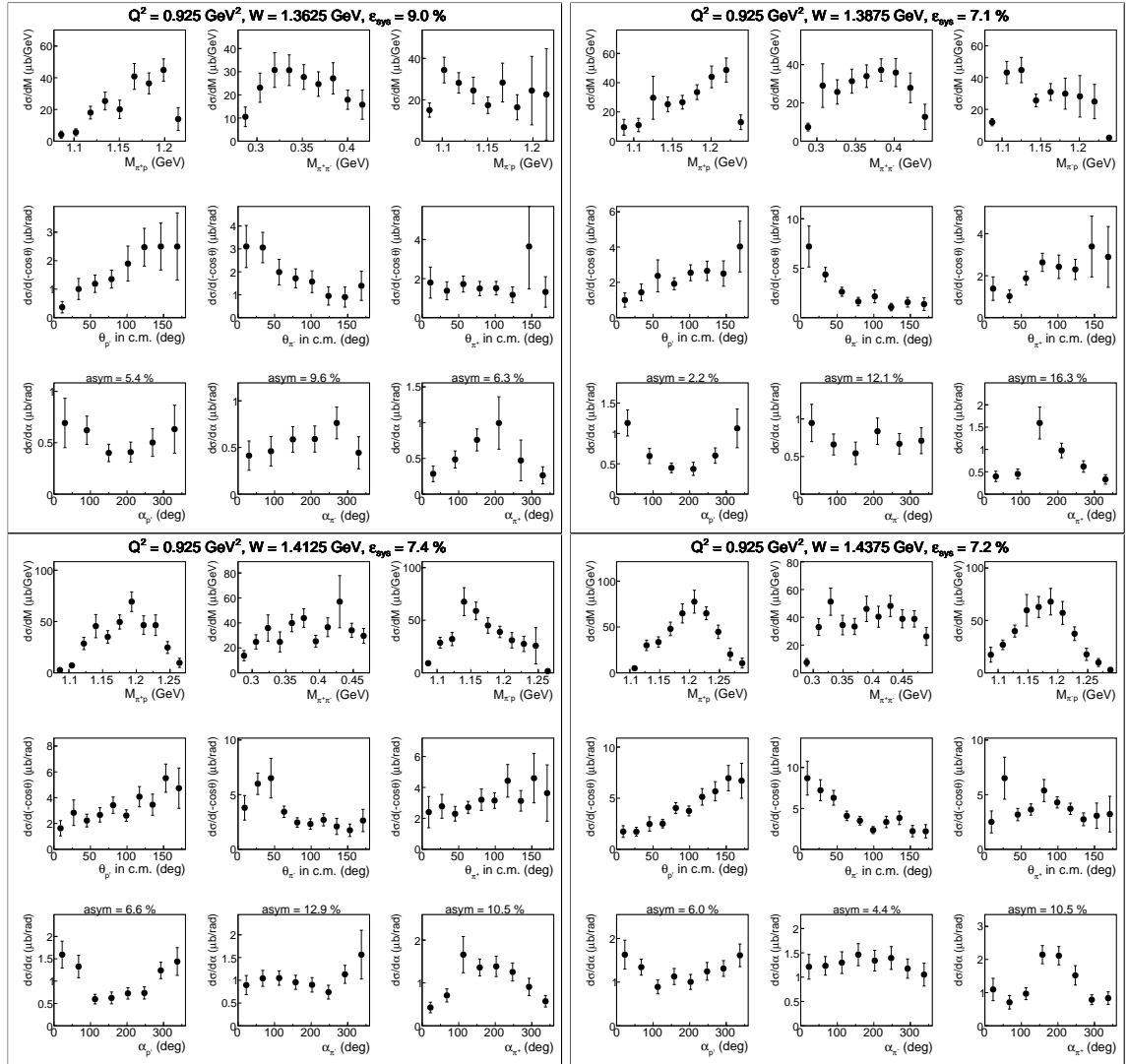


Figure A.53:

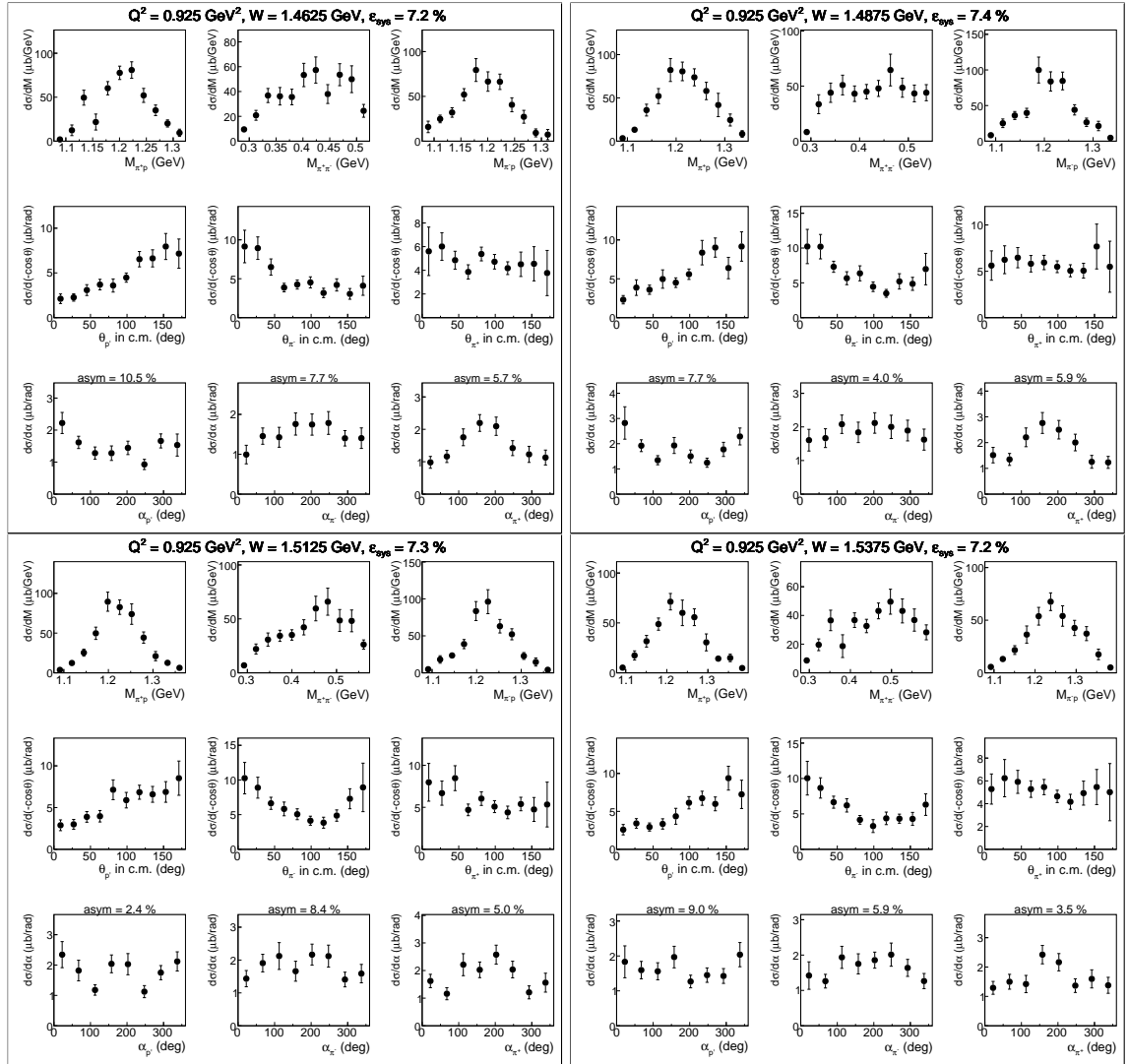


Figure A.54:

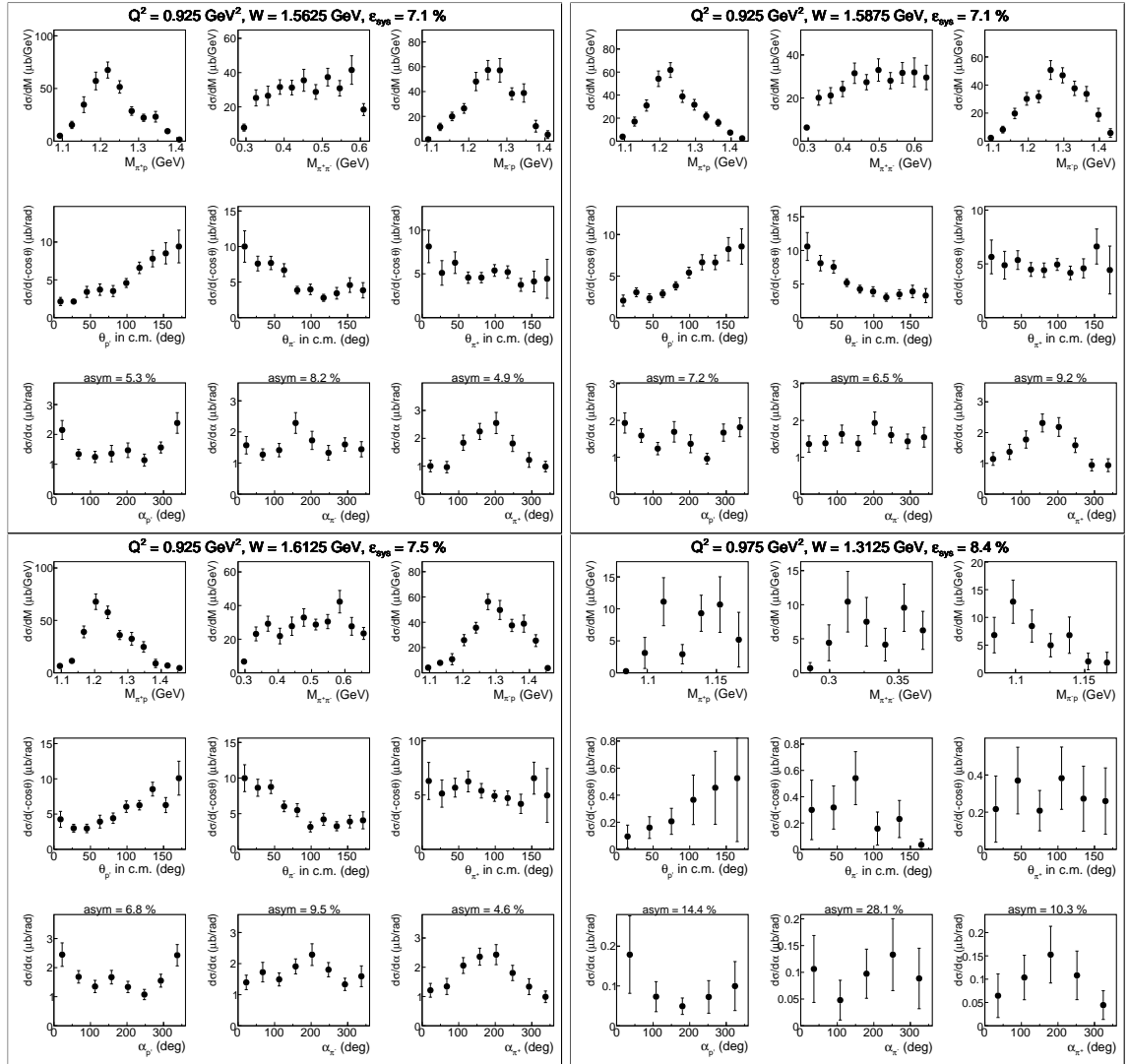


Figure A.55:

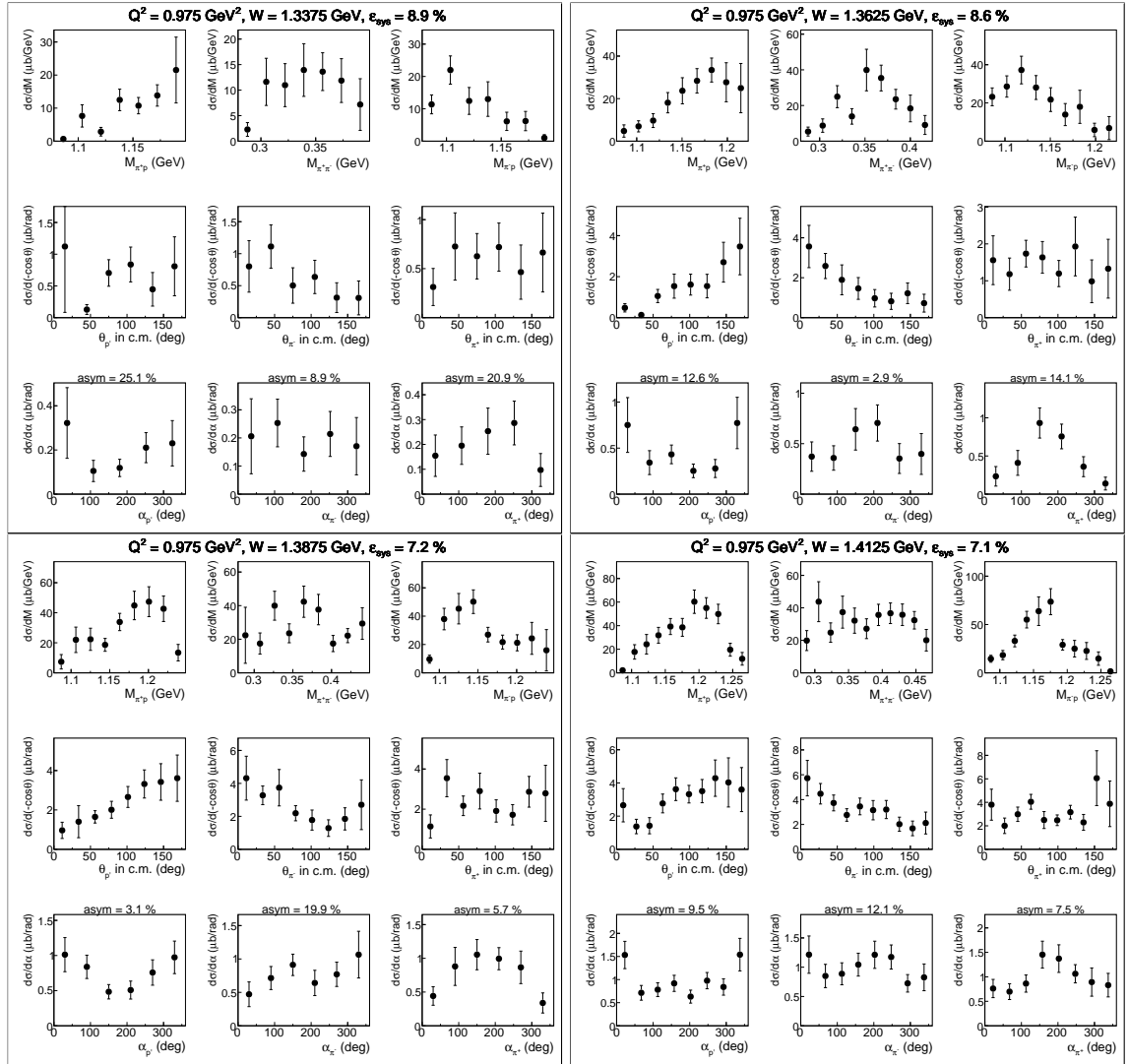


Figure A.56:

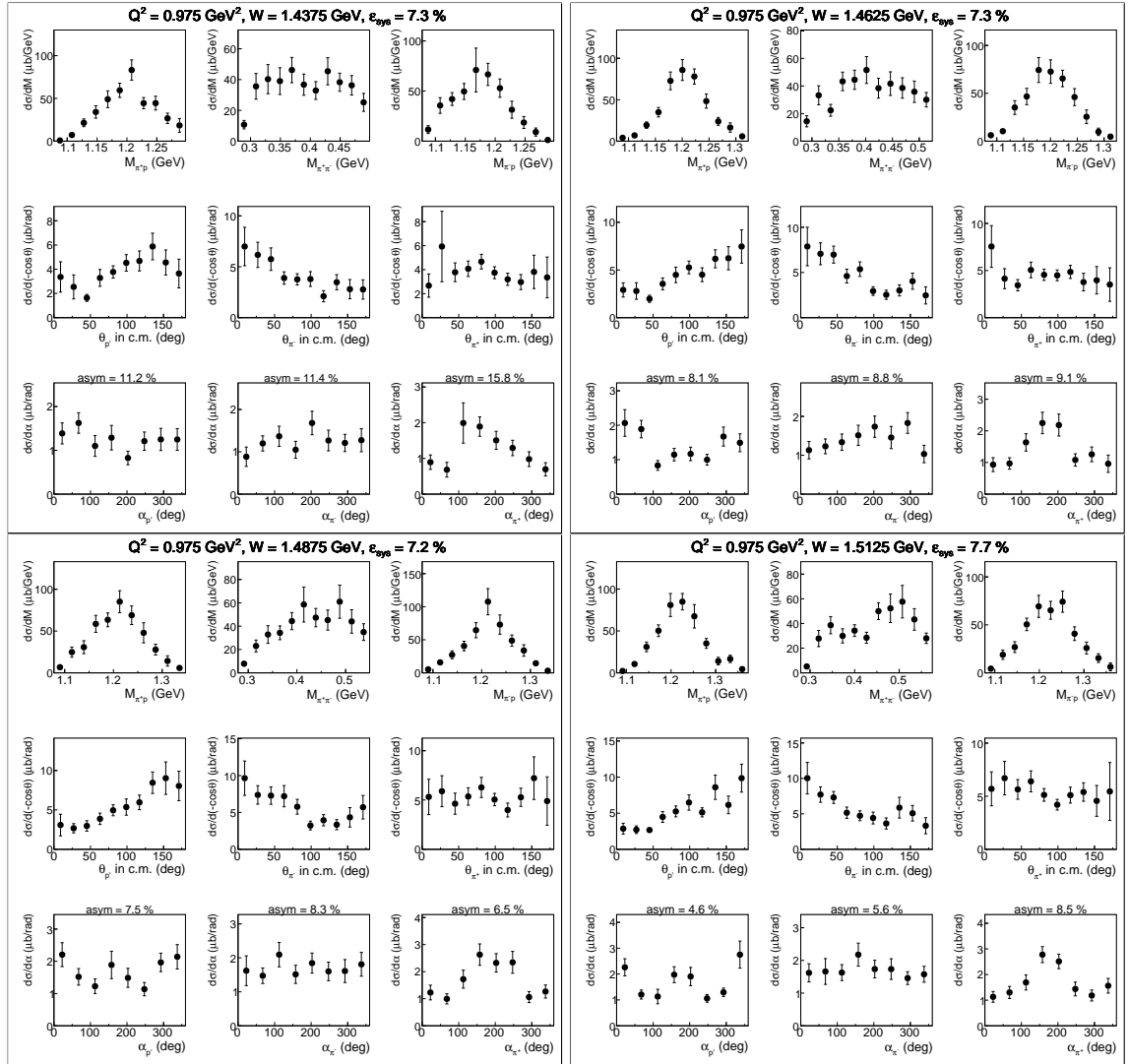


Figure A.57:

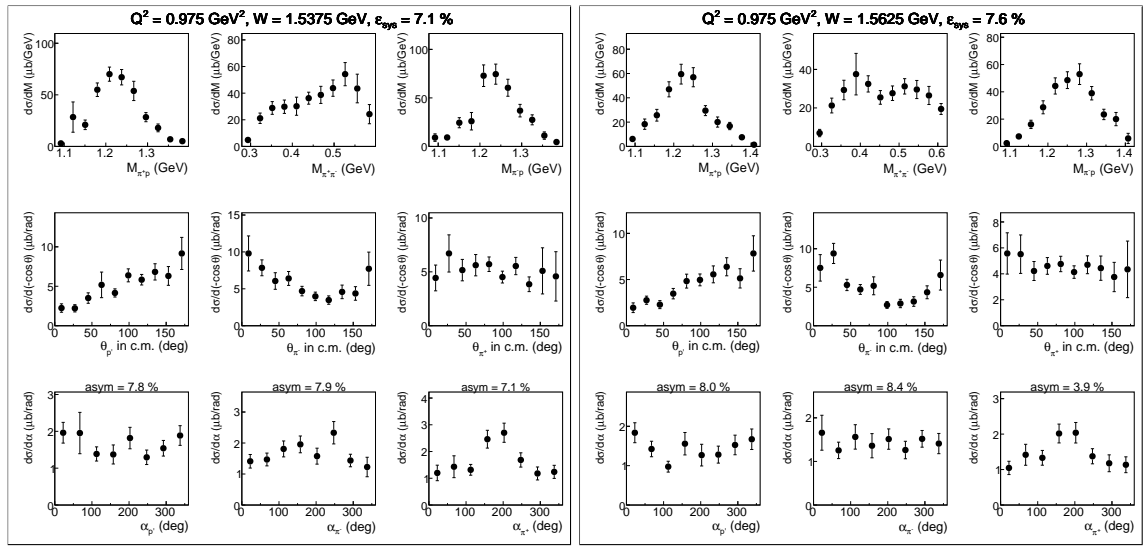


Figure A.58:

# Bibliography

- [1] B. Krusche and S. Schadmand, “Study of nonstrange baryon resonances with meson photoproduction,” *Prog. Part. Nucl. Phys.*, vol. 51, pp. 399–485, 2003.
- [2] I. G. Aznauryan and V. D. Burkert, “Electroexcitation of nucleon resonances,” *Prog. Part. Nucl. Phys.*, vol. 67, pp. 1–54, 2012.
- [3] Iu. A. Skorodumina *et al.*, “Nucleon resonances in exclusive reactions of photo- and electroproduction of mesons,” *Moscow Univ. Phys. Bull.*, vol. 70, no. 6, pp. 429–447, 2015. [Vestn. Mosk. Univ.,no.6,3(2015)].
- [4] B. A. Mecking *et al.*, “The CEBAF Large Acceptance Spectrometer (CLAS),” *Nucl. Instrum. Meth.*, vol. A503, pp. 513–553, 2003.
- [5] “CLAS physics database.” <http://clas.sinp.msu.ru/cgi-bin/jlab/db.cgi>.
- [6] V. I. Mokeev, E. Santopinto, M. M. Giannini, and G. Ricco, “The Influence of the nuclear medium on the baryon resonance excitation,” *Int. J. Mod. Phys.*, vol. E4, pp. 607–624, 1995  
[see also Refs.[1-5] there].
- [7] N. Bianchi *et al.*, “Absolute total photoabsorption cross-sections on nuclei in the nucleon resonance region,” *Phys. Lett.*, vol. B325, pp. 333–336, 1994.
- [8] J. Ahrens, “The Total Absorption of Photons by Nuclei,” *Nucl. Phys.*, vol. A446, pp. 229C–239C, 1985.
- [9] M. Osipenko *et al.*, “The deuteron structure function F2 with CLAS,” CLAS-NOTE-2005-013, arXiv:hep-ex/0507098, 2005.
- [10] M. Osipenko *et al.*, “Measurement of the deuteron structure function F(2) in the resonance region and evaluation of its moments,” *Phys. Rev.*, vol. C73, p. 045205, 2006.
- [11] M. Osipenko *et al.*, “Measurement of the Nucleon Structure Function F2 in the Nuclear Medium and Evaluation of its Moments,” *Nucl. Phys.*, vol. A845, pp. 1–32, 2010.

- [12] M. Osipenko *et al.*, “A Kinematically complete measurement of the proton structure function  $F(2)$  in the resonance region and evaluation of its moments,” *Phys. Rev.*, vol. D67, p. 092001, 2003.
- [13] B. Krusche, “Photoproduction of mesons from nuclei: In-medium properties of hadrons,” *Prog. Part. Nucl. Phys.*, vol. 55, pp. 46–70, 2005.
- [14] J. V. Noble, “Modification of the nucleon’s properties in nuclear matter,” *Phys. Rev. Lett.*, vol. 46, pp. 412–415, 1981.
- [15] M. Ripani *et al.*, “Measurement of Two Pion Decay of Electroproduced Light Quark Baryon States with CLAS,” *CLAS-Analysis-2002-109*, 2002.
- [16] M. Ripani *et al.*, “Measurement of  $ep \rightarrow e'p\pi^+\pi^-$  and baryon resonance analysis,” *Phys. Rev. Lett.*, vol. 91, p. 022002, 2003.
- [17] G. V. Fedotov *et al.*, “Analysis report on the  $ep \rightarrow e'p\pi^+\pi^-$  reaction in the CLAS detector with a 1.515 GeV beam for  $0.2 < Q^2 < 0.6$  GeV $^2$  and  $1.3 < W < 1.6$  GeV,” *CLAS-Analysis-2007-117*, 2007.
- [18] G. V. Fedotov *et al.*, “Electroproduction of  $p\pi^+\pi^-$  off protons at  $0.2 < Q^2 < 0.6$  GeV $^2$  and  $1.3 < W < 1.57$  GeV with CLAS,” *Phys. Rev.*, vol. C79, p. 015204, 2009.
- [19] E. L. Isupov *et al.*, “Measurements of  $ep \rightarrow e'\pi^+\pi^-p'$  Cross Sections with CLAS at  $1.40$  Gev  $< W < 2.0$  GeV and  $2.0$  GeV $^2 < Q^2 < 5.0$  GeV $^2$ ,” *Phys. Rev.*, vol. C96, no. 2, p. 025209, 2017.
- [20] E. Golovatch *et al.*, “First results on nucleon resonance photocouplings from the  $\gamma p \rightarrow \pi^+\pi^-p$  reaction,” *Phys. Lett.*, vol. B788, pp. 371–379, 2019.
- [21] A. Trivedi and R. W. Gothe, “Measurement of New Observables from the  $p\pi^+\pi^-$  Electroproduction off the Proton,” *CLAS-Analysis-2019-102*, 2018.
- [22] G. V. Fedotov *et al.*, “Analysis report on the  $ep \rightarrow e'p\pi^+\pi^-$  reaction in the CLAS detector with a 2.039 GeV,” *CLAS-Analysis-2017-101 (CLAS-NOTE-2018-001)*, 2017.
- [23] G. V. Fedotov *et al.*, “Measurements of the  $\gamma_vp \rightarrow p'\pi^+\pi^-$  cross section with the CLAS detector for  $0.4$  GeV $^2 < Q^2 < 1.0$  GeV $^2$  and  $1.3$  GeV  $< W < 1.825$  GeV,” *Phys. Rev.*, vol. C98, no. 2, p. 025203, 2018.
- [24] <http://clasweb.jlab.org/bos/browsebos.php>.
- [25] S. Stepanyan, “Proposal for the Production of the DST’s to Distribute CLAS Data,” *CLAS-NOTE-99-002*, 1999.

- [26] Iu. Skorodumina, G. V. Fedotov, and R. W. Gothe, “TWOPEG-D: An Extension of TWOPEG for the Case of a Moving Proton Target,” *CLAS12-NOTE-2017-014*, 2017, arXiv:1712.07712.
- [27] K. Egiyan *et al.*, “Determination of electron energy cut due to the CLAS EC threshold,” *CLAS-NOTE-99-007*, 1999.
- [28] G. Adams *et al.*, “The CLAS Cherenkov detector,” *Nucl. Instrum. Meth.*, vol. A465, pp. 414–427, 2001.
- [29] M. Osipenko, A. Vlassov, and M. Taiuti, “Matching between the electron candidate track and Cherenkov counter hit,” *CLAS-NOTE-2004-020*, 2004.
- [30] P. K. Khetarpal, *NEAR THRESHOLD NEUTRAL PION ELECTROPRODUCTION AT HIGH MOMENTUM TRANSFERS*. Ph. D. Thesis: [https://www.jlab.org/Hall-B/general/thesis/Khetarpal\\_thesis.pdf](https://www.jlab.org/Hall-B/general/thesis/Khetarpal_thesis.pdf).
- [31] M. Ungaro and K. Joo, *e1-6 Electron Identification*. CLAS web page: <https://userweb.jlab.org/~ungaro/maureepage/proj/pi0/e-pid/e-pid.html>.
- [32] S. T. G. Mutcler and E. Smith, “CLAS TOF Scintillator Positions,” *CLAS-NOTE-1998-008*, 1998.
- [33] K. Park *et al.*, “Kinematics Corrections for CLAS,” *CLAS-Note-2003-012*, 2003.
- [34] “e1e target assembly.” [https://userweb.jlab.org/~skorodum/e1e\\_target/tar\\_e1e\\_web.pdf](https://userweb.jlab.org/~skorodum/e1e_target/tar_e1e_web.pdf).
- [35] Yu. Skorodumina *et al.*, “Investigating of the exclusive reaction of  $\pi^+\pi^-$  pair electroproduction on a proton bound in a deuteron,” *Bull. Russ. Acad. Sci. Phys.*, vol. 79, no. 4, pp. 532–536, 2015. [Izv. Ross. Akad. Nauk Ser. Fiz. 79, no. 4, 575 (2015)].
- [36] Iu. Skorodumina, G. V. Fedotov, *et al.*, “TWOPEG: An Event Generator for Charged Double Pion Electroproduction off Proton,” *CLAS12-NOTE-2017-001*, 2017, arXiv/1703.08081[physics.data-an].
- [37] R. Machleidt, K. Holinde, and C. Elster, “The Bonn Meson Exchange Model for the Nucleon Nucleon Interaction,” *Phys. Rept.*, vol. 149, pp. 1–89, 1987.
- [38] E. Byckling and K. Kajantie, *Particle Kinematics*. Jyvaskyla, Finland: University of Jyvaskyla, 1971.
- [39] L. W. Mo and Y.-S. Tsai, “Radiative Corrections to Elastic and Inelastic  $ep$  and  $\mu p$  Scattering,” *Rev. Mod. Phys.*, vol. 41, pp. 205–235, 1969.
- [40] N. Markov *et al.*, “Single  $\pi^0$  Electroproduction off the Proton in the Resonance region,” *CLAS-Analysis-2014-106*, 2014.

- [41] B. Laforge and L. Schoeffel, “Elements of statistical methods in high-energy physics analyses,” *Nucl. Instrum. Meth.*, vol. A394, pp. 115–120, 1997.
- [42] E. N. Golovach *et al.* <http://depni.sinp.msu.ru/~golovach/EG/>.
- [43] Y. Tian and R. W. Gothe, “Exclusive  $\pi^-$  Electroproduction off the Neutron in Deuterium in the Resonance Region,” *CLAS-Analysis-2021-101*, 2020.
- [44] Iu. Skorodumina, G. V. Fedotov, and R. W. Gothe, “Testing Parameterizations of the Deuteron Quasi-Elastic Peak,” *CLAS12-NOTE-2019-003*, 2019, arXiv:2003.02337.
- [45] P. Bosted *et al.* <https://userweb.jlab.org/~bosted/fits.html>.
- [46] P. E. Bosted and M. E. Christy, “Empirical fit to inelastic electron-deuteron and electron-neutron resonance region transverse cross-sections,” *Phys. Rev.*, vol. C77, p. 065206, 2008.
- [47] K. M. Hanson, J. R. Dunning, M. Goitein, T. Kirk, L. E. Price, and R. Wilson, “Large angle quasielastic electron-deuteron scattering,” *Phys. Rev.*, vol. D8, pp. 753–778, 1973.
- [48] S. Rock, R. G. Arnold, P. E. Bosted, B. T. Chertok, B. A. Mecking, I. A. Schmidt, Z. M. Szalata, R. York, and R. Zdarko, “Measurement of elastic electron - neutron scattering and inelastic electron - deuteron scattering cross-sections at high momentum transfer,” *Phys. Rev.*, vol. D46, pp. 24–44, 1992.
- [49] S. Rock *et al.*, “Measurement of elastic electron - neutron scattering and inelastic electron - deuteron scattering cross-sections at high momentum transfer,” *SLAC-PUB-5239*, 1991.
- [50] A. Bodek, M. E. Christy, and B. Coopersmith, “Effective Spectral Function for Quasielastic Scattering on Nuclei,” *Eur. Phys. J.*, vol. C74, no. 10, p. 3091, 2014.
- [51] L. Durand, “Inelastic Electron-Deuteron Scattering Cross Sections at High Energies. 2. Final-State Interactions and Relativistic Corrections,” *Phys. Rev.*, vol. 123, pp. 1393–1422, 1961.
- [52] P. E. Bosted, “An Empirical fit to the nucleon electromagnetic form-factors,” *Phys. Rev.*, vol. C51, pp. 409–411, 1995.